

Dissertation
submitted to the
Combined Faculty of Mathematics, Engineering and Natural Sciences
of Heidelberg University, Germany

for the degree of
Doctor of Natural Sciences

Put forward by
Riccardo Franceschi
born in: San Benedetto del Tronto, Italy

Oral examination: November 6th, 2023

THE FUNDAMENTAL PROPERTIES OF PLANET-FORMING
DISKS: A MODEL-DATA COMPARISON

RICCARDO FRANCESCHI

REFEREES:

PROF. DR. THOMAS HENNING
PROF. DR. MATTHIAS BARTELMANN

Abstract

This thesis presents a comprehensive investigation of the properties of protoplanetary disks, the birthplaces of planets. This work is motivated by the rapidly increasing quality of observational data, which necessitates better theories and ways to compare them with what we observe.

Firstly, we showcase how the size of the millimeter continuum emitting region constrains disk masses. We assess the method's efficacy by conducting detailed dust evolution calculations and considering diverse disk properties, particularly in disks exhibiting radial substructures.

We then constrain the disk dust grain size distribution by observing only the largest and smallest grains within it. Merging physical dust models with radiative transfer calculations, we compare the model outcomes with the observations of the IM Lup disk, revealing a segregated grain size distribution and providing new insight into grain formation mechanisms and potential triggers for planetesimal formation.

Additionally, we characterize the inner disk of the very low-mass star 2MASS-J16053215-1933159 through atomic and molecular hydrogen lines. Using the observational capabilities of the James Webb Space Telescope (JWST), we measure gas temperature, mass, and the stellar accretion rate while showcasing JWST potential in the characterization of protoplanetary disk structures.

Lastly, we investigate the gas density and temperature across Class II protoplanetary disks in Taurus using the NOEMA instrument. Employing machine-learning-enhanced chemistry and analyzing optically thin and thick CO isotopologue emission, we successfully constrain disk masses and temperatures.

Zusammenfassung

Diese Arbeit präsentiert eine umfassende Untersuchung der Eigenschaften protoplanetarischer Scheiben, den Geburtsorten der Planeten. Diese Arbeit ist durch die schnell zunehmende Qualität der Beobachtungsdaten motiviert, die bessere Theorien und Möglichkeiten, diese Daten mit dem Beobachteten zu vergleichen, erforderlich macht.

Zunächst zeigen wir, wie die Größe der Millimeter-Kontinuumemissionsregion die Scheibenmassen einschränkt. Durch die Durchführung detaillierter Berechnungen der Staubeentwicklung und bei Berücksichtigung verschiedener Scheibeneigenschaften beurteilen wir die Wirksamkeit der Methode, insbesondere bei Scheiben mit radialen Unterstrukturen.

Anschließend schränken wir die Verteilung der Korngröße des Scheibenstaubs ein, indem wir nur die größten und kleinsten Körner darin beobachten. Indem wir physikalische Staubmodelle mit Berechnungen des Strahlungstransports kombinieren, vergleichen wir die Modellergebnisse mit den Beobachtungen der IM-Lup-Scheibe, offenbaren eine getrennte Korngrößenverteilung und liefern neue Einblicke in die Kornbildungsmechanismen und mögliche/potentiale Auslöser für die Bildung von Planetesimalen.

Zusätzlich charakterisieren wir die innere Scheibe des sehr massearmen Sterns 2MASS-J16053215-1933159 durch atomare und molekulare Wasserstofflinien. Mithilfe der Beobachtungsmöglichkeiten des James Webb Space Telescope (JWST) messen wir die Gastemperatur, die Masse und die Sternakkretionsrate und demonstrieren gleichzeitig das Potenzial des JWST bei der Charakterisierung protoplanetarischer Scheibenstrukturen.

Schließlich untersuchen wir mit dem NOEMA-Instrument die Gasdichte und -temperatur in protoplanetaren Scheiben der Klasse II im Taurus. Durch den Einsatz von durch maschinelles Lernen unterstützter Chemie und durch die Analyse optisch dünner und dicker CO-Isotopologemissionen können wir Scheibenmassen und Temperaturen erfolgreich einschränken.

Alla mia famiglia.

Contents

1	Introduction	1
1.1	Background	2
1.2	The ingredients of a protoplanetary disk	5
1.2.1	Mass	7
1.2.2	Vertical structure	10
1.2.3	Substructures	11
1.2.4	Temperature	13
1.2.5	Astrochemistry in disks	14
1.3	Thesis motivation and outline	17
2	Modeling a protoplanetary disk	19
2.1	Disk physical model	19
2.1.1	Radial density distribution	19
2.1.2	Thermal structure	21
2.1.3	Vertical density distribution	22
2.2	Dust structure	23
2.3	Simulating the observations: radiative transfer	25
2.4	The radiative transfer equation	26
3	Mass determination from dust evolution	29
3.1	Motivation	29
3.2	Methodology	31
3.3	Dust line location	35
3.3.1	Dust line definition	35
3.3.2	Radial density bumps	37
3.3.3	Fragmentation velocity	38
3.4	Simulation results	38
3.5	Population synthesis	43
3.6	Surface density distributions with pressure bumps	48
3.7	Applicability to individual disks	50
3.7.1	TW Hya	52
3.7.2	AS 209	56
3.8	Summary and conclusions	58
4	Constraining the turbulence and the dust disk in IM Lup: Onset of planetesimal formation	61
4.1	Motivation	61
4.2	Disk model	64

4.2.1	Vertical structure	65
4.2.2	Dust	66
4.2.3	Dust opacity	68
4.3	Observations	70
4.3.1	Near-infrared scattered light: height of small grain distribution	71
4.3.2	Millimeter continuum emission: Large grains in the disk midplane	72
4.4	Inferred disk model parameters	74
4.4.1	Dust mass	76
4.4.2	Distribution of the dust populations	80
4.4.3	Grain evolution timescales	83
4.4.4	Viscous turbulence parameter	87
4.5	Fitting the outer disk	87
4.6	Conclusions	90
5	Mid-infrared atomic and molecular hydrogen lines in the inner disk around a low-mass star	93
5.1	Motivation	93
5.2	Observations	95
5.3	Analysis and Results	97
5.3.1	Molecular hydrogen	97
5.3.2	Atomic hydrogen	100
5.3.3	Atomic line emission models	104
5.4	Discussion	108
5.5	Conclusions	110
6	Modeling the CO isotopologs emission of the T Tauri stars in the Taurus region	113
6.1	Motivation	113
6.2	Observations	115
6.3	Disk model	117
6.3.1	Physical model	117
6.3.2	Chemical model	120
6.3.3	Fitting to the observations	121
6.4	Results	122
6.4.1	Temperature profiles	127
6.4.2	Disk vertical structure	127
6.4.3	Foreground cloud absorption	128
6.5	Conclusions	128
7	Summary and Outlook	131
7.1	Summary	131
7.2	Outlook	133
A	PRODIGE model-data comparison	137
	List of Figures	151
	List of Tables	155

CHAPTER 1

Introduction

Wondering about the origin of the Earth is perhaps an inevitable consequence of the emergence of consciousness in human beings, marking the beginning of our history. Theories about the origin of the World can be found in many early writings, tracing back to 6 000 years ago, but they arguably survived in oral form for up to 10 000 years, with every culture developing its own creation myth. These theories, while could be viewed as early attempts at science, are grounded in a religious-philosophical framework. Among these theories, the ancient Greek philosophers are particularly noteworthy. Their contributions have left an enduring impact on modern astronomy, with many contemporary viewpoints tracing back to their ideas, observations, and methodologies. For instance, Eratosthenes (276-194 BCE) calculated the Earth circumference using shadows cast by the Sun at different locations, giving a first understanding of planetary distances. The first star catalog traces back to Hipparchus (190-120 BCE), the "Hipparchus Catalogue," containing over 1 000 stars. Ptolemy (90-168 CE) authored the "Almagest", a seminal work on the motions of planets and stars, and is considered one of the most influential scientific texts in history. While his geocentric model placed Earth at the center of the universe, the Almagest observations and calculations replaced most older views in astronomy and laid the groundwork for subsequent theories.

However, it wasn't until the 18th century that the investigation of Earth's origin was put into a scientific framework, departing from mythological explanations thanks to the introduction of the nebular theory. Emanuel Swedenborg, a Swedish scientist and theologian, laid the early groundwork by proposing that stars and planets originate from a primordial nebula. The formation and evolution of planetary systems were also famously studied by the philosopher Emmanuel Kant, who argued that the planets in the Solar System formed by local density enhancement of material around the Sun. Building on these ideas, French mathematician and

astronomer Pierre-Simon Laplace refined this theory. He suggested that planets originate from a vast cloud of gas and dust, or nebula, in space, collapsing due to gravity and spinning into a disk. The core forms a star, while the remaining material births planets and celestial bodies. This description closely mirrors the current understanding of planet formation.

Fast forward to our days, planet formation studies are now strictly part of natural sciences. For astronomers, this is a particularly fascinating topic not only because of our curiosity but because it is the only field in astronomy where it is possible to go beyond the detection of radiation from faraway sources. The Earth and our Solar System are perfect laboratories which we explored with a large number of space missions since 1959 when the spacecraft *Luna 1* was the first object to leave the Earth's gravitational zone.

1.1 Background

Protoplanetary disks are an inevitable consequence of star formation processes and are thought to be the nursery of planets. This idea is supported by the ever-increasing number of observed substructures resulting from the perturbations caused by planet-formation processes. Therefore, the characterization of the physical and chemical properties of planet-forming disks is fundamental to understanding planet formation. Star formation process originates in molecular clouds, composed of cold interstellar gas (mostly molecular hydrogen) and dust resulting from the galaxy evolution processes. These clouds are not homogeneous, static structures. Initially, they are held together by a balance of gravity and gas pressure force, turbulence, and magnetic field pressure. Local perturbations, however, can trigger gravitational instabilities in a fragment of the cloud, which collapses isothermally. Due to the presence of angular momentum within the collapsing region, the collapse results in the formation of a circumstellar disk perpendicular to the direction of the annular momentum. These disks are also called protoplanetary disks because they contain enough material to form planets and they are thought to harbor planet formation processes (e.g., Dutrey et al. 2004; Mordasini et al. 2012; Birnstiel et al. 2016). However, only a small percentage of this angular momentum will be transferred to the forming star itself (Shu et al. 1987). As the gas collapses, the rotation of the core increases due to the conservation of angular momentum until it becomes fast enough to prevent further accretion. Instead, the infalling material forms a disk around the core. Most of the angular momentum is then redistributed to a small portion of gas retained in a disk with a size ranging from 100 au to 1000 au Terebey et al. 1984. This phenomenon can be observed in our own Solar System, where the Sun contains 99.96% of the total mass, but only

0.6% of the total angular momentum, while the majority of the angular momentum is found in the orbiting planets and debris. As the central object continues to collapse, the density increases and the forming core becomes more and more opaque to its own radiation. This leads to an increase in temperature and pressure until the gravitational collapse halts, forming a hydrostatic core. New material keeps flowing on this core until it reaches temperatures high enough to dissociate H_2 molecules (between 2000 K and 3000 K) and ionize atomic hydrogen ($\sim 10^4$ K). The dissociation of these species drains energy from the core, which can resume its collapse until a second hydrostatic core is formed, and a protostar is born.

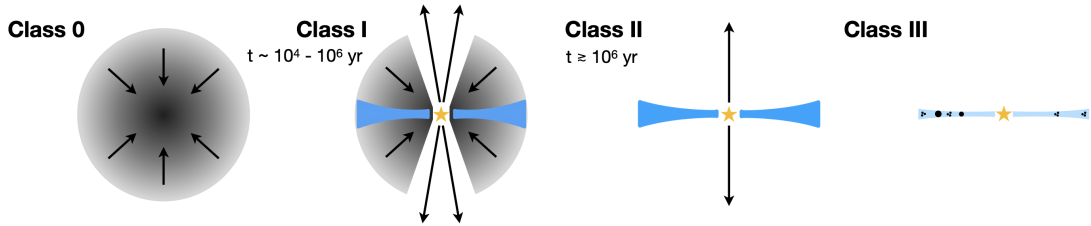


Figure 1.1: Evolutionary phases of a YSO, showing the different geometries at each phase, as described in the text. Credit: Pohl (2018).

Protoplanetary disks are expected to be observable around low-to-intermediate mass Young Stellar Objects (YSOs), stars that are yet to initiate hydrogen-to-helium fusion and enter the Main Sequence (MS) stage of evolution. High-mass stars evolve fast, and they are still accreting material from their environment while they reach the MS. The intense radiation from MS stars cleans up their neighborhood, and all the information about their birth environment is lost. Low-mass stars ($< 2 M_{\odot}$) before reaching the MS are called T Tauri stars (Joy 1942, 1945, 1949), while intermediate-mass stars ($2 - 8 M_{\odot}$) are called Herbig Ae/Be stars (Herbig 1960; Strom et al. 1975; Finkenzeller & Mundt 1984). The physical properties of YSOs are often derived from their spectral energy distribution (SED), measuring the emitted flux as a function of frequency or wavelength. Depending on the amount and distribution of circumstellar material, the SED will have different profiles as this material absorbs the radiation from the central protostar and re-emits it at different wavelengths. The classification commonly used in the literature follows the disk evolutionary stages, from the formation of the protostar to when it reaches its MS. The classification scheme is:

- **Class 0:** Earliest evolution stage of YSOs, they are embedded in a high-mass envelope, residual of the collapsing fragment of the molecular cloud, and undergo significant accretion. The dense envelope obscures the light emitted by the YSO, and it is not visible at the optical wavelengths. They

are detected by their thermal emission at longer wavelengths ($> 10 - 20 \mu\text{m}$), with a SED peaking at far-infrared or millimeter wavelengths.

- **Class I:** These objects are more evolved than Class 0 YSOs, have a less massive envelope, and are starting to clear their surroundings. The central star is now visible at mid-infrared wavelengths. The SED has, therefore, a rising contribution at near-infrared wavelengths, and peaks in the mid or far-infrared emission.
- **Class II:** These sources are characterized by a prominent protoplanetary disk, and the envelope is now completely dispersed. The disk is characterized by an optically thick emission in the infrared while being optically thin at millimeter and sub-millimeter wavelengths.
- **Class III:** In the later stages, the gaseous disk is completely dispersed, and their SED shows very little to no excess in the infrared. A debris disk, responsible for any surviving infrared excess, or a planetary system, now surrounds the star.

Once the disk is formed, it reaches a steady-state solution for its density, temperature, and velocity distributions. However, the disk structure is not in an equilibrium state. These disks keep accreting material onto the star, with typical accretion rates between $10^{-10} M_{\odot}/\text{yr}$ and $10^{-8} M_{\odot}/\text{yr}$ (e.g., Gullbring et al. 1998a; Andrews et al. 2010; Manara et al. 2016; Rigliaco et al. 2015; Manara et al. 2023). This accretion is driven by the removal of angular momentum through turbulent viscosity, driving stellar outflows and winds dispersing what is left of the molecular cloud over a timescale of $10^4 - 10^5$ yr, leaving behind just the YSO and its circumstellar material. The observational signatures of the accretion are ultraviolet (UV) continuum excess from the shock of material falling onto the central star, extremely broad emission lines, (such as H_{α} , Br_{γ} , and Ca II , and forbidden emission lines from stellar winds and jets (Muzerolle et al. 1998; Calvet et al. 2004; Natta et al. 2006; Herczeg & Hillenbrand 2008; Rigliaco et al. 2012; Antonucci et al. 2014; Alcalá et al. 2019; Manara et al. 2023).

However, the total angular momentum has to be conserved and for the matter to flow inwards, angular momentum should be transported outwards. Still, a steady state solution for the disk can be found since the accretion timescales are much longer than the dynamical timescale of the disk which Shakura & Sunyaev (1973) argued (in the context of black hole accretion, but it can be adapted for protoplanetary disks) that this can be achieved by a disk-wide viscosity described by the parameter ν :

$$\nu = \alpha c_s H, \quad (1.1)$$

where α is a proportionality factor, H the disk pressure scale height, and c_s the sound speed. This is known as the α -prescription, from which it derives the α -disk model, the standard disk model used in the literature (Lynden-Bell & Pringle 1974; Pringle 1981).

As with the molecular clouds from which originates, protoplanetary disks are composed of 99% gas and 1% dust. Knowledge of the total dust mass and dust evolution processes is crucial for planet formation studies since dust grains are the building blocks of planets. However, since the gas dominates the disk structures, it sets the physical and chemical conditions of the environment in which the grains evolve. Therefore, simultaneous observations of the gas molecular emission and the dust thermal emission are necessary to constrain the environment of planet formation processes. For instance, the gas viscosity in Eq.1.1 determines how efficiently the gas flows drag dust grains in their motions, facilitating their mutual collisions. When colliding, these grains can stick together and grow, starting planet formation processes (see Chapter 3 and Chapter 4, Brauer et al. (2008); Birnstiel & Andrews (2014); Birnstiel et al. (2016); Powell et al. (2017)). While small grains are coupled to the gas structure and follow its motions, large grains are less affected by the gas and slowly settle in the midplane. Moreover, the gas orbit is supported by both the centrifugal velocity and the radial pressure force, resulting in an orbit with a sub-Keplerian velocity. The large grains, decoupled from the gas, are not affected by the pressure gradient, and will therefore orbit at their Keplerian velocity. The differential velocity between gas and dust causes a headwind against the grains, making them lose angular momentum and drift toward the central object. For this reason, the large grains are only found in a thin layer in the disk midplane and are less radially extended than gas or small grains. The observations of the protoplanetary disk HD 163296 in Figure 1.2 (de Gregorio-Monsalvo et al. 2013) clearly show the difference between the compact continuum emission of large grains due to their radial drift and the extended gas structure, traced by the CO emission. This further proves that dust and gas evolve differently, but not independently from each other.

1.2 The ingredients of a protoplanetary disk

Protoplanetary disks inherit the composition of the molecular cloud where they form. However, unlike those clouds, the majority of the solid mass within the disks is concentrated in substantial millimeter-sized grains. These grains are not well

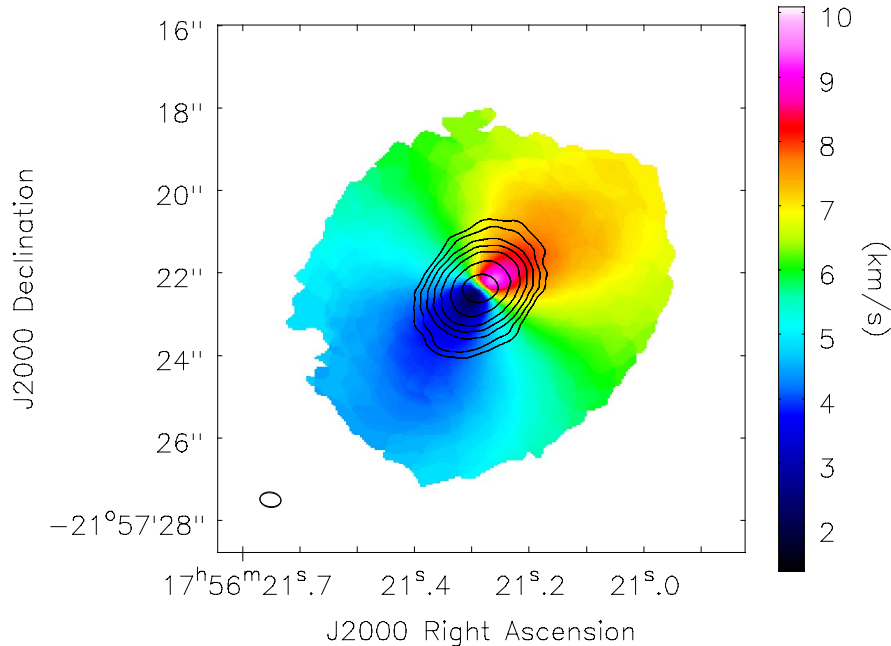


Figure 1.2: Dust and gas emission observed in the protoplanetary disk HD 163296 (de Gregorio-Monsalvo et al. 2013). The contours show the dust continuum emission at $870 \mu\text{m}$, while the color map shows the CO (3-2) emission integrated over all the velocity channels. The elliptical $0.5'' \times 0.7''$ beam is shown in the bottom left, corresponding to $60 \text{ au} \times 84 \text{ au}$ at the source distance of 122 pc.

mixed to the gas but are instead confined to a thin layer in the midplane region of the disk (see Figure 1.3). The bulk of the gas is composed of H_2 molecules, with typical temperatures below 100 K. The dust initially inherits the same properties as interstellar dust and is composed of a mixture of silicates and carbonaceous grains of sub-micron sizes (Henning & Stognienko 1996; Draine 2003). In the cold regions of the disk, molecules are removed from the gas phase by freezing out on the grain surfaces, which are then coated by an icy mantle.

Molecular lines are an excellent instrument to probe the different physical conditions found in protoplanetary disks, as their numerous transitions are excited in different conditions. At the low temperatures of the bulk disk mass ($< 100 \text{ K}$), the low rotational transitions are excited ($J \lesssim 10$), with the higher rotational transitions found in the atmosphere, warmed by the stellar radiation. In the inner disk, the temperatures get high enough to also excite vibrational transitions (see Figure 1.3). Table 1.1 shows which molecular traces are commonly adopted to trace different disk properties.

Dust emission is a powerful tracer of the physical properties of a disk. Despite comprising only 1% of the disk material (at least until the gas disperses in more developed sources), dust is easier to detect as it emits in a broad spectrum rather than through narrow molecular lines. Consequently, numerous studies have been

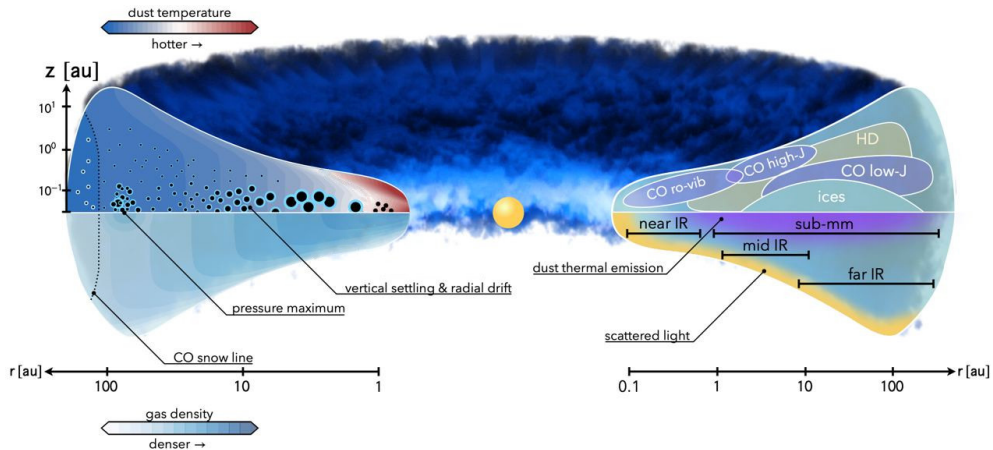


Figure 1.3: Illustration of the structure of a protoplanetary disk, adapted from Miotello et al. (2022). *Left* - Gas density and dust temperature distributions. The size distribution is illustrated by the black circles, with larger grains in the midplane at smaller radii, and small grains diffused through the gas structure. *Right* - Observational signatures of the disk structure. The top panel shows the emitting regions of the main gas tracer, the CO molecule. The bottom panel shows the emitting region of the dust thermal and scattered light emission.

dedicated to investigating the structure of dust (Testi et al. 2014; Andrews 2015; Andrews et al. 2018). The continuum emission has two primary contributors, thermal (re-processed stellar energy, which dominates) and scattered (reflected starlight) radiation. The thermal emission is dominated by large millimeter grains at millimeter wavelengths. These grains are found in the disk midplane as a result of sedimentation processes and offer valuable insight into the high-density regions of the disk, where planet formation occurs. Scattered light radiation at optical and near-infrared wavelengths is produced by starlight scattered off by small dust grains with dimensions similar to the incoming radiation wavelength ($\sim 1 \mu\text{m}$). The observed emission is coming from the disk surface layer and is a powerful instrument to probe the disk vertical structure and geometric parameters (such as its inclination and position angle).

1.2.1 Mass

The total disk mass is one of its fundamental parameters, determining disk physics and evolution and the content of future planetary systems. For instance, Mordasini et al. (2012) demonstrate that the disk mass determines the likelihood of a disk producing hot-Jupiters (planets physically similar to Jupiter, but with short orbital periods), while also determining the disk accretion rate (Alcalá et al. 2014, 2017; Venuti et al. 2014, 2019; Manara et al. 2016, 2017, 2023; Hartmann et al. 2016). However, how to measure the total disk mass is one of the most

Table 1.1: Molecular tracers of disk properties.

Molecules	Disk property
CO, ^{13}CO , C^{18}O , C^{17}O	density and temperature
HD, CS, H_2CO	density
NH_3 , H_2	temperature
HCO^+ , N_2H^+ , C^+	ionization
HCN, CN, C_2H	photoprocesses
Complex Organic Molecules	surface chemistry
DCO^+ , N_2D^+ , DCN	deuterium fractionation

Note: adapted from Henning & Semenov (2013).

controversial questions in the field. The main reason is that the H_2 molecule, carrying the bulk of the mass, is really hard to observe in typical disk physical conditions due to its molecular physics (Field et al. 1966). This molecule has large energy spacing between its rotational levels in the ground vibrational state. Moreover, being a homo-nuclear molecule it has no dipole moment and only weaker quadrupole transitions making them hard to excite at the low disk temperatures. Only in the very inner disk, where temperatures rise above 100 K, its emission becomes relevant, and it does not trace the bulk disk mass (Thi et al. 2001; Pascucci et al. 2013; Trapman et al. 2017). Hydrogen-deuteride, HD, is a more direct tracer of H_2 since they are chemically very similar (Bergin et al. 2013; Kama et al. 2020). However, HD emission only comes from the warm regions of the disk (30 – 50 K) and it can only provide upper limits to the disk masses. Moreover, deep knowledge of the disk thermal structure is needed to link the HD emission to its abundance.

A valuable indicator of a disk physical properties is the emission of the CO molecule, which is the next most abundant after H_2 and efficiently emits at the disk’s cold temperatures. However, the primary CO isotopologue ($^{12}\text{C}^{16}\text{O}$) becomes optically thick even at low column densities, limiting its ability to trace only the disk surfaces where the emission originates. To probe the majority of the disk mass and delve deeper into the disk structure, observations of rare CO isotopologues are required. These isotopologues become optically thick at deeper layers and can trace the disk properties down to the disk midplane (Booth et al. 2019; Calahan et al. 2021; Schwarz et al. 2021).

A study by Williams & Best (2014) demonstrated that combining optically thin and thick isotopologues (^{13}CO and C^{18}O) allows for constraining disk masses using parametric models, even with limited knowledge of the disk properties. Their

models, however, omitted CO chemistry and relied on a parametrized temperature structure and fixed CO isotopologue abundances. This approach however relies on the uncertain CO/H₂ conversion factor, as CO may be depleted from the gas phase through processes such as freezing out on grain surfaces, isotope-selective photodissociation, and conversion to more complex chemical species (e.g. van Zadelhoff et al. 2001; Miotello et al. 2016; Schwarz et al. 2016). Recent works also suggest that there is a strong carbon depletion in some disks, such as TW Hya, HD 163296, and DM Tau (Kama et al. 2016; McClure et al. 2016; Schwarz et al. 2016; Zhang et al. 2020), reducing the relative abundance of CO with respect to H₂ and making CO-based mass estimates uncertain. Therefore, to accurately convert from CO mass to H₂ mass, a more comprehensive understanding of the disk structure is required.

Another approach often used in the literature is to use (sub-) millimeter observations of the dust emission which at these wavelengths is optically thin and therefore the flux F_ν can be directly related to the mass (Beckwith et al. 1990):

$$M_{disk} = \frac{F_\nu d^2}{\varepsilon \kappa_\nu B_\nu(\langle T \rangle)}, \quad (1.2)$$

where ε is the dust-to-gas ratio, κ_ν is the dust opacity, and $B(\langle T \rangle)$ is the Planck function at the average disk temperature.

However, these mass estimates rely on a set of assumptions and usually come with large uncertainties. For instance, the dust-to-gas ratio is not well constrained in disk environments, and it can evolve to significantly higher values compared to the classical ISM values (see Chapter 3,4). The CO/H₂ ratio is also not well constrained, as CO can be depleted from the gas phase (McClure et al. 2016; Krijt et al. 2020; Powell et al. 2022). The dust opacity is also challenging to constrain, and another source of uncertainty is the mass carried by grains larger than millimeter sizes, which cannot be directly observed.

Over the course of a protoplanetary disk's lifespan, the radial distribution of mass undergoes substantial changes. Notably, the central star can accrete gas (Alcalá et al. 2014; Hartmann et al. 2016; Manara et al. 2017), or winds and outflows may dissipate it (Gorti et al. 2016). Understanding the distribution of surface density offers valuable indications of the predominant processes at play. This mass distribution also significantly influences potential planet formation locations and their resulting masses (Miguel et al. 2011; Morbidelli & Raymond 2016). The two key parameters to model a disk radial structure are the surface density distribution $\Sigma(r)$ and the disk outer radius R_{out} . However, as with disk masses, these parameters are hard to constrain from the observations, they are not uniquely defined in the literature, both empirically and theoretically, and are usually based

on some assumption on the shape of the mass radial distribution.

1.2.2 Vertical structure

The vertical structure of the gas is essentially determined by the force balance between the vertical pressure gradient and the gravitational force toward the midplane. In contrast, the vertical distribution of dust is more complex to characterize, as dust grains do not evolve independently from the gas. Multiple factors impact the vertical arrangement of dust grains. While gravity tends to settle grains in the disk midplane, turbulent gas motions keep the grains coupled to the gas structure. The dominant effect depends on the degree of coupling between grains and gas. The coupling of dust particles depends on the grain size through their Stokes number (roughly the ratio of the timescale needed to synchronize with gas velocity and the orbital timescale). Under typical assumptions, the Stokes number reduces to (Cuzzi et al. 2001; Birnstiel et al. 2012):

$$St = \frac{t_{stop}}{t_{orbit}} = \frac{\pi a \rho_s}{2 \Sigma_{gas}}, \quad (1.3)$$

where t_{stop} and t_{orbit} are the grains stopping and orbital timescales, a the grain size, ρ_s the internal mass density of the grains, and Σ_{gas} the gas surface density. This equation intuitively illustrates that the grain-gas coupling depends on the $a - \Sigma_{gas}$ ratio. Larger grain size a correlates with weaker coupling to gas flows. Conversely, higher gas density enhances coupling. Large millimeter-sized dust grains remain then unaffected by the gas structure and reside only within a thin layer in the disk midplane due to gravitational effects. On the other hand, small micron-sized dust grains are well-coupled to the gas and essentially track its motions.

This difference between the vertical distribution of large and small grains is evident in how diverse disk structures appear across various observed wavelengths. Notably, infrared (IR) observations detect stellar radiation scattered off by micron-sized grains on the disk surface, while optically thick millimeter continuum observations trace settled millimeter-sized dust grains in proximity to the midplane. The most visually striking example is given by the observations of the IM Lup disk. In Figure 1.4, where we compare near-infrared scattered light observations from the Spectro-Polarimetric High-contrast Exoplanet REsearch (SPHERE) instrument (Avenhaus et al. 2018) to the millimeter continuum observations from the Atacama Large Millimeter-submillimeter Array (ALMA) interferometer (Andrews et al. 2018).

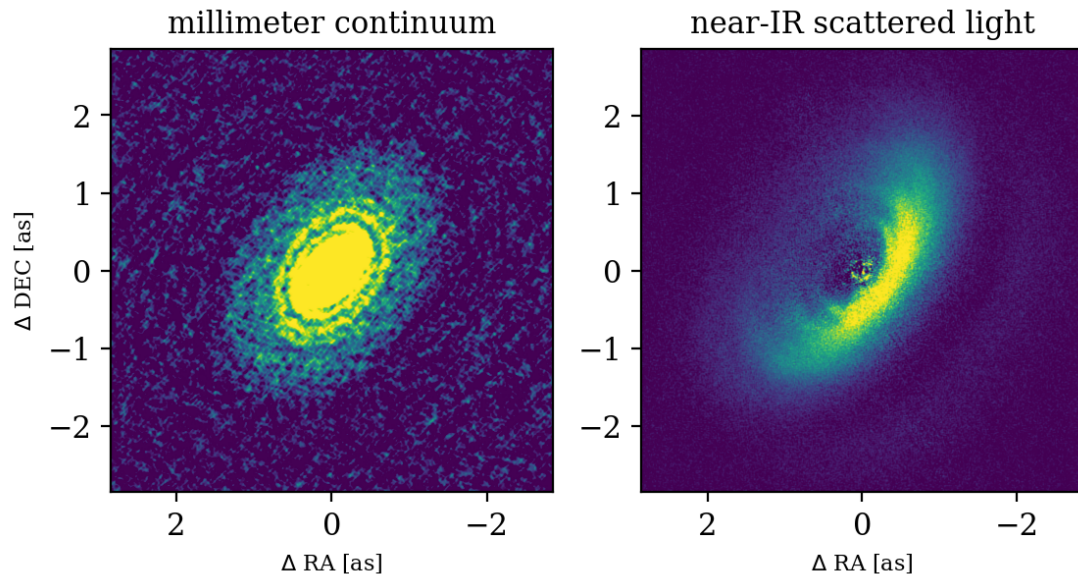


Figure 1.4: The different disk geometry observed in the IM Lup disk in different tracers. (*left*) ALMA millimeter continuum observations (Andrews et al. 2018), revealing a flat distribution of large grains in the disk midplane. (*right*) SHPERE Near-IR scattered light observations (Avenhaus et al. 2018), displaying the vertically flared disk surface layer traced by micron-size grains.

1.2.3 Substructures

Thanks to the continuous development of observational facilities, high angular resolution data reveal a diverse array of substructures in most disks such as rings, gaps, spirals, and shadows (e.g. Pinilla et al. 2015; Long et al. 2018; Andrews 2020). How prominent these substructures are in each disk strongly varies from disk to disk. For instance, the TW Hya disk presents very shallow rings, while the disk around AS 209 shows numerous and clearly distinguishable rings. The ALMA Disk Substructures at High Angular Resolution Project (DSHARP) (Andrews et al. 2018) revealed a prevalence of substructures in young protoplanetary disks, in particular gaps and rings (see Figure 1.5).

These substructures can originate from various physical processes. Rings, for instance, may be formed when a disk undergoes significant mass loss due to photoevaporation or winds, as well as the presence of one or more giant planets that create gaps by clearing the central cavity. The size and depth of the gap depend not only on the planet mass but also on the gas properties, such as viscosity and scale height (e.g., Kanagawa et al. 2015; Dong & Fung 2017), since the tidal torques must outweigh the opposing effects of viscous diffusion to create a gap. In the case of cold and massive disks, self-gravity can trigger gravitational instability across the disk, resulting in the formation of spiral arms. Another possible origin of spiral arms is tidal forces from a giant planet, causing disk perturbations through

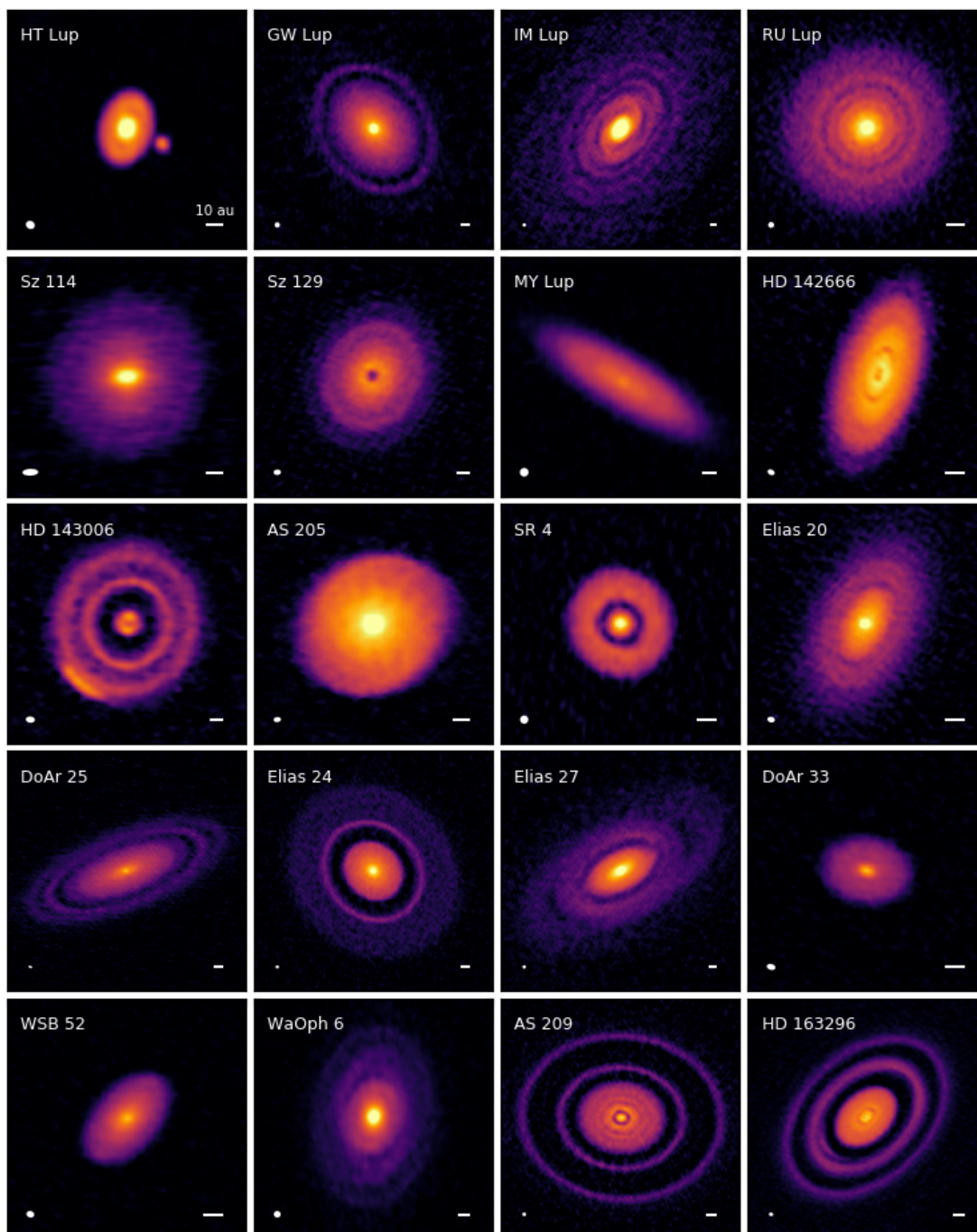


Figure 1.5: A gallery of 1.25 mm continuum emission observed by ALMA as part of the DSHARP project. Beam sizes and 10 au scalebars are shown in the lower left and right corners of each panel, respectively. Credit: Andrews et al. (2018).

gravitational interactions. In this case, spiral arms can emerge both within and outside the planet's orbit.

1.2.4 Temperature

Understanding the thermal structure of the disk is crucial, as it governs the disk chemical composition, dust dynamics, and gas instabilities. This, in turn, directly influences molecular excitation conditions, emission line intensities, and dust continuum fluxes, making knowledge of the disk thermal structure vital for interpreting observations. Notably, the estimated mass in Eq.1.2 critically relies on the assumed dust temperature. Similarly, the temperature impacts molecular line emission intensity, affecting both line emissivity based on excitation conditions (density and temperature) and the disk's chemical evolution by determining emitting molecule abundance.

According to theoretical models, the distribution of dust temperature exhibits a notable vertical gradient increase while diminishing radially outward (e.g. Andrews 2015; Avenhaus et al. 2018). This outcome is attributed to both stellar irradiation and the vertical arrangement of dust grains. Predominantly, the dust temperature is determined by the stellar irradiation intercepted by these grains. Light from the star is either absorbed or scattered by minute grains situated in the upper disk layers, which consequently re-emit radiation toward the midplane. This is particularly important in planet formation studies since the disk midplane hosts the bulk of gas and dust mass, determining the composition and formation mechanism of planetary cores.

A common approach to estimating the dust temperatures is the forward modeling of the infrared Spectral Energy Distribution (SED), the amount of energy emitted at a given wavelength. By assuming a disk surface density profile and dust opacity, these models simulate the propagation of energy across the disk and generate synthetic SEDs for comparison with observations. The integration of SEDs with spatially resolved observations can aid in mitigating uncertainties (Pinte et al. 2008).

An alternative approach to constrain the disk thermal structure is based on the emission of molecular gas lines. Molecular line emission, however, originates from specific regions within the disk. Consequently, a single transition can only characterize the gas temperature exclusively within a distinct part of the disk (specifically where it predominantly emanates from). This is because of the different optical depths of each transition, effectively causing each transition to delineate a unique disk region. For instance, in the case of fully optically thick transitions, like the low J transition ^{12}CO lines, the emission solely traces down to the $\tau \approx 1$ surface,

and the bulk of CO mass remains undetected. To capture the full disk thermal structure, it is necessary to observe a multitude of tracers emitting from diverse density and temperature ranges (as shown in Table 1.1).

1.2.5 Astrochemistry in disks

To understand how molecular emission traces the protoplanetary disk physical properties we need to understand the chemical processes that bring to the formation of these molecules. A recent review on this topic can be found in Öberg & Bergin (2021), and we outline here the main concepts of the chemistry in disks.

The mass density during star and planet formation, despite being relatively high compared to other astrophysical environments, is quite low compared to planetary atmospheres, and the molecular complexity typical of the Earth’s atmosphere cannot be found in protoplanetary disks. Three-body reactions involving the collision of three species like $A + B + C \rightarrow ABC^* \rightarrow AB + C$, where the third particle C carries away the $A - B$ bond formation energy, are restricted by timescales, as the collision timescales must be shorter than the dissociation timescales of excited molecular complexes. Three-body collisions only occur in the very dense inner disk midplane region, where the gas number density can be as high as $10^{12} - 10^{13} \text{ cm}^{-3}$. Moreover, disks are cold environments, and atomic and molecular species lack the kinetic energy to overcome most reaction barriers, thus increasing the role of ion-molecule chemistry and neutral-neutral reactions involving radicals and open-shell species (radical and open-shell species have unpaired electrons in their atomic structure leading to high chemical reactivity).

In Table 1.2 we show the primary reactions involved in disk chemistry. In the absence of three-body reactions, bonds primarily form through radiative association, and the bond formation energy is carried away by photons. In interstellar environments, radiative association predominantly governs gas-phase bond creation. However, the formation of molecules through radiative association is still not very efficient, as a substantial number of collisions is required since molecular vibrational transitions are much slower ($\sim 10^{-3} \text{ s}$) than dissociation time scales ($\sim 10^{-13} \text{ s}$). Therefore, this pathway is only efficient when the reactants are abundant enough to cause a high number of collision events, meaning that at least one of the reagents must be hydrogen. Excited molecules can also expel electrons to dissipate the reaction excess energy. However, this is only possible for negatively charged molecular ions (anions), as the ionization energy for neutral molecules is generally high. Consequently, at least one of the reacting atoms must already be an anion. This pathway for molecule formation appears to be ineffective due to the prevalence of positively charged ions (cations) and their rapid recombination with

Table 1.2: Key chemical processes in protoplanetary disks, adapted from Semenov et al. (2010). (*) RF denotes the local UV radiation field.

Name	Representation	Rate
Radiative association	$A + B \rightarrow AB + h\nu$	$10^{-10} - 10^{-17} \text{ cm}^3 \text{ s}^{-1}$
Ion-molecule	$A^+ + B \rightarrow C^+ + D$	$10^{-7} - 10^{-10} \text{ cm}^3 \text{ s}^{-1}$
Neutral-neutral	$A + B \rightarrow C + D$	$10^{-10} - 10^{-16} \text{ cm}^3 \text{ s}^{-1}$
Charge transfer	$A^+ + B \rightarrow B^+ + C$	$10^{-9} \text{ cm}^3 \text{ s}^{-1}$
Radiative recombination	$A^+ + e^- \rightarrow A + \nu$	$10^{-12} \text{ cm}^3 \text{ s}^{-1}$
Dissociative recombination	$AB^+ + e^- \rightarrow A + B$	$10^{-7} \text{ cm}^3 \text{ s}^{-1}$
Ionization	$A + h\nu \rightarrow A^+ + e^-$	$10^{-10} \times RF^* \text{ cm}^3 \text{ s}^{-1}$
Dissociation	$AB + h\nu \rightarrow A + B$	$10^{-10} \times RF^* \text{ cm}^3 \text{ s}^{-1}$
Accretion	$A + g \rightarrow A(g)$	$\geq 10^{-6} \text{ cm}^3 \text{ s}^{-1}$
Surface reaction	$A(g) + B(g) \rightarrow AB(g)$	$\geq 10^{-9} \text{ cm}^3 \text{ s}^{-1}$
Desorption	$A(g) + h\nu/e^-/T \rightarrow A$	$0 - 10^5 \text{ s}^{-1}$

anions. Moreover, unstable anions are quickly removed through photoreactions (Millar et al. 2007).

A more effective way to have chemical reactions is through grain-gas interactions. Since dust grains are macroscopic particles, they can efficiently dissipate excess energy through collisions and thermal radiation. Hydrogen atoms can overcome energy barriers through tunneling, leading to reactions with each other and other atoms, leading to the formation of more complex molecules and radicals. The dust grains, functioning as a "third body", act as catalysts and make these reactions possible. The resulting molecules might either stick to the grain surface or desorb (evaporate) from it into the gas phase. These molecules trapped on the grain surface form an ice layer, which eventually sublimates into the gas phase thanks to external radiation and the intrinsic heat of the grain. As molecules return to the gas phase, more reactions become possible thanks to the wider array of chemical species now available. It is now possible to form more complex molecules thanks to neutral-neutral and ion-neutral interactions ($A + B \rightarrow C + D$).

These forming molecules can also be dissociated through several processes, such as photon absorption (photodissociation), interaction with electrons (dissociative recombination), and high-velocity collisions during shocks. Photodissociation dominates in interstellar and circumstellar regions exposed to external UV radiation. It involves the breaking of molecular bonds upon photon absorption ($AB + h\nu \rightarrow A + B$). Since typical bonding energies exceed 5 eV, only UV or higher energy photons can break these bonds. While most molecules can directly photodissociate by absorbing photons at energies equal to or higher than their dissociation energy, H_2 and other small molecules dissociate upon absorbing photons at specific frequencies. For these molecules (especially for abundant ones such as H_2 and CO), this effect is often much more efficient than dust absorption. Even a small amount of molecules can be enough to fully absorb the incoming UV radiation and shield other regions from the disk, a process known as self-shielding. This is particularly important for the chemical evolution of these molecules, as self-shielding inhibits the reactions mediated by photons. For instance, Miotello et al. (2014) studied isotopologue-selective photodissociation processes of the ^{13}CO , $C^{18}O$, and $C^{17}O$ isotopologues. They found that isotopologue-selective photodissociation significantly affects their chemical model and the isotopologue line intensity can be underpredicted up to a factor of 40 if these processes are not accounted for. Disk mass based on CO isotopologue emission can be underestimated by up to almost two orders of magnitudes.

1.3 Thesis motivation and outline

The rapid development of observational facilities has provided protoplanetary disk studies with an unparalleled quality of data in terms of sensitivity and spatial resolution. As data quality continues to improve, it constantly challenges our understanding of protoplanetary disks, requiring increasingly sophisticated models at smaller and smaller scales. This thesis aims to use a combination of theoretical models and observational data to find new ways to constrain the fundamental properties of disks. In Chapter 2 we review the common techniques to model the structure of protoplanetary disks, and how to use them to produce synthetic observations, focusing on the techniques used in the works presented here. Four projects are then presented in separate chapters. Each project aims to introduce innovative methods for constraining various fundamental properties of disks:

Chapter 3: Can we constrain the gas mass of protoplanetary disks from large grains emission? As previously discussed, observing the disk dust component is considerably more straightforward than observing the gas, even though it represents only a minor fraction of the total disk mass. However, the dynamics of dust grains are influenced by the underlying gas structure. To quantify this interaction, dust evolution calculations are employed to estimate the degree to which the grains are affected by the gas. These models are then used to calibrate the relation between the dust evolution timescales and the disk gas mass. By using ALMA continuum millimeter observations of two sources, TW Hya and AS 209, we demonstrate that this calibrated information is a reliable proxy for the total gas mass present in the disks.

Chapter 4: How can observations constrain the dust distribution when the dust emission appears so different at different wavelengths? As previously discussed in Section 1.2.2, the dust emission in protoplanetary disks displays significant variation at different wavelengths in their structures. However, it is impractical to observe the dust emission across all wavelengths to fully recover the grain distribution. In this chapter, our objective is to construct a comprehensive model of the size distribution and vertical/radial structure of dust particles in protoplanetary disks utilizing already available observational data. Specifically, we focus on recovering the dust distribution in the IM Lup protoplanetary disk by comparing our models to SPHERE near-infrared scattered light and ALMA millimeter continuum observations through radiative transfer calculations. This study showcases the feasibility of constraining the full grain size distribution by using information solely on the largest and smallest grains in the distribution.

Chapter 5: Is it possible to directly constrain the properties of the innermost region of protoplanetary disks? The innermost region of protoplanetary disks is of particular interest for planet formation studies, as it is where these processes are more likely to occur. However, characterizing these regions poses an observational challenge, demanding high angular resolution data, with many tracers being optically thick due to high temperatures and densities. Despite these obstacles, the main disk component, molecular hydrogen, can be directly observed in these environments. In this chapter, we present the JWST-MIRI mid-infrared spectrum of the disk surrounding the very low-mass star 2MASS-J16053215-1933159. Through the analysis of atomic and molecular hydrogen lines, we constrain the physical properties of the emitting gas, highlighting the potential of JWST to significantly advance our understanding of the physical and chemical structure of protoplanetary disks.

Chapter 6: How can we effectively constrain disk properties from CO isotopologues emission? While ^{12}CO and its rarer isotopologues are arguably the most effective tracer of the main disk component, molecular hydrogen, the conversion from CO abundance to H_2 abundance is all but certain. This conversion process relies on physical-chemical models, which are computationally expensive, posing difficulties in direct comparisons with observations. To overcome this issue, we employ machine learning-accelerated chemistry, a novel approach to predict the disk chemical composition without the need to run a full chemical network. By utilizing this technique, we fit disk physical models to CO isotopologue emission data obtained from the IRAM Northern Extended Millimeter Array (NOEMA). The combination of optically thin and thick CO isotopologue lines in our analysis allows us to simultaneously constrain the disk temperature and mass distribution more effectively. This leads to stronger constraints on CO-based mass estimates, addressing the challenge of obtaining reliable disk masses from CO emission data.

Finally, In Chapter 7, we summarize the key findings and conclusions from the various studies presented throughout this thesis. We then outline potential future projects and research directions that could further enhance our knowledge of protoplanetary disks built upon the methodologies presented in this thesis.

Modeling a protoplanetary disk

To test our understanding of the physics of protoplanetary disks, we need to build theoretical models to predict the observational signatures of the disk properties. The most fundamental disk parameters are the density and temperature distribution. As we saw in Chapter 1, these parameters are the starting point for all kinds of disk analysis, from the gas chemical composition to planet formation. To predict the observational signatures of the disk properties, these models need to be integrated too radiative transfer models to generate synthetic images through ray-tracing techniques. This chapter serves as a brief review of the current methods employed in modeling protoplanetary disks, focusing on the techniques utilized in the remainder of the thesis.

2.1 Disk physical model

2.1.1 Radial density distribution

Let us consider a gas element rotating around a stellar object. This element will be orbiting at its Keplerian velocity $v_K = \sqrt{GM_\star/r}$, where G is the gravitational constant, M_\star the stellar mass, and r the radial coordinate. The specific angular momentum of the gas element is:

$$\ell = v_K r = \sqrt{GM_\star r}. \quad (2.1)$$

However, the gas element is not isolated and there are other forces at play. First of all, gas experiences its own internal pressure, leading to a radial pressure gradient decreasing with radius. To keep its Keplerian orbit, the gas has to slow down and rotate at a sub-Keplerian speed so that the centrifugal force and the

radial pressure force keep balancing the gravitational pull. Moreover, the gas possesses a specific viscosity, causing redistribution of angular momentum between nearby gas elements due to their differential rotation. Due to the conservation of angular momentum, this leads to a scenario where a portion of the gas is drift inwards toward the central star, while another portion moves outward from it. Understanding the mechanisms of the redistribution of angular momentum is the core question of accretion disks and the origin of the viscosity is still unclear. Shakura & Sunyaev (1973) suggested that the viscosity may originate from turbulent motions, and parametrized the turbulent viscosity using a scaling factor α , the so-called α -disk model:

$$\nu = \alpha c_s^2 / \Omega(r) \quad (2.2)$$

where c_s is the sound speed and Ω the gas angular velocity. Following Pringle (1981), we can use this viscosity prescription to derive a solution for the disk surface density distribution. The equation for the conservation of the angular momentum equation can be written as:

$$r \frac{\partial}{\partial t} (r^2 \Omega \Sigma_g) + \frac{\partial}{\partial r} (r \Omega \cdot r^2 \Sigma_g v_r) = \frac{1}{2\pi} \frac{\partial G}{\partial r} \quad (2.3)$$

where Σ_g is the gas surface density radial distribution and G is the net effect of the viscous torque due to the differential radial velocity of the gas:

$$G = 2\pi r \cdot \nu \Sigma_g r \frac{d\Omega}{dr} \cdot r. \quad (2.4)$$

If we combine the angular momentum conservation with the continuity equation:

$$r \frac{\partial \Sigma_g}{\partial t} + \frac{\partial}{\partial r} (r \Sigma_g v_r) = 0, \quad (2.5)$$

we obtain the evolution equation of the evolution of the disk surface density distribution:

$$\frac{\partial \Sigma_g}{\partial t} = \frac{3}{r} \frac{\partial}{\partial r} \left[r^{1/2} \frac{\partial}{\partial r} (\nu \Sigma_g r^{1/2}) \right]. \quad (2.6)$$

With the right assumptions, this equation can be solved analytically. The most common solution is the so-called Lynden-Bell & Pringle profile (Lynden-Bell & Pringle 1974; Pringle 1981). They assume a thin, axisymmetric disk with a constant accretion rate onto the central star and a self-similar, stationary solution. The self-similarity assumption implies that the disk properties are described by power-law functions of the radius, meaning that certain ratios of quantities are

constant. This is expressed as $\Sigma_g(r) \propto r^{-\gamma}$ and $\Omega(r) \propto r^{-\alpha}$, where γ and α are constants. In other words, we assume that disks do not have a characteristic size, and small and large disks have the same structure. Using all of these assumptions, we obtain the Lynden-Bell & Pringle self-similar solution:

$$\Sigma_g(r) = \Sigma_c \left(\frac{r}{r_c} \right)^{-\gamma} \exp \left[- \left(\frac{r}{r_c} \right)^{2-\gamma} \right], \quad (2.7)$$

where Σ_c is the surface density at the radial position r_c , and γ is the exponent of the distribution.

2.1.2 Thermal structure

The simplest analytical description of the disk temperature distribution is again a self-similar solution:

$$T = T_c \left(\frac{r}{r_c} \right)^{-q} \quad (2.8)$$

with T_c the temperature at the radial position r_c and q the exponent of the distribution. This expression has been used by Williams & Best (2014) to study the CO emission of disks in the Taurus region and found typical values of $q \approx 0.4 - 0.6$. However, this prescription is limited since it does not account for vertical temperature gradients in the disk. A better representation of the disk thermal structure is to consider two gas layers, a midplane, and an atmosphere layer, smoothly connected by a sine function:

$$T(r, z) = \begin{cases} T_{\text{mid}} + (T_{\text{atm}} - T_{\text{mid}}) \left[\sin \left(\frac{\pi z}{2z_q} \right) \right]^{2\delta} & \text{if } z < z_q, \\ T_{\text{atm}} & \text{if } z \geq z_q, \end{cases} \quad (2.9)$$

where T_{mid} and T_{atm} are power-law profiles like in Eq. 2.8, δ describes the steepness of the profile and z_q the height over the disk midplane where the disk reaches its atmospheric temperature. In the literature it is usually assumed $\delta = 2$ and $z_q = 4 H_p$, where H_p is the pressure scale height:

$$H_p = \sqrt{\frac{k_B T_{\text{mid}} r^3}{GM_* \mu m_H}} \quad (2.10)$$

with k_B is the Boltzmann constant, $\mu = 2.3$ the mean molecular weight of the gas, and m_H is the mass of atomic hydrogen. Williams & Best (2014) explored the impact of these parameters on the disk temperature distribution and found that they do not affect significantly the luminosity of CO lines.

Another approach for estimating the temperature distribution involves utilizing

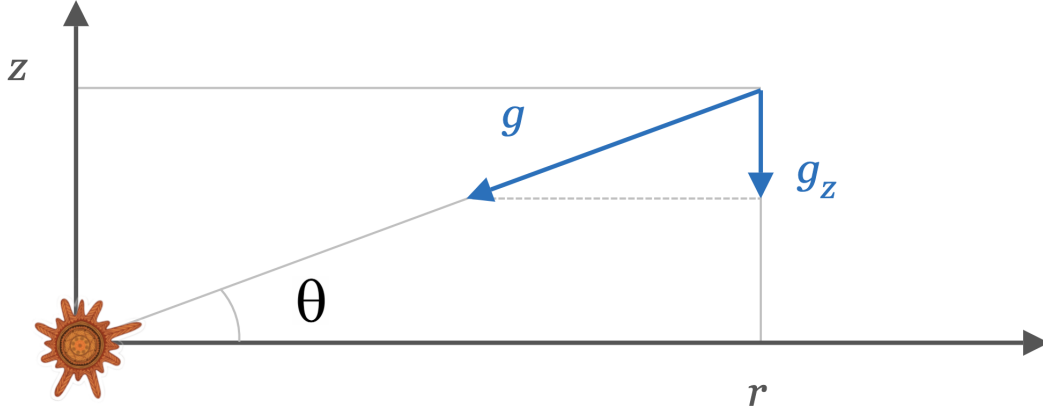


Figure 2.1: The structure of a vertically thin disk is determined by the balance between the vertical component of the stellar gravitational attraction and the pressure force.

radiative transfer calculations to model the propagation of stellar photons through the disk structure. As these photons travel through the disk, they can be absorbed, leading to the heating of the gas. By balancing the heating and cooling processes, we can derive the disk temperature. This procedure can also be applied iteratively to determine the density and temperature structure self-consistently. The vertical structure of the disk is linked to its temperature, as indicated by its scale height from Eq. 2.10. Starting with an initial assumption for the temperature and density distribution, we can use radiative transfer calculations to compute a new disk temperature distribution. Subsequently, this updated temperature profile gives us a new hydrostatic solution for the density. A radiative transfer calculation with the new density structure will then produce a new temperature distribution. This process can be iterated until a self-consistent temperature and density distribution is achieved.

2.1.3 Vertical density distribution

The disk vertical mass distribution is assumed to be in hydrostatic equilibrium, where the vertical component of the disk gravity is balanced by the gas pressure force. The vertical balance of forces is given by:

$$\frac{dP}{dz} = -\rho_g g_z, \quad (2.11)$$

where P is the gas pressure, ρ_g the gas density, and g_z is the vertical component of the gravitational acceleration. Referring to Figure 2.1, g_z is given by:

$$g_z = g \sin \theta = \frac{GM_\star}{r^2 + z^2} \frac{z}{(r^2 + z^2)^{1/2}}. \quad (2.12)$$

Since protoplanetary disks are vertically thin, assuming $z \ll r$ we get:

$$g_z \simeq \frac{GM_\star}{r^3} = \Omega_K^2 z, \quad (2.13)$$

where $\Omega_K = \sqrt{GM_\star/r^3}$ is the Keplerian angular velocity. As a first guess, we assume that the disk is vertical isothermal (a reasonable assumption since the temperature is determined by the stellar irradiation). The equation of state is then $P = \rho_g c_s^2$, where c_s is the isothermal sound speed:

$$c_s = \sqrt{\frac{k_B T}{\mu m_H}}. \quad (2.14)$$

The vertical hydrostatic equilibrium from Eq. 2.11 then becomes:

$$c_s \frac{d\rho_g}{dz} = -\rho_g \Omega_K^2 z. \quad (2.15)$$

The solution to this differential equation is:

$$\rho_g(z) = \rho_0 \exp\left(\frac{-z^2}{2H_g^2}\right), \quad (2.16)$$

where $H_g = c_s/\Omega_K$ is the disk vertical scale height and ρ_0 is the midplane volume density. The midplane volume density can be written in terms of the gas surface density from Section 2.1.1:

$$\Sigma_g(r) = \int \rho_g(r, z) dz = \sqrt{2\pi} H_g \rho_0. \quad (2.17)$$

The final expression for the gas volume density distribution is then:

$$\rho_g(z) = \frac{\Sigma_g(r)}{H_g \sqrt{2\pi}} \exp\left(\frac{-z^2}{2H_g^2}\right). \quad (2.18)$$

2.2 Dust structure

In Chapter 1, we explored how a protoplanetary disk is composed of both gas and dust particles, with a ratio of approximately 100 to 1. Despite their relative abundance, dust significantly shapes the properties of protoplanetary disks. While gas components follow a sub-Keplerian orbit due to pressure gradient, dust grains lack such pressure force and would maintain their Keplerian velocity if not influenced by the gas. This differential velocity between gas and dust leads to a headwind from the surrounding gas on dust grains. Consequently, these grains decelerate, lose angular momentum, and progressively drift towards the central star (Weidenschilling 1977; Brauer et al. 2008; Birnstiel et al. 2012). The effi-

ciency of this process depends on grain size, where small grains have little inertia and are carried along with the gas, tracing its flow. At the same time, larger millimeter-sized grains become decoupled from the gas but are affected by the headwind, causing a gradual drift toward the central star. Notably, centimeter or larger grains—often referred to as boulders—possess such large inertia that gas has negligible influence on their motions. The drift velocity can be expressed as follows (Weidenschilling 1977):

$$v_{\text{drift}} = -\frac{2\Delta v}{s_t + St^{-1}}, \quad (2.19)$$

where St is the Stokes number and Δv is the difference between the orbital velocity of the dust grain and the gas. This headwind velocity is given by (Weidenschilling 1977; Nakagawa et al. 1986):

$$\Delta v = -\frac{\partial P}{\partial r} \frac{1}{2\rho_g \Omega_K}, \quad (2.20)$$

and the Stokes number is:

$$s_t = \frac{t_{\text{stop}}}{\Omega_K} = \frac{\pi a \rho_s}{2\Sigma_g}, \quad (2.21)$$

where ρ_s is the internal volume density of the grain. The drift velocity from Eq. 2.19 is determined by the size of their grains through the Stokes number, and the maximum drift velocity is achieved when $s_t = 1$. The dynamics of dust grains can be categorized through their Stokes number:

- **Small grains:** with $s_t \ll 1$, these grains have a large surface-to-mass ratio and become quickly coupled to the gas flows, with minimal drift velocities.
- **Large grains:** with $s_t \approx 1$, these grains have a low surface-to-mass ratio and start to decouple from the gas. They feel a strong headwind and are the particles with the largest drift velocity.
- **Boulders:** with $s_t \gg 1$, these grains are completely decoupled from the gas, and their dynamic is determined by gravitational interactions.

The same process affects the vertical distribution of grains. If no gas was present, dust grains would naturally orbit around the central stars with different inclinations, leading to a vertical velocity component. Due to their close coupling with the gas flows, small particles undergo a gradual vertical motion towards the midplane, although this process is counteracted by turbulent mixing that elevates the dust back into higher regions over the midplane. In contrast, larger particles are less affected by the gas and quickly settle in the midplane. Consequently, this

phenomenon of vertical settling gives rise to a distinct gradient in the dust grain size distribution. Larger grains are found closer to the midplane, while smaller grains show an extended vertical distribution (Villenave et al. 2020).

The timescale for grains to settle toward the midplane is $t_{\text{sett}} = zv_{\text{sett}}^{-1} = \Omega_K \text{St}^{-1}$ where v_{sett} is the settling velocity. Even small micron-size grains will have a large v_{sett} at the small densities typical of the disk atmosphere. However, as these grains move toward the midplane, the gas density will increase, decreasing their Stokes number and stopping their settling. This process is counteracted by turbulent mixing, and to estimate the combined effect of these processes we define the Péclet number. Following the calculations of Birnstiel et al. (2016) the Péclet number writes as:

$$\text{Pe} = \frac{t_{\text{diff}}}{t_{\text{sett}}} = \frac{\text{St}}{\alpha} \left(\frac{z}{H_g} \right)^2. \quad (2.22)$$

When $\text{Pe} \gg 1$ the settling timescale is shorter than the diffusion timescale, and the grains are quickly removed from that region. When $\text{Pe} \ll 1$ diffusion dominates and grains are suspended within the gas. We expect then the dust density to significantly drop when $\text{Pe} = 1$, which allows us to derive a dust scale height:

$$H_d = H_g \sqrt{\frac{\alpha}{\text{St} + \alpha}}. \quad (2.23)$$

Assuming that the disk is geometrically thin, the dust vertical distribution is a Gaussian profile with scale height H_d :

$$\rho_d(z) = \rho_{d,0} \exp\left(-\frac{z^2}{2H_d^2}\right), \quad (2.24)$$

where $\rho_{d,0}$ is the midplane dust density.

2.3 Simulating the observations: radiative transfer

In Section 2.1.2, we discussed the application of radiative transfer calculations to compute the disk temperature by modeling the interaction of stellar photons with the disk structure. This very process governs the emitted radiation from the disk, captured by our instruments for our scientific analysis. These calculations account for a range of processes, including scattering, absorption, and re-emission of radiation by dust grains, as well as spectral line emission or absorption when molecules undergo changes in energy levels. By employing radiative transfer cal-

culations, we can generate synthetic images based on theoretical models, allowing their comparison to observations and enabling us to assess their accuracy.

2.4 The radiative transfer equation

Let us consider a radiation field at frequency ν , at a location \mathbf{x} , propagating in a direction \mathbf{n} , expressed by $I_\nu(\mathbf{x}, \mathbf{n})$. Energy can be added to the field (e.g., by stellar irradiation, dust thermal emission, molecular line emission) or absorbed (by dust or line absorption). The change in the radiation field when traveling through a path s is given by:

$$\frac{dI_\nu}{ds}(\mathbf{x}, \mathbf{n}) = j_\nu(\mathbf{x}, \mathbf{n}) - \alpha_\nu(\mathbf{x})\rho(\mathbf{x})I_\nu(\mathbf{x}, \mathbf{n}), \quad (2.25)$$

where j_ν is the emissivity (amount of radiation emitted along s), α_ν is the extinction (amount of radiation absorbed along s). Both j_ν and α_ν can have a contribution from both dust continuum and molecular line effects, and they can be written as:

$$j_\nu(\mathbf{x}, \mathbf{n}) = j_{\nu,\text{dust}}(\mathbf{x}, \mathbf{n}) + j_{\nu,\text{line}}(\mathbf{x}, \mathbf{n})\varphi_\nu \quad (2.26)$$

$$\alpha_\nu(\mathbf{x}, \mathbf{n}) = \alpha_{\nu,\text{dust}}(\mathbf{x}, \mathbf{n}) + \alpha_{\nu,\text{line}}(\mathbf{x}, \mathbf{n})\varphi_\nu, \quad (2.27)$$

where φ_ν is the normalized line profile function. The dust contribution to the emission comes from absorbed radiation re-emitted as thermal emission and scattered light:

$$j_{\nu,\text{dust}}(\mathbf{x}, \mathbf{n}) = \alpha_{\nu,\text{dust,abs}}B_\nu(T_{\text{dust}}) + \alpha_{\nu,\text{dust,sca}}J_\nu(\mathbf{x}, \mathbf{n}), \quad (2.28)$$

where $J_\nu = 1/4\pi \int I_\nu d\Omega$ is the local mean intensity assuming isotropic scattering, and $B_\nu(T)$ is the Planck function:

$$B_\nu(T) = \frac{2h\nu^3}{c^2} \frac{1}{\exp\left(\frac{h\nu}{k_{\text{B}}T}\right) - 1} \quad (2.29)$$

The line emission/absorption is caused by a molecular species changing its energy state from an energy level i to an energy level j . When the molecule goes from a higher to a lower energy state, the excess energy is emitted in the form of a photon with the same energy as the difference in the energy level. Shifting from a lower energy level to a higher energy level requires an external stimulus, leading to the absorption of a photon whose energy corresponds to the difference between the energy levels. Therefore, we can write:

$$j_{ij} = \frac{h\nu_{ij}}{4\pi} n_i A_{ij} \varphi_{ij}, \quad (2.30)$$

$$\alpha_{ij} = \frac{h\nu_{ij}}{4\pi} (n_j B_{ji} - n_i B_{ij}) \varphi_{ij}, \quad (2.31)$$

where n_i is the population of the energy level i , A_{ij} is the Einstein coefficient for the spontaneous emission of radiation, and B_{ij} is the coefficient for the absorption and stimulated emission.

The radiative transfer equation from Eq. 2.25 can be simplified dividing by α_ν :

$$\frac{dI_\nu(\mathbf{x}, \mathbf{n})}{\alpha_\nu(\mathbf{x}) ds} = \frac{j_\nu(\mathbf{x}, \mathbf{n})}{\alpha_\nu(\mathbf{x})} - I_\nu(\mathbf{x}, \mathbf{n}) \Rightarrow \frac{dI_\nu(\mathbf{x}, \mathbf{n})}{d\tau_\nu} = S_\nu(\mathbf{x}, \mathbf{n}) - I_\nu(\mathbf{x}, \mathbf{n}), \quad (2.32)$$

where $\tau_\nu = \int \alpha_\nu(\mathbf{x}) ds$ is the optical depth and S_ν is the source function, which describes the radiative properties of the medium. The solution to this differential equation is:

$$I_\nu(\tau) = I_{\nu,0} e^{-\tau} + S_\nu(1 - e^{-\tau}), \quad (2.33)$$

where $I_{\nu,0}$ is the background radiation. In the optically thick regime ($\tau \gg 1$), the background radiation is fully absorbed by the medium, causing the radiation field to simplify to the source function S_ν . In the optically thin regime ($\tau \ll 1$), the radiation is primarily influenced by the external field. Consequently, The radiation field has an exponential transition from $I_{\nu,0}$ to S_ν , and the optical depth is the characteristic length of this transition.

In the case of local thermodynamic equilibrium (LTE), S_ν simply becomes the Planck function $B_\nu(T)$. In the low-frequency limit ($h\nu \ll kT$ the Planck function becomes proportional to the temperature and tends to the Rayleigh-Jeans law:

$$B_\nu(t) \approx 2\nu^2 k_B T / c^2 \propto T. \quad (2.34)$$

This is an important approximation in radioastronomy, as it directly links the observed emission to the source properties. The source brightness is often measured in terms of its “brightness temperature”.

Mass determination from dust evolution

The content of this Chapter is based on **Franceschi et al. (2022)**, published in *Astronomy & Astrophysics (A&A)*, 657, A74.

Details of authorship: I am the first author of this paper, working under the supervision of Prof. Thomas Henning. I computed the dust opacity and evolution using publicly available tools developed by Prof. Tilman Birnstiel. I conducted the analysis supported by discussions with Prof. Thomas Henning and Prof. Tilman Birnstiel. Dmitry Semenov provided useful comments on the opacity effect on the analysis result. Paola Pinilla provided comments to Sec. 3.6 and insight on the effect of radial structures. Figure 3.9 was produced by Prof. Tilman Birnstiel. The text was written by myself, with the contribution of Prof. Tilman Birnstiel in Section 3.5. All co-authors provided comments on the text.

3.1 Motivation

In Section 1.2 we discussed how the mass of protoplanetary disks is of prime importance for disk evolution and planet formation studies. Specifically, the disk mass is fundamental for pebble accretion models when studying the evolution of dust grains. As an example, Lambrechts & Johansen 2014 show that the disk mass must ensure a high enough radial flux of pebbles (millimeter to centimeter sizes) so the core of that giant planet may form before the disk is depleted from gas. The disk mass cannot be directly determined as most of its mass resides in H_2 , which is a symmetric molecule without a dipole moment and millimeter rotational transitions. The disk surface density distribution is traditionally inferred from dust continuum emission or molecular tracers, such as HD and CO (e.g., Bergin

et al. 2013; Ansdell et al. 2016; Long et al. 2017; Bergin & Williams 2018; Kama et al. 2020).

The dust surface density is measured from its thermal emission at (sub)millimeter wavelengths, assuming it is optically thin, and converted to a total surface density through an assumed dust-to-gas ratio (e.g., Andrews & Williams 2005, 2007). The drawback in using this approach is that the dust-to-gas ratio is not well constrained in the disk environment, and it can be significantly different from the canonical interstellar value 10^{-2} (Williams & Cieza 2011) due to dust evolution. To estimate the surface density of solid material, opacity must also be assumed, which is an additional source of uncertainty (e.g., Henning & Stognienko 1996; Andrews & Williams 2005; Birnstiel et al. 2018). Moreover, continuum observations do not trace emission from grains that are much larger or much smaller than the observed wavelength. It is therefore possible that dust mass estimates are missing a significant fraction of the total dust mass. This is even more true if part of the emission is optically thick (Liu 2019; Zhu et al. 2019).

The emission from CO rotational transitions of one or more of its optically thin isotopologues can also be used to estimate the gaseous content of a disk via an assumed CO-to-H₂ ratio (e.g., Schwarz et al. 2016; Zhang et al. 2017; Booth et al. 2019). However, this conversion factor is quite uncertain, as there is mounting evidence that CO is depleted from the gas phase through freeze out, isotope-selective photodissociation and conversion to more complex chemical species (e.g., van Zadelhoff et al. 2001; Miotello et al. 2016; Schwarz et al. 2016), and the typical assumed CO abundance of 10^{-4} based on interstellar estimates has been questioned.

HD, on the other hand, is a more direct tracer of molecular hydrogen, and the derived disk mass from HD measurements for TW Hya is higher by 2 orders of magnitude than CO estimates, due to CO depletion from the gas phase (Bergin et al. 2013; McClure et al. 2016; Schwarz et al. 2016; Kama et al. 2020). However, HD emission only comes from warm regions in the disk ($T \sim 30 - 50 K$) (Bergin et al. 2013; Trapman et al. 2017) and can therefore only provide lower limits to the gas mass. Moreover, HD observations only exist for TW Hya (Bergin et al. 2013), GM Aur and DM Tau (McClure et al. 2016), and there have not been new HD observations after the *Herschel* mission has ended.

Given the difficulties in converting observable disk quantities to a total gas mass, in this paper we used theoretical models to test the novel approach to disk mass measurements introduced in Powell et al. (2017, 2019). This method links the maximum radial extent of the emission at a given wavelength, the so-called dust line, to the local surface density of the disk. Previous theoretical studies (Birnstiel et al. 2012; Birnstiel & Andrews 2014) demonstrate that dust evolution

is driven by grain growth and fragmentation. These processes are regulated by drift in the outer disk and cause segregation of the radial distribution of grains with their size. In Powell et al. (2017, 2019), multiwavelength observations of dust continuum emission have been used to derive the grain size distribution and to estimate the gas surface density distribution for a sample of protoplanetary disks.

In this paper, we tested the theoretical foundation of this approach through numerical modeling in order to take all grain evolution processes into account. The model is described in Section 3.2, and in Section 3.3 we discuss the definition of dust lines and how these can be used to estimate the disk surface density. We also investigate under which conditions dust trapping will limit the applicability of dust lines for the estimates of disk masses. In Section 3.4 we study the model dependence on the physical parameters. Once we verify the goodness of the dust line as a mass estimator, we calibrate it using a population of synthetic disks in Section 3.5. Next, we proceed to study how deviation from a smooth gas distribution may affect a mass estimate in Section 3.6. Finally, in Section 3.7 we apply it to individual disks and compare our results with the observationally derived results in Powell et al. (2017, 2019).

3.2 Methodology

Powell et al. (2017, 2019) show how considerations about drift and growth timescales can be used to estimate the gas surface density at the outer edge of the emitting region of any given dust grain population (they call this location the *dust line*). Our aim is to test and supplement this idea with dust evolution models. To this purpose we briefly summarize their method.

In the outer regions of evolved disks, particle drift dominates both grain growth and collisional fragmentation. It determines the grain size distribution and, in particular, the maximum grain size at any given radial location. In this simplified scenario, grain evolution happens in two regimes: a fragmentation regime in the inner disk and a drift regime in the outer disk. Grains in the outer disk have too low relative velocities for fragmentation to affect their evolution, and their maximum size at any given radius is determined by the drift. In the inner disk, however, the relative velocities are higher, and grain evolution is fragmentation limited (Birnstiel et al. 2012; Birnstiel & Andrews 2014).

The timescale on which particles grow (e-folding timescale) can be estimated to be (Brauer et al. 2008; Birnstiel et al. 2012):

$$t_{growth} = \frac{1}{\epsilon \Omega_K}, \quad (3.1)$$

where ϵ is the local dust-to-gas ratio and Ω_K the Keplerian angular velocity, although the initial stage of this growth might be longer (Powell et al. 2019). If particle growth is not halted by collisional effects such as fragmentation or bouncing (Güttler et al. 2010; Zsom et al. 2010; Birnstiel et al. 2012), then the radial migration limits the grain particle sizes, since large grains migrate faster than growth can replenish them. The largest achievable grain size, called the drift limit, is therefore given by equating the drift and growth timescales (Birnstiel et al. 2012), where the drift timescale is:

$$t_{drift} = \frac{r}{v_{drift}}, \quad (3.2)$$

and v_{drift} is the radial drift velocity (Whipple 1972). The radial drift occurs because of the head-wind from the subkeplerian gas flows against the Keplerian grains, that lose angular momentum. The drift velocity is (Weidenschilling 1977):

$$v_{drift} = -\frac{2\Delta v}{St + St^{-1}}, \quad (3.3)$$

where Δv is the difference between the gas and the grains orbital velocity, and St is the Stokes number, the dimensionless ratio of stopping time to the dynamical timescale $St = t_{stop} \Omega_K$ (which depends on the grain size). If particle growth and drift have had enough time to proceed, then particles that drift on timescales shorter than the age of the disk should not exist. In other words, particles of a given size need to be located in regions where their drift timescale is comparable or longer than the disk age. The sharp edges observed in millimeter emission of a number of disks (e.g., Pérez et al. 2015; Andrews et al. 2016; Tazzari et al. 2016) are therefore interpreted by Powell et al. (2017) as separating the well coupled ($t_{drift} > t_{disk}$) and significantly decoupled grains ($t_{drift} < t_{disk}$). Since in the drift limit ($t = t_{drift}$) the maximum grain size at a given location is directly proportional to the local dust surface density Σ_d (Birnstiel et al. 2012), these sharp edges can be used to link the maximum grain size to Σ_d . Larger particles have smaller drift timescales, meaning that the dust lines will evolve with disk age, and we expect the location of the dust lines to decrease with the disk age. This motivates Powell et al. (2017) to equate the above timescales to the disk age at the position of the dust outer edge. To the additional constraint of equating the timescales at the dust line location to also the disk age gives us a relation for the dust-to-gas ratio appearing in Eq.3.1:

$$\epsilon = \frac{1}{t_{disk} \Omega_K}. \quad (3.4)$$

This allowed us to constrain both the dust and gas surface densities if the

particle size is known. If continuum observations are assumed to be dominated by grains of size $a = \lambda/2\pi$, according to the Mie scattering theory, then multi-wavelength observations that show dust lines at different positions can be used to reconstruct the surface densities of dust and gas and thus one can derive mass estimates of the solids and the gas that do not depend on opacities, but are based on dynamical considerations (i.e., drift speeds and collisional times).

Smaller particles have a longer drift timescale, and their emission will come from a broader region, while for larger grains the emission region will shrink. Following the derivation in Powell et al. (2017), this condition leads to an expression for the gas surface density at the edge of a given dust population emitting region, the so-called *dust line location*:

$$\Sigma(r) = \frac{t_{disk} v_0 \rho_s a}{r}, \quad (3.5)$$

where v_0 is the drift velocity of the fastest-drifting grains (with $St = 1$), ρ_s the internal density of grains (taken to be 1.6 g/cm^3) and r is the maximum radius where grains of size a can be found. If multiwavelength observations of the continuum emission are available, the size of each one of these emitting regions, assuming an emitting grain population of size $\lambda_{obs}/2\pi$, can be put in Eq.3.5 to estimate the gas surface density at the dust line location. These estimates can then be used to fit theoretical models to the gas surface density distribution, such as the Lynden-Bell-Pringle self-similar solution. This approach has been used to estimate the disk mass of TW Hya (Powell et al. 2017) and the masses of a sample of other disks (Powell et al. 2019) from dust continuum observations.

To test this method, we modeled grain evolution using the two population model described in Birnstiel et al. (2012). The dust is evolving in a viscous environment by considering two populations of grains: a small grain population which remains well coupled to the gas structure, with a size of $0.1 \mu\text{m}$, and a large grain population which may grow and drift (that carry most of the mass). This model is ideal for our purpose as it is computationally inexpensive and it is calibrated to match the grain size and mass flux in more comprehensive full population models.

Modeled disks were initially populated with micron-sized particles with a dust-to-gas ratio $1/100$. Particles can stick and grow when colliding if their relative velocity is below a threshold, set to 10 m/s in our model, based on numerical and laboratory experiments (e.g., Gundlach et al. 2011; Wada et al. 2009). Dust dynamics is dominated by drift and turbulent diffusion. Dust diffusion is assumed to be the same as the turbulent gas viscosity (Youdin & Lithwick 2007) and the turbulent velocities are proportional to $\sqrt{\alpha}$ (Ormel & Cuzzi 2007), where α is the disk effective viscosity parameter (Shakura & Sunyaev 1973).

We modeled the disk evolution through gas viscosity, growth and radial drift of solid material. The gas structure was assumed to follow the Lynden-Bell & Pringle (1974) self-similar solution, following from mass and momentum conservation:

$$\Sigma(r) = \Sigma_c \left(\frac{r}{r_c} \right)^{-\gamma} \exp \left[- \left(\frac{r}{r_c} \right)^{2-\gamma} \right]. \quad (3.6)$$

Following Birnstiel et al. (2012), at each radius, we evolved the small and large grain populations. The maximum grain size was set to the lowest value between the drift limit and the fragmentation limit or was limited by the growth time if particles had not yet grown to one of the size limits. Fragmentation of dust particles stops further growth because the relative velocity of grains increases with their Stokes number. When they reach the fragmentation threshold velocity, particle collisions destroy the grains instead of sticking them together to form larger grains. Since the grains' relative velocities due to turbulence increase with grain size, the maximum grain size in the fragmentation-limited regime can be estimated as:

$$a_{frag} = f_r \frac{2}{3\pi} \frac{\Sigma_g}{\rho_s \alpha} \frac{u_f^2}{c_s^2}, \quad (3.7)$$

where $f_r \approx 0.37$ is a calibration factor obtained from full dust evolution codes (Birnstiel et al. 2012), Σ_g is the local gas surface density, ρ_s is the grain internal density, c_s is the gas sound speed and u_f is the fragmentation velocity.

In the drift limited regime, large grains are removed when their drift timescale is shorter than the time required to form these grains. In this regime, the grains drift at least as fast as they grow, and the maximum grain size is reached when the drift and growth timescales are equal:

$$a_{drift} = f_d \frac{2\Sigma_d}{\pi\rho_s} \frac{V_k^2}{c_s^2} \gamma^{-1}, \quad (3.8)$$

where $f_d \approx 0.55$ is another calibration factor, Σ_d is the dust surface density, V_k is the Keplerian velocity, and $\gamma = d \log P / d \log r$.

The grains' relative velocities are determined by drift and turbulence. The temperature structure establishes the maximum turbulent velocity, determining where the disk is going to be drift- or fragmentation-dominated. The temperature of the dust is assumed to be a power-law that depends on the stellar luminosity L_\star :

$$T_d(r) = T_{10} \left(\frac{r}{10 \text{ au}} \right)^{1/2} \left(\frac{L_\star}{L_\odot} \right)^{1/4}, \quad (3.9)$$

where T_{10} is the temperature at 10 au, taken to be 30 K (Andrews et al. 2013; Tripathi et al. 2017).

3.3 Dust line location

3.3.1 Dust line definition

The dust line is defined as the outer edge of the disk observed at a specific (sub)millimeter wavelength. In some cases, where the continuum emission abruptly ends, this definition is straightforward. However in other cases, where the emission continuously decreases, this definition needs to be refined. From an observational point of view, the most straightforward definition would be an "emission" dust line, that is, the radius enclosing a fixed fraction of the disk's total luminosity at a specific wavelength. On the other hand, the physical quantity that concerns us is the dust mass distribution for a given grain size. The most convenient way would be then to define a "mass" dust line using the surface density distribution of the most emitting grains. However, it is not clear if these two possible definitions of dust line location overlap.

The emission at a given wavelength λ_{obs} is dominated by grains with characteristic size $\lambda_{obs}/2\pi$, and we can link the emission dust line to the mass dust line for the grain population $a = \lambda_{obs}/2\pi$. However, even if this grain population is dominating the emission, other grains are contributing as well. To study the link between dust populations and the emission dust line we take the example of the opacity curve for a single grain population as a function of the grain size at $\lambda_{obs} = 0.87$ mm in Figure 3.1 (Simon et al. 2019). The most emitting grains span an order of magnitude in grain size and have their opacity increased by at least an order of magnitude compared to other grain sizes. Their radial position can be reliably traced by a given percentage of the disk flux, but we still do not know how to relate this flux-defined dust line to a single dust population.

The shape of the opacity curve can be used to solve this degeneracy. The opacity curve presents a sharp drop in opacity around the characteristic size $\lambda_{obs}/2\pi$ where the maximum opacity is reached. Moving toward smaller grains, the opacity drops abruptly over a narrow range of grain sizes. This steep part of the opacity was termed the *opacity cliff* by Rosotti et al. (2020) and is highlighted in Figure 3.1. An approximate solution to grain emission in the optically thin limit (and the Rayleigh–Jeans low-frequency approximation) is:

$$I_\nu = \frac{2k_B T \nu^2}{c^2} \cdot (\kappa_\nu \Sigma_d), \quad (3.10)$$

where ν is the observed frequency, k_B is the Boltzmann constant, T is the dust temperature, κ_ν is the dust opacity at the observed wavelength, and Σ_d is the dust surface density. In disks T , Σ_d and maximum grain size drop with radius. Moving from the inner disk outward (where $2\pi a \gg \lambda$) the opacity is initially increasing with radius, but then at the opacity cliff, it is quite abruptly dropping to a lower, roughly constant value. Outside of this drop, the dust suddenly has a lower opacity while T and Σ_d keep dropping, so there is little emission outside the opacity cliff. This initial increase and sudden drop of $\kappa(r)$ (due to the size sorting) is the feature that gives rise to the dust line. The grain size at the edge of the emission region is therefore the one at which the opacity cliff occurs, and this location corresponds to the edge of the surface density profile of this grain population. From an observational point of view, identifying the emission dust line at a wavelength λ_{obs} with the mass dust line for the grain population $a = \lambda_{obs}/2\pi$ is a good approximation, and from now on we use the more generic term dust line.

Optical depth effects are another potential issue in the identification of the dust line location. If the dust emission is optically thin, it is straightforward to associate a steep drop in the brightness profile to the dust line. If the emission is instead optically thick, one could argue that the drop in density could be hidden in the optically thick region, and that the dust line is misplaced at the location where the emission goes from being optically thick to optically thin. Since the observed drop in the emission is sharp (Birnstiel & Andrews 2014; Andrews et al. 2012; Powell et al. 2017), it is not expected to originate from opacity effects (that would show a much smoother transition). Indeed, observations show an intensity drop of about one order of magnitude over a very narrow radial range ($\Delta r/r \lesssim 0.1$). As the dust line location falls within this radial range, we take $\Delta r/r$ as the dust line relative error.

Given the previous considerations, we identify the dust line location as the radius enclosing 99% of the total dust emission, that is well representing the outer edge of the dust density profile in our simulations. The exact percentage of the total emission can vary, depending on the disk structure. This parameter can be tuned to match the location of the sharp intensity drop in the brightness profile, typical of the dust line. While other methods are possible, such as fitting the profiles with a broken power law or a similar function with a sharp cut-off, we found that the reliability of these methods can be impaired by the quality of the observations, and can be unreliable in disks showing radial substructures.

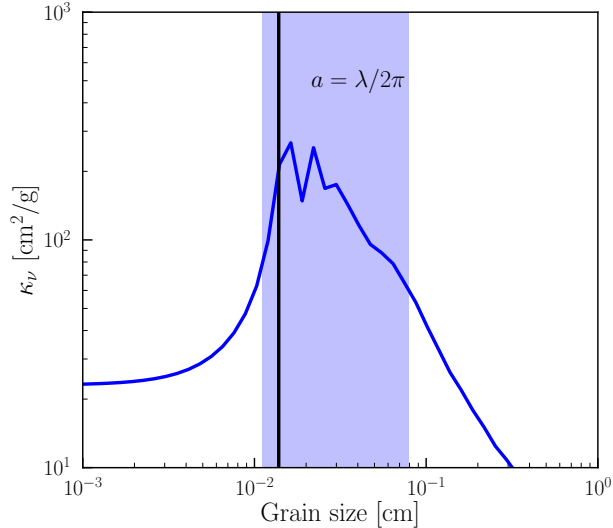


Figure 3.1: Dust opacity for a single grain population as a function of grain size at $\lambda = 0.87$ mm (Birnstiel et al. 2018). The shaded region represents the grain size range dominating the emission at 0.87 mm, the vertical black line indicates the size of grains dominating the emission according to the Mie scattering theory, with size $a = \lambda/2\pi$.

3.3.2 Radial density bumps

As shown in Section 3.2, when the dust evolution is dominated by drift, the dust line location can be used as a proxy of the local disk gas surface density. However, observations show that disks often have features that can be interpreted as pressure bumps and dust traps (e.g., Dullemond et al. 2018; Huang et al. 2018b; Pinilla et al. 2020), suggesting that other physical processes could be determining the exact dust line location. To estimate the disk surface density distribution using dust lines we must first understand how drift is affected by these substructures. Indeed, bumps in the density profile create a positive pressure gradient slowing down the inward drift (e.g., Pinilla et al. 2012). This can in turn move the dust lines to an outer radial position, and we must take this effect into account when estimating the disk surface density from the dust line location. If dust grains are efficiently trapped we would observe an increase in the emission at a range of (sub)millimeter wavelengths at the bump location, since millimeter-sized grains will be trapped. The width of this emission feature is going to change with wavelength, as large particles that are more affected by drift will be trapped more efficiently than small particles. With multiwavelength observations, we would be able to distinguish dust lines from traps. On the other hand, if the bump is not efficiently trapping the grains, it will only slow down the drift of the grains, and the dust line will not be affected.

3.3.3 Fragmentation velocity

In our simulations, we assumed a fragmentation threshold of 10 m/s, as discussed in Section 3.2. However, recent studies suggest lower thresholds to be more realistic. For instance, Musiolik & Wurm (2019) demonstrates that even ices have no advantage over silicates in collisional growth processes, and the lower grain stickiness can lower the fragmentation threshold down to ~ 1 m/s.

To test how the fragmentation threshold affects our results, we ran our simulations with a lower threshold of 1 m/s. Our approach to the disk mass estimate requires the dust lines to lay in the outer disk, where dust evolution is drift dominated. By increasing the fragmentation threshold, we increase the size of the fragmentation limited inner disk, where our method cannot be applied. At low fragmentation velocities, it may be necessary to verify if the dust lines of larger grains are determined by drift or fragmentation. This can be done by checking that these dust lines do not gather at the same radial location. However, when the dust lines are drift dominated, the fragmentation threshold has no effect on the mass estimate. This is demonstrated by our models, which show no difference in the dust line location in the outer disk for disks of the same mass and a fragmentation threshold of 1 m/s and 10 m/s

3.4 Simulation results

In this section, we show our model results and explore how different disk parameters affect the location of the dust line. The parameters taken into account are the disk mass M_{disk} , the stellar mass M_{star} , the age of the disk t_{disk} and the initial dust-to-gas mass ratio ϵ . As we are studying the evolution of large grains that are found in the disk mid-plane, we assumed the emission coming from vertical slabs of constant temperature and opacity (razor-thin disk). The brightness profile is then given by the simple radiative transfer equation:

$$I_\nu = B_\nu(T) (1 - e^{-\tau_\nu}), \quad (3.11)$$

where $B_\nu(T)$ is the Planck function and τ_ν the optical depth at a frequency ν .

The parameter study is based on a reference model of a disk with a column density $\Sigma_c = 175$ g/cm², corresponding to a disk mass of $0.11 M_\odot$. For each parameter explored, we fixed the other parameters at the values used in the reference model, shown in Table 3.1. The plots in Figure 3.2 show how the dust emission profiles compare to the surface density distribution of the most emitting grains. It is clear from the plot that the dust line location represents the outer edge of the dust surface density distribution quite well.

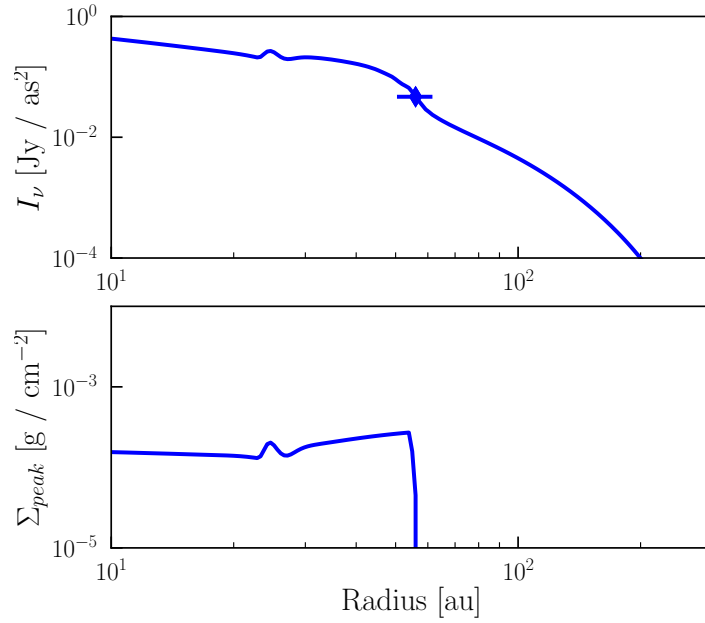


Figure 3.2: Reference model for the parameter study. The upper plot shows the dust emission profile at 0.87 mm, as predicted by the model. The dust line location, as defined in the text, is highlighted on the profile. The lower plot shows the surface density distribution of the most emitting grains. The dust line location in the first plot matches the outer edge of the density distribution in the lower plot for the same disk mass

Table 3.1: Physical parameters for the reference model.

Parameter	Value
M_{disk}	$0.11 M_{\odot}$
r_c	30 au
ϵ_0	0.01
M_*	$0.8 M_{\odot}$
L_*	$0.28 L_{\odot}$
t_{disk}	5 Myr

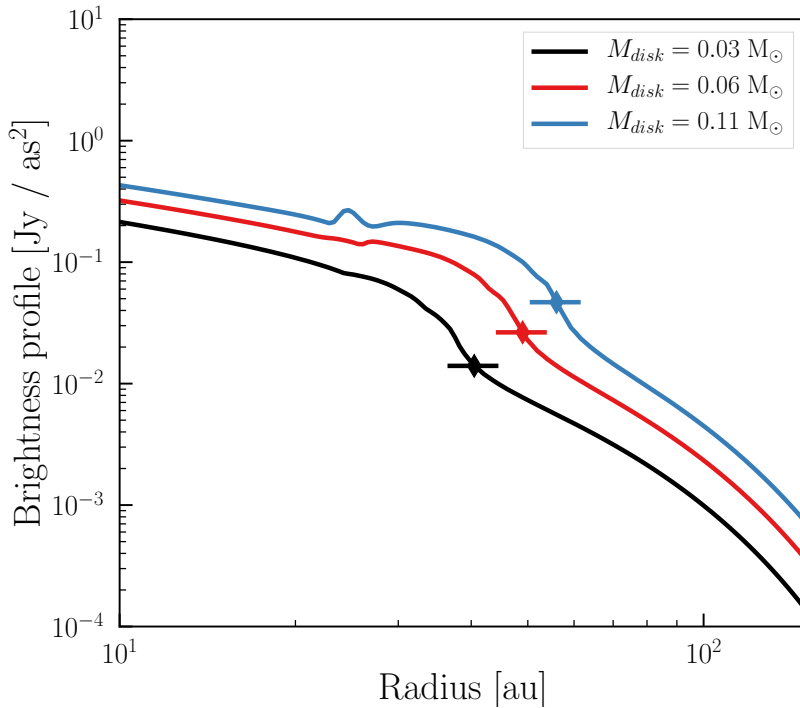


Figure 3.3: Dependence of the brightness profile on the disk mass. The dust line location, indicated by the dots on the profiles, shows a strong dependence on the disk mass.

Lastly, we discuss the effect of assuming a different gas surface density profile. As previously discussed, if the presence of substructure dominates the dust evolution, the dependence of the size of the emission region on the disk mass could be lost. The distinction between the two regimes is essential for the reliability of this technique.

Disk mass

The first requirement for any mass estimator is, by definition, to have a strong dependence on the disk mass, given in our case by Eq.3.5. To test this dependence we simulated the evolution of disks of different masses and study the changes in their brightness profiles, shown in Figure 3.3. The dust line locations in these profiles show a visible dependence on the disk mass. While this result confirms that the dust line location could be used as a good mass estimator, it does not match the relation $M_{disk} \propto r^{-1}$ given by Eq.3.5. One possible explanation is that Eq.3.5 only takes into account local dust evolution processes, neglecting the contribution to the dust distribution from particles drifting from outer radial locations. Our dust evolution model takes into account all these processes, possibly explaining the difference between our result and the prediction given by Eq.3.5.

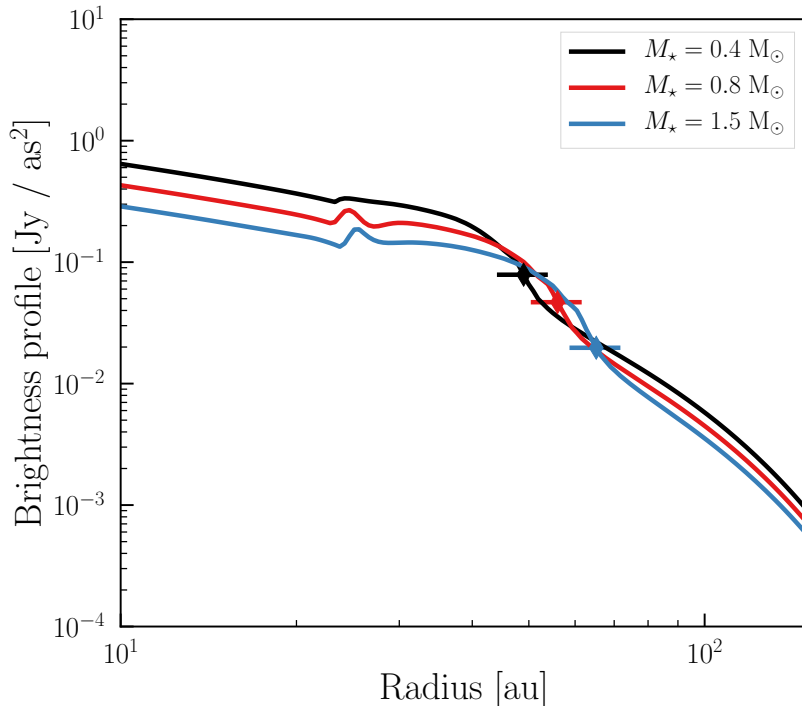


Figure 3.4: Dependence of the brightness profile on the stellar mass. The stellar mass affects the drift efficiency, however this parameter does not change significantly the dust line location.

Stellar mass

The amount of drift a grain undergoes depends on how well it is coupled to the gas structure. This is quantified by the Stokes number $St = t_{stop} \Omega_K$. Through the Keplerian frequency, the amount of drift depends on the stellar mass as $St \propto 1/\sqrt{M_\star}$ (e.g., Birnstiel et al. 2016; Chiang & Youdin 2010). This behavior is confirmed by the results presented in Figure 3.4, where the dust line location depends on the stellar mass.

In more realistic cases M_{disk} and M_\star are correlated, and Pinilla et al. (2020) suggest the disk mass to be a fraction of the stellar mass (5%). Even in this case the dust line location is dependent on the $M_{disk} - M_\star$ parameter. Care has to be taken when applying the mass estimator to disks around stars of different masses.

Disk age

The age of the disk determines how long particles have been drifting. Therefore, the dust line location is very sensitive to this parameter, as shown in both Eq.3.5 and Figure 3.5. As the age of the disk increases, the grains drift over a larger distance toward the inner disk. This effect is degenerate with the disk mass, and it is not possible to distinguish a younger, less massive disk from an older and more

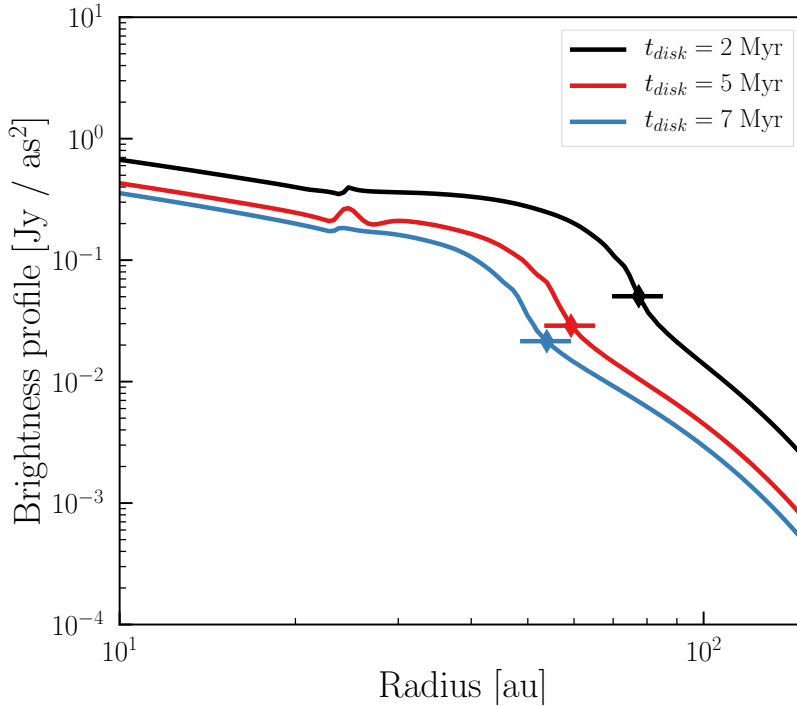


Figure 3.5: Dependence of the brightness profile on the age of the system. The location of the dust line has a strong dependence on this parameter, and any uncertainty on the disk age is directly propagated into the disk mass value.

Table 3.2: The dependence of the dust line location with the disk parameters, as described in Section 3.4.

M_{disk} [M_{\odot}]	M_{\star} [M_{\odot}]	t_{disk} [Myr]	ϵ	Dust line location [au]
0.03, 0.06, 0.11	0.8	5	0.01	40, 49, 56
0.11	0.4, 0.8, 1.2	5	0.01	53, 56, 61
$0.05 \cdot M_{\star}$	0.4, 0.8, 1.2	5	0.01	30, 49, 69
0.11	0.8	2, 5, 7	0.01	72, 56, 52
0.11	0.8	5	0.01, 0.05, 0.1	56, 56, 56

massive one. Therefore, an independent age estimate is central to a reliable mass estimate. However, especially for young stars, the age of the system is subject to significant observational uncertainties. The proper tuning of this parameter is likely to be the major source of uncertainties of the model.

Initial dust-to-gas ratio

The strength of this approach is that the mass estimate is independent of the dust-to-gas ratio, as we are looking at just the size of the emitting region and not its intensity profile. However Figure 3.6 shows that not only the dust line location, but also the intensity does not depend on the dust-to-gas ratio assumed at the

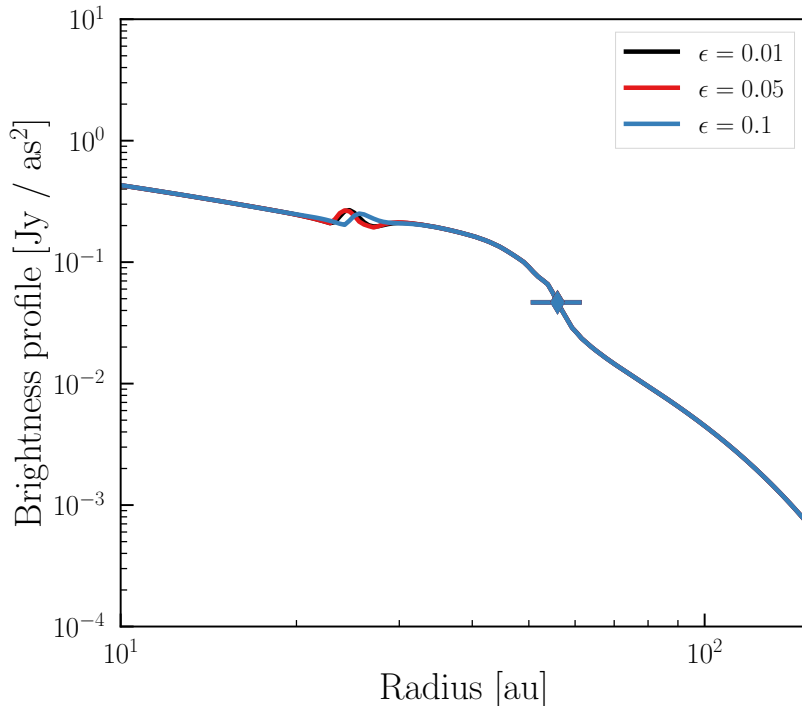


Figure 3.6: Dependence of the brightness profiles on the initial disk dust to gas ratio. The profiles are independent on the assumed initial ratio, suggesting that by this age most of the dust evolution already happened and it is not affecting our results.

beginning of the disk evolution. The drift timescale (Birnstiel et al. 2012), when equal to the disk age, can be written in terms of the dust-to-gas ratio:

$$\epsilon = \frac{1}{t_{disk}\Omega_K}. \quad (3.12)$$

Therefore, disks of different dust-to-gas ratios evolve toward this equilibrium value. Dust evolution happens mostly in the first few Myr, and within a lifetime of a Class II disk would reach the equilibrium value regardless how high or low it was initially. This is shown in Figure 3.7, where we see the evolution of the dust surface density distribution and the dust-to-gas from 1 Myr to 5 Myr assuming an initial dust-to-gas ratio of 0.1 and 0.01. After a few Myr, the dust-to-gas ratio (and Σ_d consequently) reach an equilibrium value dependent on the disk age, given by Eq.3.12, regardless of the assumed initial value.

3.5 Population synthesis

In the previous section, we have shown how disk parameters affect the dust line location, suggesting that it is a good tracer for the disk mass. We now discuss how well Eq.3.5 (Powell et al. 2017) estimates the mass of our synthetic

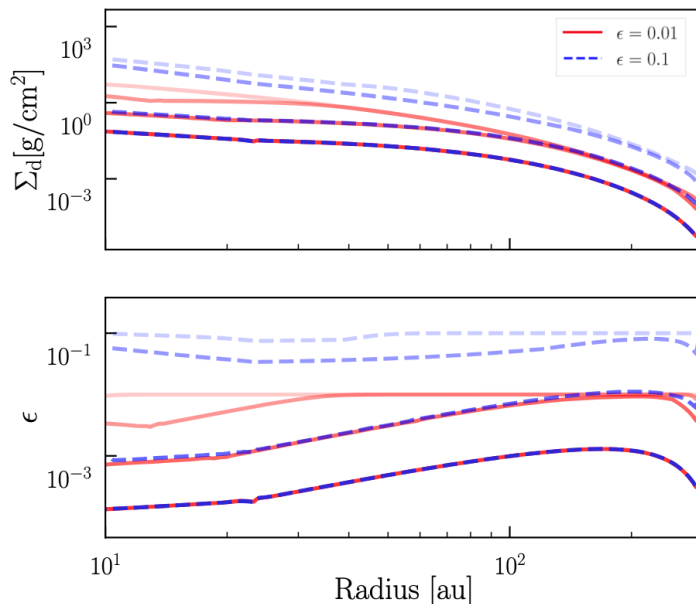


Figure 3.7: Time evolution, between 1 Myr and 5 Myr, of the dust surface density distribution (top) and the dust-to-gas ratio (bottom) assuming an initial dust-to-gas ratio of 0.01 (red) and 0.1 (blue), with darker lines for older ages. This plot shows how most of the dust evolution happens within the first few Myr. After that the dust density profile and the dust-to-gas ratio are independent of the assumed initial dust-to-gas ratio.

disk models. We simulated a large number of disks on a grid of values for the parameters discussed in Section 3.4, summarized in Table 3.3. We then estimated the dust line location of four different dust populations from the 0.087 cm, 0.1 cm, 0.3 cm, and 0.9 cm emission profiles. In Section 3.3, we showed that the location enclosing 99% of the dust emission at a wavelength λ is well representing the dust line location of grains of size $\lambda/2\pi$. Alternatively, to analyze more consistently the large number of disks in this section, we took a more error-proof approach by fitting the dust emission profiles with a fitting function such as the one shown in Figure 3.8. This function is composed of an inner and outer power law (inner and outer disk) with an exponential taper, plus a sigmoid function at the dust line location to reproduce the characteristic steep emission drop.

This approach assumes a regular, monotonically decreasing profile, a condition satisfied in our synthetic population, but not in more realistic disks with evidence of substructures such as rings and gaps. In this section, we estimate the dust line location by fitting the synthetic profiles to have a more error-proof estimate, as necessary when working with a large number of disks. In the other sections of the paper, we again place the dust line on the location enclosing 99% of the dust emission, as this definition works also in the presence of radial features and can be easily double-checked when working with a small number of disks.

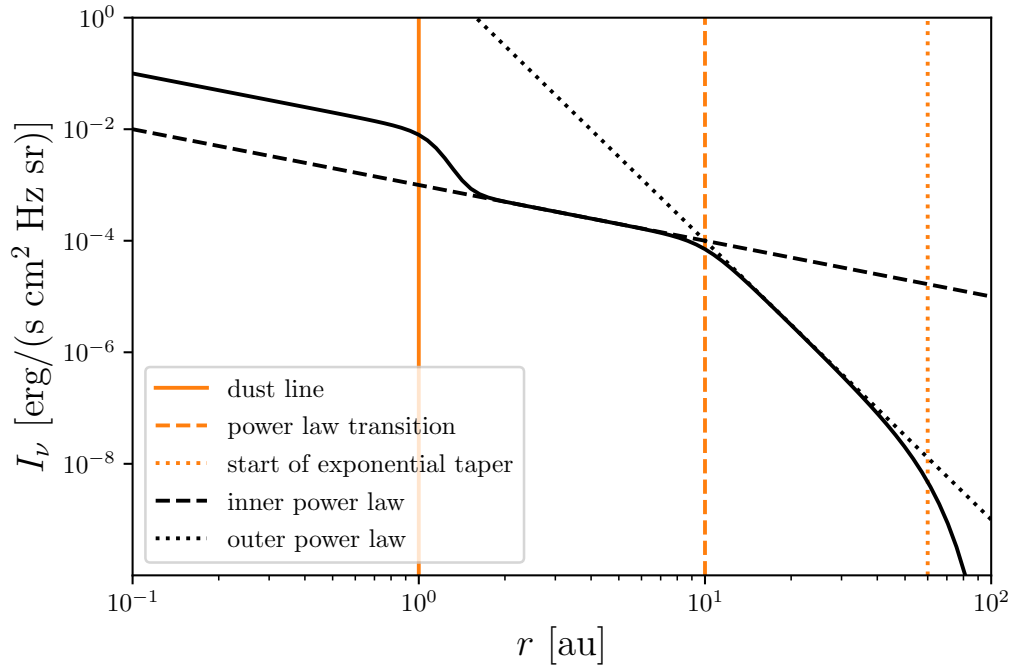


Figure 3.8: Function adopted to fit the simulated brightness profiles. This function accurately finds the outer edge of the dust emission.

Table 3.3: Input parameters of the synthetic disk population.

Parameter	Value
M_{disk}	$[10^{-3} - 0.2] M_{\odot}$
M_{*}	$[0.2 - 2] M_{\odot}$
α	$[10^{-4} - 0.03]$
v_{frag}	$[1 - 20] \text{ m/s}$
r_c	$[30 - 200] \text{ au}$
t_{disk}	5 Myr

Using these dust line location estimates, we followed the same scheme used in Powell et al. (2017). We calculated the gas surface density at the dust line locations using Eq.3.5, which we then fitted to a Lynden-Bell-Pringle self-similar profile, as in Eq.3.6, to estimate the gas distribution and its total mass. We compared these mass estimates to the input model masses to test how tight the correlation between the estimated mass and the model mass is. The result of this study, shown in Figure 3.9, is in agreement with the results in Section 3.4, supporting the strong dependence of the dust line location on the disk mass, but also provide further interesting information.

The first interesting point is how well correlated the model disk masses and the dust line based estimates are, although with some scattering due to the dependence

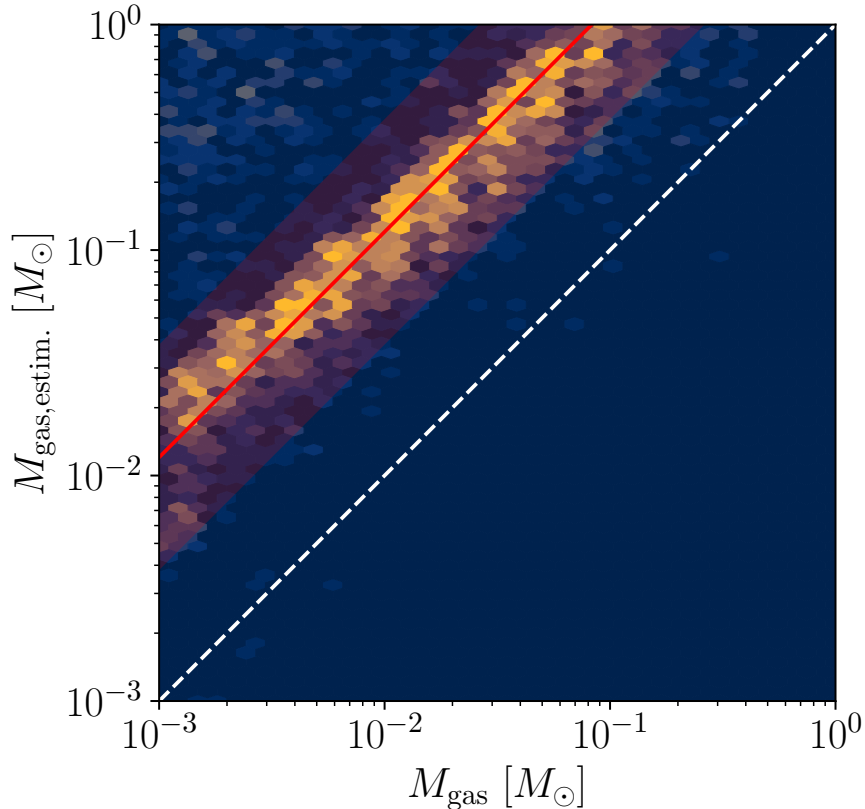


Figure 3.9: Comparison between input disk masses and the estimates from the dust line location. The shaded red area includes the best 68% of the disks, the red line is the median mass of these disks, and the white line is the correlation function for a perfect match. The dust line location systematically overestimates the disk mass by about one order of magnitude.

on the other disk parameters as we discussed already in Section 3.4. However, the plot also shows that mass estimates derived from Eq.3.5 do overestimate systematically the disk mass. Indeed, Eq.3.5 is derived from local considerations on the timescales of the processes involved in dust evolution at the dust line location, as we discussed in Section 3.2. However, the dust line locations of different grain populations are not independent, as the total dust mass flux has to be conserved as the grains drift toward the inner disk. When assuming that the dust evolution happens on a timescale of about the age of the disk, we are implicitly assuming that the dust mass flowing through the dust line is negligible compared to its total mass at this location. This is a good approximation in the outer disk, the main mass reservoir, but it breaks down in the inner disk. As a matter of fact, the gas surface density estimates from Eq.3.5 for our synthetic population get worse at smaller radial locations. Since Eq.3.5 holds in the outer disk, it provides sufficient constraints to the disk mass from the dust line of small grains, explaining the strong correlation seen in Figure 3.9.

Other interesting information can be derived by fitting a power law to the

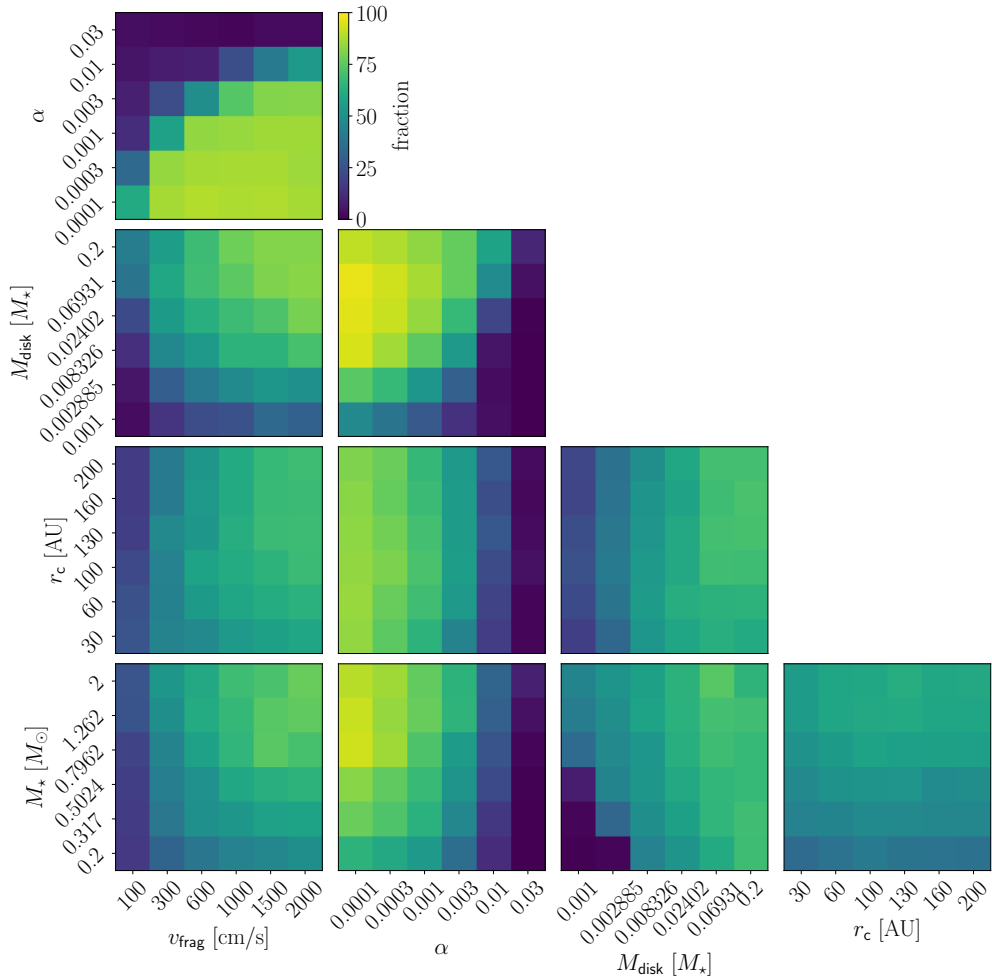


Figure 3.10: Projection of the posterior probability distribution of our fit. The disks are evenly distributed over the parameter space, except for very low disk mass or high turbulence.

data. From the posterior probability distribution function of the disk parameters, we can check for which parameter range the dust line location correctly predicts the disk mass. Figure 3.10 shows the parameter distribution for the disks whose mass estimate is within a factor of 3 of the calibrated relation. This plot states what fraction of these simulations with the given parameter choices are within this constraint. The plot shows that the correlation between the dust line mass estimate and the model masses breaks down for highly turbulent disks ($\alpha \gtrsim 10^{-2}$) and for very low disk masses ($\lesssim 10^{-4} M_{\odot}$). In these cases, the assumption of drift-dominated dust evolution is no longer satisfied, and the dust line location is less and less dependent on the disk mass. However, these values are unrealistic in most observed disks, and therefore this does not affect the reliability of mass estimates based on the dust line location.

3.6 Surface density distributions with pressure bumps

We have shown that the dust line location is a reliable tracer for the disk mass in the case of a smooth gas surface density distribution, confirming the general concept of Powell et al. (2017, 2019). We stress here that the results of the population synthesis study given in the previous section do not affect our method: by simulating the dust evolution, rather than relying on a calibrated Powell expression, our results are independent on the assumptions from which Eq.3.5 is derived. Moreover, disks often show substructures, such as rings and gaps in their brightness distribution, often interpreted as regions of high/low pressure, or pressure bumps (e.g., Pinilla et al. 2012; Rosotti et al. 2020). Because pressure bumps help to reduce or completely suppress the radial drift, the outer edge of the dusty disk or dust line is directly influenced by the potential presence of pressure bumps. To include density bumps in our gas distribution we assumed Gaussian perturbations as in Pinilla et al. (2020):

$$\Sigma'(r) = \Sigma(r) \cdot (1 + B(r)), \quad (3.13)$$

with

$$B(r) = A \exp - \left(\frac{(r - r_p)^2}{2w^2} \right), \quad (3.14)$$

where $\Sigma'(r)$ is the unperturbed density from Eq.3.6 and A is the amplitude, r_p the center, and w the width of the Gaussian perturbation, that we assumed to be equal to the pressure scale-height H_p . The width has to be larger or equal to H_p to ensure the stability of the bumps (e.g., Pinilla et al. 2012; Dullemond et al. 2018). A narrower bump has a higher pressure gradient and a stronger effect on the dust evolution. This is studied by setting $w = H_p$. We considered two kinds of bumps: weak bumps with $A = 1$, and strong bumps with $A = 4$. Hydrodynamical simulations from Zhang et al. (2018) show that bumps with $A = 1$ and $A = 4$ resemble the presence of a giant planet of mass $0.3 M_{\text{Jup}}$ and $1 M_{\text{Jup}}$, respectively. For this range of masses, the bump width does not appear to change with A , justifying our assumption to use the same width.

As discussed in Section 3.2, particle trapping is likely to happen inside radial substructures. Since dust lines differ in their location at different wavelengths, this suggests a different distribution for particles of different sizes. If a ring is an efficient particle trap, we would expect an increase in the dust continuum emission at every wavelength at the trap location. However the dust evolution is still drift dominated outside of the density bump, and dust lines at a different location than the bump radius could be used to estimate the disk mass. When a density bump

Table 3.4: Disk mass M_{disk} and critical radius r_c (from Eq.3.6), initial dust-to-gas ratio ϵ_0 , stellar mass M_* and luminosity L_{star} , and age of the system t_{disk} used in the dust evolution model, as measured in TW Hya as a test case.

Parameter	Value
M_{disk}	[0.01 – 0.2] M_{\odot}
r_c	30 au
ϵ_0	0.01
M_*	0.8 M_{\odot}
L_*	0.28 L_{\odot}
t_{disk}	5 Myr
A	[1, 4]
r_p	40 au
w	4.3 au

affects the dust line, such an effect could be accounted for by dust evolution models to yield a correct mass estimate.

The first test is to study how a bump affects the dependence of the dust line on the disk mass by evolving several disks with different masses and adding a bump at 40 au. The used disk parameters are shown in Table 3.4, and the simulation results in Figure 3.11 and Figure 3.12 with a narrow and wide bump ($A = 1$ and $A = 4$, respectively). The size of the emitting region is still tracing the dust line location, which is still strongly dependent on the disk mass. The location of the dust line depends on the bump amplitude A , but it is still mainly determined by the disk mass.

Another parameter that can affect the dust line location is the bump location. We expect bumps in the outer disk to have a stronger effect on the grain evolution, as more grains will cross the bump during the disk lifetime. Our models show that bumps outside the dust line have a larger effect on the dust line location than bumps inside the dust line location, however this does not affect the applicability of the method.

Such a case is shown in Figure 3.13 for a disk model with an outer bump with an amplitude $A = 1$. The profiles show a drop in the brightness typical of the dust line inside the bump, whose location can be blindly used to provide a disk mass estimate. This result does not change with the bump amplitude as shown in Figure 3.14 for a disk model with a bump of amplitude $A = 4$. In this disk model, more grains gather at the bump, but in the region inside the trap we can still observe a drift-defined dust line. As in the case of a bump in the inner disk, the dust line location is dependent on the bump amplitude, but it is still drift dominated and it can be used to provide a mass estimate.

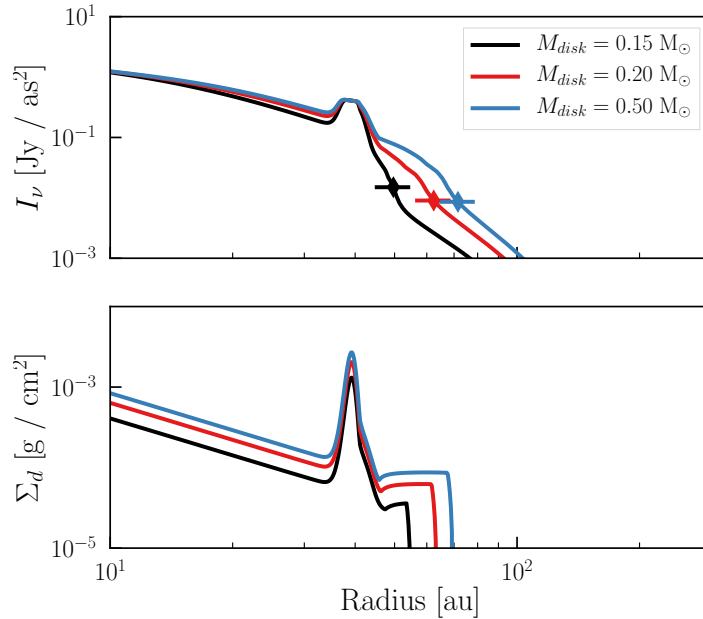


Figure 3.11: Dependence of the dust line location on the disk mass in the presence of a weak bump in the gas density at 40 au. The upper plot shows the dust emission profile at $\lambda = 0.87$ mm, as predicted by the model. The dust line location, as defined in the text, is highlighted on the profiles. The lower plot shows the surface density distribution of the most emitting grains. The dust line location in the first plot matches the outer edge of the density distribution in the lower plot for the same disk mass.

When the disk presents a more complex structure featuring multiple bumps, the dust line location may lose its dependence on the disk mass. As the number of radial substructures increases, the more extended are the regions of the disk that are not drift dominated, and dust lines in these regions will have weak dependence on the disk mass. In this case, resolved observations at different millimeter wavelengths should all show similar brightness profiles. In this complex case other methods need to be used to estimate the disk mass.

In general, modeling the dust evolution is necessary to provide a reliable mass estimate. In Figure 3.15 we show an example of a disk with multiple radial features where the dust line location is independent on the disk mass, and is tracing the location of a pressure bump. This disk model has the same parameters as in Table 3.4, with weak bumps at 40 au, 80 au and 120 au.

3.7 Applicability to individual disks

In this section we show results from disk evolution models of TW Hya, with smooth structures, and AS 209, with very sharp and strong structures. We modeled the dust evolution of these two disks to explore the relation between dust line

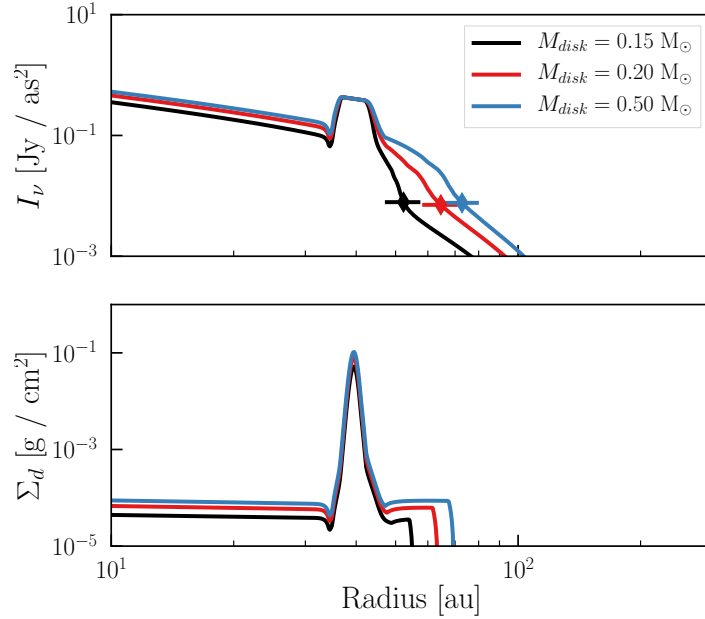


Figure 3.12: Dependence of the dust line location on the disk mass in the presence of a strong bump in the gas density at 40 au. The upper plot shows the dust emission profile at $\lambda = 0.87$ mm, as predicted by the model. The dust line location, as defined in the text, is highlighted on the profiles. The lower plot shows the surface density distribution of the most emitting grains. The dust line location in the first plot matches the outer edge of the density distribution in the lower plot for the same disk mass.

positions, bumps and disk masses. We then compared the disk masses inferred from the dust line locations with the input model parameters.

In an old disk with a smooth structure, such as TW Hya, we would expect the dust evolution to be drift dominated. Bumps in the gas density profile could cause a departure from the simple relation between local surface density and dust line location given by Eq. 3.5. However, the dust line location should still maintain a strong correlation with the disk mass, and a mass estimate could still be provided by matching the model prediction of dust line locations with dust continuum data.

When dealing with a structure with a higher contrast between gaps and rings, such as in AS 209, the global effect of drift on dust evolution is much weaker. Stronger radial features make the correlation between disk mass and dust lines weaker, and even if the grains are not trapped by the substructures, there will be a large uncertainty in the mass estimate.

The age of the disk is typically assumed to be the same as that of the host star which are subject to significant uncertainties. Given the form of Eq.3.5, the disk mass scales linearly with the age estimate. An older disk implies that grains are allowed to drift to more inward radial locations, therefore an increase in the age is indistinguishable from a decrease in the disk mass in determining the dust line

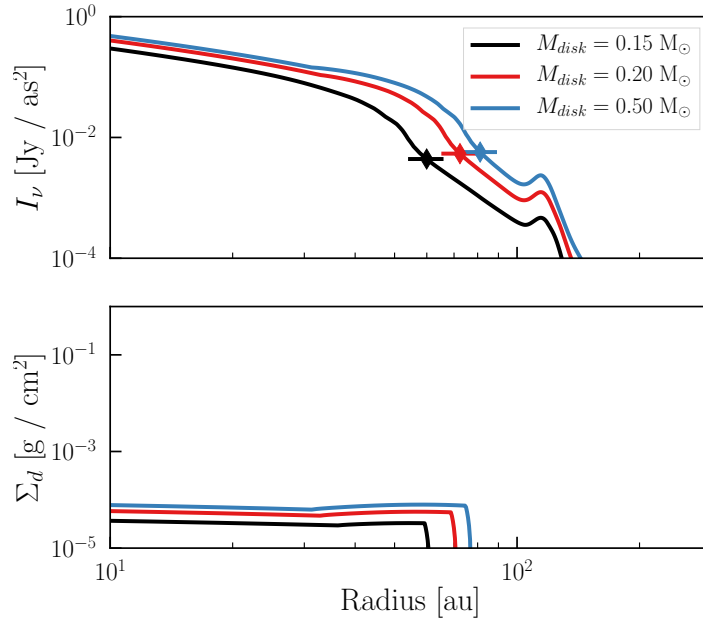


Figure 3.13: Dependence of the dust line location on the disk mass in the presence of a weak bump in the gas density at 120 au. The upper plot shows the dust emission profile at $\lambda = 0.87$ mm, as predicted by the model. The dust line location, as defined in the text, is highlighted on the profiles. The lower plot shows the surface density distribution of the most emitting grains. The dust line location in the first plot matches the outer edge of the density distribution in the lower plot for the same disk mass.

location. The disk age is likely the highest source of uncertainty in the model, as shown in Section 3.4.

3.7.1 TW Hya

TW Hya is one of the most well-studied disks, and it is a good benchmark to test our model. In the literature the TW Hya disk mass has been estimated using integrated dust emission (Andrews et al. 2012; Menu et al. 2014), CO line emission (Rosenfeld et al. 2012; Kama et al. 2016) and HD line emission (Bergin et al. 2013; McClure et al. 2016; Trapman et al. 2017). The mass of TW Hya was also derived by Powell et al. (2017) using the dust line location as we described. All these estimates are reported in Table 3.5.

The discrepancy between the mass derived from the dust line can be explained by a few factors. Evolving disks can be depleted of dust (e.g., Birnstiel et al. 2012), and optical depth effect can lead to a mass underestimation when using dust emission. HD-derived mass is very sensitive to the assumed thermal structure: Trapman et al. (2017) suggest a disk mass for TW Hya about one order of magnitude lower than Bergin et al. (2013) using a different disk structure. With regard to CO line emission, there is evidence of severe carbon depletion from the

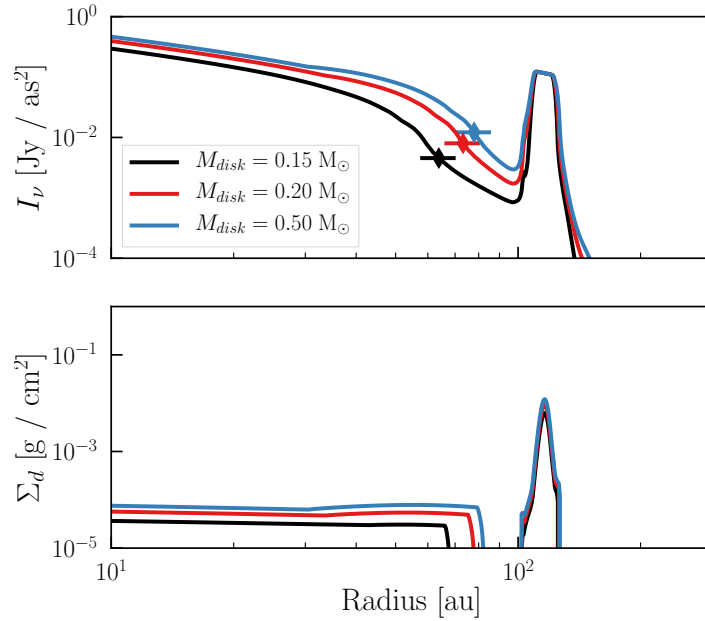


Figure 3.14: Dependence of the dust line location on the disk mass in the presence of a strong bump in the gas density at 120 au. The upper plot shows the dust emission profile at $\lambda = 0.87$ mm, as predicted by the model. The dust line location, as defined in the text, is highlighted on the profiles. The lower plot shows the surface density distribution of the most emitting grains. The dust line location in the first plot matches the outer edge of the density distribution in the lower plot for the same disk mass.

gas phase (Kama et al. 2016; Miotello et al. 2017) that questions the reliability of CO-based estimates. A survey of the Lupus star-forming region by Ansdell et al. (2016) showed that CO-derived disk masses are not compatible with the measured accretion rates. An independent mass estimator, such as the dust line location, can lead to a better understanding of the disk structure from the discrepancy between mass estimates from different techniques.

For our representative dust evolution model of TW Hya we used the same parameter setup as in Powell et al. (2017) and checked how well we could reproduce the dust continuum observations. Spatially resolved CO observations (Rosenfeld

Table 3.5: TW Hya mass estimates from different methods. - (1) Andrews et al. (2012); Menu et al. (2014); (2) Rosenfeld et al. (2012); Kama et al. (2016); (3) Bergin et al. (2013); (4) Trapman et al. (2017), (5) Powell et al. (2017).

Integrated dust emission	$0.018 M_{\odot}^1$
CO Line Emission	$0.003 M_{\odot}^2$
HD Line Emission	$> 0.05 M_{\odot}^3$
	$[7.7 \cdot 10^{-3}, 2.3 \cdot 10^{-2}] M_{\odot}^4$
Dust Line Location	$0.11 M_{\odot}^5$

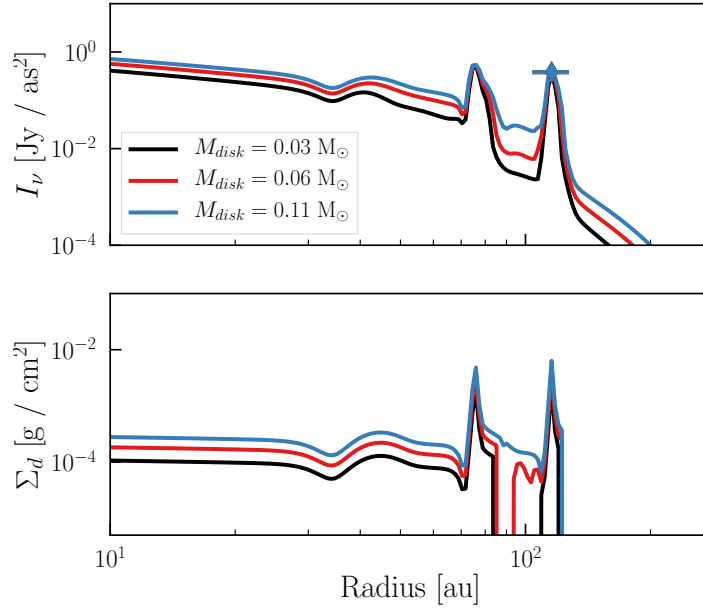


Figure 3.15: Dependence of the dust line location on the disk mass in the presence of weak bumps at 40 au, 80 au and 120 au. The upper plot shows the dust emission profile at $\lambda = 0.87$ mm, as predicted by the model. The dust line location, as defined in the text, is highlighted on the profiles. The lower plot shows the surface density distribution of the most emitting grains. Both the dust line location and the outer edge of the dust surface density distribution trace the location of the outer bump and do not depend on the disk mass.

et al. 2012) are well reproduced by the Linden-Bell & Pringle solution (Eq.3.6) with best fit parameters $r_c = 30$ au and $\gamma = 1$. As Σ_c depends on the assumed CO-to-H₂ ratio, this remains a free parameter. The C¹⁸O column density profile derived in Zhang et al. (2017) features a peak in the gas surface density at 70 au. We included this feature by adding a scaling factor to our gas density profile (see also Huang et al. 2018b):

$$\Sigma(r) = \Sigma_c \left(\frac{r}{r_c} \right)^{-\gamma} \exp \left[- \left(\frac{r}{r_c} \right)^{2-\gamma} \right] \times f(r), \quad (3.15)$$

where f is setting the shape of the bump in the gas column density profile:

$$f(r) = \begin{cases} 1 + A \exp \left(-\frac{(r-R_{bump})^2}{2\sigma_{in}^2} \right), & r < R_{bump} \\ 1 + A \exp \left(-\frac{(r-R_{bump})^2}{2\sigma_{out}^2} \right), & r > R_{bump}, \end{cases} \quad (3.16)$$

with the model parameters are as listed in Table 3.6.

Table 3.6: Parameter values assumed for TW Hya.

Parameter	Value	Parameter	Value
M_*	$0.8 M_\odot$	σ_{in}	12 au
M_{disk}	$0.11 M_\odot$	σ_{out}	6 au
r_c	30 au	t_{disk}	5 Myr
γ	0.9	T_{10}	40 K
A	3	a_{turb}	0.01
R_{bump}	70 au		

Using this setup we evolved the TW Hya disk and tested the model results against observational data for the dust continuum emission at 0.87 mm, from Andrews et al. (2016), as shown in Figure 3.16. As a proof of concept in the figure we also show the model result without including the bump located at 70 au, placing the location of the dust line ~ 20 au closer to the star. To fit this smooth model with the observations, we would need to assume a disk mass about $\sim 50\%$ smaller than the mass derived with the presence of the bump.

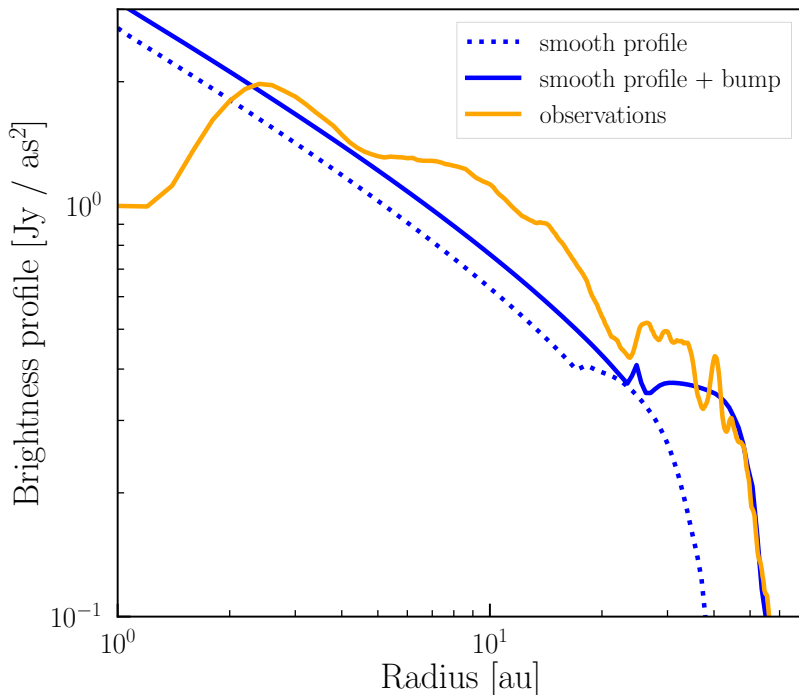


Figure 3.16: Comparison of the dust continuum emission at 0.87 mm as predicted by our model (blue solid line) and the observational data (orange solid line) from Andrews et al. (2016). The blue dotted line shows the model result without accounting for radial structures, highlighting their importance for this mass estimate.

Using this model, we were able to reproduce the dust line location from ob-

servations using a disk mass of $0.11 M_{\odot}$, in accord to Powell et al. (2017) who estimated the same disk mass with a different combination of grain size and drift velocity, not accounting for the bump in the gas density distribution. This explains why the mass estimates are in agreement, in contrast of what one would expect from our population synthesis study, showing that the Powell expression overestimates the disk mass by a factor of ~ 12 . This estimate is consistent with the lower limit of $0.05 M_{\odot}$ given by HD measurements (Bergin et al. 2013; Kama et al. 2016), but not with the more recent estimate $7.7 \cdot 10^{-3} M_{\odot} \leq M_{disk} \leq 2.3 \cdot 10^{-2} M_{\odot}$ from Trapman et al. (2017). This new mass is up to a factor of ~ 5 larger than the mass derived from CO observations, depending on the model (Thi et al. 2010; Gorti et al. 2011), showing therefore evidence of moderate depletion of CO (Powell et al. 2017).

3.7.2 AS 209

In this section, we test our model for a disk with strong radial substructures, AS 209. For this disk, surface density profiles are available in the literature, either from CO observations (Huang et al. 2016) or multiwavelength continuum observations (Tazzari et al. 2016). Unfortunately high spatial resolution data of CO gas emission are not available. To model the gas structure we used the same parameterization of the dust distribution given in Fedele et al. (2018), an extensive study of the disk radial structures based on high-resolution Atacama Large Millimeter/submillimeter Array (ALMA) data. The reader should keep in mind that this is an approximation: the purpose of this section is to show a practical application of our model to a disk with prominent radial features and not an accurate modeling of the disk structure around AS 209. The gas surface density distribution is:

$$\Sigma(r) = \Sigma_c \left(\frac{r}{r_c} \right)^{-\gamma_1} \exp \left[- \left(\frac{r}{r_c} \right)^{2-\gamma_2} \right] \times \delta(r), \quad (3.17)$$

where $\sigma(r)$ is the density scaling factor:

$$\delta(r) = 1 - A_{G1} \phi(R_{G1}, \sigma_{G1}) + A_{R1} \phi(R_{R1}, \sigma_{R1}) - \quad (3.18)$$

$$A_{G2} \phi(R_{G2}, \sigma_{G2}) + A_{R2} \phi(R_{R2}, \sigma_{R2}) \quad (3.19)$$

where the right end terms are Gaussian functions $A \phi(R, \sigma)$, centered on R with width σ and amplitude A , representing the rings and gaps in the gas structure. The values used in this model are shown in Table 3.7.

Table 3.7: Parameter values assumed for AS 209.

Parameter	Value	Parameter	Value
M_*	0.9 M_\odot	R_{R1}	78.65 au
M_{disk}	0.11 M_\odot	σ_{R1}	8.95 au
r_c	80 au	A_{G2}	0.025
γ_1	-0.24	R_{G2}	103.2 au
γ_2	2.19	σ_{G2}	15.6 au
A_{G1}	0.03	A_{R2}	4.8
R_{G1}	61.7 au	R_{R2}	129.3 au
σ_{G1}	8 au	σ_{R2}	10.5 au
A_{R1}	0.80		

Using this parametrization we simulated the evolution of AS 209, and compared the emission at 0.87 mm wavelength with the distribution of grains dominating the emission at this wavelength in Figure 3.17. The figure shows how in the case of a disk with prominent radial features, such as AS 209, grains gather at the ring locations, therefore the dust line location is tracing the trap location and lose the dependency with the disk mass. The trapping happens for grains of all sizes, therefore this result does not change with the observed wavelength as observed recently by Long et al. (2020) when comparing ALMA observations at two wavelengths of protoplanetary disks with structures. In Figure 3.18 we see how the disk shows the same profile at 1.3 mm, and the dust line location lays at the outer bump location at both wavelengths. Multiwavelength observations can reveal when dust lines trace a bump location, that is, when the dust line cannot be used as a mass estimator. Particle trapping can affect the applicability of the mass estimate method.

*full

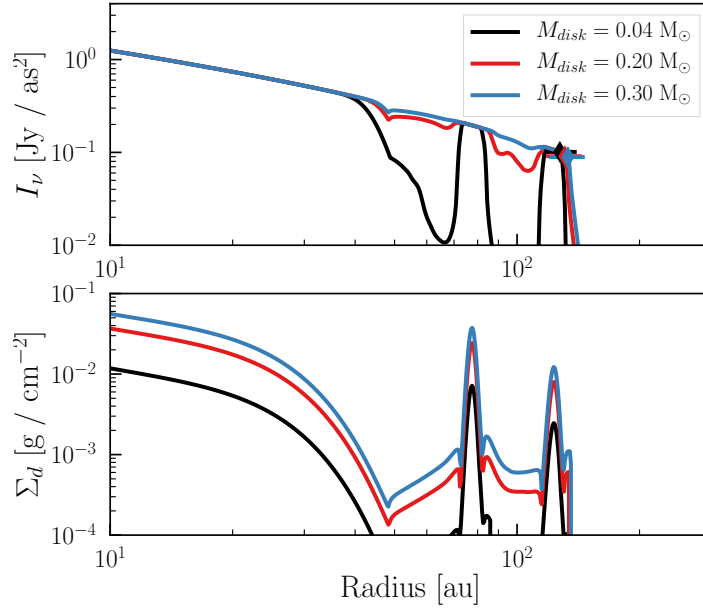


Figure 3.17: Comparison between the brightness profile at 0.87 mm and the density distribution of the most emitting grains.

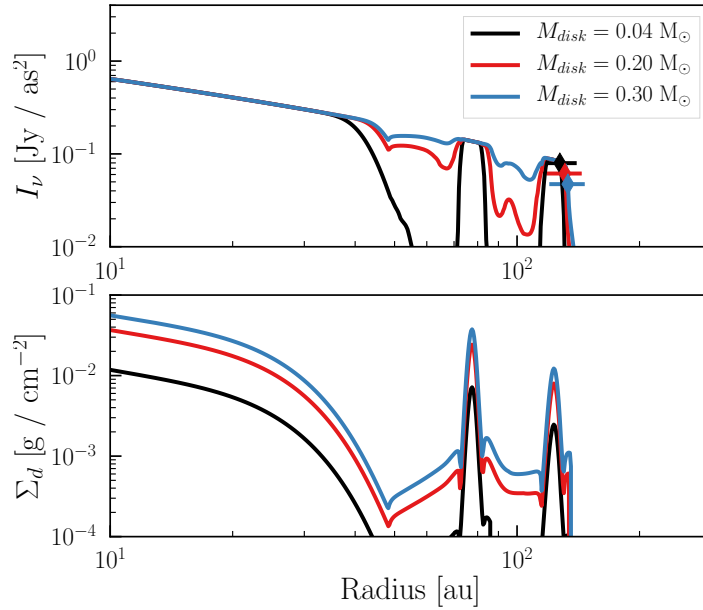


Figure 3.18: Comparison between the brightness profile at 1.3 mm and the density distribution of the most emitting grains.

3.8 Summary and conclusions

We used dust evolution models to test the applicability of the disk outer edge (dust lines) located at multiple wavelengths as a disk gas mass tracer, as proposed in Powell et al. (2017, 2019). The dust line location is related to the maximum

radial location at which grains of size $2\pi/\lambda_{obs}$ can be observed. The robustness of this method comes from its independence on an assumed tracer abundance to derive the total gas mass. The assumption made to derive a disk mass is that the dust evolution is drift dominated, meaning that the age, growth and drift timescale are the same at the late stages of disk evolution for the grains at their dust line location. This is a reasonable assumption for evolved disks ($t_{disk} \gtrsim 1Myr$), confirmed by previous results in the literature. At the same time, the relation between dust line location and disk mass can be dubious in disks showing radial features. These substructures can affect the grains drift timescale, and the relation between dust line location and disk mass is no longer unique.

To test the reliability of the dust line location as a mass estimator, we used numerical models of grain evolution to study the dust evolution in disks. We first analyzed the dependence of the dust line location on the disk mass, age, dust-to-gas ratio and stellar mass. We find that the dust line location is mainly dependent on the disk mass and the age of the system. The disk mass and age are degenerate, and to apply this method we need a reliable age estimate. Any uncertainty in the age estimate is propagated to the mass estimate.

Once we know the dust line to be mainly dependent on the disk mass, as the next step we calibrated its relation to the total disk mass. We applied the dust line-disk mass relation from Powell et al. (2017, 2019) to a population of synthetic disks, and while the disk masses from the models and the ones derived from the dust line are tightly correlated as expected, we found that the masses derived from the Powell et al. (2017) expression are overestimated by a factor of 12 ± 0.5 , bringing this mass estimate more in line with gas-based estimates. This result improves on the argument presented in Powell et al. (2017), based on local considerations of the grain evolution on the dust line location, by taking into account that the dust lines of different populations are not independent, as the total mass flux has to be conserved. This is not taking into account the effect of radial structures on dust evolution, and care needs to be used in comparing this result to other mass estimates. This study also demonstrates that the reliability of this mass estimate is not affected by the disk physical properties, except for a high turbulent parameter ($\gtrsim 10^{-2}$) or a very low disk mass ($\lesssim 10^{-4} M_{\odot}$), as this would break the assumption of drift dominated dust evolution.

We then tested the effect of perturbations on the surface density distribution of disks: these substructures affect the dynamical timescale of grains and the location of their dust line. We find that, when these structures do not act as efficient dust traps, the dust line location moves further out, while keeping a strong dependence on the disk mass. Therefore, while the dust line- M_{disk} relation depends on the disk structure, it is still a good mass estimator. When instead radial structures act as

efficient particle traps, the dust line location is no longer dependent on the disk mass, and it only traces the trap location. From an observational point of view, we know when the dust line is tracing the trap location by looking at multiwavelength dust continuum observations. In case of trapping, we expect grains of all sizes to be trapped, and dust lines at different wavelength will be observed at the same location. In this case, we will need to resort to other mass estimators.

Lastly, to show the applicability of the method to real data, we used this technique to estimate the mass of two well studied disks: TW Hya, characterized by an overall smooth gas structure, and AS 209, a disk featuring several gaps and traps. Our method successfully derived a mass estimate for TW Hya of $0.11M_{\odot}$, a factor of ~ 5 higher than CO based mass estimates. The disk in AS 209, on the other hand, is an example of when the dust line location is not an appropriate mass estimator. This disk presents evidences of particle trapping, and our model predicts a gathering of the dust lines for different dust populations at the location of the outer ring. In this case the dust line location is tracing the location of particle traps, and as such is depending not on the disk mass but on the location of the structures in the gas profile.

To summarize, in this paper we provide evidence showing that the dust line location is a reliable mass estimator when the dust evolution is drift dominated, although the exact relation between dust line and disk mass depends on the structure of the studied disk. This confirms the analysis of Powell et al. (2017, 2019). This relation in turn can be calibrated by running a simple two population dust evolution model that, when there is no particle trapping in the disk, provides us the location of the dust line location for each observed dust population for a given disk mass.

Constraining the turbulence and the dust disk in IM Lup: Onset of planetesimal formation

The content of this Chapter is based on **Franceschi et al. (2023)**, published in *Astronomy & Astrophysics (A&A)*, 671, A125.

Details of authorship: I am the first author of this paper, working under the supervision of Prof. Thomas Henning and in close collaboration with Prof. Tilman Birnstiel. The feasibility of this analysis was investigated in a preliminary study in Anirudh Sharma Master Thesis. The observational data used in this work are publicly available. I developed the disk model and the fitting algorithm to the observational data, with the support of Prof. Tilman Birnstiel. I conducted the analysis of the best-fit model supported by Prof. Thomas Henning and Prof. Tilman Birnstiel. The text was written by myself, with the contribution of Prof. Tilman Birnstiel in Section 4.4.3. All co-authors provided comments on the text.

4.1 Motivation

In Section 1.2.2 we discussed how the dust distribution in protoplanetary disks strongly depends on the grain sizes. We discussed how small dust grains ($\sim 1 \mu m$) are well coupled to the gas structure, extending, thus, vertically over several scale heights, following the gas distribution. Dust settling in turbulent disks was extensively studied (e.g., Dubrulle et al. 1995; Schr apler & Henning 2004; Fromang

& Nelson 2009; Zsom et al. 2011; Woitke et al. 2016). We also discussed how large millimeter grains settle much faster towards the disk midplane, where the growth process is particularly efficient because of the high densities. By constraining the distribution of both large and small dust grains, we can extrapolate the grain’s vertical size distribution, probing fundamental disk properties such as the turbulent structure and the dust-to-gas ratio.

Disks tend to have a flared structure (Kenyon & Hartmann 1987; Bell et al. 1997; Chiang & Goldreich 1997). Flaring occurs when the midplane temperature falls off more slowly than r^{-1} . The disk surface then flares outward with increasing radius as a consequence of vertical hydrostatic equilibrium. With the development of our observational techniques, we characterized several examples of disks with a flared structure (e.g., Pinte et al. 2016; Avenhaus et al. 2018; Villenave et al. 2020; Law et al. 2022). For instance, Law et al. (2022) recently observed a correlation between the CO emitting height and the disk size in a sample of disks observed with the Atacama Large Millimeter/submillimeter Array (ALMA). Using the dust emission, Avenhaus et al. (2018) measured the flaring of V4046 Sgr, RXJ 1615, and IM Lup with the Very Large Telescope (VLT) Spectro-Polarimetric High-contrast Exoplanet REsearch (SPHERE) instrument. These near-infrared polarized light images show unprecedented details of the disk’s surface layer by tracing the scattering of small, micron-sized dust grains. At these wavelengths, the disk is expected to be optically thick and the observed light is dominated by light scattered by the dust grains on the disk surface. Among these disks, IM Lup observations are arguably among the most impressive images of a protoplanetary disk, as part of the Disks ARound TTauri Stars with SPHERE (DARTTS-S) survey by Avenhaus et al. (2018), targeting eight TTauri stars, at $1.25 \mu\text{m}$ and $1.65 \mu\text{m}$ wavelengths. With its intermediate inclination ($\sim 56^\circ$), we have a three-dimensional (3D) perspective on the disk around IM Lup, which can be used to constrain the vertical disk structure and the small grain distribution in a model-independent way.

The large dust grain properties can be similarly constrained through observations. At (sub)millimeter wavelengths, ALMA data has provided a new understanding of the properties and distribution of large, millimeter-sized dust grains, found in the disk midplane (e.g., Andrews et al. 2016; Huang et al. 2017; Pinte et al. 2018). IM Lup was also part of the Disk Substructures at High Angular Resolution Project (DSHARP) survey (Andrews et al. 2018 and following papers), conducted with ALMA. The survey led to the characterization of substructures for 20 nearby protoplanetary disks using observations at 1.25 mm (240 GHz).

By combining ALMA and SPHERE images, it is possible to further characterize the structure of disks and examine how they affect the planet formation processes. The SPHERE and ALMA data show two very different geometries

of the disk. In the near-infrared, the disk shows strong flaring and a prominent vertical structure. This implies that small grains are: well coupled to the gas structure, located in the upper layers of the disk, and prevented from settling (Avenhaus et al. 2018). The millimeter image, on the other hand, shows a flat disk, which suggests that the larger dust grains are well settled to the midplane. The disk emission differs also in its radial extent: the ALMA data extend up to 290 au, while the SPHERE data go as far as 400 au. These two images can be used to model the distribution of the largest and smallest dust grains, which we can then use to constrain the full grain size distribution.

Pinte et al. (2008) took a similar approach and combined infrared spectra and scattered light emission with millimeter thermal emission to constrain the parameter range of their IM Lup model. The data consists of scattered light detected with the WFPC2 instrument on board the Hubble Space Telescope (HST), along with Spitzer near and mid-infrared spectroscopy and SubMillimeter Array (SMA) millimeter emission. These authors combined a manual exploration of the model parameter space with a more rigorous fitting of the parameters that cannot be directly inferred from the observations. They found IM Lup to be a massive disk, with a mass of about $\sim 0.1 M_{\odot}$, assuming a 1% dust-to-gas ratio, extending up to ~ 400 au, but with a low $H\alpha$ emission hinting at a low accretion rate. However, a low accretion rate would be a surprising result for a massive disk and these authors suggested that may be due to a period of low or moderate accretion. More recently, the accretion rate was measured by Alcalá et al. (2017, 2019), using the spectrum observed with the VLT/X-Shooter spectrograph and the far-ultraviolet continuum excess emission observed with the HST Cosmic Origins Spectrograph (HST-COS) and HST Space Telescope Imaging Spectrograph (HST-STIS). These studies reported a high mass-accretion rate of $10^{-8} M_{\odot} \text{ yr}^{-1}$. Pinte et al. (2008) found that a dust population perfectly mixed with the gas cannot explain both the dust infrared spectral features and the millimeter continuum. Millimeter-sized grains must be present in the disk, but their emission cannot come from the same region as the infrared emission. The lower modeling power and quality of the data available at the time of this study, however, did not allow us to uniquely constrain the stratified dust disk structure; and so, other disk models apart from their best-fit model may match the applied data.

In this paper, we introduce a comprehensive modeling of protoplanetary disk dust distribution, focusing, in particular, on the vertical distribution of small grains. We then test this model by fitting it to the high-resolution millimeter ALMA data of IM Lup and near-infrared polarized radiation SPHERE data using a Markov chain Monte Carlo (MCMC) algorithm. This allows us to constrain the complete dust grain size distribution of the disk. Finally, we discuss our results

and how they affect our understanding of the dust structure of protoplanetary disks.

4.2 Disk model

The gas distribution for our disk physical model is the axisymmetric, self-similar Lynden-Bell & Pringle profile (Lynden-Bell & Pringle 1974):

$$\Sigma(r) = \Sigma_c \left(\frac{r}{r_c} \right)^{-\gamma} \exp \left[\left(-\frac{r}{r_c} \right)^{2-\gamma} \right], \quad (4.1)$$

where r_c is the characteristic radius and γ is the gas surface density exponent. To recover the vertical gas distribution, we need to compute the vertical scale height of the disk. This scale height is expressed by the ratio of the sound speed, c_s , to the Keplerian angular velocity Ω :

$$H_p(r) = \frac{c_s}{\Omega} = \left(\frac{k_B T_{mid}(r) r^3}{\mu m_H G M_\star} \right)^{1/2}, \quad (4.2)$$

where k_B is the Boltzmann constant, $T_{mid}(r)$ the midplane gas temperature distribution, $\mu = 2.3$ the reduced mass of the H_2 molecule, m_H the hydrogen atomic mass, G the gravitational constant, and M_\star the stellar mass. This equation comes from balancing the vertical pressure force of the gas with the gravitational force towards the midplane. Using this scale height, we obtain the gas density at a radius r and height z :

$$\rho(r, z) = \frac{\Sigma(r)}{\sqrt{2\pi} H_p(r)} \exp \left(-\frac{1}{2} \left(\frac{z}{H_p(r)} \right)^2 \right). \quad (4.3)$$

The two terms $H_p(r)$ and $T_{mid}(r)$ are coupled with each other: the amount of starlight penetrating to the disk midplane is determined by H_p . This radiation increases the midplane temperature T_{mid} , which results in a higher pressure scale height. Therefore, H_p and T_{mid} need to be consistent with each other, and the disk structure must be computed iteratively. To estimate the amount of heating from stellar irradiation, we need to compute the optical depth as a function of the location in the disk and the flaring angle $\varphi(r)$, the angle at which the stellar radiation hits the disk surface. The flaring angle is, according to Chiang & Goldreich (1997):

$$\varphi(r) = \frac{0.4R_\star}{r} + r \frac{d}{dr} \left(\frac{H_s}{r} \right), \quad (4.4)$$

where H_s is the surface height of the disk. We note that this is a different

quantity than the pressure scale height, H_p , (which is usually lower) and is defined by the height above the midplane where the optical depth to the stellar radiation is unity.

Given the irradiation angle, $\varphi(r)$, which is assumed to not depend on z , the optical depth to the stellar radiation is:

$$\tau_\star(r, z) = \frac{\kappa_{P,\star}}{\varphi(r)} \int_z^\infty \varepsilon \rho_g(r, z') dz', \quad (4.5)$$

where $\kappa_{P,\star}$ is the Planck mean opacity at stellar wavelengths, ε is the assumed dust-to-gas ratio, and ρ_g is the gas density.

We now wish to find the value of z , at a given r , at which $\tau_\star = 1$. Dullemond et al. (2001) found that this is equivalent to solving:

$$1 - \operatorname{erf}\left(\frac{H_s}{\sqrt{2} H_p}\right) = \frac{2 \varphi}{\tau_\star}, \quad (4.6)$$

where erf is the error function:

$$\operatorname{erf} z = \frac{2}{\sqrt{\pi}} \int_0^z e^{-t^2} dt. \quad (4.7)$$

This estimate for H_s can now be used to derive the flaring index from Eq.4.4. Since the flaring angle determines T_{mid} , which determines H_p , these equations can be solved iteratively to derive H_p , H_s , φ , and T_{mid} consistently.

4.2.1 Vertical structure

To calculate the irradiation of the disk by the star in a 2D model, we use a ray-tracing technique, a 1+1D approach (Dullemond et al. 2002). This allows us to approximate a full 2D solution by calculating the transport of the stellar radiation through the disk, even though there is no radial transfer of thermal energy in the gas. This is a good approximation of the disk structure achievable within a reasonable computation time. Computational time is a strong constraint on our model: each new set of parameters we test against the observational data requires the calculation of a new disk structure and new radiative transfer calculations to produce the images to compare to the observations. A faster disk model allows us to test more parameters with the same computational resources and a better sampling of our posterior parameter distribution.

Ray-tracing consists of a simple integration on the lines $\zeta = z/r = \text{const}$. The stellar flux can then be rewritten as:

$$F_\star(r, \zeta) = \frac{L_\star}{4\pi (r^2 + z^2)} e^{-\tau_\star(r, \zeta)}, \quad (4.8)$$

and the optical depth as:

$$\tau_{\star} = \sqrt{1 + \zeta^2} \int_{R_{\star}}^r \rho_g(r', \zeta) \kappa_{P,\star} dr'. \quad (4.9)$$

From this radiation field, we can compute the temperature as:

$$T(r, \zeta) = \left[\frac{\pi}{\sigma_{SB}} \left(J_{diff}(r, \zeta) + \frac{\kappa_{P\star}}{\kappa_P(T)} J_{\star}(r, \zeta) \right) \right]^{1/4}, \quad (4.10)$$

where σ_{SB} is the Stephan-Boltzmann constant, $\kappa_{P\star}$ the mean Planck opacity at stellar wavelength, and $\kappa_P(T)$ is the mean Planck opacity of the dust at temperature, T . Values J_{diff} and J_{\star} are the mean intensity from dust re-emission and the intensity from stellar radiation, which can be derived from Eq. 4.8 and the dust opacity (discussed in Sect. 4.2.3). Once we have the temperature profile, we can solve for the vertical density profile from Eq. 4.3. This will be a different profile from the one used to solve Eq. 4.10, so we iterate these solutions until convergence.

4.2.2 Dust

We discuss above the fact that ALMA and SPHERE observations indicate that the disk around IM Lup is composed of at least two dust populations: one of small grains, coupled to the gas structure and vertically extended, and one of large grains settled to the midplane. These are just two parts of a continuous size distribution of grains, as predicted by dust coagulation models (e.g., Dullemond & Dominik 2005; Brauer et al. 2008; Birnstiel et al. 2010, 2012). Since a detailed dust coagulation and fragmentation model is computationally expensive, parametric functions to model the dust grain distribution are common in the literature.

We assume that the largest grain size at each radial location is given by a power-law distribution:

$$a_{max}(r) = a_0 \left(\frac{r}{r_c} \right)^{-\gamma}, \quad (4.11)$$

where a_0 is the maximum grain size at radius, r_c . From this maximum grain size at any radial location, we can reconstruct the grain size distribution using:

$$n(a) \propto \begin{cases} a^{-q} & \text{for } a_{min} \leq a \leq a_{max}, \\ 0 & \text{else,} \end{cases} \quad (4.12)$$

where a_{min} is 10^{-5} cm, a_{max} is given by Eq.4.11 and $n(a)$ is normalized to the total dust volume density:

$$\rho_d = \int_0^\infty n(a) m(a) da, \quad (4.13)$$

with $m(a)$ the mass of a grain of radius a . The value of the index q in Eq. 4.12, one of our model parameters, has already been investigated in previous studies. Measurements of the interstellar extinction (e.g., Mathis et al. 1977) found $q \approx 3.5$, which is also consistent with more recent submillimeter observations of debris disks (Ricci et al. 2015). However, the physics of gas-rich young protoplanetary disk is very different from the one of gas-depleted debris disks. Birnstiel et al. (2011) used dust coagulation and fragmentation models to fit an analytic multi-power law to dust evolution models.

The total dust surface density is derived from the gas density using a dust-to-gas ratio of:

$$\varepsilon(r) = \varepsilon_0 \left(\frac{r}{r_0} \right)^{-p}, \quad (4.14)$$

where ε_0 is the dust-to-gas ratio at the normalization radius, r_0 .

From this estimate of the dust density, we compute the vertical dust distribution by balancing turbulent diffusion and vertical settling. Assuming steady state, this is equivalent to solving (Dubrulle et al. 1995; Schr apler & Henning 2004; Fromang & Nelson 2009):

$$\frac{\partial}{\partial z} \left(\log \frac{\rho_d}{\rho} \right) = - \frac{\Omega^2 \tau_s}{D} z, \quad (4.15)$$

where τ_s is the grains stopping time, D is the turbulent diffusivity, and Ω the Keplerian angular velocity. A grain stopping time is the typical time it takes for a grain initially at rest to reach the local gas velocity. This depends on the grain bulk density, ρ_s , and its size, a :

$$\tau_s = \frac{\rho_s a}{\rho c_s}, \quad (4.16)$$

where c_s is the local sound speed. Different grain populations will have different vertical distributions, as larger grains quickly settle toward the midplane, while small grains remain coupled to the vertical structure of the gas. In our models, we divide the grain distribution from Eq.4.12 in 30 populations of different grain sizes, logarithmically spaced between a_{min} and a_{max} , and solve their vertical distribution in Eq.4.15.

The turbulent diffusivity, D , is a parametrization of how the grains are removed from the midplane by turbulent velocity fluctuations of the gas. The simplest case is to assume that it is constant:

$$D = \frac{\alpha c_s H_p}{Sc}, \quad (4.17)$$

where Sc is the Schmidt number, which has been measured to be of order one in zero net MHD turbulence (Johansen & Klahr 2005; Johansen et al. 2006). The diffusivity is intimately linked to the turbulence properties of the gas flows, therefore assuming it to be constant in space is a reasonable assumption when the turbulence is homogeneous. The most likely deviation from homogeneous turbulence is MHD effects, which are vertically and radially stratified (Dzyurkevich et al. 2013). As a consequence, the diffusivity coefficient, D , will change with the disk height, z , at any given radius. In our models, we do not explore MHD effects on the disk structure, and we use a constant diffusivity as in Eq. 4.17

4.2.3 Dust opacity

To compare our models to the observations, we produced synthetic emission maps of the dust structure. It requires us to calculate the opacity of the dust distribution derived in Sect. 4.2.2. We follow the approach of Birnstiel et al. (2018). This work analyzed the millimeter emission of DSHARP disks (including IM Lup) to study the dust properties of these sources.

The grain opacity is strongly affected by the grain composition. Here, we adopt the same composition used in the DSHARP project (Birnstiel et al. 2018), a mixture of water ice, astronomical silicates, troilite, and refractory organic material (see Table 4.1). Birnstiel et al. (2018) had assumed particles without porosity, however grains are expected to have larger porosities, at least in the initial stage of collisional growth (e.g., Krijt et al. 2015); therefore, we assumed grains with 30% porosity.

To calculate the dust mass absorption and scattering coefficients, κ_ν^{abs} and κ_ν^{sca} , as a function of frequency, ν , we need the optical constants of the composing materials, $n(\lambda)$ and $k(\lambda)$, which depend on the observed wavelength λ . In Table 4.1 we report the dust composition assumed and the laboratory experiments providing the optical constants of the composing materials. Deriving the optical constants of a medium composed of multiple materials is a challenging task, as it depends on how we assume these materials are distributed in the dust grains. For general cases, some computationally expensive numerical models need to be used, but in some limit cases, analytic solutions are possible. For a homogeneous mix of the grain components, the solution is given by the Bruggemann rule (see Bohren & Huffman 1998 for more details). The resulting optical constants are shown in Figure 4.1.

To calculate the size dependent opacities, κ_ν^{abs} and κ_ν^{sca} , from the optical con-

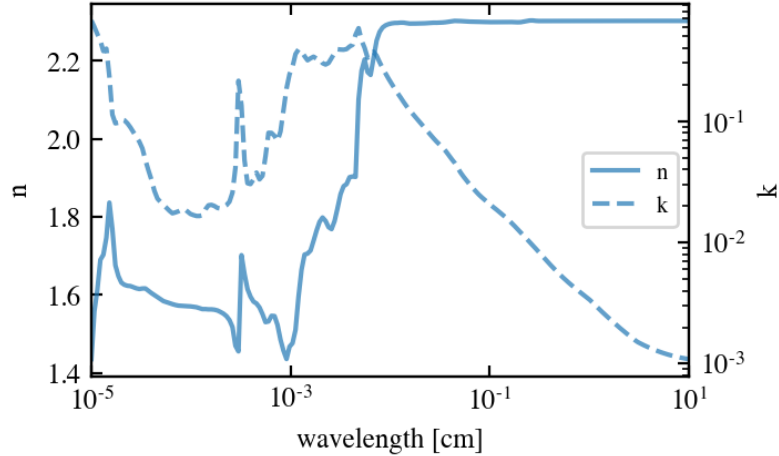


Figure 4.1: Medium optical constant for the dust composition in Table 4.1 (Birnstiel et al. 2018)

Table 4.1: DSHARP dust composition from Birnstiel et al. (2018). The bulk density of the mix is $\rho_2 = 1.675 \text{ g/cm}^3$. References are: (1) Warren & Brandt (2008); (2) Draine (2003); (3) Henning & Stognienko (1996).

material	bulk density	mass fraction	volume fraction	reference
		[g/cm ³]		
water ice	0.92	0.200	0.3642	(1)
astronomical silicates	3.30	0.3291	0.1670	(2)
troilite	4.83	0.0743	0.0258	(3)
refractory organics	1.50	0.3966	0.4430	(3)

stants in Figure 4.1, we use the `dsharp_opac`¹ code, introduced by Birnstiel et al. (2018), based on the original Mie calculation code by Bohren & Huffman (1998).

To derive the total absorption opacity, we created a grid of 30 grain sizes, logarithmically spaced between 10^{-5} and 10 cm. The opacity $\kappa_\nu^{abs, tot}$ (Eq.4.12) at frequency, ν , is then averaged over the grain distribution $n(a)$ from Eq.4.12:

$$\kappa_\nu^{abs, tot} = \frac{\int_{a_{min}}^{a_{max}} n(a) m(a) \kappa_{abs}^{sca}(a) da}{\int_{a_{min}}^{a_{max}} n(a) m(a) da}, \quad (4.18)$$

where $a_{min} = 10^{-5}$ cm and a_{max} is taken from Eq. 4.11. Similarly, we calculate the total scattering opacity, $\kappa_\nu^{sca, tot}$. Finally, to predict the map of the dust continuum and scattered light emission from the model described above using these opacities, we simulated the 3D radiative transfer with the Monte Carlo radiative transfer code `RADMC-3D`² (Dullemond et al. 2012a)

¹https://github.com/birnstiel/dsharp_opac

²<https://www.ita.uni-heidelberg.de/~dullemond/software/radmc-3d/>

4.3 Observations

To constrain the vertical dust grain height in a disk, we need a disk meeting three requirements. First, the disk must be moderately inclined ($\sim 30 - 70^\circ$), so that its 3D structure can be reconstructed from its 2D projection on the sky. Secondly, it must show some ring structures in the scattered light emission to estimate the vertical extension of small grains as a function of radius. Finally, we required millimeter continuum observations to constrain the large grain distribution in the disk midplane. The faint, smooth, and extended emission observed in the scattered light in the disk around IM Lup makes this disk the ideal candidate for a test study. The methods developed here can then be applied in a future work to other axisymmetric disks and extended to include the effects of radial structures on the radial grain distribution due to mixing and drift, using methods similar to the ones presented in this work for the vertical grain distribution.

The protoplanetary disk around IM Lupus has been extensively studied in infrared scattered light (Pinte et al. 2008; Stapelfeldt et al. 2014; Avenhaus et al. 2018), the millimeter continuum (Pinte et al. 2008; Cleeves et al. 2016; Andrews et al. 2018; Pinte et al. 2018), and gas line emission (Cleeves et al. 2016; Pinte et al. 2016). In particular, Zhang et al. (2021) used high-resolution ALMA observations to study CO isotopologue emission and retrieved the gas mass and distribution of several disks, including IM Lup. In our models, we assume the gas distribution derived in this work. This disk is the best candidate to test the simultaneous modeling of large and small grains, with the bonus of having extensive models of its gas structure to check the consistency of our results. Indeed, the efficient coupling of small grains to the gas implies similarities in their spatial distribution. To constrain our models, we use two sets of observations. One is the SPHERE measurements of the $1.65 \mu\text{m}$ near-infrared polarized emission, tracing the scattering of stellar radiation by small grains on the disk surface (Avenhaus et al. 2018). The second is the 1.25 mm continuum emission from the large grains in the disk midplane, detected by ALMA as part of the DSHARP disk survey (Andrews et al. 2018). A summary of the parameters of IM Lup can be found in Table 4.2

There are two possible approaches to compare our model images to the observations: either we directly compare the model images to the observed images or we compare their radial emission profiles. We chose the latter to ensure we give the same weight to both the millimeter and near-infrared data when constraining the models. Indeed, a direct comparison of disk models to data from different instruments is a challenging task, especially in this case where the image resolution element is defined differently (beams for ALMA data and pixels for SPHERE data). On the other hand, using azimuthally averaged brightness profiles allows

Table 4.2: IM Lup stellar and disk properties. References are: (1) Avenhaus et al. (2018); (2) Gaia Collaboration et al. (2016); (3) Zhang et al. (2021); (4) Alcalá et al. (2019).

inc	PA	d	age	M_{disk}	T_{eff}	L_{\star}	M_{\star}
[deg]	[deg]	[pc]	[Myr]	[M_{\odot}]	[K]	[L_{\odot}]	[M_{\odot}]
$56 \pm 2^{(1)}$	$145 \pm 2^{(1)}$	$158 \pm 0.5^{(2)}$	$1.1 \pm 0.2^{(1)}$	$0.2^{(3)}$	$4350^{(4)}$	$2.6^{(4)}$	$1.1^{(3)}$

us to avoid the subtleties of working directly on the imaging data. Since either approach is valid and neither one offers a greater advantage over the other, we chose to work with the azimuthally averaged profiles to simplify our analysis.

In addition, we constrained our models using only the data outside of the 1 arcsec (158 au) radius. We are primarily interested in characterizing the difference between the small and large grain distribution, so we focus on the outer regions of the disk where this difference is maximized. Secondly, the SPHERE coronagraph is obscuring the inner 0.1 arcsec (~ 16 au) of the disk, making the observed inner disk always dimmer than in the models. Finally, IM Lup observations show evidence both in the large grain (Huang et al. 2018a) and small grain emission (Avenhaus et al. 2018) up to 1 arcsecond. Here, we do not address the effect these structures have on the dust distribution, which will be addressed in a follow-up study, and we focus on the region outside the 1 arcsec radius.

4.3.1 Near-infrared scattered light: height of small grain distribution

The disk around IM Lup has been observed in its scattered light emission by the Hubble Space Telescope (HST) (Pinte et al. 2008) and SPHERE (Avenhaus et al. 2018), as shown in Figure 4.2. Scattered light images of an inclined disk such as IM Lup are expected to show azimuthal asymmetries due to the anisotropic nature of scattering by dust grains. These anisotropies are caused by both grain properties and the flared disk geometry. Grain scattering favors scattering in the forward direction, and the disk region closer to the observer is the brightest (e.g., Mulders et al. 2013). Moreover, the fraction of light that gets polarized by grain scattering depends on the grain structure, composition, and scattering angle.

The disk geometry also affects how much light is scattered by the disk surface. These images trace stellar radiation scattered by the small grains near the disk surface because the disk is optically thick at infrared wavelengths (e.g., Grady et al. 2000, 2009; Hashimoto et al. 2011; Monnier et al. 2017) and a flared disk geometry can cause an excess in its infrared emission.

IM Lup scattered light emission has its outer edge at ≈ 340 au, and a faint

Table 4.3: IM Lup small grain ring parameters, as in Avenhaus et al. (2018).

radius [au]	flaring	height [au]
91.9 ± 3.2	0.18 ± 0.03	16.5 ± 3.3
152.1 ± 4.8	0.18 ± 0.04	27.4 ± 6.9
240.8 ± 4.8	0.23 ± 0.04	55.4 ± 10.7
332.8 ± 12.7	0.25 ± 0.05	83.2 ± 19.8

halo extending up to ≈ 700 au (Avenhaus et al. 2018). The SPHERE data reveal several ring structures. If we assume these rings to be circular and centered on the star, we can fit ellipses to the peak flux of the rings to estimate radius, inclination, position angle, and the vertical displacement from the midplane due to the height of the small grains. These measurements are carried out in Avenhaus et al. (2018) and reported in Table 4.3 as well for convenience.

They find that the dust scattering surface is described by a power law in radius:

$$H_s(r) = H_0 \left(\frac{r}{r_0} \right)^\beta, \quad (4.19)$$

where H_0 is the dust scale height at the fiducial radius r_0 , and β the flaring index. The height of the scattering surface is typically about three to four times the pressure scale height.

We use these results to extrapolate the radial scattered light emission profile of IM Lup. The flaring index gives us the information necessary to reconstruct the disk 3D structure from its projected 2D image on the sky plane, the SPHERE data. This can be done using the GoFish package (Teague 2019). To preserve the information about the non-isotropic nature of the polarized scattered light emission, we extract the emission profiles in four different directions. As shown in Figure 4.2, we chose four cones 10° wide in PA in the forward and backward scattering direction, and the two side directions 90° away. We applied this same procedure to the simulated disks, then we compared the models to the observations by fitting these four profiles.

4.3.2 Millimeter continuum emission: Large grains in the disk midplane

The second set of observational constraints is the high resolution (~ 5 au) millimeter continuum emission from large grains in the disk midplane, at $\lambda_{obs} = 1.25$ mm. These data come from the ALMA DSHARP program (Andrews et al. 2018). Since both our model and the continuum emission are azimuthally axisym-

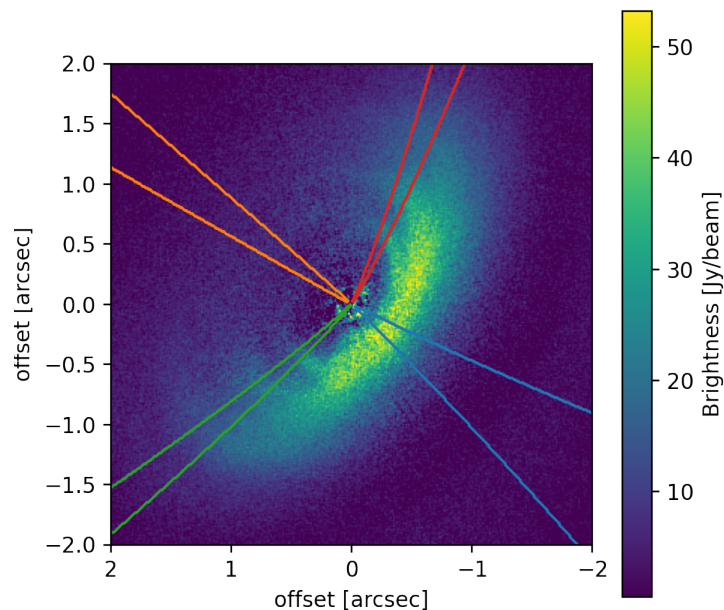


Figure 4.2: IM Lup polarized emission at $1.65 \mu m$ wavelength observed by SPHERE (Avenhaus et al. 2018). The cones show the regions over which we extract the radial profiles we use to compare our models.

metric, we compared our models to the azimuthal average of the observations. As with the scattered light emission, the millimeter emission shows radial structures in the inner disk, a spiral pattern extending from 25 au to 110 au (Huang et al. 2018b). Outside of this region, there is a gap in the emission profile. For this reason, we constrained our models with the observed emission profile outside the 1 arcsec radius, as with the scattered light data. The 1.25 mm emission has a sharp truncation at 295 au, also found in previous studies (Pinte et al. 2018), and extends up to about 400 au.

Tazzari et al. (2021) analyzed the 0.9 mm, 1.3 mm, and 3.1 mm emission for the 26 brightest disks in the Lupus region, including IM Lup. One of their most interesting results is that they measure very little variation in disk size across different wavelengths. This behavior is common for highly structured disks, such as IM Lup and the other DSHARP sources. For instance, it was also described by Pinilla et al. (2015, 2021), who studied the effect of disk radial structures on the dust grain size distribution. The most obvious explanation would be a physical drop in the dust density, but an emission drop can also be explained by an opacity feature. For example, Rosotti et al. (2019) and Powell et al. (2017) argued that the outer edge of the emission profile at a given millimeter wavelength is also the

location where the maximum grain size corresponds to the opacity resonance at that wavelength ($a_{max} \sim \lambda/2\pi$). When the maximum grain size, decreasing with radius, falls below this size, the grain opacity drops quickly, and we observe a sharp truncation in the emission profile. This is in accord with the predictions of dust growth models and radial drift (e.g., Birnstiel et al. 2016; Powell et al. 2019, Chapter 3). However, if this truncation were caused by radial drift, at different wavelengths we would observe truncation at different radii since radial drift affects different grain sizes with different efficiency. This is not what was measured by Tazzari et al. (2021), suggesting that the outer edge of the continuum emission is caused by a drop in the dust density – and not by an opacity feature.

While Tazzari et al. (2021) conclude that observations of millimeter continuum emission are not enough to distinguish which scenario is most likely in IM Lup, Avenhaus et al. (2018) are more specific and identify a outer edge at 340 au in the dust scattered light emission. This structure could trap grains at its location, and the grains could follow a different distribution inside and outside the ring. In our model, we recover the small grain distribution from the large grain distribution using the power law distribution in Eq.4.12. However, if the grain distribution changes at the two sides of the ring and there is no large grain emission in the outer disk, we cannot recover the small grain abundance using this approach. Therefore, in our fitting routine we do not include the region outside the ring location, at 340 au.

4.4 Inferred disk model parameters

Starting from the geometrical structure of IM Lup, inferred directly from the observations as discussed in Sect. 4.3, and previous modeling efforts of its gas structure (Zhang et al. 2021), we can put quantitative constraints on the disk physical parameters using the Markov chain Monte Carlo sampler `emcee`³. The physical distributions explored by the fit are the grain size distribution, the maximum grain size radial distribution, the dust-to-gas ratio radial distribution, and the turbulent viscosity parameter α_{turb} , according to the standard Shakura & Sunyaev (1973) viscosity recipe.

The grain size distribution is given by Eq.4.12:

$$n(a) \propto a^{-q}, \quad (4.20)$$

with the exponent of the distribution q as a fitting parameter. The maximum

³<https://emcee.readthedocs.io/en/stable/>

grain size radial distribution is given by Eq.4.11:

$$a_{max} = a_0 \left(\frac{r}{r_c} \right)^{-p}, \quad (4.21)$$

with $r_c = 300$ au and a_0, p as fitting parameters. The dust-to-gas ratio radial distribution is given by Eq.4.14:

$$\varepsilon(r) = \varepsilon_0 \left(\frac{r}{r_{in}} \right)^{-\gamma} \quad (4.22)$$

with $r_{in} = 160$ au and ε_0 , and γ as our fitting parameters. We assume the dust-to-gas ratio. and the maximum grain size distribution to have the same r_{cutoff} . Finally, we have the turbulent viscosity parameter, α_{turb} . This parameter sets the gas viscosity, ν , as shown in Eq.4.17. The turbulent diffusivity is used to compute the settling velocity and the turbulent diffusion coefficient of the dust species. These are used in turn to compute their settling mixing equilibrium, as discussed in Sect. 4.2.2.

This results in a model with six independent parameters ⁴. The fitting is based on the definition of a reduced χ^2 . For the ALMA 1.25 mm emission, we measured the reduced χ^2 between the observed emission profile and the azimuthal average of the synthetic millimeter images. Concerning the scattered light, as described in Sect. 4.3.1, we measured the average brightness profiles within four segments 10° wide in PA, along the major and minor axes (as in Figure 4.2). To give the same weight to the ALMA and SPHERE profiles, we considered the average χ^2 of the scattered light brightness profiles:

$$\chi_{tot}^2 = \chi_{mm}^2 + \frac{1}{4} \left(\sum_{i=1}^4 \chi_{sca}^{(i)} \right), \quad (4.23)$$

where $\chi_{sca}^{(i)}$ are the average brightness profiles in the four directions of the SPHERE images.

The best-fit parameters are reported in Table 4.4 and the comparison between the synthetic and observed profiles is shown in Figure 4.3. In Figure 4.4, we compare the simulated images to the observations. The best-fit model aptly reproduces both the ALMA and SPHERE images. The simulated emission profiles at both wavelengths (and the four directions for the scattered light images) match the observations. Models and observations are less in accord in the inner disk (< 1 arcsec). As discussed in Sect. 4.3, the inner disk shows evidence of structures that we have not included in our models, and the coronagraph used

⁴The source code can be found at:
https://github.com/rfranceschi/IMLup_SPHERE_fit

Table 4.4: IM Lup best fit parameters of Eq.4.20-4.22. The fit values and the uncertainties are given by the 16th, 50th, and 84th percentiles of the samples in the marginalized distributions.

parameter	value
q	$3.33_{-0.05}^{+0.03}$
p	$9.9_{-0.9}^{+0.6}$
a_0	$1.12_{-0.07}^{+0.07} \times 10^{-2}$ cm
ε_0	$5.8_{-0.2}^{+0.5} \times 10^{-3}$
γ	$0.84_{-0.05}^{+0.08}$
α_{turb}	$2.9_{-0.8}^{+0.5} \times 10^{-3}$

in SPHERE observations masks the emission in the very inner disk of the scattered light image. Our 1+1D disk model (as discussed in Sect. 4.2) does not take into account radial transfer of energy and the differences between model and the data in the inner disk structure is within the model uncertainty of using a 1+1D model, rather than a full 2D model. Therefore, we do not include the profiles within 1 arcsecond in our χ^2 calculation, as they do not significantly affect our outer disk model.

4.4.1 Dust mass

A key result of our modeling is the constraints on the dust mass of the disk. In the optically thin case, the millimeter flux is proportional to the disk dust mass times the dust opacity. The opacity at millimeter wavelengths is the highest for millimeter-sized grains, but it is only a factor of a few higher than the millimeter opacity of submillimeter-sized grains (e.g., Woitke et al. 2016; Birnstiel et al. 2018, also Figure 4.1). If millimeter grains are absent, we can still observe the millimeter emission from submillimeter-sized grains. However, dust mass estimates from the continuum millimeter emission are usually based on the assumption that the emission is coming from millimeter-sized grains. This assumption, however, cannot be justified by looking only at the millimeter emission. Our study takes into account both the emission from small and large grains, without assuming the size of the emitting grains. However, the reader should keep in mind that our grain distribution is constrained by the observations only in the region between 160 au and 340 au, as explained in Sect. 4.3.1-4.3.2, and our dust mass estimate may be off because the dust distribution in the inner disk is extrapolated from the best-fit dust distribution in the 160-340 au region.

The gas mass is fixed at $0.2 M_{\odot}$, derived from thermo-chemical modeling of

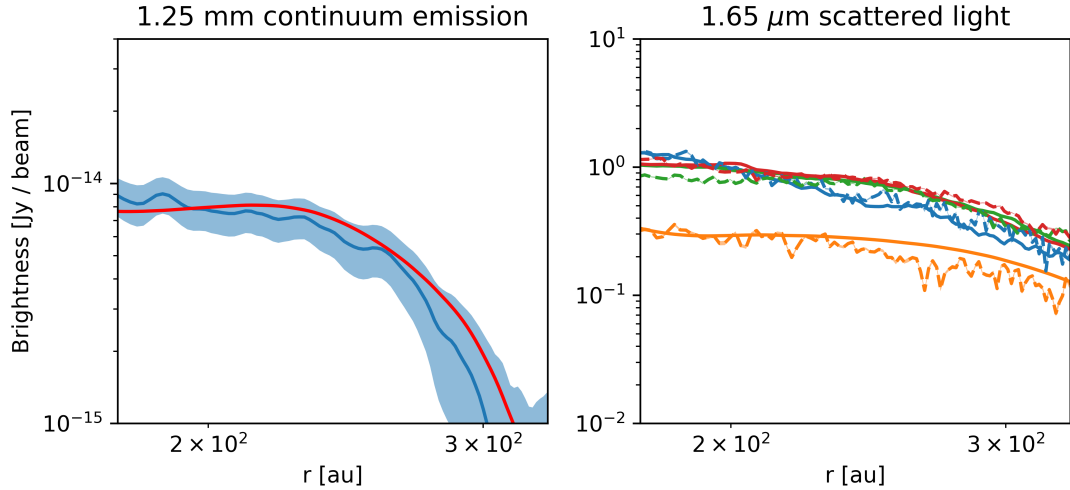


Figure 4.3: Comparison between the observation and best fit radial profiles for the millimeter continuum emission (left) and near-infrared scattered light emission (right). The shaded region shows the observation noise level. In the right plot, the four colors indicate the profiles in the four different directions (same as in Figure 4.2).

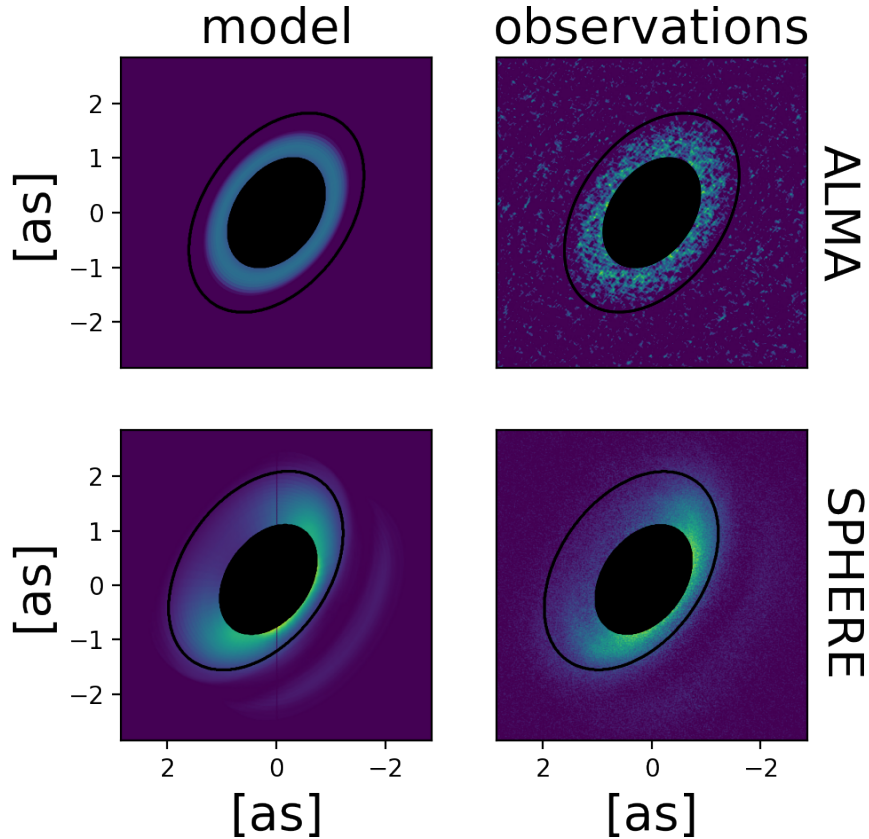


Figure 4.4: Comparison between the simulated 1.25 mm continuum and 1.65 μm polarized emission, and the ALMA and SPHERE data. The black masks show the region inside 1 arcsec radius, not included in our fitting, where radial structures are observed. The black circle is the 2.5 arcsec radius, the outer edge of the disk.

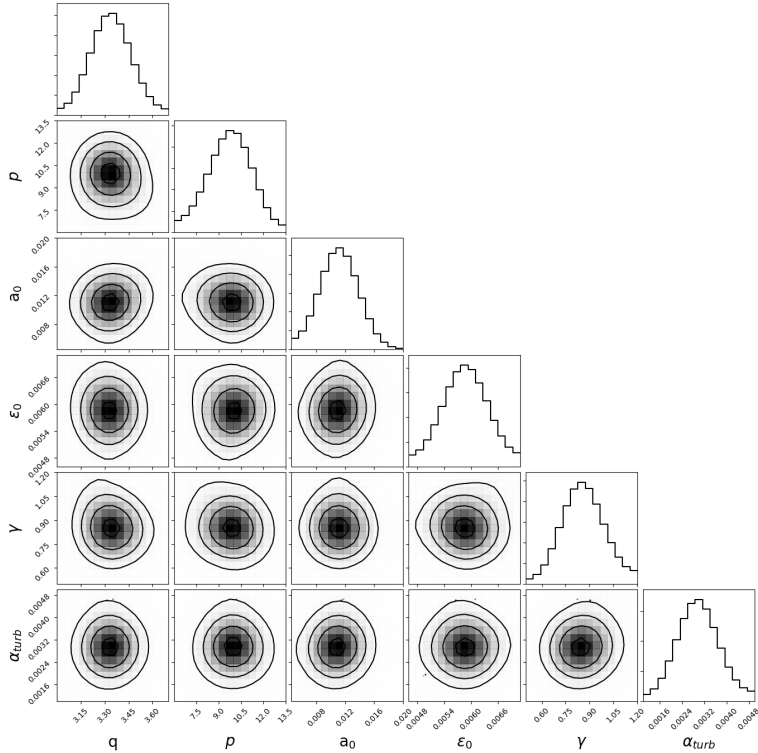


Figure 4.5: Posterior distribution of the fitting parameters described in Sect. 4.2. The parameters follow a Gaussian distribution, showing that the parameters are well constrained and not correlated.

ALMA high resolution CO emission maps (Zhang et al. 2021). While it could be possible to find multiple grain size distributions reproducing the millimeter and near-infrared emission, the corner plot in Figure 4.5 shows us that this is not the case, as the posterior probability distribution converge to a unique solution. As a further proof that the presence of millimeter grains is necessary to simultaneously match the millimeter and near-infrared emission, we also run our fitting routine using a model where the grain size is not allowed to be larger than 10^{-3} cm. In this case, the disk model predicts a high abundance of small grains to match the millimeter emission, while still poorly reproducing the data. The large abundance of small grains causes the disk to be more flared than it appears the observations, suggesting that millimeter grains are required to reproduce the observed geometry.

As a further test, we check how well our model constrains the maximum grain size distribution by changing the a_0 parameter from Eq. 4.11 in our best-fit model. By halving a_0 , the millimeter image appears to be much less extended than the observations, since now millimeter-sized grains are less extended in the radial direction. The disk appears more flared in the scattered light, causing the disk surface in the forward direction to be more aligned to the observed line of sight. The scattered light polarization, in this direction, is at its minimum and therefore

the disk appears much dimmer in this region compared to the observations. If we instead double a_0 , the millimeter emitting region is now more extended than in the observations, but also dimmer, since we have lost some millimeter-sized grains to produce larger grain sizes. In the scattered light, the disk is now less flared than the best-fit model. This causes the light in the forward scattering direction to be more polarized and here we observe a brightness excess compared to the observations. These effects of the maximum grain size distribution on both the millimeter and scattered-light profiles prove that this distribution is well constrained by our model and that the presence of millimeter-sized grains is necessary to simultaneously explain both the millimeter continuum and the near-infrared scattered light observations.

From the dust-to-gas ratio of our best fit model, we find a dust mass of $1.5 \times 10^{-4} M_\odot$ in the fitted region. When we extrapolate our model results to the whole disk structure, we get a total dust mass of $4 \times 10^{-3} M_\odot$. This dust mass estimate is about half the previous estimate of $0.01 M_\odot$ by Pinte et al. (2008), based on 1.3 mm continuum emission obtained with the Submillimeter Array (SMA) (Panić et al. 2009). This difference comes from the different assumptions made on the grain size distribution, as they assumed well-mixed dust populations with a fixed maximum grain size. They found that a maximum size of 3 mm and a disk dust mass of $0.01 M_\odot$ reproduces the 1.3 mm emission, but not the silicate emission features from micron-sized grains observed in the mid-IR spectra. They suggest that to account for all observables a spatial dependence of the dust grain size distribution is necessary, with larger grains closer to the disk midplane and small grains on the disk surface. Indeed, our model features a vertical distribution of grain sizes, with a radial dependence of the maximum grain size. This results in a lower abundance of large grains in the outer disk. Since these grains carry most of the dust mass (see also the discussion in Sect. 4.4.2), our model results in a lower dust mass than the one found in Pinte et al. (2008). Moreover, Pinte et al. (2008) used an older estimate of the disk distance of 190 au, based on Hipparcos parallax measurement (Wichmann et al. 1998), which is higher than the value used in this work, namely, 158 au (Gaia Collaboration et al. 2016). In their model, the emission of large grains (which carry most of the dust mass) is then brighter by a factor of about 1.4, leading to an overestimation of the dust mass of the same factor.

To better understand the best-fit dust distribution we look at the vertical distribution of the dust properties, and how they change with the radial location. In Figure 4.6, we show the Stokes number, the dust vertical profile, $\rho_d(z)/\rho_d(0)$, and the vertical dust-to-gas ratio, $\rho_d(z)/\rho_g(z)$. The Stokes number is defined as the grain stopping timescale times the Keplerian frequency: $St = \tau_{stop} \Omega_K$, and

it describes how fast the grains drift towards the inner disk. At smaller radii, we have a high Stokes number close to the midplane. This is due to large grains that are quickly drifting towards the inner disk, while at larger radii the midplane has already been depleted from the larger grains by drift. Above the midplane, we have a low Stokes number at all radii. This is caused to the vertical sedimentation of larger grains, suggesting that the vertical sedimentation happens on a much faster rate than the radial drift.

At different radii, we find significant differences in the dust-to-gas ratio vertical profiles. At larger radii, the profiles get flatter, with an overall lower ratio, while at smaller radii the dust-to-gas ratio is strongly peaked at the mid-plane, where it gets as high as 0.3. This is an important result, as at such high dust-to-gas ratios streaming instabilities can start to develop, possibly setting up the right conditions for planetesimal formation (Youdin & Lithwick 2007; Johansen et al. 2009; Bai & Stone 2010). Moreover, while not included in our disk model, observations show evidence of structures in the disk midplane inside the 160 au radius (as discussed in Sect. 4.3.2). If there are indeed active planet formation processes in the inner disk, the growing planets could then imprint non-axisymmetrical structures (e.g., Lovelace et al. 1999; Li et al. 2000). Our model, independently from this observational evidence, suggests that at this radius we find the right condition for the developing of streaming instabilities, possibly triggering planet-formation processes which, in turn, could be the origin of the structures observed in the inner disk.

4.4.2 Distribution of the dust populations

The dust mass distribution of different grain populations is an important topic for the understanding of dust evolution and planet formation. Our best-fit model is in agreement with a vertical and radial stratification of dust grains. We find micron-sized grains on the disk surface ($z/r \approx 0.2$) and in the outer disk. They are however missing in the midplane at the smaller radii, where they can efficiently grow to form larger grains, as shown in Figure 4.7.

Submillimeter grains (Figure 4.8) are more abundant than micrometric grains and are likewise depleted at smaller radii by the grain growth process. They also extend vertically in the disk, though they do not reach the disk surface ($z/r \approx 0.1$). As these grains are a product of dust evolution, they are not found in the outer disk, where they are removed by radial drift.

Millimeter-sized grains (Figure 4.9) are instead found exclusively in the midplane. In contrast to smaller grains, their density increases at smaller radii, as they are a product of dust evolution, which happens on shorter timescales in this

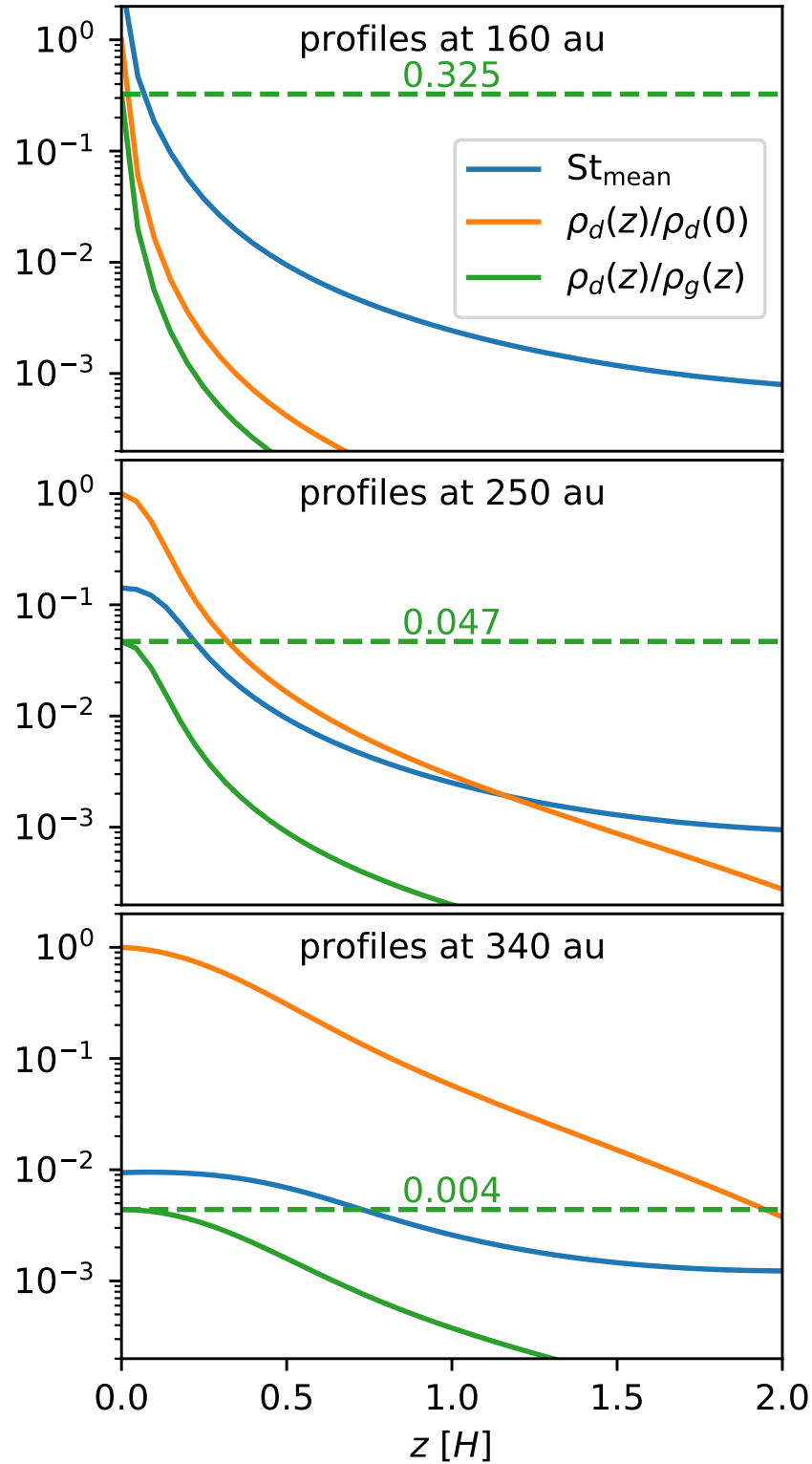


Figure 4.6: Stokes number, dust vertical profile, and dust-to-gas ratio at 160, 250, and 340 au radii (from top to bottom).

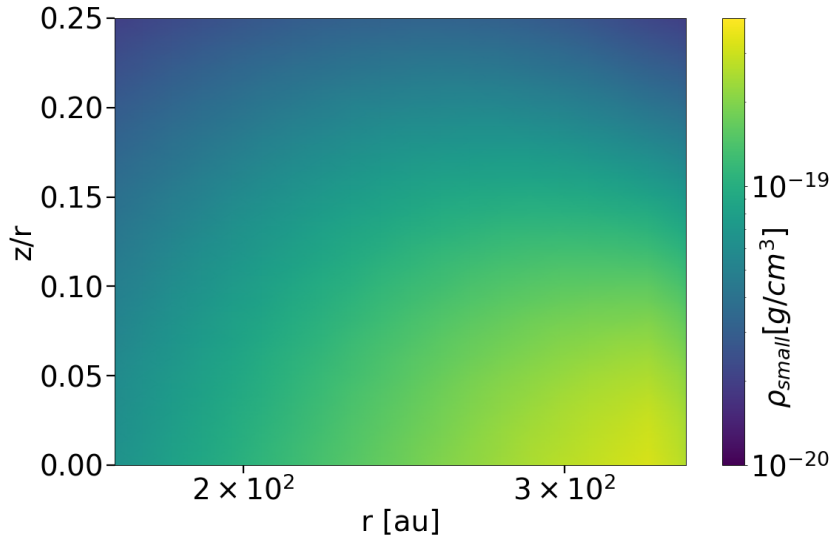


Figure 4.7: Density distribution of micrometric grains ($a_{\text{grain}} < 10^{-3}$ cm). These grains are more abundant in the regions where large grains are removed by radial drift (outer disk) and vertical settling (disk surface), and depleted in the midplane at smaller radii by dust growth processes.

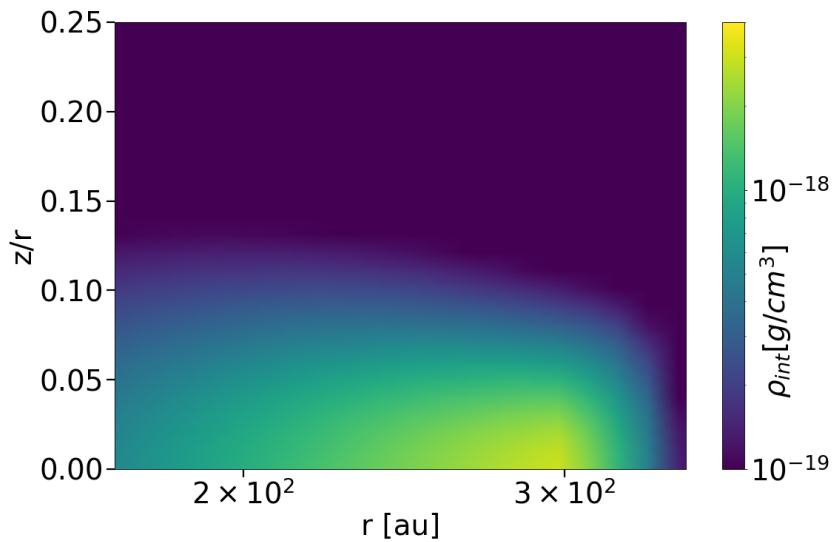


Figure 4.8: Density distribution of submillimeter grains (10^{-3} cm $< a_{\text{grain}} < 10^{-1}$ cm). These grains have a moderate vertical extension and are depleted at both small and large radii, where they are removed by dust evolution processes.

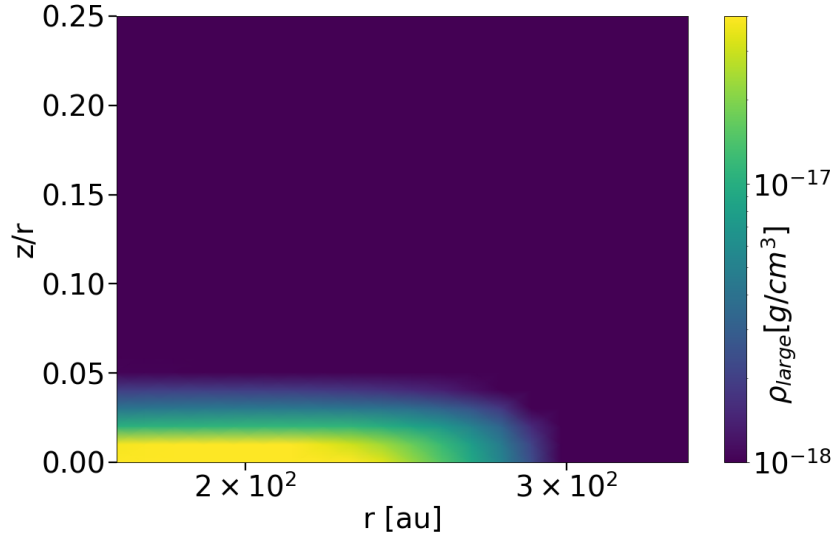


Figure 4.9: Density distribution of millimeter grains ($a_{\text{grain}} > 10^{-1}$ cm). These grains have a moderate vertical extension and are depleted at both small and large radii, where they are removed by dust evolution processes.

context. They are more affected by radial drift, so they are less extended in radius than smaller grains.

The total dust mass, and the mass fraction in small, intermediate, and large grains, is tightly constrained by our fit. In Figure 4.10, we show the mass ratio of each dust population to the total dust mass and the total dust mass of the ten highest likelihood models. The ratios and the total dust mass are in accord within all the models, proving that they are well constrained by observing both large and small grain emission.

In Sect. 4.4.1, we discuss how the millimeter emission does not necessary trace the emission of millimeter-sized grains, as is usually assumed. It is then worthwhile to check whether, according to our model, this is a good assumption for the IM Lup disk. The best-fit grain size distribution, in Figure 4.11, shows that according to our model, the millimeter-sized distribution and the observed millimeter continuum emission overlap, and therefore the millimeter grains dominate the emission.

4.4.3 Grain evolution timescales

Since our dust structure is the outcome of a parametric model (and not of a dust evolution simulation), the grain distribution shown in Figure 4.11 may not be physically consistent with the disk gas structure. Moreover, our model suggests a steep maximum grain size distribution, as shown both in Figs. 4.5 and 4.11. The parametrization assumed for the maximum grain size distribution, Eq. 4.11,

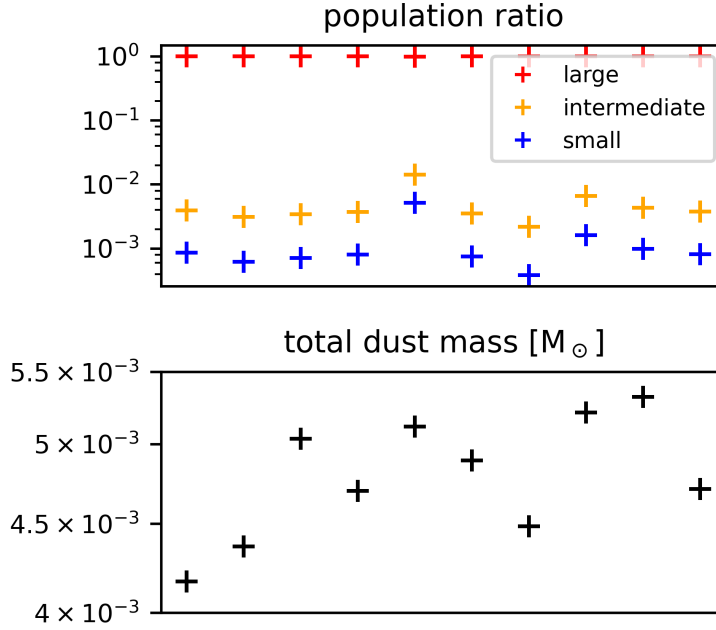


Figure 4.10: Mass ratios of large ($a_{\text{grain}} > 10^{-2}$ cm), intermediate ($10^{-3} < a_{\text{grain}} < 10^{-2}$ cm), and small grains ($a_{\text{grain}} < 10^{-3}$ cm) of the ten best-fit models, from upper to lower panels.

does not hold for all grain sizes. Once grains reach centimeter sizes, they break each other apart by colliding, limiting the maximum grain size to 1 mm to 1 cm, depending on the turbulence strength and gas density (e.g., Birnstiel et al. 2011; Zsom et al. 2011). This prevents grains from growing to unphysically large sizes in the region inside 1 arcsecond, however, we did not include this region in our fit due to the presence of radial structures, as discussed in Sect. 4.3.2. However, it is worthwhile to investigate if the resulting grain distribution is physically consistent.

In Figure 4.12, we compare the collisional, settling, and drift timescales to the disk age, averaged over the grain size distribution. With the exception of the disk midplane, where grains can efficiently grow, the collisional timescale is much longer than the disk age. Here, grains do not have enough time to grow through collision processes and they cannot produce grains larger than micron sizes. However, our model predicts the presence of submillimeter grains even outside of the midplane, which then must be produced by other processes. A possible explanation is coagulation driven by sedimentation (Zsom et al. 2011). To understand this process we must first discuss the grain settling timescales. Figure 4.12 shows that small grains have a settling timescale of about the disk age on the disk surface, and did not have enough time to start settling to the midplane. Deeper in the disk, the settling timescale gets shorter and grains start to settle towards the midplane. The difference in the settling velocity of grains drives their coagulation, as explored

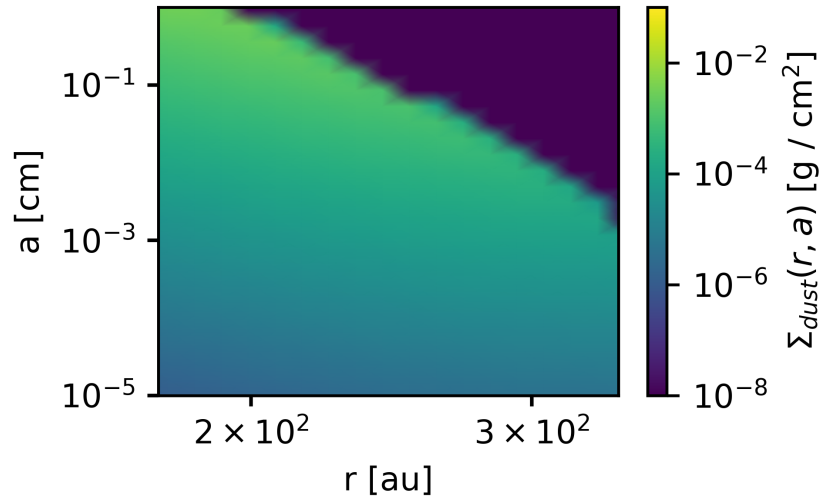


Figure 4.11: Dust surface density of the best-fit model, as a function of grain size and radial position.

by several authors (e.g., Dullemond & Dominik 2004, 2005; Schr apler & Henning 2004). Zsom et al. (2011) showed that coagulation driven by sedimentation can be a very efficient process for grain growth, and can produce millimeter-sized grains as early as after 10^4 orbital timescales (10^4 years at 1 au). Since the age estimates of IM Lup range from 0.5 Myr (Andrews et al. 2018) to 1 Myr (Andrews et al. 2018), this provides enough time for the formation of the large grains predicted by our model. The distribution of submillimeter grains shown in Figure 4.8 is right inside the region where the settling timescale is shorter than the age of the disk, while the millimeter grain distribution corresponds to the region where the settling timescale is ten times shorter than the age of the disk. This anti-correlation between the grain size and the low level of turbulence suggests that in the disk grain growth may be driven by sedimentation instead of turbulent collisions. For a more thorough justification of our model grain distribution, however, we would need to use 2D dust evolution models, which we leave to a future work.

Finally, the drift happens on a much longer timescale than the disk age everywhere but in the midplane, while only being efficient at radii smaller than about 250 au. It is interesting to point out that these regions match the ones where submillimeter and millimeter grains are found (see Figure 4.8-4.9). This is also in accord with the discussion in Section 4.4.1, where we show how the Stokes number gets higher at smaller radii.

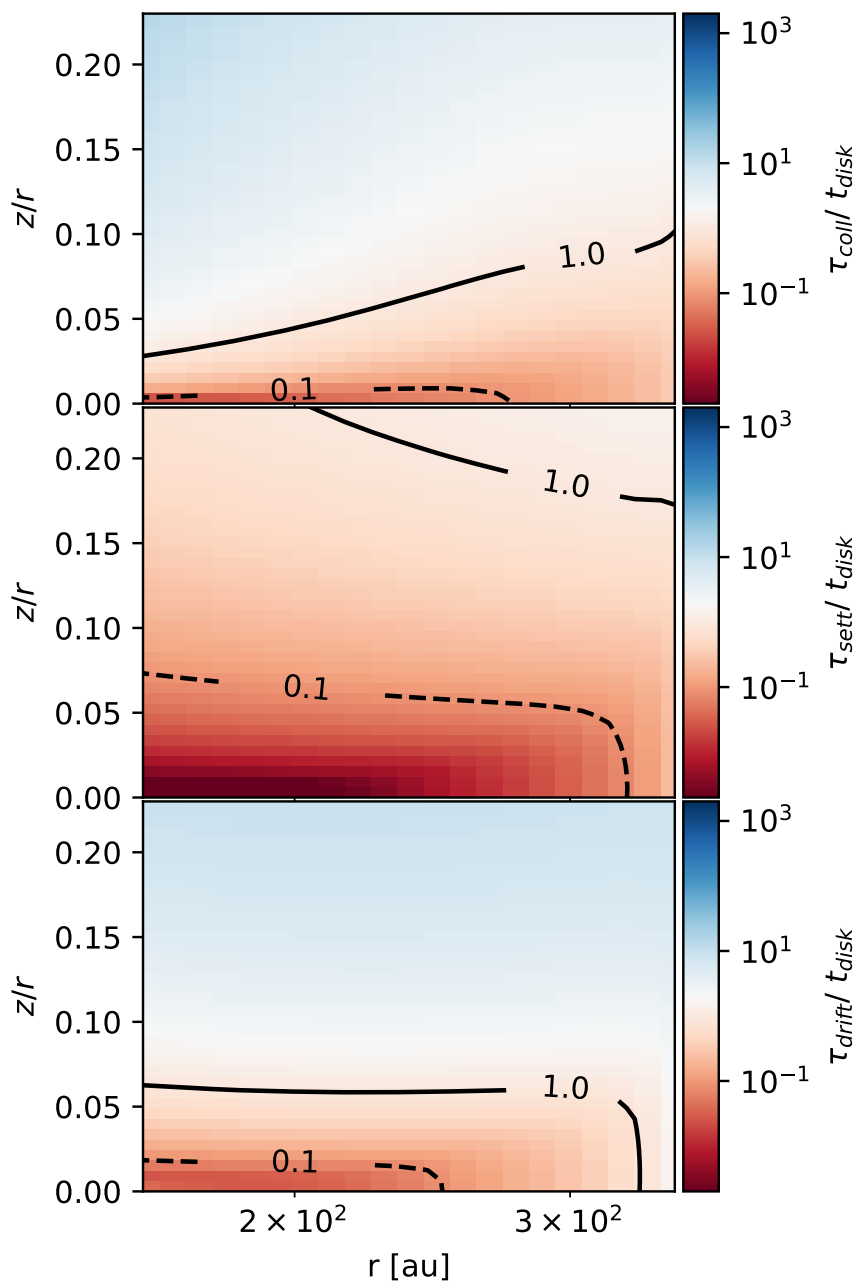


Figure 4.12: Comparison of the collisional, settling, and drift timescales to the disk age, from top to bottom.

4.4.4 Viscous turbulence parameter

Previous studies have constrained the value of α_{turb} to be about $\alpha_{turb} = 10^{-3}$, based on the observation of turbulent motions in the disks (Hughes et al. 2011; Flaherty et al. 2017). However, a more precise value is more complex to obtain as the relation between the turbulent motions and α_{turb} depends on the nature of the turbulence (Cuzzi et al. 2001). Our best-fit model is in agreement with these findings, with $\alpha_{turb} = 3 \times 10^{-3}$. This is lower than the previous measurement by Pinte et al. (2018) ($\alpha_{turb} = 9 \times 10^{-3}$). In this work, they fit a parametrical disk model to ALMA band 6 dust continuum emission and CO, ^{13}CO , and C^{18}O line emission. The α_{turb} is then estimated from the vertical dust settling in their best-fit model.

To check how the turbulence parameter affects the grain distribution, we ran two models with the same parameters as our best-fit model, but with a low ($\alpha_{turb} = 10^{-4}$) and high ($\alpha_{turb} = 10^{-2}$) level of turbulence. In Figure 4.13 we show how the millimeter emission profiles of the new models compare to the profile of ALMA data. The millimeter profiles are unaffected by the change in α_{turb} , and this is a further indication that the millimeter emission is coming from the large grains in the midplane, which is not impacted by turbulence.

The near-infrared emission, on the other hand, changes significantly with the turbulence strength. A highly turbulent viscosity results in more grains in the disk atmosphere, as it prevents the dust from settling into the midplane. When $\alpha_{turb} = 10^{-2}$, the disk appears much more flared in the near-infrared, whereas when $\alpha_{turb} = 10^{-4}$, the near-infrared emission originates very close to the disk midplane, as the turbulence is not strong enough to sustain micron-sized grains.

This behaviour is also described by Rich et al. (2021). While these authors did not measure the value of α_{turb} (they assumed a nominal value of $\alpha_{turb} = 10^{-3}$), they used an analytical model to manually explore the effect of α_{turb} on the ^{12}CO emission height and small dust grain scattering surface. By decreasing the value of α_{turb} , they found a lower scattering surface for small grains, in accordance with our model prediction.

4.5 Fitting the outer disk

In Sect. 4.3.2, we discuss how the observations justify our assumption that the dust distribution changes the 340 au annulus, where a outer edge in the dust emission was observed (Avenhaus et al. 2018). In our model, the abundance of small grain follows the one of the larger grains. However, if the dust distributions changes at the ring location, and there are no large grains in the outer disk, we

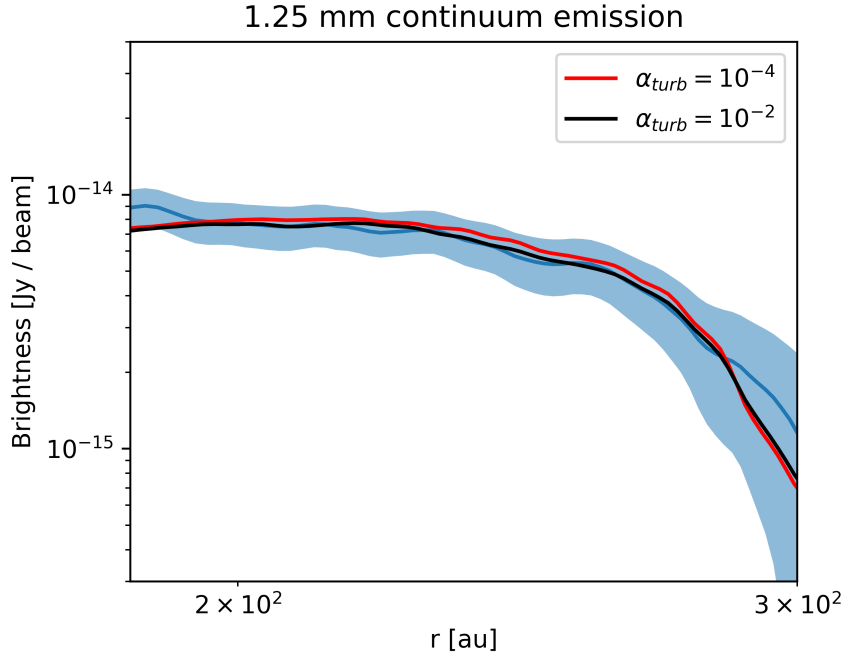


Figure 4.13: Comparison of the best-fit model millimeter emission profile but with low (red) and high turbulence (black) to the observed profile (blue).

cannot derive the abundance of small grains as the ring affects the large and the small grains differently. Another possible explanation for the sharp truncation in the millimeter profile could be an opacity feature. When the maximum grain size, decreasing with radius, drops below the one which emits most efficiently ($a = \lambda/2\pi$ according to the Mie scattering theory), we observe a sharp truncation of the emission profile. In our tests, we explored each of these two cases to check if they can reproduce the observations until the outer edge of the scattered light emission, at 400 au, instead of constraining our fit to the region inside the location of the ring, at 340 au.

To test if the observations can be explained by an opacity feature, we follow the same approach discussed in Sect.4.2, but we add to the fit the region outside the ring. This new model cannot reproduce both the continuum and the scattered light profiles. The model profiles which best fit the continuum emission are shown in Figure 4.14. The grain distribution reproducing both the brightness and the size of the continuum emitting region does not produce a small grain population that would scatter light with enough efficiency to reproduce the scattered light emission.

The model that best matches the scattered light data is shown in Figure 4.15. This small grain distribution is coupled to an abundance of large grains that is too low to reproduce the continuum emission. Since this approach cannot reproduce, at the same time, the small and large grain emission, we conclude that the sharp

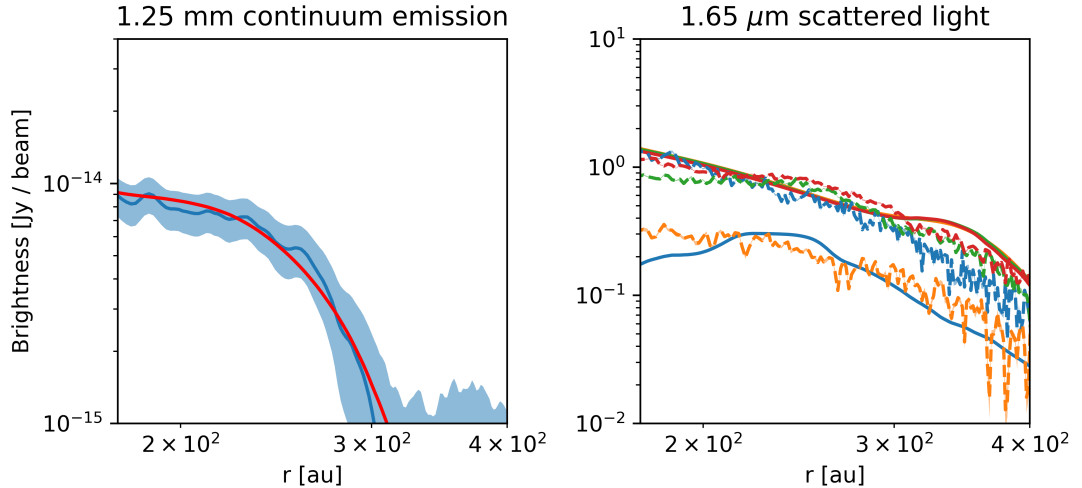


Figure 4.14: The model without truncation in the dust distribution best reproducing the continuum data. This model does not include enough small grains to reproduce the scattered light observations.

drop in the continuum emission is not caused by an opacity effect, and a physical truncation of the dust distribution is necessary to explain the data.

To test whether a cutoff in the dust density can reproduce the observations, we modified Eq. 4.11 and Eq. 4.14 by adding an exponential cutoff:

$$a_{max} = a_0 (r/r_c)^{-\alpha} \exp(-r/r_{cutoff})^{-p_1}, \quad (4.24)$$

$$\varepsilon = \varepsilon_0 (r/r_{in})^{-\alpha} \exp(-r/r_{cutoff})^{-p_2}, \quad (4.25)$$

where p_1 , p_2 , and r_{cutoff} are new fitting parameter, for a total of eight parameters. The physical drop in the continuum emission at a specific wavelength can be explained by either a cutoff in the maximum grain size distribution or in the dust-to-gas ratio. Since we do not have a theoretical argument to confirm the distribution for which the cutoff is more physically justifiable, we allow for the possibility of a cutoff in both distributions, and allowed the fit to find the one that fits the observed small and large grain emission. The profiles of best model produced by this approach is shown in Figure 4.16. This model places a cutoff of both the maximum grain size and the dust to gas ratio at 300 au, the location of the outer edge of the continuum emission. This model well reproduces both the continuum and scattered light data, with the exception of the outer part of the disk. Here, the truncation removes the small grains emitting in the scattered light and in the model, we observe a sharp drop in the emission not present in the observations. While a truncation of the large grain distribution is necessary to reproduce the continuum observations, this would cause a similar truncation in

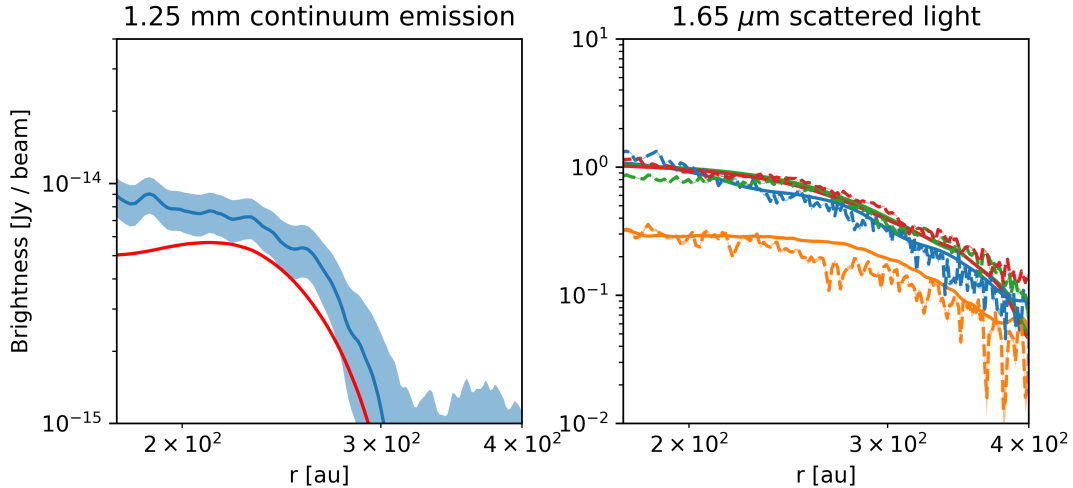


Figure 4.15: The model without truncation in the dust distribution best reproducing the scattered light data. This model does not have enough millimeter grains to match the observed continuum emission.

the small grain distribution. This is not, however, what we observe in the data, because the ring in the dust structure affects the distribution of large grains, but not the one of small grains. Since there are no large grains in the outer part of the disk, we cannot use our model to constrain the small grain distribution from the one of the large grains; thus we constrained our fit to the region where the continuum emission indicates the presence of large grains.

4.6 Conclusions

We present in this paper a model for the dust structure in IM Lup reproducing both ALMA midplane millimeter continuum emission and SPHERE near-infrared scattered light emission from the disk surface. While these two wavelength are particularly sensitive to large (ALMA) and small (SPHERE) particles, we used these data to build a model for the full grain size distribution. The geometrical disk parameters are taken from the SPHERE DARTTS-S survey (Avenhaus et al. 2018) and the gas mass from modeling CO isotopologues emission from ALMA data (Zhang et al. 2021). The dust radial and vertical grain size distribution, as well as the dust-to-gas ratio, successfully reproduce ALMA millimeter continuum emission from the disk midplane (Andrews et al. 2018) and SPHERE near-infrared scattered light emission from the disk surface (Avenhaus et al. 2018).

Our main results can be summarized as follows:

1. The posterior probability distribution of the model parameters shows a single solution for the dust distribution, which can reproduce the observations. We

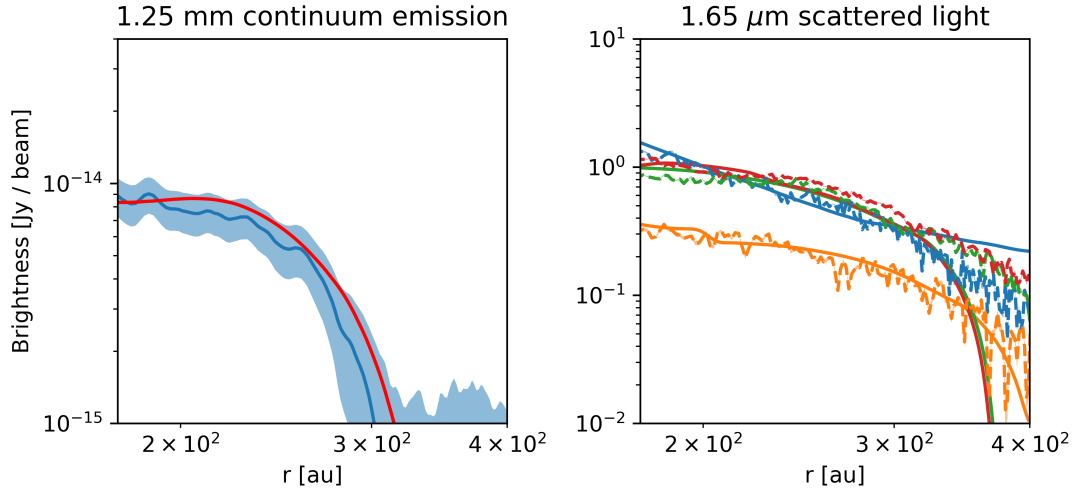


Figure 4.16: Best-fit model with a truncation of the maximum grain size and dust-to-gas ratio distribution. This model well reproduces both the continuum and scattered light data in the region inside the truncation, but adds a sharp drop in the scattered light profiles not seen in the observations.

find that $\sim 99\%$ of the dust mass is carried by millimeter or larger grains, and a 10^{-4} mass fraction of micron-sized grains is sufficient to reproduce the scattered light emission surface observed by SPHERE. Assuming a gas mass of $0.2 M_{\odot}$ inferred from CO emission (Zhang et al. 2021), we estimated a dust mass of $4 \times 10^{-3} M_{\odot}$.

2. The turbulent parameter α_{turb} determines which particle sizes are sedimented and which are well mixed to the gas. We constrained the turbulence parameter to 3×10^{-3} , which is slightly higher than the usual assumed value of 10^{-3} . The turbulence strength does not affect the model millimeter emission, dominated by large grains unaffected by turbulence. On the other hand, the disk flaring observed in the near-infrared is strongly affected by the turbulence. At low values of α_{turb} , the disk can appear flat also at small wavelengths, since small grains are free to settle to the midplane.
3. Large millimeter-sized grains in the midplane are necessary to reproduce the near-infrared observations. It requires a vertical stratification of the dust populations, rather than being well mixed to the gas, with millimeter-sized grains in the disk midplane and micron-sized grains on the disk surface, in accordance with dust coagulation models which include fragmentation (e.g., Dullemond & Dominik 2005; Birnstiel et al. 2010).
4. The dust distribution shows a strong radial gradient in the particle size, a feature often associated with a pressure trap. It causes the disk to have

a steep maximum grain size distribution, as the structures slow down the radial drift of the larger grains, which gather together on the inner side of the ring (e.g., Pinilla et al. 2015, 2021).

5. We find a vertical dust distribution with most of the mass carried by large grains in the disk midplane. The existence of large particles and the low turbulence in such a young disk point towards sedimentation-driven coagulation.
6. As a consequence of the strong radial gradient of the particle size distribution, we find millimeter and larger grains and a high dust-to-gas ratio in the disk midplane at smaller radii. It could be linked to the increase in brightness and the spiral structures observed in the inner disk, as in this environment dust drift is reduced and streaming instability can start to develop, possibly triggering planetesimal formation.

With these results, we demonstrate that the dust properties of a protoplanetary disk can be inferred from the properties of large and small grains. This limits the amount of observational diagnosis needed to characterize the dust structure of a protoplanetary disk.

Mid-infrared atomic and molecular hydrogen lines in the inner disk around a low-mass star

The content of this Chapter is based on a paper submitted to *Astronomy & Astrophysics (A&A)*.

Details of authorship: I am the first author of this paper, working under the supervision of Prof. Thomas Henning. Benoît Tabone provided useful comments on the analysis methods, while Prof. Thomas Henning and Prof. Ewine van Dishoeck helped shape the scientific discussion. Ewine van Dishoeck gave suggestions on the chemical analysis. Giulia Perotti helped with the structure and background of the paper. The data used in this paper was reduced in a paper by Benoît Tabone. The text was written by myself, with all co-authors providing comments.

5.1 Motivation

While molecular hydrogen is the most abundant molecule in the universe, it is intrinsically hard to observe since it is a symmetric and homonuclear diatomic molecule (Thi et al. 2001; Carmona et al. 2011; Trapman et al. 2017). Dipole ro-vibrational transitions are forbidden, and only weak electric-quadrupole transitions are allowed. Molecular hydrogen emission can only be observed in high-temperature or high-luminosity environments. Its emission has been detected in a number of classical T Tauri disks (Beck et al. 2008; Manara et al. 2021; Gangi

et al. 2023), coming from a warm layer above the optically thick dust emission (Carmona et al. 2011). Atomic hydrogen lines are also often detected and originate from accretion flows (Fang et al. 2009; Hartmann et al. 2016). Given the challenges in observing hydrogen emission, protoplanetary disks are usually characterized through other observational signatures. Dust emission is more easily observed (Andrews et al. 2018), and extensive modeling efforts can be found in the literature (see e.g. Testi et al. 2014; Miotello et al. 2022 for reviews). The disk gas structure remains less characterized, but with the development of observational facilities, it is now possible to study the gas through the emission of molecular tracers. For instance, the Atacama Large Millimeter/submillimeter Array (ALMA) observations of optically thin and optically thick CO isotopologues have been used to constrain the disk mass and temperature (Miotello et al. 2016, 2018; Zhang et al. 2021; Calahan et al. 2021; Schwarz et al. 2016, 2021; Pascucci et al. 2023). Yoshida et al. (2022) measured the pressure broadening of CO line emission and derived the gas surface density in the inner disk of TW Hya. Law et al. (2022) and Paneque-Carreño et al. (2023) used CO emission to study the disk vertical gas structure, while Lodato et al. (2023) measured the disk mass from the perturbations on the CO gas orbit induced by the disk self-gravity in the disks around IM Lup and GM Aur.

The HD molecule serves as a more direct indicator of H₂ since they are chemically very similar. The disk mass derived from HD measurements for TW Hya is higher than the CO-based estimate by about two orders of magnitudes, likely due to the depletion of CO from the gas phase (Bergin et al. 2013; McClure et al. 2016; Schwarz et al. 2016; Kama et al. 2020). However, HD emission primarily originates from warm regions within the disk (around $T \approx 30 - 50$ K) (Bergin et al. 2013; Trapman et al. 2017), providing only lower limits to the gas mass. Additionally, HD has been detected only in TW Hya (Bergin et al. 2013), GM Aur, and DM Tau (McClure et al. 2016), and no new HD observations have been conducted since the conclusion of the *Herschel* mission.

Other emission lines are now commonly observed as well, each tracing different disk properties (Öberg et al. 2021). HCO⁺ and N₂H⁺ trace the gas ionization in the molecular layer, a fundamental parameter to disk chemistry (Cleeves et al. 2015; Teague et al. 2015; Aikawa et al. 2021) and can also be used to measure gas depletion (Smirnov-Pinchukov et al. 2020; Anderson et al. 2021; Trapman et al. 2022).

The InfraRed Spectrograph (IRS) on the *Spitzer* Space Telescope observed emission lines that can be used to characterize the gas surrounding young stellar objects (YSOs). For instance, a higher [Ne II] luminosity in the inner disk originates either from stellar jets or from photoevaporative disks driven by stellar

high-energy photons (van Boekel et al. 2009; Lahuis et al. 2007; Pascucci et al. 2007; Güdel et al. 2010; Baldovin-Saavedra et al. 2011, 2012). Pascucci et al. (2006) estimated the upper limit of gas masses in the inner disk of a sample of young solar-like stars from the non-detection of mid-infrared H_2 lines. They found that none of their systems have a mass greater than $0.05 M_{Jup}$ within the first tens of au of the inner disk. Atomic hydrogen recombination lines are now commonly detected in the infrared spectra of YSOs and are used as an accretion tracer, as high HI luminosity is correlated with high accretion luminosities in the observed disks (e.g. Antonucci et al. 2011; Alcalá et al. 2014; Antonucci et al. 2016; Beuther et al. 2023). In particular, Rigliaco et al. (2015) detected the strongest of the Humphreys Series lines in the mid-infrared, the HI (7-6) line ($12.37 \mu\text{m}$), and derived an empirical relation between the HI (7-6) line luminosity and the accretion luminosity.

This paper presents observations of the disk surrounding the very low-mass star 2MASS-J16053215-1933159 (referred to as J160532) using the James Webb Space Telescope (JWST) Mid-Infrared Instrument (MIRI) Medium Resolution Spectrometer (MRS). These observations were obtained as part of the MIRI mid-Infrared Disk Survey (MINDS). A comprehensive analysis of the MIRI data has been detailed in Tabone et al. (2023), with a primary focus on hydrocarbon chemistry. The study revealed strong emission lines of C_2H_2 , C_4H_2 , and C_6H_6 while detecting no H_2O . This suggests that the inner disk of J160532 exhibits an abundance of hydrocarbons, indicating more active chemistry in comparison to disks around higher-mass stars and a notably high C/O ratio.

The MIRI spectrum of this source shows numerous atomic and molecular hydrogen emission lines that we investigate in this paper. We use the HI recombination lines to measure the source accretion rate and the atomic gas properties and the H_2 emission to constrain the gas rotational temperature and column density.

5.2 Observations

The target source, J160532, is an M dwarf star, the most common class of stars found in our Galaxy, and frequently hosting exoplanets (Dressing & Charbonneau 2015; Sabotta et al. 2021). Constraining the physical properties of disks around these stars provides important information about planet formation models. The star is located in the Upper Scorpius star-forming region, with a distance of 152 ± 1 pc (Gaia Collaboration et al. 2022) and an age of 2.6 ± 1.6 Myr (Miret-Roig et al. 2022). The source is an M4.75 spectral type star, with mass $M_\star = 0.14 M_\odot$ and luminosity $L_\star = 0.04 L_\odot$ (Pascucci et al. 2013; Luhman et al. 2018; Carpenter et al. 2014). The spectral energy distribution (SED) of the source indicates the

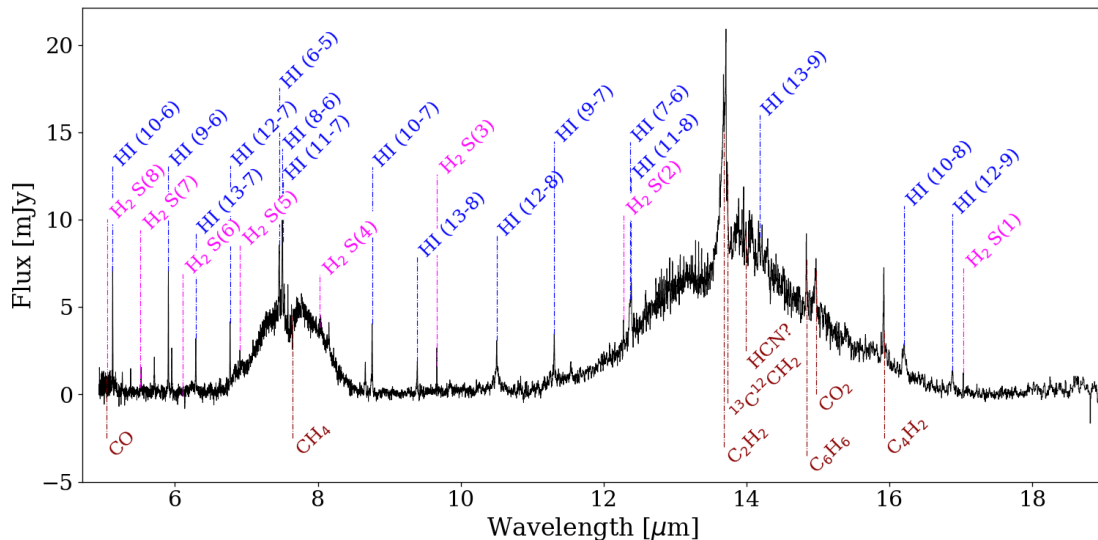


Figure 5.1: JWST MIRI-MRS continuum-subtracted spectrum of J160532. We identify several molecular (pink) and atomic hydrogen (blue) transitions, highlighted in the figure. A study of other molecular species (dark red) can be found in Tabone et al. (2023)

presence of a protoplanetary disk and the non-detection of millimeter continuum emission indicates a dust mass less than $0.75 M_{\text{Earth}}$, corresponding to a total gas and dust mass of less than $0.2 M_{\text{Jup}}$ for a standard gas-to-dust ratio of 100 (Barenfeld et al. 2016).

The data analyzed in this paper were first presented in Tabone et al. (2023), where details about the observations, data reduction, and analysis are presented. Below we briefly summarize the main aspects. The data were observed by the JWST MIRI instrument (Rieke et al. 2015; Wright et al. 2015; Labiano et al. 2021; Wright et al. 2023) in Medium Resolution Spectroscopy (MRS) mode (Wells et al. 2015; Argyriou et al. 2023) on 2022 August 1, for a total exposure time of 2.22 hours. These data were observed as part of the Cycle 1 Guaranteed Time Observation (GTO) program 1282, the MINDS program (PI: Thomas Henning). The details of the data reduction of the uncalibrated data can be found in Tabone et al. (2023). The spectral resolving power R ranges from 3500 to 1500 from the shortest to the longest wavelengths, equivalent to a velocity resolution of about 90 km s^{-1} to 200 km s^{-1} . The spectrum has been corrected for the source small radial velocity -1.98 km s^{-1} (Jönsson et al. 2020). The extinction for this source is particularly low, and no correction was needed for these data. To better analyze the spectral features, we perform a low-order fit of the continuum and of the two broad bumps at $7.7 \mu\text{m}$ and $13.7 \mu\text{m}$, corresponding to optically thick C_2H_2 emission (see Tabone et al. 2023 for a detailed description of the procedure). The resulting spectrum is shown in Fig.5.1.

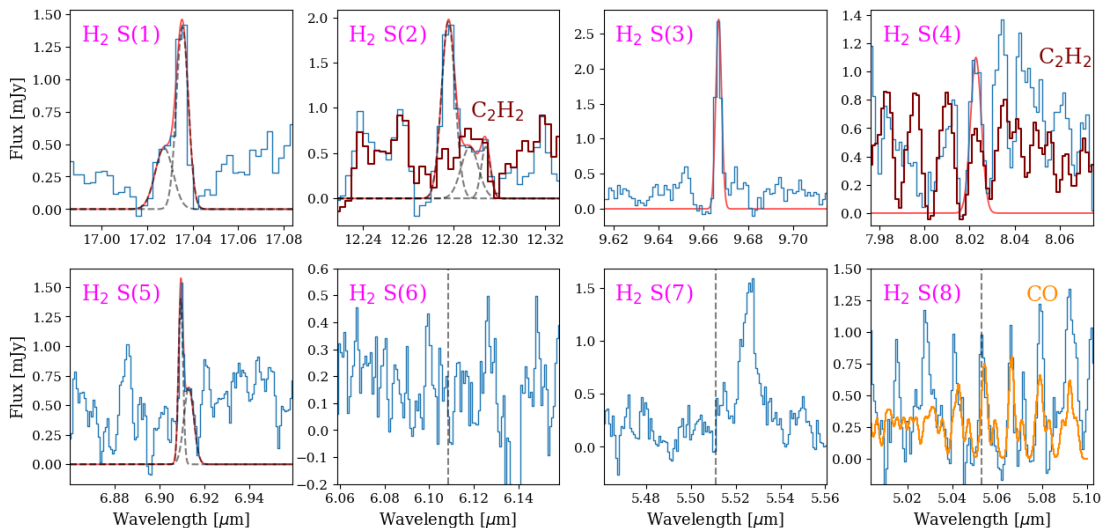


Figure 5.2: Molecular hydrogen pure rotational lines within the spectral range. The red profiles show line fitting using one or multiple Gaussian functions (dashed lines) in the case of line blending with other spectral features. The rest wavelength of the undetected lines is indicated by a slashed vertical line. In dark red we show the C_2H_2 rescaled model from (Tabone et al. 2023) to show the features location. In orange, we show an eye-fit of a CO slab model. The $S(2)$ line is blended with a C_2H_2 line. The $S(6)$ and $S(7)$ transitions fall in a crowded spectral region, and could not be identified. The $S(8)$ transition is found in a region populated by several CO $v = 1 - 0$ P-branch lines, and cannot be identified either.

5.3 Analysis and Results

5.3.1 Molecular hydrogen

As reported in Tabone et al. (2023), the spectrum shows HI, H_2 , and molecular (C_2H_2 , C_4H_2 , CO_2 among many others) features. The molecular component was analyzed in that paper. Here we focus on the HI and H_2 emission lines, reported in Fig. 5.1. With the high resolving power and sensitivity of the MIRI-MRS instrument, we detect five pure rotational $\nu = 0 - 0$ transitions of H_2 , while the typically fainter rotational transitions with higher vibrational states remain undetected (Fig. 5.2). The emitting region is unresolved, with no evidence of extended emission, meaning that it is coming from the inner, warm region of the disk. These lines are expected to be optically thin due to the small transition probabilities, and they can be used to constrain the temperature and column density of the emitting gas.

To accurately measure the line fluxes, we perform a linear fit of the continuum in a wavelength window of $0.03 \mu m$ centered on each line. The error in the flux density is the standard deviation on a nearby spectral segment that does not contain spectral features. The H_2 lines are fitted using one or multiple Gaussian

Table 5.1: Measured parameters of the identified pure rotational molecular hydrogen lines.

Transition	Line Center [μm]	Integrated Flux 10^{-13} [erg s $^{-1}$ cm $^{-2}$]
$S(1)$	17.305	0.9 ± 0.2
$S(2)$	12.279	2.4 ± 0.4
$S(3)$	9.665	2.8 ± 0.2
$S(4)$	8.025	3.1 ± 0.9
$S(5)$	6.910	2.2 ± 0.7

profiles when the line shows evidence of blending with other spectral features to remove their contribution. This is done using the Levenberg-Marquardt least-squares minimization. The H_2 line flux is then calculated by integrating the main Gaussian component. In our calculations, the width of the Gaussian profiles is left as a free parameter. However, when working at the spectral resolution scale, one could also fix the width of the Gaussian profiles at the local spectral resolution element. We find that both methods give very similar results, within our error estimates, and we choose to leave the Gaussian width as a free parameter. The $\nu = 0 - 0$ $S(6)$, $S(7)$, and $S(8)$ lines are in a spectral region rich in other spectral features, and their profiles could not be extracted. In particular, the $S(8)$ line falls between 4.9 and 5.1 μm , where several CO $\nu = 1 - 0$ P-branch lines are found, indicative of high-temperature gas ($T > 1000$ K) (Tabone et al. 2023). The $S(1)$ line is blended with a C_2H_2 line, identified in a previous analysis (Tabone et al. 2023). The $S(4)$ line is also in proximity to C_2H_2 spectral features. However, we still include this line in our analysis since it produces results consistent with those from the other H_2 rotational lines. The line profiles and the best-fit profiles are shown in Fig. 5.2, and the line parameters are reported in Tab. 5.1.

We now use the measured fluxes to build a rotational diagram (Goldsmith & Langer 1999) to estimate the emitting gas temperature and column density. Assuming a Boltzmann distribution, for optically thin emission the observed fluxes F_J must satisfy the relations:

$$\frac{4\pi F_J}{hc\nu_J\Omega g_J A_J} = \frac{N_{\text{tot}}}{Q_{\text{rot}}} e^{-E_J/k_B T_{\text{rot}}} \quad (5.1)$$

where h is the Planck constant, k_B the Boltzmann constant, c is the speed of light, ν_J is the line frequency, $\Omega = \pi(r_{\text{em}}/d)^2$ is the emitting area solid angle, A_J the Einstein coefficient, $g_J = 2J + 1$ is the statistical weight of the transition, N_{tot} is the molecule column density, $Q(T_{\text{rot}})$ is the partition function, E_J is the transition energy, and T_{rot} is the rotation temperature. The ortho-to-para ratio is

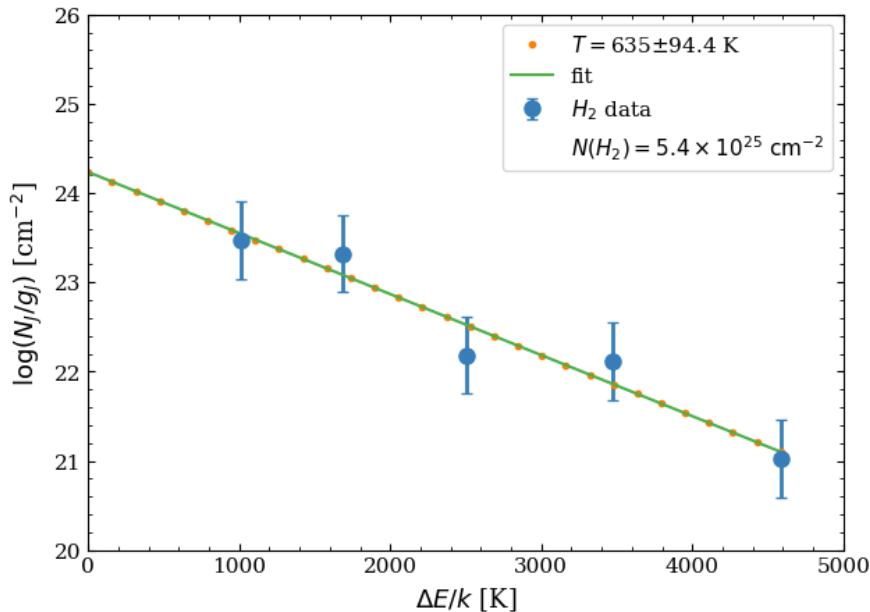


Figure 5.3: Rotation diagram of H_2 rotational transitions. A linear fit was performed on the measured fluxes, and the diagram shows a single component for the emitting gas with a temperature of about 635 K and mass $2.3 \times 10^{-5} M_{\text{Jup}}$.

assumed to be 3 in local thermodynamical equilibrium (LTE). Assuming optically thin emission at LTE with temperature T_{rot} , we can estimate the column density and temperature of the gas:

$$\ln \left(\frac{4\pi F_J}{hc\nu_J g_J A_J} \right) = -\frac{E_J}{k_B T_{\text{rot}}} - \ln \left(\frac{Q_{\text{rot}}}{N_{\text{tot}} \Omega} \right). \quad (5.2)$$

This expression allows the construction of a rotational diagram. In this graphical representation, the variables are $x = E_J/k_B$ and $y = \log(N_J/g_J)$, where $N_J = 4\pi F_J/hc\nu_J A_J$. The second term on the right-hand side is treated as a constant. When plotted, this diagram is expected to produce a straight line with a slope of $-1/T_{\text{rot}}$ and an intercept that provides the mass of the emitting gas, under the assumption of a specific emission area. The resulting rotation diagram is shown in Fig. 5.3. The emitting area can be estimated from an optically thick line. We assume the H_2 emission to have the same emitting radius r_{em} as the C_2H_2 emission, 0.033 au (Tabone et al. 2023). We find a temperature of 635 ± 94 K and a column density of $190 \pm 110 \text{ g cm}^{-2}$, corresponding to a total mass of warm H_2 gas of $(2.3 \pm 1.3) \times 10^{-5} M_{\text{Jup}}$.

The warm gas traces only the innermost region of the disk and its mass represents only a small fraction of the total disk mass. From the non-detection of millimeter continuum emission, Barenfeld et al. (2016) give an upper limit to the disk mass of $0.2 M_{\text{Jup}}$. By making a few assumptions, we can give a rough estimate of the disk mass based on our measured warm H_2 mass. We assume a small

disk size $r_0 = 10$ au, and a power-law distribution for the disk surface density distribution:

$$\Sigma(r) = \Sigma_0 \left(\frac{r}{r_0} \right)^{-1}. \quad (5.3)$$

By knowing the gas surface density at $r = 0.033$ au from our H_2 emission analysis, we can use this equation to get a total disk mass estimate of $0.05 M_{\text{Jup}}$, which is in agreement with the upper limit of $0.2 M_{\text{Jup}}$ from Barenfeld et al. (2016).

5.3.2 Atomic hydrogen

Atomic hydrogen recombination lines trace stellar accretion and ejection processes, as demonstrated by their broad profiles consistent with almost free-falling material (e.g., Alcalá et al. 2014). These lines are now commonly used to measure mass accretion rates in YSOs (Antoniucci et al. 2011, 2014; Biazzo et al. 2012; Antoniucci et al. 2016; Gravity Collaboration et al. 2023), although they can also originate from winds and jets (Beck et al. 2010; Bally 2016; Ercolano & Pascucci 2017). While it is necessary to account for both accretion and wind processes to reproduce all the spectral features, a tight empirical correlation has been measured between the integrated flux of HI recombination lines and the accretion luminosities L_{acc} . This correlation has been extensively studied for optical and near-infrared lines, such as the $\text{H}\alpha$, $\text{Br}\gamma$, $\text{Pa}\beta$ (Antoniucci et al. 2014; Alcalá et al. 2014, 2017), and $\text{Pf}\beta$ (at $4.6 \mu\text{m}$) lines (Salyk et al. 2013). However, for the embedded phases of star formation or for sources significantly affected by extinction, we must rely on longer wavelengths. Only a few space-based studies are available in the literature, based on data obtained with the Infrared Space Observatory and *Spitzer* space telescope (e.g., van Dishoeck et al. 1998; Gibb et al. 2000; Molinari et al. 2008; An et al. 2011). In particular, Rigliaco et al. (2015) explored the relations between the HI (7-6) line luminosity at $12.37 \mu\text{m}$ and the accretion luminosity using *Spitzer* data on a sample of classical T Tauri stars. With the MIRI instrument, it is now possible to study in detail the mid-infrared atomic hydrogen recombination lines.

We detect 20 atomic hydrogen recombination lines in the spectrum of J160532, with the principal quantum number of the lower energy levels between 5 and 8 (Pfund, Humphreys, and higher series). To estimate the line fluxes, we follow the same procedure used to analyze H_2 in Sec. 5.3.1, and the lines are shown in Fig. 5.4. The main Gaussian component of the line fits has a width ranging from about 100 to 200 km s^{-1} , compatible with the local spectral resolution. Our results are summarized in Tab. 5.2. The line fluxes are shown in an excitation diagram in

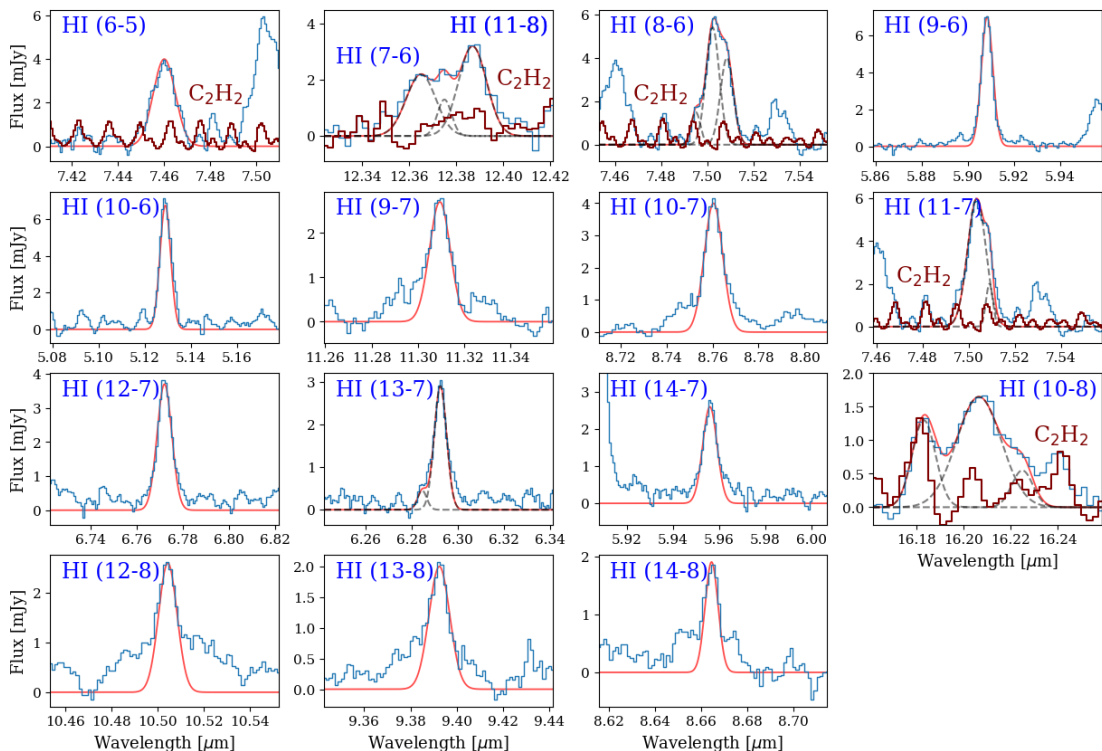


Figure 5.4: Atomic hydrogen recombination lines. The red profiles show line fitting using one or multiple Gaussian functions (dashed lines) in the case of line blending with other spectral features. The dark red profile is the C_2H_2 model from Tabone et al. (2023)

Fig. 5.5. This diagram highlights that the intensities of the HI lines deviate from what would be expected in optically thin emission conditions. Moreover, lines with the same upper energy level do not overlap in the plot, contrary to what would be expected in the scenario of optically thin emission.

We measure the mass accretion rate from the HI (7-6) line at $12.37 \mu\text{m}$ using the method introduced by Rigliaco et al. (2015), who derives the following empirical relation between the HI (7-6) integrated flux and the accretion luminosity in classical T Tauri stars:

$$\log L_{\text{HI (7-6)}}/L_{\odot} = (0.48 \pm 0.09) \times \log L_{\text{acc}}/L_{\odot} - (4.68 \pm 0.10). \quad (5.4)$$

The standard relation between the mass accretion rate \dot{M}_{acc} and L_{acc} was introduced by Gullbring et al. (1998b):

$$\dot{M}_{\text{acc}} = \frac{L_{\text{acc}} R_{\star}}{GM_{\star}} \left(1 - \frac{R_{\star}}{R_{\text{in}}}\right)^{-1}, \quad (5.5)$$

where $M_{\star} = 0.14 M_{\odot}$ is the stellar mass, R_{in} the radius at which the stellar magnetosphere disperses the accreting gas, and $R_{\star} = 0.45 R_{\odot}$ is the stellar radius.

Table 5.2: Measured parameters of the identified atomic hydrogen recombination lines.

Transition	Line Center [μm]	Integrated Flux 10^{-16} [$\text{erg s}^{-1} \text{cm}^{-2}$]
6-5	7.460	25.9 ± 5.8
7-6	12.372	9.4 ± 1.0
8-6	7.503	20.9 ± 1.0
9-6	5.908	37.7 ± 1.3
10-6	5.129	44.6 ± 2.2
9-7	11.309	7.1 ± 1.0
10-7	8.760	15.7 ± 1.0
11-7	7.508	32.0 ± 5.3
12-7	6.772	19.4 ± 5.3
13-7	6.292	14.9 ± 1.9
14-7	5.957	17.1 ± 1.9
10-8	16.209	4.5 ± 1.3
11-8	12.387	9.7 ± 1.1
12-8	10.504	7.1 ± 0.9
13-8	9.392	7.7 ± 1.0
14-8	8.665	5.3 ± 1.0

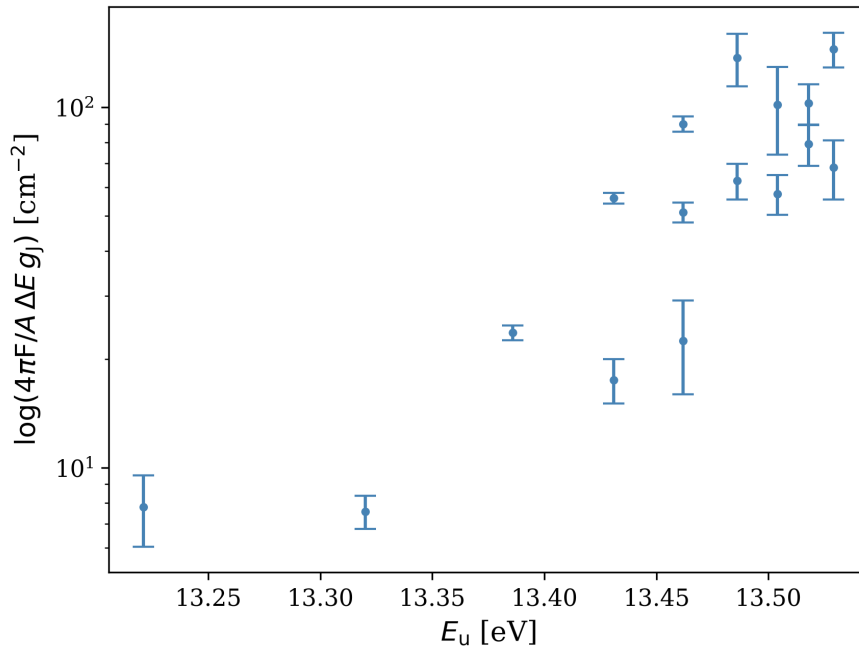


Figure 5.5: Excitation diagram of the HI lines. These lines are produced by shocked material for which the Boltzmann distribution does not apply, therefore the y-axis is in terms of integrated line flux rather than column density.

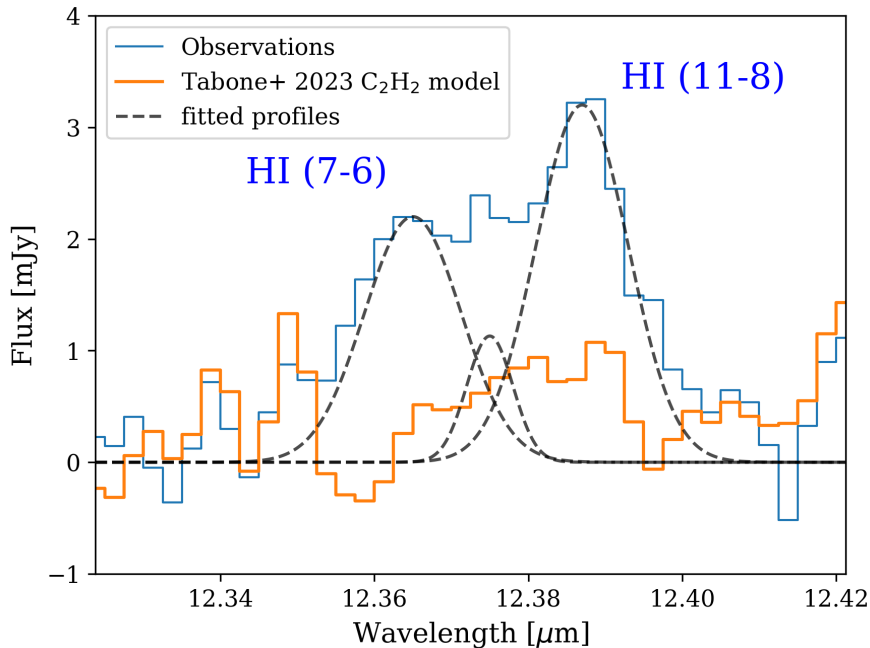


Figure 5.6: Emission lines used to measure the accretion rates. The black dashed profile on the left is the HI (7-6) line, the one on the right is the HI (11-8) line, while the central component is C_2H_2 emission, according to the predictions of Tabone et al. (2023) (the orange profile).

R_{in} is usually assumed to be $5 R_{\star}$ (Herczeg & Hillenbrand 2008; Alcalá et al. 2014; Rigliaco et al. 2015), while R_{\star} is derived from the stellar effective temperature $T_{\text{eff}} = 3850$ K and the stellar luminosity L_{\star} using the Stefan–Boltzmann relation $L_{\star} = 4\pi R_{\star}^2 \sigma T_{\text{eff}}^4$, where σ is the Stefan–Boltzmann constant and T_{eff} is estimated from the spectral type M4.75 (Fang et al. 2017).

Notably, the HI (7-6) line at $12.372 \mu\text{m}$ is located near another atomic hydrogen recombination line, the HI (11-8) transition at $12.387 \mu\text{m}$. This is evident from the observed line profile (see Fig. 5.6), which displays two dominant Gaussian components, each approximately 150 km s^{-1} wide. The HI (7-6) line is shifted by about -4 km s^{-1} compared to its rest frequency, while the HI (11-8) by about 64 km s^{-1} , which is compatible with the line rest frequency given the local resolution of about 110 km s^{-1} . Additionally, a third, weaker component is present, with a width similar to the local resolution element, around $\sim 60 \text{ km s}^{-1}$. Comparatively, the widths of the two main components align with those of the other atomic hydrogen lines. We identify the component at the shorter wavelength as the HI (7-6) line, while the component at the longer wavelength corresponds to the HI (11-8) line. The third component could be the Q -branch of a weak P , Q , and R -branch pattern of optically thick C_2H_2 emission modeled by Tabone et al. (2023), centered at $12.379 \mu\text{m}$ (Fig. 5.6). The two identified components have peak flux densities of 2.3 mJy and 3.5 mJy , and luminosities of $4.9 \times 10^{-7} L_{\odot}$

and $6.8 \times 10^{-7} L_{\odot}$ respectively. From the HI (7-6) luminosity we get an accretion luminosity of $4.0 \pm 2.5 \times 10^{-4} L_{\odot}$ using Eq. 5.4, corresponding to a mass accretion rate of $1.0 \times 10^{-10} M_{\odot} \text{ yr}^{-1}$. However, this relation was calibrated by Rigliaco et al. (2015) using *Spitzer* data, which lacked the spectral resolution necessary to distinguish between the HI(7-6) and HI(11-8) profiles. Since both lines are excited at similar energies, the excitation of one line implies the excitation of the other. Therefore, we argue that the fluxes used by Rigliaco et al. (2015) to measure the accretion luminosity were not solely the HI (7-6) line but rather the combined fluxes of both the HI (7-6) and HI (11-8) lines. The contribution to the total flux given by the C₂H₂ component is negligible and does not affect the measured accretion luminosity. By considering the total line flux, we obtain an accretion luminosity of $(3.1 \pm 1.9) \times 10^{-3} L_{\odot}$, corresponding to a mass accretion rate of $(4.0 \pm 2.5) \times 10^{-10} M_{\odot} \text{ yr}^{-1}$. This result is in good agreement with the mass accretion rate estimate of $4.17 \times 10^{-10} M_{\odot} \text{ yr}^{-1}$ reported by Fang et al. (2023) based on the H α emission. A follow-up study utilizing the higher spectral resolution data from the JWST on a sample of sources could validate the hypothesis that the accretion rate measured using Eq. 5.4 uses the combined HI (7-6) and HI(11-8) fluxes.

Finally, Antonucci et al. (2016) studied the Balmer and Paschen decrements in a sample of 36 low-mass Class II sources. While they did not find any correlation between the line decrements and the source properties, they found a tentative correlation between the decrement shape and the mass accretion rate. If we assume their results to be valid also for other HI series (a reasonable assumption since they originate from the same physical process), the decrement shape in our source (Fig. 5.8) falls in their Type 3, bumpy profile category. The disks in this category have mass accretion rates between $10^{-10} - 10^{-9} M_{\odot} \text{ yr}^{-1}$, which is in accord with our measured value of $(4.0 \pm 2.5) \times 10^{-10} M_{\odot} \text{ yr}^{-1}$.

5.3.3 Atomic line emission models

To constrain the physical properties of the gas from which the HI lines originate, we compare the observed line fluxes to predictions from two standard emission models. The first model employed was the classic Case B recombination line model (Baker & Menzel 1938; Storey & Hummer 1995), which assumes that Lyman lines are optically thick and all other transitions are optically thin, and that level populations are determined through radiative cascade from the continuum. The second model utilized is the more recent local line excitation approach developed by Kwan & Fischer (2011), which considers the local physical conditions of the gas to consistently evaluate the line emissivities. The input physical param-

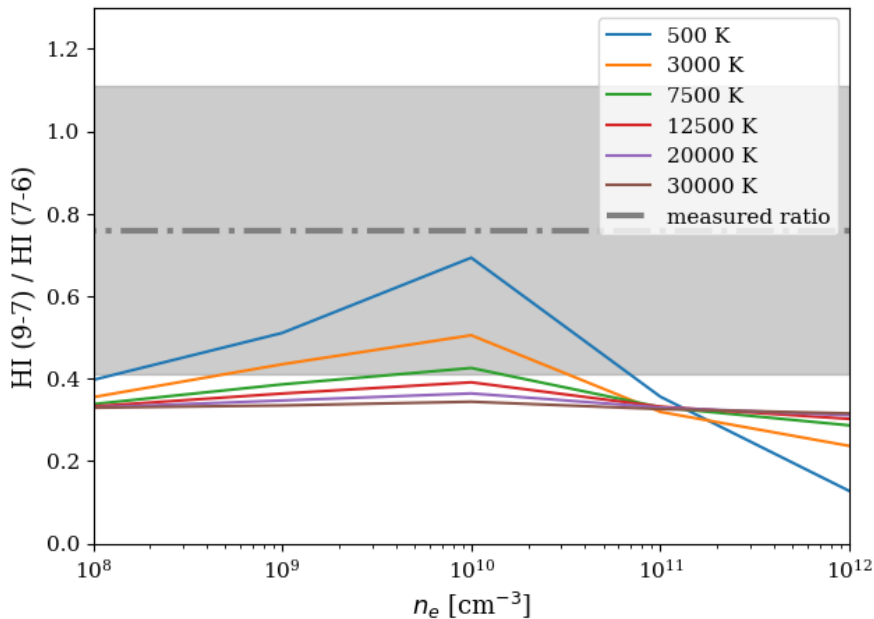


Figure 5.7: HI (9-7) and HI (7-6) line ratio as a function of electron density from the Case B recombination model compared to our measured ratio, the gray dotted line. The shaded area is the uncertainty of the measured ratio.

eters of this model are the gas temperature, the hydrogen density, the ionization rate (which was not specified in the Case B models), and the gas velocity gradient transverse to the radial direction. These parameters are chosen to reflect the typical physical condition in accreting YSOs.

The Case B recombination model is commonly used in the literature to derive the physical properties of accreting gas onto T Tauri stars. It assumes that the gas is optically thick to Lyman series photons and optically thin to the photons linked to other transitions. Storey & Hummer (1995) computed the line fluxes for hydrogenic atoms as a function of temperature and electron density for the Case B recombination model, which are available online¹. Using this model, we compare in Fig. 5.7 the HI (9-7) and HI (7-6) lines for a temperature range of 500-30 000 K and electron density n_e between 10^8 cm^{-3} and 10^{12} cm^{-3} to our measured value of $\sim 0.76 \pm 0.35$. According to this model, the gas temperature varies widely and it is poorly constrained, ranging from 500 K to 12 500 K, electron density between 10^8 cm^{-3} and 10^{11} cm^{-3} . The highest temperatures are observed at column densities of $\sim 10^{10} \text{ cm}^{-3}$.

In Fig. 5.8 we show the line ratios as a function of the upper level quantum number N_{up} , for different line series, with lower energy levels 6, 7, and 8. In computing the ratio, we use as a reference the HI (9-6) (H $\nu\gamma$) line, the cleanest line in our sample. However, choosing a different line does not significantly affect

¹<http://cdsarc.u-strasbg.fr/viz-bin/Cat?VI/64>

the shape of the line ratio distribution. In Fig. 5.8 we also show the predicted values for the Case B model for a range of temperatures from 500 K to 10 000 K and densities from 10^8 cm^{-3} to 10^{12} cm^{-3} . The Case B line ratios poorly reproduce the observations, especially for the lower lines in the series. This plot highlights the effect of the optical depth on the line fluxes. In the case of optically thin emission, we expect the ratio of lines with the same upper level to be the ratio of the Einstein coefficients of the transitions. However, our observed lines contradict this expectation. For instance, the ratio of the HI (9-7) and HI (9-6) lines is about 5.3. This value is much higher than the Einstein coefficient ratio of about 0.9. This discrepancy suggests that these lines cannot be considered optically thin, as assumed in the Case B recombination theory. This model therefore is not an appropriate description of these data.

The HI (9-7) and HI (7-6) line ratio was also computed following a different approach by Kwan & Fischer (2011), hereafter denoted KF model, where they measure the optical depth of each transition instead of assuming optically thin emission. They also include in their calculation the gas ionization rate and the velocity gradient, not accounted for in the Case B recombination model, and tuned these parameters to reflect the typical physical condition of accreting YSOs. Using the data available online² we compare again the model ratio of the HI (9-7) and HI (7-6) line to our measurement, for temperatures between 5 000 K and 20 000 K and atomic hydrogen densities between 10^8 cm^{-3} and 10^{12} cm^{-3} (see Fig. 5.9). The KF model predicts that all the temperatures are compatible with our measured line ratios, and constrains the hydrogen density to $7 \times 10^9 - 4 \times 10^{10} \text{ cm}^{-3}$. Compared to the Case B model, the proper treatment of the lines optical depth gives us much tighter constraints. Since the ionization degree of n_e/n_H typically ranges between 0.1-1.0, this density range is in agreement with the constraints from the Case B model. Case B models with temperatures up to 7 500 K and atomic hydrogen densities of about $10^{10} - 10^{11} \text{ cm}^{-3}$ (with $n_e/n_H = 0.1$) are in agreement with the low temperature (5 000 K), high density (a few 10^{10} cm^{-3}) KF models, while densities below 10^{10} cm^{-3} cannot be reached given our measured line ratio. However, we cannot give an upper limit to the atomic hydrogen densities according to the KF models, as the line ratio was not calculated for temperatures lower than 5 000 K. When looking at the model prediction of the other HI line fluxes of the Case B model, the fit to the data is quite poor. In fact, the observed line fluxes require temperatures lower than 500 K. These low temperatures are unlikely for shocked accreting HI gas. This indicates that these lines may not be optically thin, as assumed in the Case B model (van den Ancker et al. 2000; Edwards et al. 2013; Rigliaco et al. 2015), and this model cannot be used to model the emission

²<http://iopscience.iop.org/0004-637X/778/2/148/suppdata/data.tar.gz>

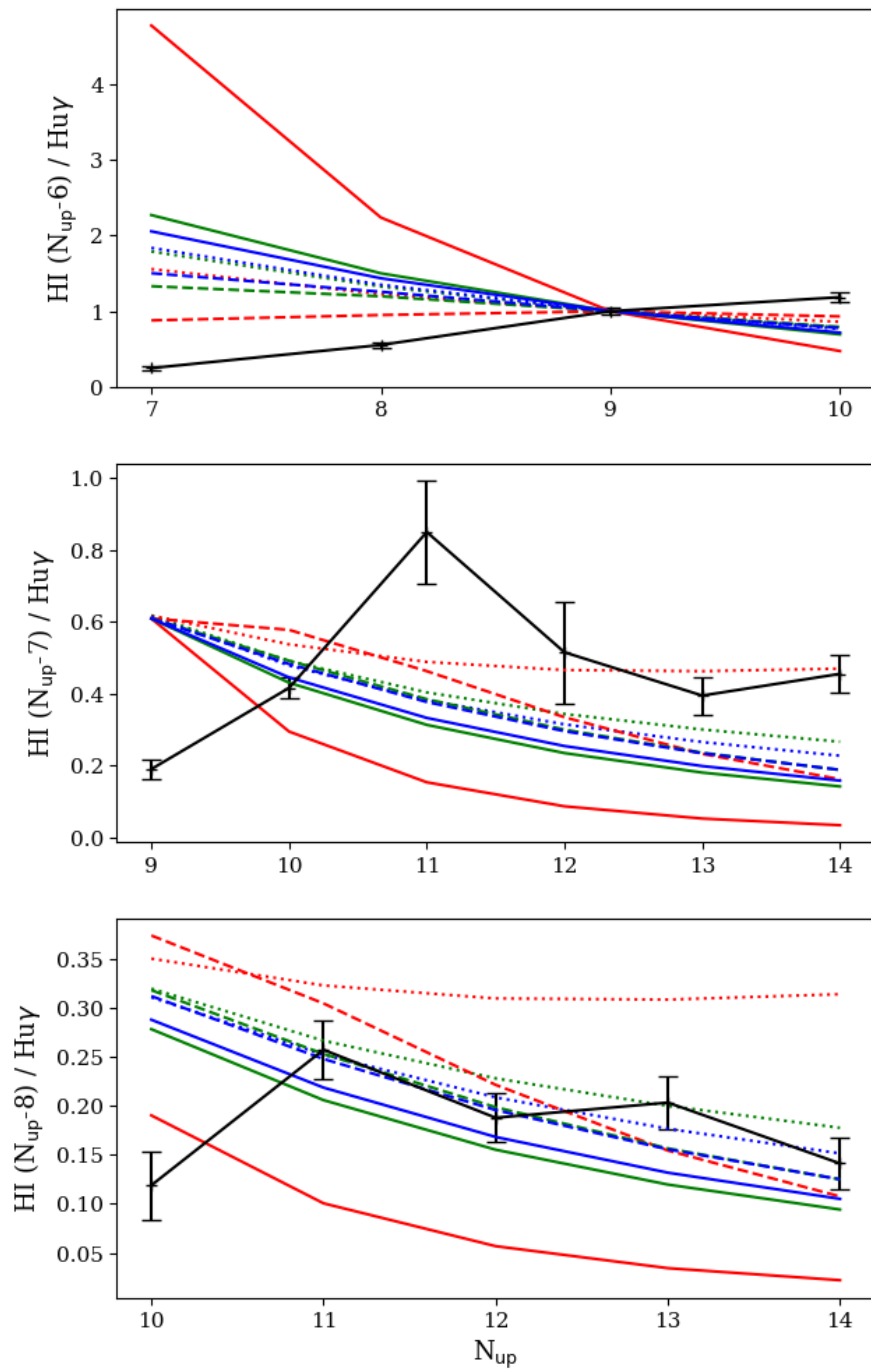


Figure 5.8: The observed HI line flux ratios for transition with lower energy levels (from top to bottom) 6, 7, and 8 (solid black line). The other lines are the predicted values by the Case B model. The model densities are 10^8 cm^{-3} (dotted line), 10^{10} cm^{-3} (slashed line), and 10^{12} cm^{-3} . The temperatures are 500 K (red), 5000 K (green), and 10000 K (blue).

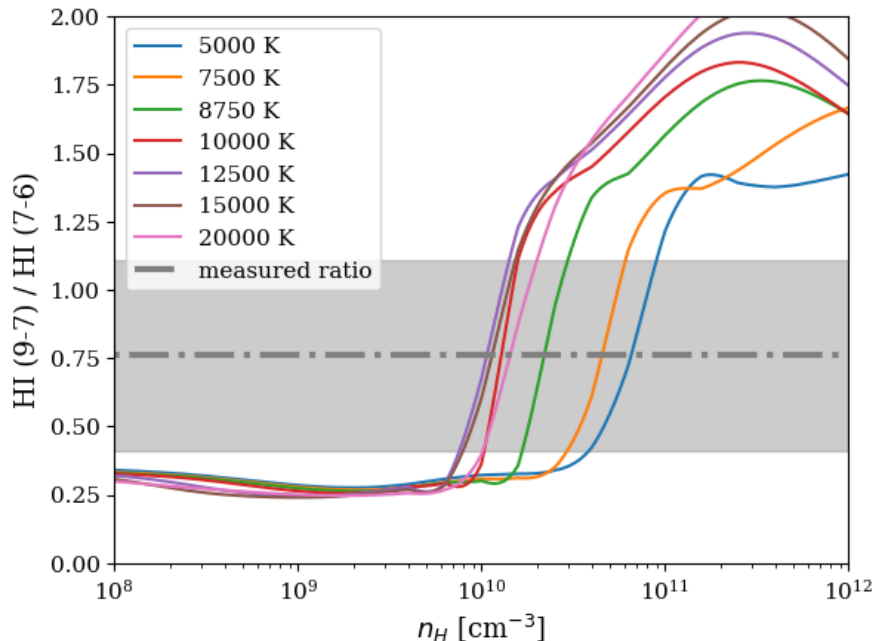


Figure 5.9: HI (9-7) and HI (7-6) line ratio as a function of atomic hydrogen density according to the KF atomic emission model (Kwan & Fischer 2011) compared to our measured ratio, the gray dotted line. The shaded area is the uncertainty of the measured ratio.

of high-density regions such as accretion flows in YSOs.

5.4 Discussion

H₂ emission in classical T Tauri stars can originate from either the inner region of a protoplanetary disk, excited by UV radiation, or shocked gas in stellar outflows (Beck et al. 2010; Carmona et al. 2011). We analyze the profiles of the detected H₂ lines to constrain the origin and formation mechanism of these lines. As discussed in Sec. 5.3.1, the H₂ emission comes from a spatially unresolved component with no evidence of outflows. The emission is observed at a velocity consistent with the rest velocity of the star. However, the data are also compatible with a stellar wind or outflow coming from the very inner disk with a projected velocity $\lesssim 90 \text{ km s}^{-1}$. To further constrain the origin of these lines, we measure the full width at zero intensity (FWZI) of the profiles, giving us the maximum projected velocity of the emitting H₂, and compare this value to the Keplerian velocity at the emitting radius 0.033 au. We measure a mean FWZI of $160 \pm 110 \text{ km s}^{-1}$, and given that the Keplerian velocity at the emitting radius is 60 km s^{-1} , this measurement is compatible with Keplerian motions of the gas within the assumed emitting radius. However, it is important to note that we lack information about the disk geometry, and the projected Keplerian velocity might be below 60 km s^{-1} , depending on the

disk inclination.

We perform the same analysis of the FWZI of the HI line profiles to investigate their origin. As discussed in Sec. 5.3.2, we assume that HI emission traces accretion flows of free-falling gas on the stellar surface. Following the assumption that the gas is accreting from a radius $R_{in} = 5 R_{\star}$ (see Sec. 5.3.2), we get a free-fall velocity of 315 km s^{-1} . The average FWZI for HI lines is $370 \pm 140 \text{ km s}^{-1}$, supporting the hypothesis that this emission comes from free-falling gas accreting on the central object.

The accretion rate we derive using the atomic hydrogen lines is consistent with those measured in other YSOs. Alcalá et al. (2017) measured the accretion rate of YSOs in the Lupus region. Their measured accretion rates range from $\sim 5 \times 10^{-12} M_{\odot} \text{ yr}^{-1}$ to $\sim 6 \times 10^{-8} M_{\odot} \text{ yr}^{-1}$, and our measured mass accretion rate of $\sim 4 \times 10^{-10} M_{\odot} \text{ yr}^{-1}$ correspond to an average accretion for the YSOs in their sample. Alcalá et al. (2017) also derive an analytical relation between $L_{acc} - L_{\star}$ and one between $\dot{M}_{acc} - M_{\star}$. Using their relation for L_{acc} :

$$\log L_{acc} = (1.26 \pm 0.14) \cdot \log L_{\star} - (1.60 \pm 0.13), \quad (5.6)$$

we find $L_{acc} = (4.4 \pm 2.4) \times 10^{-4} L_{\odot}$. This measurement is about one order of magnitude lower than our measured value of $(3.1 \pm 1.9) \times 10^{-3} L_{\odot}$. There is, however, a significant scatter in the data used to derive Eq. 5.6, and our measurement falls within this scatter. Using their relation for \dot{M}_{acc} for low-mass stars ($< 0.2 M_{\odot}$):

$$\log \dot{M}_{acc} = (4.58 \pm 0.68) \cdot \log M_{\star} - (6.11 \pm 0.61), \quad (5.7)$$

we derive $\dot{M}_{acc} = (1.0 \pm 1.8) \times 10^{-10} M_{\odot} \text{ yr}^{-1}$, in agreement with our measured value of $(4.0 \pm 2.5) \times 10^{-10}$.

Numerous spectroscopic surveys in several star formation regions have observed a correlation between the accretion rate \dot{M}_{acc} and the stellar mass M_{\star} (Alcalá et al. 2014; Venuti et al. 2014, 2019; Manara et al. 2016, 2017; Hartmann et al. 2016), with reported slopes ranging from approximately 1.6 to 2. Recently, Manara et al. (2023) compared all of these data and presented their findings in their Fig. 4. Their analysis demonstrates that the observations align well with the relationship $\dot{M}_{acc} \propto M_{\star}^2$. In Fig. 5.10, we reproduce their plot and incorporate our own measured \dot{M}_{acc} for J160532. This plot confirms that the accretion rate for this particular source adheres to the $\dot{M}_{acc} \propto M_{\star}^2$ relationship, classifying it as a standard accretor compared to other YSOs. It is important to highlight that our determined accretion rate is not exceptionally high, despite the prominent presence of HI lines in the spectrum. In fact, it falls within the lower range when compared to similar sources with measured accretion rates (e.g., Rigliaco et al.

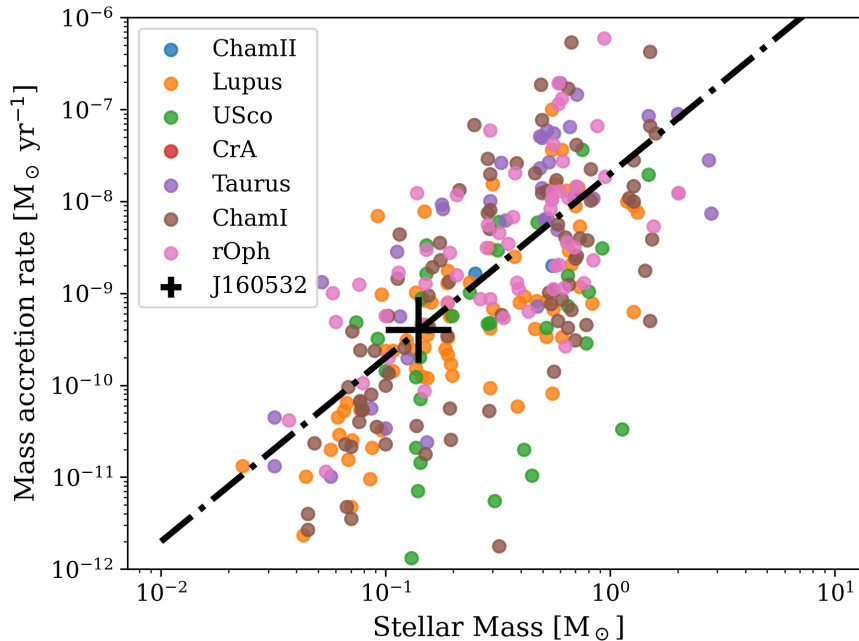


Figure 5.10: \dot{M}_{acc} as function of M_\star^2 from several star formation regions, reproduced from Manara et al. (2023). The dashed line shows their eye-fit of the $\dot{M}_{acc} \propto M_\star^2$ relation. The black cross is our measurement of the J160532 \dot{M}_{acc} .

2015; Manara et al. 2016; Alcalá et al. 2017). This clear detection of HI lines is likely attributed to the remarkably low dust extinction, enabling us to penetrate deeply into the disk and obtain an unobstructed view of the accretion layer.

5.5 Conclusions

In this paper, we present the full JWST-MIRI spectrum of the disk around the very low-mass star 2MASS-J16053215-1933159. These observations reveal numerous atomic and molecular hydrogen lines in the mid-infrared spectrum of this source. We utilize HI recombination lines to measure the accretion rate of the source and H₂ emission to constrain the rotational temperature and column density of the disk gas.

With the high resolving power and sensitivity of the MIRI-MRS instrument, we detect several pure rotational $\nu = 0 - 0$ H₂ transitions. The observed lines are optically thin due to their small transition probabilities, allowing us to constrain the temperature and column density of the gas. To accurately measure the line fluxes, we perform a linear fit of the continuum and fit Gaussian profiles to the H₂ line profiles, while accounting for blending with other spectral features. Using the measured fluxes, we construct a rotational diagram to estimate the temperature and column density of the emitting gas. Under the assumption of optically thin emission in local thermodynamic equilibrium, our calculations yield a total mass

of warm H_2 gas at $(2.3 \pm 1.3) \times 10^{-5} M_{\text{Jup}}$ with a corresponding temperature of $635 \pm 94\text{K}$. This represents only a minor portion of the entire disk mass, which is constrained to be below $0.2M_{\text{Jup}}$ due to the upper limit given by the non-detection of millimeter continuum emission.

We investigate the HI (7-6) line profile, a tracer for mass accretion. Through analyzing its profiles, we identify two main Gaussian components corresponding to the HI (7-6) and HI (11-8) atomic hydrogen recombination lines. These lines are in close proximity in wavelength, and the flux measurement used by Rigliaco et al. (2015) to assess accretion luminosity likely included contributions from both lines, rather than solely the HI (7-6) flux. When considering the combined flux, our estimated accretion luminosity $4.17 \times 10^{-10} M_{\odot}\text{yr}^{-1}$ is consistent with the measurement based on $\text{H}\alpha$ emission by Fang et al. (2023). This suggests that the previous calibration of accretion luminosities may indeed include the contribution from both lines. To further validate our hypothesis, future observations with higher spectral resolution than *Spitzer* data, such as those possible with the JWST, would be valuable. We compare our measured accretion rate with other YSOs, finding that this source has typical accretion properties.

To derive the physical properties of the accreting gas onto the star, we compare the HI (9-7) to HI (7-6) line ratio with the Case B recombination model (Baker & Menzel 1938; Storey & Hummer 1995) and the Kwan & Fischer (KF) model (Kwan & Fischer 2011). The Case B model provides limited constraints on the density and temperature, primarily because the lines are not optically thin, as assumed by this model. The KF model predicts that our measured line ratios are compatible with a range of temperatures from 5000 K to 20000 K, and atomic hydrogen densities between 10^9 cm^{-3} and 10^{11} cm^{-3} . The atomic hydrogen density is well constrained by the KF model, while the temperature is not. However, the Case B model fails to reproduce the observed line fluxes and points to temperatures lower than 500 K, not physical for accretion flows.

In summary, our observation and analysis of one of the first JWST MIRI MRS data of a faint disk reveal new important results on the circumstellar gas properties. We observed several H_2 rotational lines, which constrain the warm emitting gas temperature and mass. Moreover, the measurement of HI recombination lines can be used to estimate the mass accretion rate onto the central source, while the comparison with theoretical models gives us information on the physical condition of the emitting gas. These results, while interesting on their own, demonstrate how further investigations of protoplanetary disks with JWST will dramatically enhance our understanding of these complex astronomical environments.

Modeling the CO isotopologs emission of the T Tauri stars in the Taurus region

This Chapter is based on a paper in preparation, which will be submitted to *Astronomy & Astrophysics (A&A)* under the supervision of Prof. Thomas Henning. The paper will be submitted after including a discussion section of the scientific results and receiving comments from the co-authors. Prof. Thomas Henning supported me in defining the scientific goal of the project and in the analysis of the results. The visibility tables used in this paper have been reduced by Edwige Chapillon, Vincent Piétu, and Laure Bouscasse, and I performed the following steps in the data analysis. The `DiskCheF` package was developed in close collaboration with Grigorii Smirnov-Pinchukov, who was the main developer until he left the project, and I am now the main developer of the package. Dmitry Semenov provided support in the data analysis while providing comments on the model results.

6.1 Motivation

In Section 1.2.1 we introduced the challenges of measuring protoplanetary disk masses. In particular, we discussed how the disk physical properties can be studied through the emission of other molecules, with the help of theoretical models. The most common molecular tracer of the disk mass is the CO molecule, as it is abundant, and emits at cold temperatures ($\sim 10\text{-}50$ K) typical of the disk gas (e.g., Aikawa et al. 2002; Williams & Best 2014; Zhang et al. 2021). In particular, CO isotopologue lines are less saturated and become optically thick deeper in

the disk, tracing the gas deeper into the molecular layer. It is also the primary carrier of carbon and oxygen atoms, crucial to the chemical processes leading to the formation of more complex organic molecules (Walsh et al. 2014).

CO is a chemically stable molecule, with a relatively simple and well-known chemistry. The CO rotational transitions trace the 10-50 K gas in the so-called disk molecular layer (Molyarova et al. 2017), extending above the disk cold midplane where it is removed from the gas phase by freeze-out, until the photo-dissociation region where CO is destroyed by the external or stellar radiation field (Aikawa et al. 2002). Therefore, the temperature of the CO emitting gas cannot be lower than about 20 K, or CO molecules would be removed from the gas phase by freeze-out (Cleeves et al. 2014; Harsono et al. 2015).

However, recent studies questioned the reliability of CO as a gas tracer due to uncertainties in the CO-to-H₂ ratio. The main caveat is the uncertainty in the CO-to-H₂ ratio, as observations suggest a lower ratio than the canonical interstellar medium (ISM) value of $\sim 10^{-4}$ (Aikawa et al. 1997). Recent surveys in the Chamaeleon and Lupus star formation regions found that weak CO emission is common in protoplanetary disks (Ansdell et al. 2016; Long et al. 2017; Miotello et al. 2017), and they found that CO abundance can be depleted up to two orders of magnitude from the canonical ISM value. There are several processes that can affect the CO abundance in the gas phase, making the conversion from CO abundance to H₂ abundance uncertain. For instance, CO molecules can be frozen out in the cold disk midplane, or photodissociated in the upper disk layers by UV photons from the central star or an external radiation field. Chemical processes also affect the CO abundance, as CO is processed into other molecules (e.g., Bruderer et al. 2012; Bruderer 2013; Schwarz et al. 2018). The photodissociation or freeze-out results in lower C/H and O/H abundances, which are important parameters to disk chemistry, further affecting the CO abundance. Constraining the CO depletion factor is a challenging task, as it involves chemistry and dust and gas dynamics, but also optical depth effect since even rare CO isotopologues can be optically thick in the dense inner disk.

Isotopologue-selective processes need also to be considered, such as mutual self-shielding (Visser et al. 2009) or photodissociation. Mass estimates based on CO isotopologues can underestimate the disk mass by up to two orders of magnitude if these processes are not taken into account (Miotello et al. 2022). These processes are accounted for in more recent physical-chemical models (e.g. Miotello et al. 2014, 2016; Ruaud et al. 2022). Recent studies, moreover, compared Class I and Class II disks and found that CO gas abundances decrease rapidly in older disks. In short, to use CO emission as a proxy of the disk mass we need to deploy physical-chemical models.

In this work, we model the emission of rare CO isotopologues observed in Class II T Tauri disks in the Taurus region as part of the MPG-IRAM large guaranteed time project PRODIGE (PROtostars to DISks: Global Evolution). Previous works on these data are the studies on the Class 0/I protostars in the Perseus region (Hsieh et al. 2022; Valdivia-Mena et al. 2022). An overview of the observations of the Class II sources and a first analysis of the CO structure can be found in (Semenov et al. (*accepted*)). We introduce our analysis package developed to analyze these data `DiskCheF`¹ (Disk Chemical Fitter), a simulation tool going from the creation of a disk physical-chemical model to the fit of interferometric data.

6.2 Observations

The data consists of 6 Class II sources in the Taurus region. These are isolated T Tauri stars ($M_{star} < 1 M_{\odot}$) with ages between 1 Myr and 4 Myr and without strong foreground extinction ($A_V < 3$ mag). The disks around these stars are extended (larger than 1 arcsec) and do not show evidence of strong substructure in ALMA continuum observations (Long et al. 2018, 2019). From the Semenov et al. (*accepted*) sources we removed DG Tau. This disk shows evidence of a jet and an outflow and could be part of a wide binary system, and would require a dedicated model to reproduce the data. We also exclude from our analysis UZ Tau E, which is part of a binary system and shows a large-scale structure, probably caused by the gravitational interaction with its companion UZ Tau W. In this work, we focus on the CO isotopologue emission lines detected by the survey: CO, ^{13}CO , and C^{18}O $J = 2 - 1$ transitions with a spectral resolution of 250 kHz and spatial resolution of 0.8 – 1 arcsec. A preliminary analysis of the CO isotopologue (2-1) emission map can be found in Semenov et al. (*accepted*). They find that a foreground cloud partially obscures the CO (2-1) emission in the 4.5-6 km/s velocity range, with the exception of DM Tau, DN Tau, and IQ Tau. The CO (2-1) peak brightness temperature ranges between 6.5 – 16.0 K, 1.2 – 7.5 K for ^{13}CO (2-1), and 0.2 – 1.8 K for C^{18}O (2-1). The moderate spatial resolution (100 – 150 au) makes for smooth radial profiles, with no evidence of substructures. The sources have systematic velocities between 5.5 – 7.4 km/s, typical for sources in the Taurus region. In our analysis, we exclude the UZ Tau E disk from the Semenov et al. (*submitted*) sample. This source is a circumstellar disk around a spectroscopic binary system accompanied by the close binary system UZ Tau W, and such a complex system requires a dedicated study. In Figure 6.2 we show the

¹<https://gitlab.com/SmirnGreg/diskchef/>

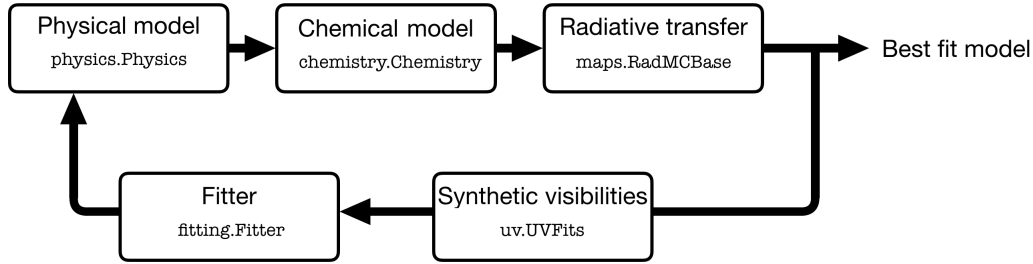


Figure 6.1: An outline of the steps in a DiskCheF model. For each step, we indicate which template can be used to create a new custom model.

Table 6.1: Stellar and disk properties, adapted from Semenov et al. (*accepted*), where further details on the sources can be found.

Source	dist. (pc)	M_{\star} (M_{\odot})	T_{eff} (K)	$\log L_{\star}$ ($\log L_{\odot}$)	PA (deg)	incl. (deg)	R_{out} au
CI Tau	159	1.0	4277	-0.09	282	47.3	518
CY Tau	129	0.5	3560	-0.61	64.5	27.1	251
DL Tau	159	1.1	4277	-0.19	320.3	42	621
DM Tau	145	0.5	3720	-0.82	65.9	-34.8	781
DN Tau	128	0.7	3806	-0.16	171.3	35.1	287
IQ Tau	131	0.6	3690	-0.67	311.6	60.6	212

moment zero emission map of our selected sources.

A similar study of CO isotopologue emission lines was performed by the MAPS collaborations (Öberg et al. 2021, and following papers) with a different science goal than the one presented in this work. While MAPS sources are both T Tauri and Herbig Ae stars from different star-forming regions, the disks in the PRODIGE survey have similar physical properties and are all located in the Taurus star formation region. Moreover, this region has a declination between $+15^{\circ}$ and $+31^{\circ}$, which is more easily observed by NOEMA. Since our disks share similar properties and are in the same star formation region, our goal is to present a general model that can be applied to all the disks in our sample. This allows us to better understand the similarities and differences within this class of disks, and how the small differences in their structure affect physical and chemical processes. In Table 6.1 we see the stellar properties and disk geometry by Semenov et al. (*accepted*).

6.3 Disk model

To model the disk structure and chemistry we developed the `DiskCheF` framework, of which this work is the first application. This is a simulation tool developed to analyze molecular line data, which can be applied to fit any interferometric data, and as a standalone disk forward modeling tool. The code philosophy is to establish a series of customizable building blocks, as each code block can be modified without affecting the functionality of other steps. The final disk model can be built by choosing any combination of the disk physical, chemical, and radiative transfer models. The preset models can be easily subclassed to add custom functionalities when needed. The `*Base` objects described below are templates showing the information needed by each step of a `DiskCheF` model (physical model, chemical model, radiative transfer model, and fitter). These objects cannot be directly used to create a disk model, and the user has to either use them as a template for the desired theoretical disk model or choose from the default models.

The starting point of `DiskCheF` is to create a disk physical model (`physics.PhysicsBase`), with information about the gas and dust density and temperature distribution. This model can then be used as input for the chemistry model (`chemistry.ChemistryBase`), which computes the abundance of the chemical species from the information on the disk's physical structure. `DiskCheF` also provides the tool `maps.RadMCBase` to convert `DiskCheF` models to `RADMC3D` models (Dullemond et al. 2012b), a code for radiative transfer calculations. `RADMC3D` can then be used to produce disk maps of line (`maps.RadMCRT`) and dust emission (`maps.RadMCRTImage`) or to calculate the disk temperature (`maps.RadMCTherm`). The workflow of `DiskCheF` modeling is shown in Figure 6.1 and in the next sections, we describe the models implemented within the `DiskCheF` framework to fit the PRODIGE data.

6.3.1 Physical model

To model the disk gas physical and thermal structure we adopt the Lynden-Bell & Pringle (1974) prescription. This model is implemented in `physics.WB100auWithSmoothInnerGap`. The radial surface density distribution of the gas is given by the Lynden-Bell & Pringle self-similar profile with a smooth inner gap:

$$\Sigma(r) = \Sigma_0 \left(\frac{r}{r_c}\right)^{-\gamma} \exp\left[-\left(\frac{r}{r_c}\right)^{2-\gamma}\right] \exp\left[-\left(\frac{r}{r_{in}}\right)^{\gamma-2}\right], \quad (6.1)$$

with:

$$\Sigma_0 = (2 - \gamma) \frac{M_{disk}}{2\pi r_c^2} \exp\left(\frac{r_{in}}{r_c}\right)^{2-\gamma}, \quad (6.2)$$

where γ is the tapering factor, r_c the tapering radius, r_{in} the inner disk radius, and M_{disk} the total disk mass. The vertical profile is given by integrating the vertical hydrostatic equilibrium equation:

$$\frac{\partial \ln \rho}{\partial z} = - \left[\left(\frac{G M_{star} z}{(r^2 + z^2)^{3/2}} \right) \left(\frac{\mu m_H}{kT} \right) + \frac{\partial \ln T}{\partial z} \right] \quad (6.3)$$

The midplane/atmosphere temperature is given by radial power law distribution:

$$T_{mid/atm} = T_{mid/atm,100} \left(\frac{r}{100 \text{ au}} \right)^{-q} \quad (6.4)$$

with $T_{mid/atm,100}$ the temperature at 100 au and q the exponent of the distribution. The value of the temperature exponent has been measured from CO data for disks in the Taurus region, and it is usually assumed that $q = 0.55$ (Williams & Best 2014) provides a good representation of the temperature distribution. The transition between the atmosphere and midplane temperature is parameterized with a sine function:

$$T_{WB}(r, z) = \begin{cases} T_{mid} + (T_{atm} - T_{mid}) \left[\sin\left(\frac{\pi z}{2z_q}\right) \right]^{2\delta} & \text{if } z < z_q, \\ T_{atm} & \text{if } z \geq z_q \end{cases} \quad (6.5)$$

where δ describes the steepness of the profile and z_q is the height over the disk atmosphere where the disk reaches the atmospheric temperature. Williams & Best (2014) explored the impact of these parameters and found that these parameters do not significantly affect the line luminosity. In the literature it is usually assumed $\delta = 2$ and $z_q = 4 H_p$, where H_p is the pressure scale height:

$$H_p = \sqrt{\frac{\kappa T_{mid} r^3}{G M_{star} \mu m_H}}, \quad (6.6)$$

where κ is the Boltzmann constant, G the gravitational constant, $\mu = 2.3$ the mean molecular weight of the gas, and m_H the mass of atomic hydrogen. Moreover, the typical interstellar radiation field in star-forming regions prevents the disk to reach unrealistically low temperatures. Following the prescription in Tazzari et al. (2021), we set a threshold $T_{floor} = 7$ K, and we use an effective temperature:

$$T^4 = T_{WB}^4 + T_{floor}^4. \quad (6.7)$$

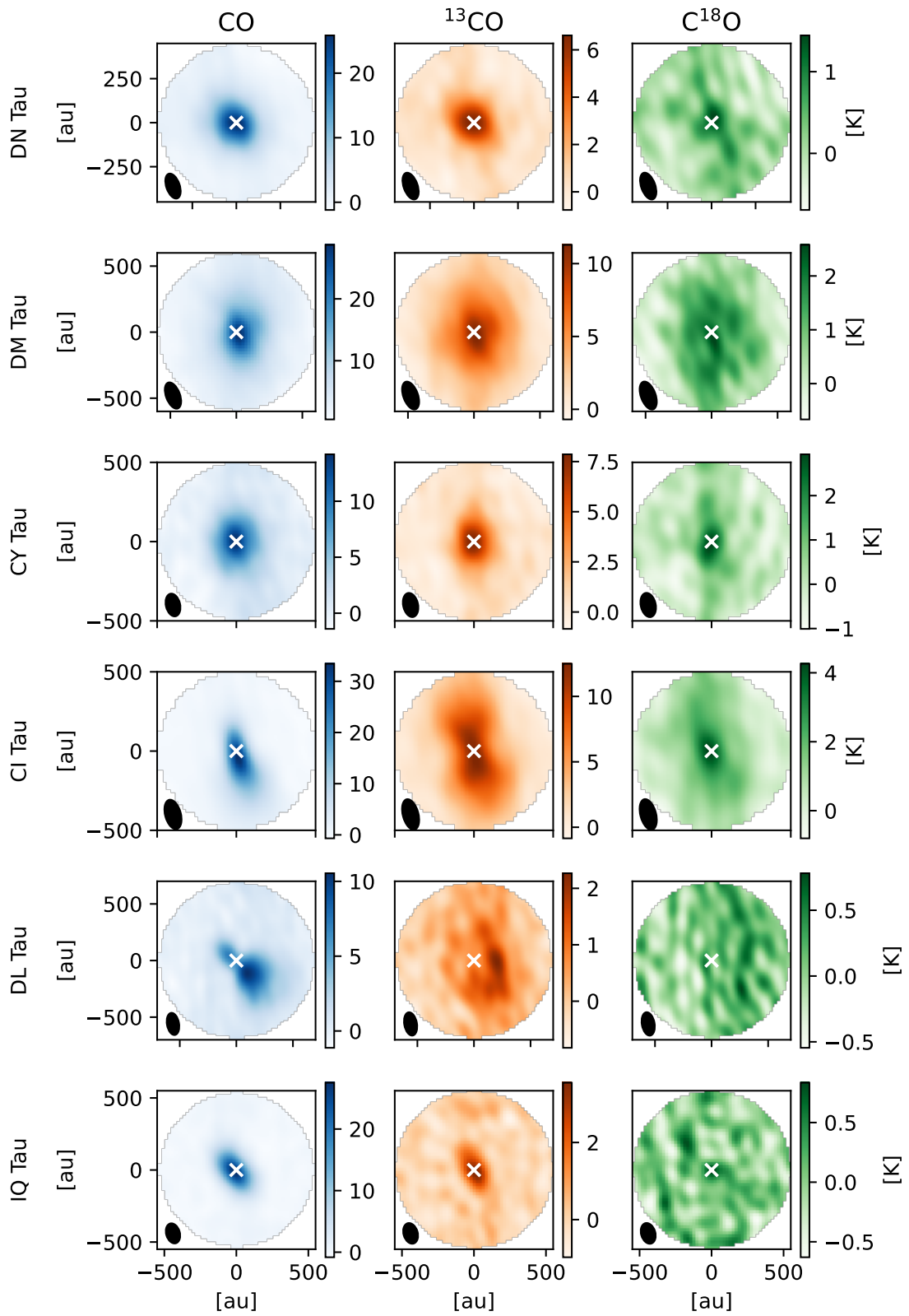


Figure 6.2: Moment zero map of the CO, ^{13}CO and C^{18}O emission for our disk sample.

6.3.2 Chemical model

The main goal of `DiskCheF` is to fit disk models to interferometric data. When the data are gas emission lines, we need a chemical model fast enough to be part of a fitting routine. A typical simplified network for the chemical evolution of a protoplanetary disk runs for a few seconds on a single CPU. However, we discussed in Section 6.1 how not accounting for all processes affecting CO isotopologue abundances, such as self-shielding or photodissociation, can underestimate the disk mass by one or two orders of magnitudes. Therefore, to study the PRODIGE CO isotopologues line emission we need a more robust chemical network. The computational time for such networks ranges from tens of minutes to days. Since our fitting routine computes in the order of 10^5 disk models to converge to a best-fit model, it adds up to unfeasible computational times.

One solution is to apply machine learning techniques to the results of chemical networks. These techniques find the correlation between the input and the output of the networks and the smallest set of disk parameters needed to predict chemical abundances without running the network for each disk model. Our chemical predictions are based on the results of the ANDES astrochemical model of a 2D axisymmetric disk (Semenov & Wiebe 2011), based on the ALCHEMIC chemical network (Semenov et al. 2010). This analysis was performed using the Python machine learning library `Scikit-learn` (Pedregosa et al. 2011). The full derivation of the correlation between the disk physical parameters and the ANDES CO isotopologue abundances is described in detail in Smirnov-Pinchukov et al. (2022).

The network describes 650 species and 7000 reactions including gas-phase and surface two-body reactions, adsorption and desorption, photoreactions and ionization/dissociation by X-ray, cosmic rays, radioactive nuclides, and reactive desorption. Following Eistrup et al. (2016), we adopt an icy molecular initial composition based on the abundances of ices in prestellar cores (Öberg et al. 2011). We run the time dependent chemical evolution till the age of 1 Myr. The disk physical structure is set through stellar mass M_\star , disk mass M_{disk} , and disk tapering radius r_c . These parameters define the distribution of density, temperature, and radiation field. The stellar mass also governs the stellar temperature and luminosity, which are calculated for the age of 1 Myr using the evolutionary model by Yorke & Bodenheimer (2008). The ionizing radiation field is computed using the Bruderer et al. (2009) X-ray prescription and the Padovani et al. (2018) cosmic ray prescription. We create a population of synthetic disks with different M_\star , M_{disk} , r_c and stellar X-ray luminosity L_X to cover a wide range of physical conditions typical for protoplanetary disks. Relying on the observational constraints on disk structure, these parameters are varied: $M_\star = [0.3, 2.5] M_\odot$, $M_{disk} = [0.1, 10] \times M_\star$,

$r_c = [20, 100]$ au, $L_X = [10^{29}, 10^{31}]$ erg/s. These parameters are used to compute 75 synthetic disks, with each disk composed of 4 000 physical bins. This amount to 300 000 data points, which took about 1 year of single CPU run time.

The main result of the machine learning analysis of the chemical network results is that CO abundances are mainly determined by the density and temperature of the gas. Further parameters, such as the ionizing and UV radiation, increase the quality of the predictions, but are a minor correction to the abundances predicted by gas density and temperature alone. While the penetrating UV radiation does play a role in the chemical evolution, we found that the effect of the local UV field is correlated to the effect of the gas density and temperature. For instance, the UV radiation is stronger in the atmosphere, that is where the gas density is lower and its temperature higher, and gas density and temperature correctly predict the effect of UV radiation as well. In the `DiskCheF` framework, we use the same prescription for the X-ray and cosmic ray radiation, part of the `physics.PhysicsBase` object, and the CO abundances are predicted from the gas density, gas temperature, and ionizing radiation by the `chemistry.SciKitChemistry` object.

6.3.3 Fitting to the observations

Once we have a physical and chemical disk model, we use RADMC3D to calculate the line radiative transfer of the CO isotopologues and produce channel maps of these lines with the same spatial and spectral resolution of the PRODIGE data. However, an interferometer like NOEMA does not produce an image of the source emission but it measures its visibilities, the complex values of its Fourier transform. There are two ways to compare the model channel maps to the data, either by working in the image plane by converting the observed visibilities to an image or to compute the synthetic visibilities of the model by knowing the antenna configuration of the interferometer. While more intuitive, working on the image plane requires several assumptions on the source, and there is no unique way to derive an image from visibility data. This effect is more severe with fewer samples of the source visibilities. While NOEMA has a great spectral resolution ideal for deep molecular line surveys, it is more limited in the visibility sampling. The second approach is to directly operate in the visibility plane, which represents the real instrument data, by knowing the spectral resolution, sensitivity, and antenna configuration. This provides a more robust comparison to the data, but if used in a fitting algorithm requires the computation of synthetic visibilities at each likelihood evaluation. To this purpose, we use the `GALARIO` computational library (Tazzari et al. 2018), a computationally efficient tool for the generation of synthetic visibilities. In `DiskCheF`, the object `uv.UVfits` can be used to read, analyze, and

visualize visibility data, including computing the χ^2 of visibility data to a channel map using `GALARIO` routines (`uv.UVfits.chi2_with()`).

With this likelihood evaluation, we can now fit the model to the observations. We adopted the nested sampling Monte Carlo algorithm `MLFriends` (Buchner 2016, 2019) using the `UltraNest`² package (Buchner 2021). This package provides computationally efficient and optimized for MPI-cluster tools to find and analyze the posterior probability distribution of the model parameters. This allows us to find more reliable results compared to traditional Markov chain Monte Carlo methods with a reasonable request of computational resources. To fit the `PRODIGE` data, we deployed 2560 logical CPUs, corresponding to about 5×10^5 likelihood evaluations within 24 hours of computational time. The disk model has 5 free parameters: the total disk mass M_{disk} and the tapering radius r_c from Eq.6.1, the midplane and atmosphere temperature $T_{mid/atm,100}$, and the coefficient q from Eq.6.4. The disk model is less dependent on the other parameters appearing in Section 6.3, and we keep them fixed to the values given in Semenov et al. (*accepted*). A list of figures with the model-data comparison and the residuals of the best-fit models can be found in Appendix A.

6.4 Results

The mass distribution is the most important result of our analysis for planet formation studies. The mass can be traced only by optically thin emission, and while CO is mostly optically thick and can only provide information on the gas temperature at its emission surface, the more optically thin isotopologues ^{13}CO and C^{18}O can be used to constrain the disk mass. To analyze the result of our study, we focus on the best-fit model for the DM Tau disk. The data quality of this disk is the highest in our sample since it is the largest and brightest one, and we can use this disk to benchmark our model. In Figure 6.3 we show the best-fit physical and chemical model for DM Tau. The figure shows how the chemical model correctly predicts the CO freeze-out from the gas phase at low temperatures.

Gas-based mass estimates can be poorly constrained due to uncertainties in the gas thermal structure. However, our approach of fitting at the same time optically thin and optically thick CO isotopologue emission allows us to constrain both the disk mass and temperature distribution, leading to more reliable mass estimates. Law et al. (2021) found that the temperature profiles of the disks in the MAPS sample follow the power law in Eq.6.4 outside of the 100-150 au radius, but they

²<https://johannesbuchner.github.io/UltraNest/>

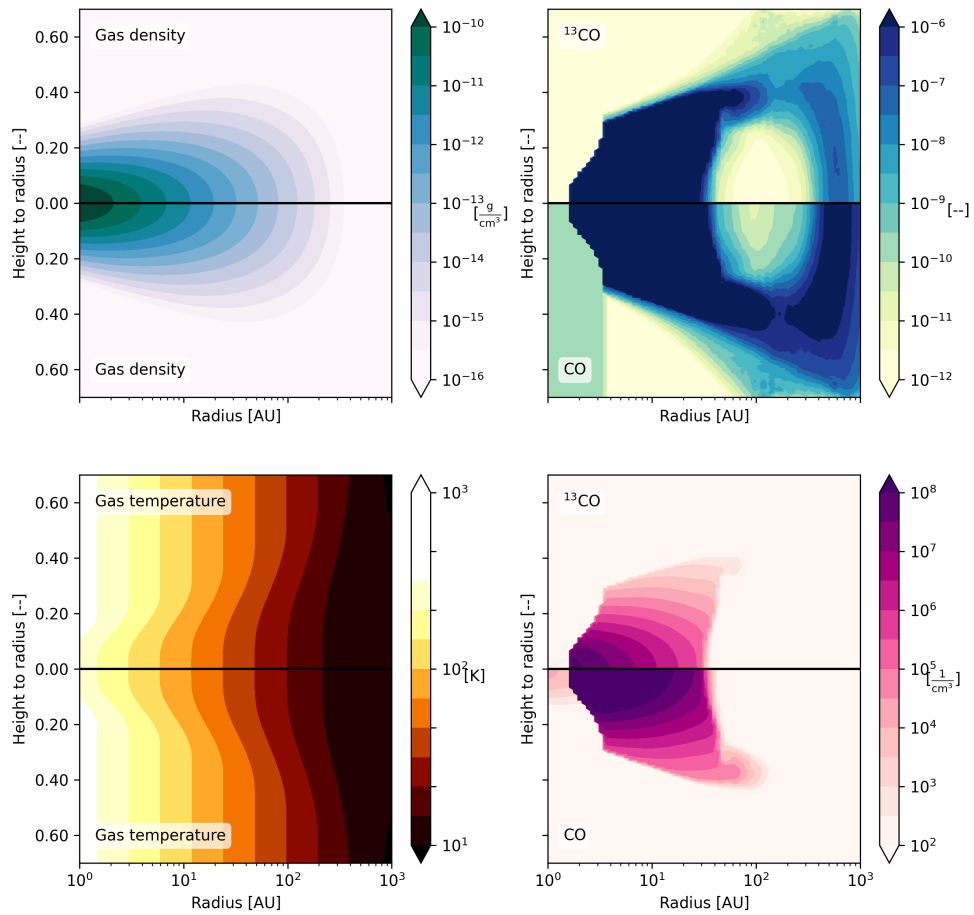


Figure 6.3: Best-fit physical and chemical model for DM Tau: (top left) gas volume density distribution, (top right) CO isotopologues number density ratio compared to H_2 , (bottom left) gas temperature distribution, (bottom right) CO isotopologues volume density distribution.

Table 6.2: Best fit of the disk physical parameters.

Source	r_c [au]	$\log_{10}(M_{disk}/M_{\odot})$	$T_{atm,100}$ [K]	$T_{mid,100}$ [K]
CI Tau	150	-1.8	35	32
CY Tau	40	-1.7	22	18
DL Tau	125	-1.6	24	20
DM Tau	200	-1.0	31	21
DN Tau	40	-1.7	27	20
IQ Tau	50	-2.3	27	19

have a flatter profile in the inner disk. Two power law profiles would provide a better fit for the data. However, the spatial resolution in our sample is about the size of the inner disk, and we cannot properly constrain the temperature profile in this region. Therefore, we assume a single power law distribution for the whole disk structure. We show the effect of this assumption on the DM Tau disk. In Figure 6.4 we show the model-data comparison, while in Figure 6.5. The residuals are higher in the inner disk, where the model underestimates the gas brightness temperature by about 2 K in the inner disk, where its emission becomes optically thick and becomes more dependent on the gas temperature. However, the mass distribution is not affected by this assumption, since it is more strongly constrained by the outer disk emission, and we still get a reliable mass estimate.

The CO (2-1) brightness of the output images is strongly affected by the disk temperature profile, and only marginally by the disk mass. Changes in the disk mass do however affect the CO (2-1) image shape at different velocity channels since the mass distribution affects the Keplerian velocity profile of the gas. The ^{13}CO (2-1) images, on the other hand, are sensitive to both the temperature and the mass distribution, as we would expect from optically thin emission. Therefore, they provide a mass estimate thanks to the temperature estimated from the CO (2-1) emission. The C^{18}O (2-1) images follow the same trend as the ^{13}CO images, but being much fainter this molecule is not always detected, and it mostly provides an upper limit to the disk mass.

Another parameter affecting the fit results is the depletion of CO from the gas. Our predictions are based on the results of the ALCHEMIC chemical network, which does not include all CO depletion mechanisms and isotopologue-selective processes, such as mutual self-shielding and isotopologue-selective photodissociation (Visser et al. 2009). This can lead to an underestimation of the disk masses, and our estimates are a lower limit (Miotello et al. 2014, 2016). This is a characteristic of machine learning methods, as the model results inherit the same drawbacks as the chemical network used to produce the data. However, machine learning-

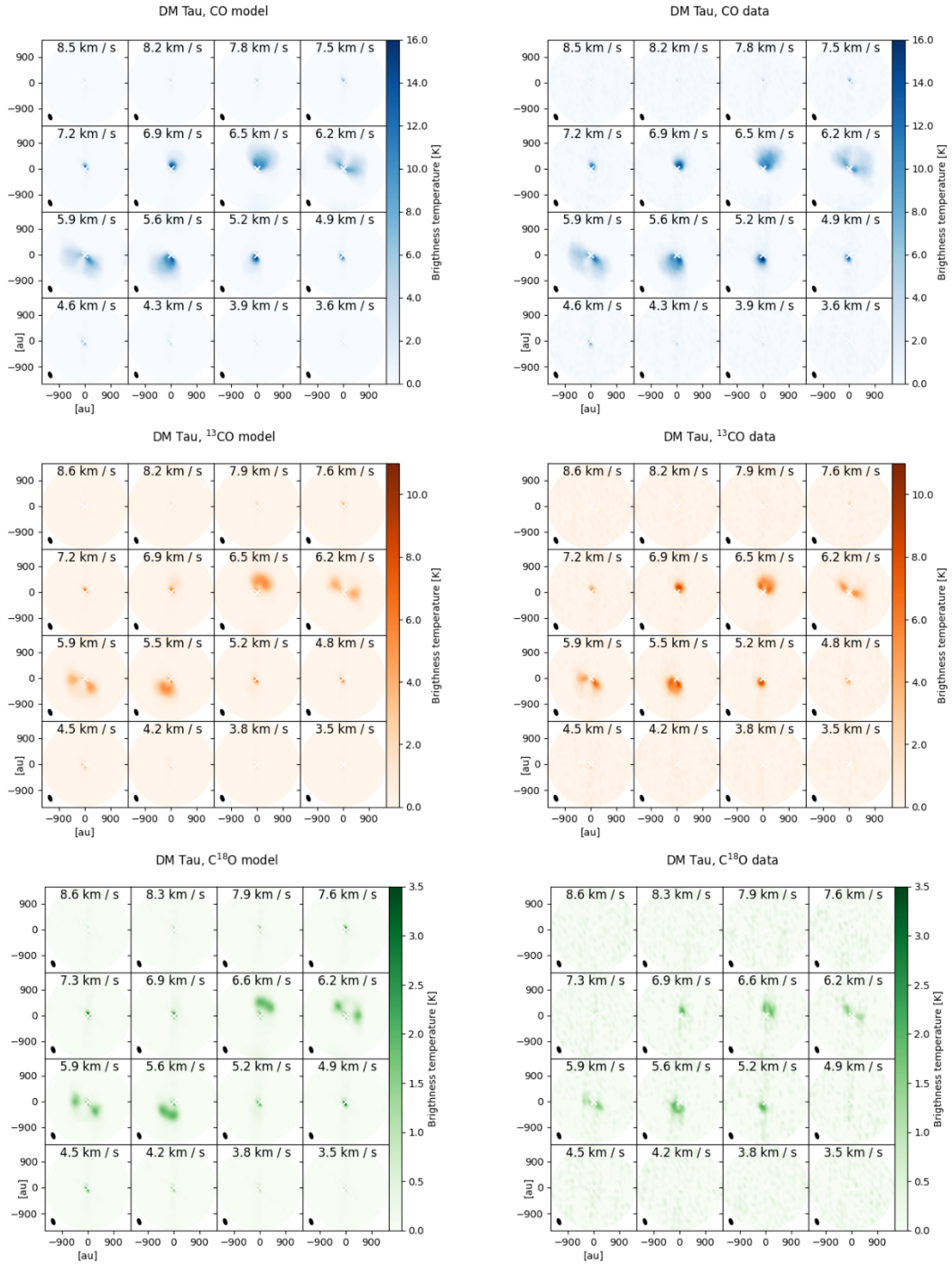


Figure 6.4: Comparison between the best-fit model and the observation of DM Tau for the CO, ^{13}CO and C^{18}O isotopologue emission.

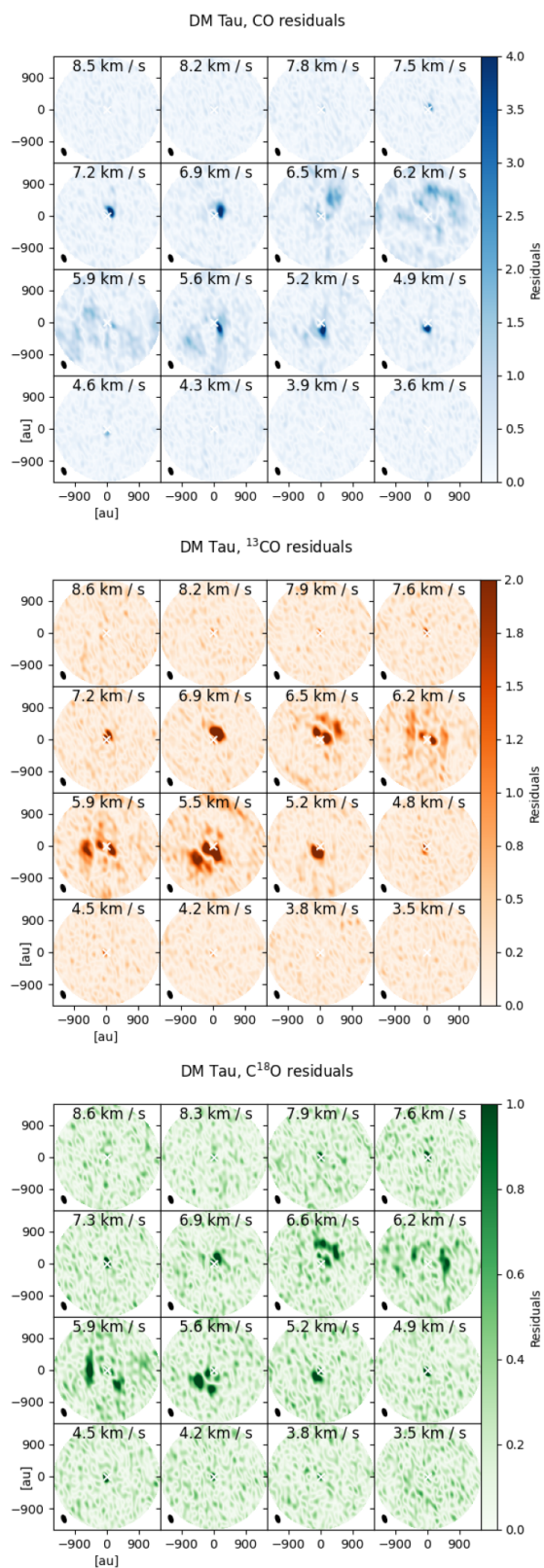


Figure 6.5: Residuals of DM Tau best-fit model for the CO, ¹³CO and C¹⁸O isotopologue emission.

accelerated chemistry makes it possible to include chemical networks in a fitting algorithm instead of a parametrized chemical model. The main result, therefore, is the application of machine learning methods to fit the disk chemical structure, as the quality of the results depends on the development of more accurate chemical networks, which can be easily implemented within the DiskCheF framework.

We expect the CO (2-1) emission to be optically thick and in thermodynamical equilibrium with the gas at the typical disk densities and temperatures. Indeed the best-fit model brightness temperature of the CO (2-1) molecule reproduces the best-fit temperature profile, with an average temperature over the beam emitting area ranging from 17.5 K in the brightest disk, DM Tau, to 11.2 K in IQ Tau. On the other hand, the ^{13}CO and C^{18}O emission is optically thin, with a ratio of ^{13}CO -to- C^{18}O emission equal to the isotopologue ratio (about 7.3). However, in the inner disk of the more massive disks, the emission ratio falls below the isotopologue ratio (about 5 in the most massive disk, DM Tau). This is an indication that the ^{13}CO emission becomes partially optically thick in the inner disk as well (smaller than our beam size, about 100 au). The C^{18}O emission remains optically thin, and our mass estimate is not affected by this opacity effect.

6.4.1 Temperature profiles

In our first modeling efforts, we used two additional fitting parameters, the exponent of the midplane and atmospheric temperature distributions $q_{md/atm}$ from Eq.6.4. However, our fitting algorithm found a complete degeneracy between T_{mid} and q_{atm} , and T_{atm} and q_{mid} . The reason is that the observed flux is the result of the integrated emission over the line of sight, and there is no difference in the emission coming from a cold midplane and a warm atmosphere, or a warm midplane and a cold atmosphere in our channel map data. This degeneracy can be solved with high angular-resolution data, which would allow measuring the height of the emitting surface in each velocity channel (Dullemond et al. 2020; Law et al. 2021). In our case, the data do not have enough angular resolution to constrain the vertical temperature profile. Therefore, we follow a common assumption made in the literature for the temperature exponent $q_{md/atm} = 0.55$.

6.4.2 Disk vertical structure

The disk physical model used to fit the data, described in Section 6.3.1, reconstructs the gas vertical distribution assuming hydrostatic equilibrium. However, recent studies have shown how the gas emission layer may differ from the one determined by the hydrostatic equilibrium. Law et al. (2021) found that the flaring indexes of the CO emission surfaces for the disk in the MAPS sample can be larger

than the one coming from hydrostatic equilibrium by a factor of a few. This effect was previously studied in the case of IM Lup, a particularly large and flared disk (Pinte et al. 2018, see also Chapter 4). Similar results have been found for the largest disk in our sample, DM Tau Dartois et al. (2003). The shape of the emitting region of CO isotopologues is determined by the stellar irradiation, rather than the disk scale height, tracing the surface of optical depth $\tau \sim 1$ with respect to the stellar irradiation, and this can affect our temperature estimate. Our best-fit model does effectively reproduce the observational data for all the disks in our survey. However, a more sophisticated physical model may be necessary to study the disk structure in more detail, such as trying to model other molecules or dust emission data.

6.4.3 Foreground cloud absorption

The optically thick CO emission in CI, CY, DG, and DL Tau is partially obscured by a foreground absorption cloud in the $\sim 4 - 6$ km/s channel. Since these disks have an LSR velocity of about 6 km/s, the cloud obscures the gas in the outer disk moving away from us in its Keplerian motions. This leads to the asymmetrical patterns in the moment zero maps shown in Figure 6.2. We exclude these channels from our likelihood estimate to find our best-fit model. By excluding part of the outer disk emission, the best-fit model will be mostly determined by the inner disk emission. As discussed in Section 6.4.2, the inner and outer disk structures can differ, especially in the case of a flared outer disk structure. This is a source of uncertainty on the mass estimate from the optically thin isotopologues for these partially obscured disks, as the temperature in the outer disk is derived from the inner disk structure, and the mass estimate from optically thin CO isotopologues is temperature-dependent.

6.5 Conclusions

The gas mass of a protoplanetary disk is an important but challenging quantity to measure. The CO emission remains the most reliable gas tracer, but CO-based mass estimates rely on the assumed gas temperature distribution and on disk chemistry. A combination of optically thin and optically thick emission lines, however, can solve the degeneracy between the temperature and the abundance of CO isotopologues emission, with the help of chemical models. In this work, we propose a machine learning-based chemical model to predict a disk chemical composition from its physical structure without the need to run a chemical network. This makes it possible to reproduce observations of line emission through

theoretical models using a fitting algorithm, which would otherwise require unreasonable computational resources. We test the applicability of this method using the CO isotopologue emission data from the PRODIGE program on the NOEMA instrument. This data consists of CO, ^{13}CO , and C^{18}O isotopologue emission from 6 Class II protoplanetary disks from the Taurus region. Our findings can be summarized as:

- The combination of optically thin and optically thick CO isotopologue emission can properly constrain the disk's physical structure, and is generally in good agreement with previous results. This approach gives tighter constrain to disk thermal structure and provides a more reliable mass estimate.
- There is evidence that the emission surface of optically thick lines does not trace the gas pressure scale height, especially for a large disk with evidence of a flared structure, such as DM Tau. The vertical gas structure could not be in hydrostatic equilibrium in the outer disk, making it challenging to reproduce the inner and outer disk emission with a single temperature profile. However most of the disk mass is found in the outer disk, and this effect does not significantly affect our mass estimates.
- The cloud absorption obscures the optical thick emission in the channels close to the rest frequency for a few disks in our sample. These channels show the emission coming from the outer regions of the disk and give us information on the temperature structure. For these obscured disks, the temperature structure is constrained only by the inner disk emission, which could have a different profile than the outer disk. In a particularly flared structure, the difference between the inner and outer disk structures adds to the uncertainty of the mass estimate.

Summary and Outlook

7.1 Summary

This thesis used extensive modeling to find new ways to constrain the fundamental properties of protoplanetary disks from observational data. This is motivated by two factors. On one side, the quality of our data is rapidly increasing, requiring better and better models to reproduce the disk properties on the increasing observed resolution. On the other side, the information we receive from our target sources is confined to radiation emanating from a single viewpoint on the source. To deepen our understanding of protoplanetary disks, we need more imaginative techniques to extract new information on the same kind of data. In Chapter 1 we gave an overview of the current state of protoplanetary disk studies, while in Chapter 2 we review the common methods employed to create a disk theoretical model.

In Chapter 3 we explored the viability of using dust line locations at multiple wavelengths as a method to estimate the gas mass of protoplanetary disks. The dust line marks the outer edge where grains of a particular size can be observed and is assumed to be a mass-independent tracer. Our analysis demonstrated that this approach holds true for evolved disks (age $\gtrsim 1$ Myr) and remains accurate even when considering variations in disk properties except for high turbulence levels or extremely low disk masses. We also investigated the effects of substructures within disks on the dust line. When such structures don't act as efficient dust traps, the dust line moves outward while still maintaining its connection to disk mass. However, if these structures effectively trap particles, the dust line becomes disconnected from disk mass.

We included a practical application and estimated the masses of two distinct disks. For TW Hya, characterized by a smooth gas structure, the dust line-based estimation closely aligns with the CO-based mass estimates. On the other

hand, for the AS 209 disk featuring gaps and traps, the dust line method proves unsuitable as a mass estimator due to the influence of particle trapping.

In Chapter 4 we used ALMA observations of the midplane millimeter continuum emission and SPHERE observations of the near-infrared scattered light emission to model the dust structure in the IM Lup protoplanetary disk. The model successfully reproduces both ALMA and SPHERE data, giving a coherent solution for the dust distribution. Most of the dust mass (approximately 99%) is found in millimeter-sized or larger grains, while only a small portion (10^{-4} mass fraction) of micron-sized grains is required to reproduce the SPHERE scattered light emission. With a gas mass of $0.2 M_{\odot}$ inferred from CO emission, the estimated dust mass stands at around $4 \times 10^{-3} M_{\odot}$. The study highlights the impact of the turbulence parameter α_{turb} on the disk flaring in the near-infrared, underscoring its role in determining the vertical distribution of particle sizes and suggesting vertical segregation of dust populations. Additionally, the strong radial gradient in particle size distribution, indicative of a pressure trap, influences the concentration of larger grains on the inner side of the ring.

In Chapter 5 we presented a comprehensive analysis of the JWST-MIRI spectrum of the disk surrounding the low-mass star 2MASS-J16053215-1933159. In these data, we identified numerous atomic and molecular hydrogen lines in the mid-infrared spectrum. The study employs HI recombination lines to deduce the accretion rate of the star and utilizes H₂ emission to derive critical properties of the disk gas. We identified several $\nu = 0 - 0$ H₂ pure rotational transitions, which provide information on the gas temperature and column density due to their optically thin nature. We performed a fit of the line profiles accounting for spectral feature blending and used it to construct a rotational diagram. This diagram estimates the temperature and column density of the emitting gas, yielding a warm H₂ gas mass of $(2.5 \pm 1.3) \times 10^{-5} M_{Jup}$ at $625 \pm 100K$. This represents only a fraction of the total disk mass, constrained to be below $0.2 M_{Jup}$ due to non-detection of millimeter continuum emission.

We then analyzed the HI (7-6) line profile, a marker of mass accretion. Through analysis, it identifies two main Gaussian components due to the contribution of another atomic hydrogen recombination line, the HI (9-7) line. The estimated accretion luminosity is consistent with measurements from H α emission, indicating the potential contribution from both lines in the past calibration of accretion luminosities. Comparing the HI (9-7) to HI (7-6) line ratio with theoretical models, we constrained the density and temperature of the emitting gas. This work highlights the potential of JWST in deepening our understanding of protoplanetary disks and their gas properties.

Finally, in Chapter 6 we proposed a novel approach to the mass estimate of

protoplanetary disks. Although CO emission serves as a reliable tracer, mass estimates rely on assumptions about temperature and chemistry. The paper introduces a new strategy that involves a machine learning-based chemical model, predicting a disk chemical composition based on its physical attributes. This approach enables the modeling of emission line observations through fitting algorithms, without the need of running complex chemical networks. To validate the method, we used CO isotopologue data from the NOEMA instrument, focusing on six Class II protoplanetary disks within the Taurus region. The key findings of this study suggest that combining optically thin and thick CO isotopologue emissions effectively constrains the disk physical structure, leading to more dependable mass estimates. However, in scenarios like DM Tau, with flared structures, the surfaces of optically thick line emissions do not uniformly reflect the gas pressure scale height, impacting modeling for inner and outer disk emissions. Moreover, the presence of cloud absorption introduces complexities, obscuring optically thick emission channels near the rest frequency. Particularly noticeable in disks with flared structures, this phenomenon contributes to uncertainties in mass estimates.

7.2 Outlook

The results of this thesis can be the proof-of-concept and the background work for additional studies. In this section, we briefly discuss some possible further investigations based on the results of this work.

In Chapter 3 we tested the dust line approach by estimating disk masses from the dust line location on a large number of synthetic models. We found that the analytic relation between the dust line location and the disk mass overestimates the real disk mass by almost an order of magnitude. This calibration factor depends on the details of the dust evolution model we use. We plan to further investigate this topic by using already available archival data to recreate the graph presented in Figure 3.9. Not only this would facilitate the calibration of the dust line estimation method using real observational data, but it would also identify any divergence in calibration factors between model-based results and empirical observations. This comparison would provide insights into the degree to which the dust evolution model aligns with real protoplanetary disk physics.

Once this method is calibrated correctly, we could use it to investigate other disk properties. For instance, it could be used to measure the amount of depletion of chemical species from the gas phase, a piece of invaluable information to disk chemical models. As this method does not depend on the dust opacity, the derived dust mass distribution can also be used to calibrate the dust opacity, helping us understand the grain properties.

In Chapter 4 we demonstrated how observing just the small and large grains in the distribution in a protoplanetary disk is enough to constrain the full grain size distribution. However, this is based on the assumption that the grain size distribution is described by a single power-law distribution. However, the shape of the grain size distribution is determined by the grain growth mechanism (Birnstiel et al. 2011), and at different grain sizes and disk locations the dust evolution is dominated by different processes, as we discussed in Section 4.4.3. Using more wavelength we can study the physical processes involved in dust evolution. By the same account, this method could be applied to other disks, to study how different disk geometries affect the dust size distribution.

In Chapter 5 we made use of the quality of the JWST-MIRI spectral data to characterize the gas properties of the disk around the very low-mass star 2MASS-J16053215-1933159. These findings not only showcase the potential of JWST for such investigations but also serve as a proof-of-concept for future observations of similar sources using JWST. Thanks to the MIRI spectral resolution, the study gave a new insight regarding the relationship between mass accretion rate and line luminosity, as previously explored by Rigliaco et al. (2015). Contrary to their initial assumption that the line flux originates from the HI (7-6) transition, the study revealed that the contribution was coming from both the HI (7-6) and HI (11-8) lines. This discrepancy suggests that the Rigliaco et al. (2015) relation was calibrated based on an incorrect premise, prompting the need for further investigations. A new possible study would involve the observation of a more extensive sample of disks at the JWST-MIRI resolution. This study would confirm whether the Rigliaco et al. (2015) relation was indeed established on the HI (7-6) line alone or was influenced by the blending of the HI (7-6) and HI (11-8) lines. This broader observation effort could significantly enhance our comprehension of the connection between mass accretion and the flux of atomic hydrogen recombination lines.

Another planned further investigation involves a comparative analysis between the results obtained for H₂ emission and the findings on hydrocarbon emission within the same dataset, as explored by Tabone et al. (2023). By combining their estimations of hydrocarbon mass with our H₂ mass estimate, we can quantify the relative abundances of these molecular species, which is crucial to understanding the chemical evolution and composition of the disk. A noteworthy aspect involves hydrocarbon grain destruction processes, which could potentially enhance the abundance of elemental carbon. Exploring such scenarios could offer deeper insights into the underlying physical processes in this specific source. Therefore, this investigation would not only unveil the relative abundance of molecular species but also explore the link between chemical reactions, molecular evolution, and physical conditions within the disk.

In Chapter 6, the application of machine learning techniques was showcased, allowing for a model-to-data fitting of molecular emission while incorporating the predictions of chemical networks. This approach was successfully demonstrated by fitting CO emission data from the NOEMA interferometer. A natural follow-up study would involve testing this method on data with higher spatial resolution, such as that obtained from the ALMA instrument. The current analysis precision is limited by the spatial resolution in the data, and an enhanced resolution could serve as a valuable means to validate the accuracy of both the physical and chemical models employed. For instance, the absence of CO depletion or isotopologue-selective photodissociation processes in the chemical model (Miotello et al. 2016) could be addressed with more advanced models, which need to be tested by higher-quality data.

Moreover, the machine-learning algorithm could be trained on other chemical networks better suited to the project's scientific goal. A follow-up is to expand on the capabilities of `DiskCheF` by incorporating additional and more sophisticated physical and chemical models. This expansion aims to include a broader range of chemical species, whose abundance cannot be predicted solely from the gas temperature and density as for CO, boosting the accuracy and comprehensiveness of the analyses conducted.

APPENDIX A

PRODIGE model-data comparison

In this appendix, we show the channel maps for all the disk observed on NOEMA as part of the PRODIGE program, and compare them channel by channel to the best-fit models, as described in Chapter 6. We also include the residuals channel map, the difference between the best-fit model and the observations.

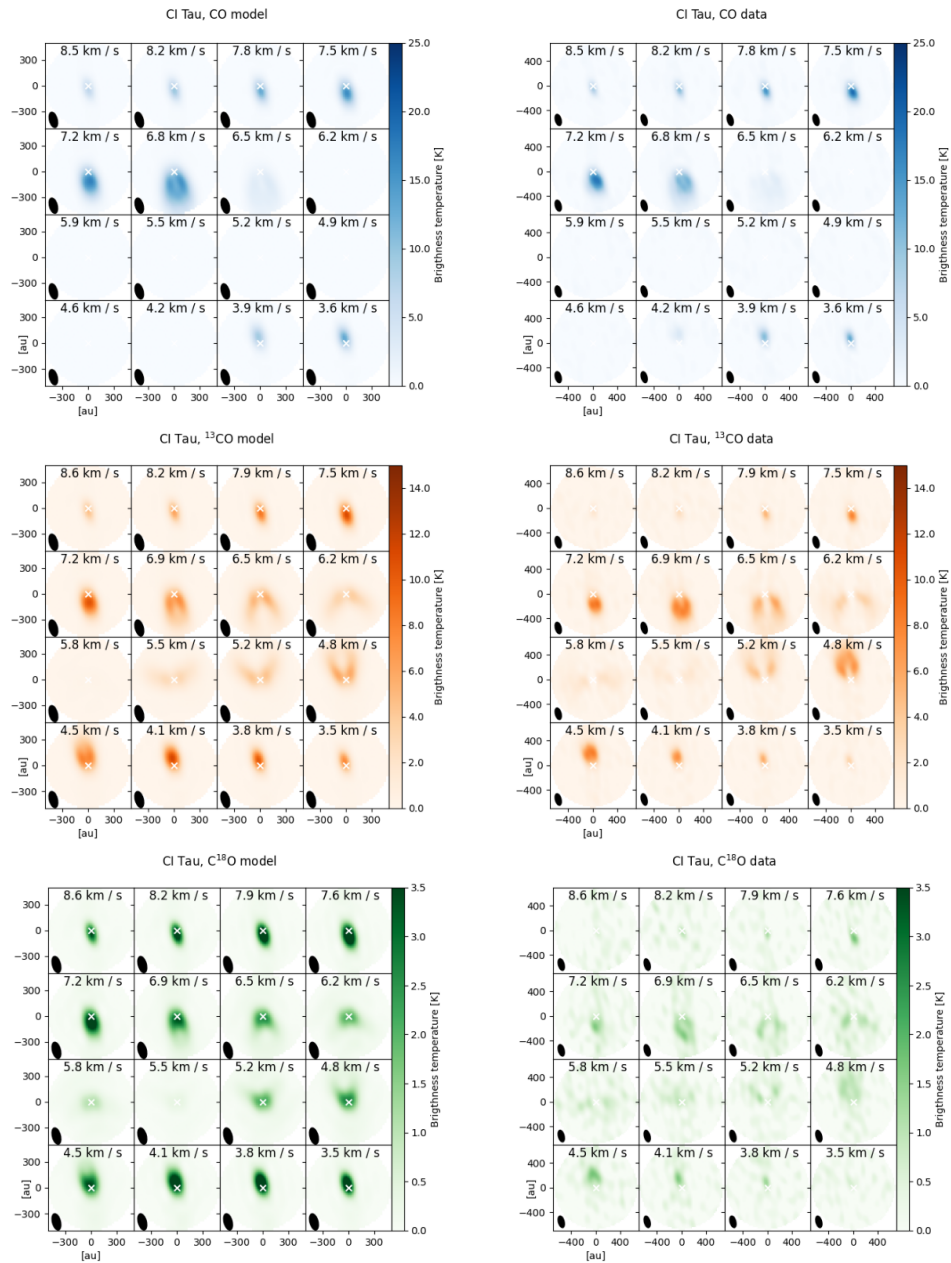


Figure A.1: Comparison between the best-fit model and the observation of CI Tau for the CO, ^{13}CO and C^{18}O isotopologue emission.

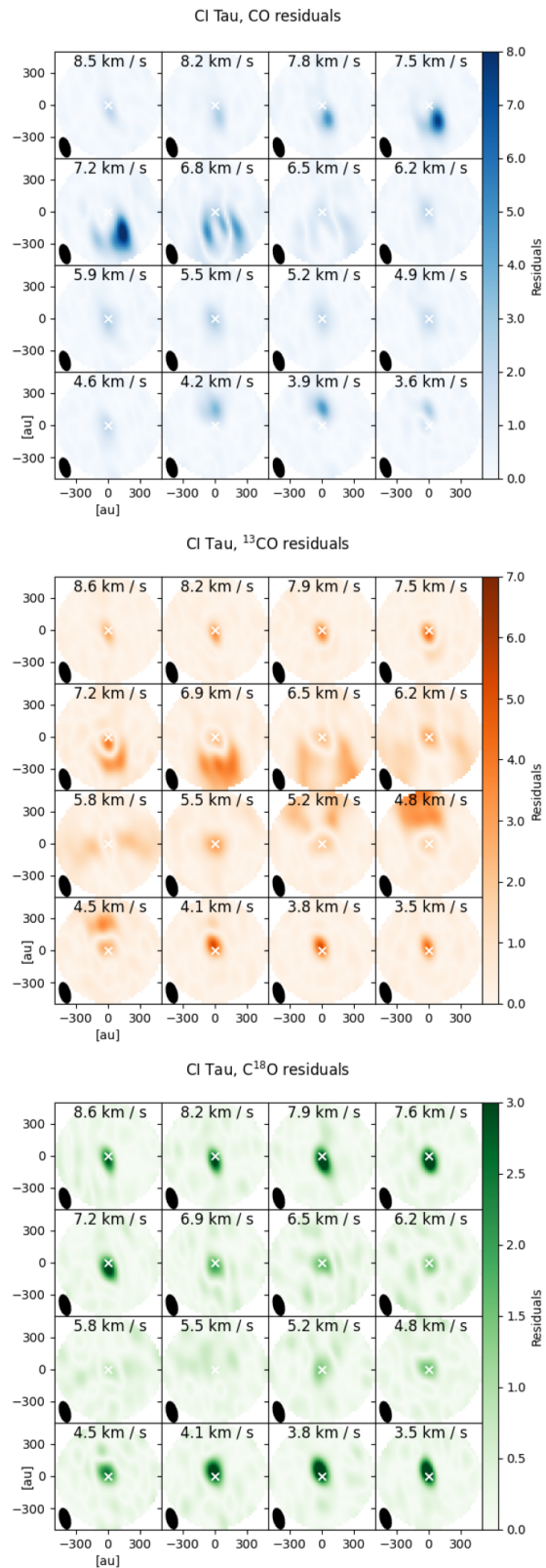


Figure A.2: Residuals of CI Tau best-fit model for the CO, ^{13}CO and C^{18}O isotopologue emission.

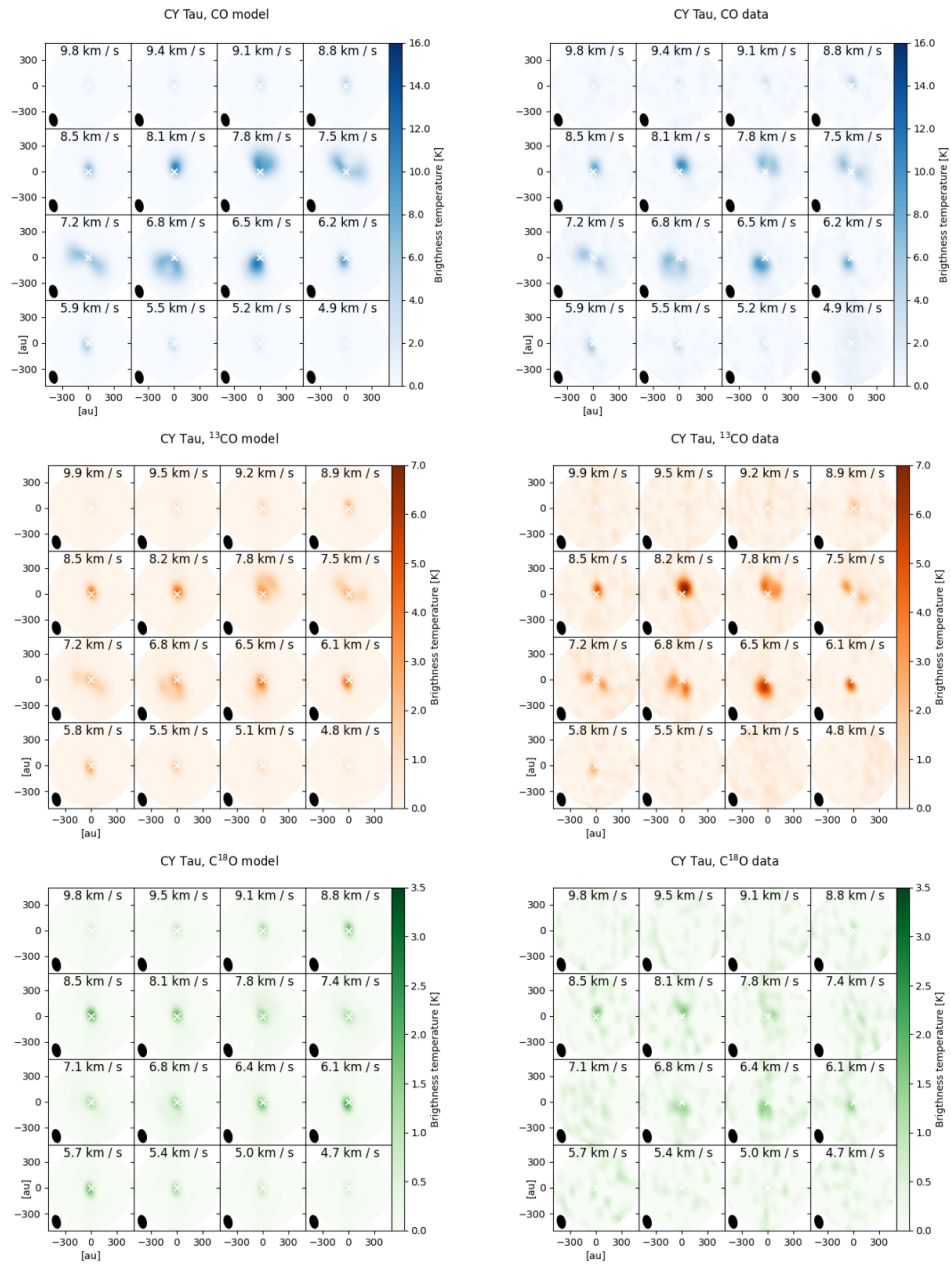


Figure A.3: Comparison between the best-fit model and the observation of CY Tau for the CO, ^{13}CO and C^{18}O isotopologue emission.

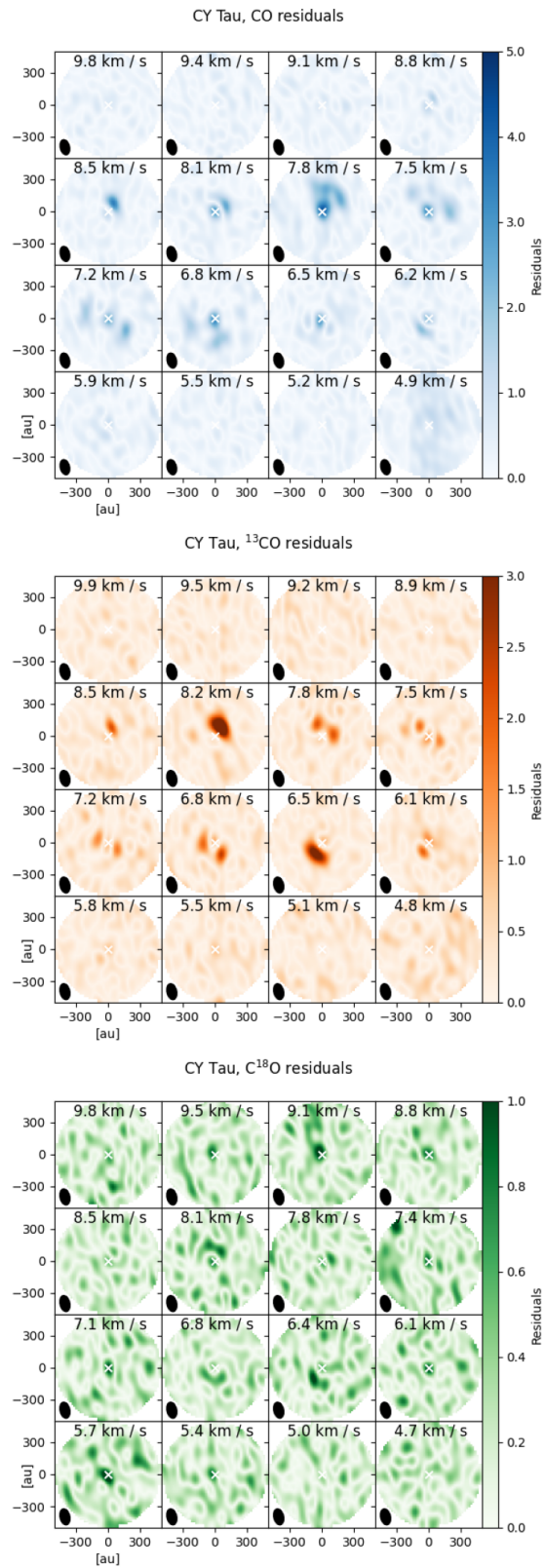


Figure A.4: Residuals of CY Tau best-fit model for the CO, ^{13}CO and C^{18}O isotopologue emission.

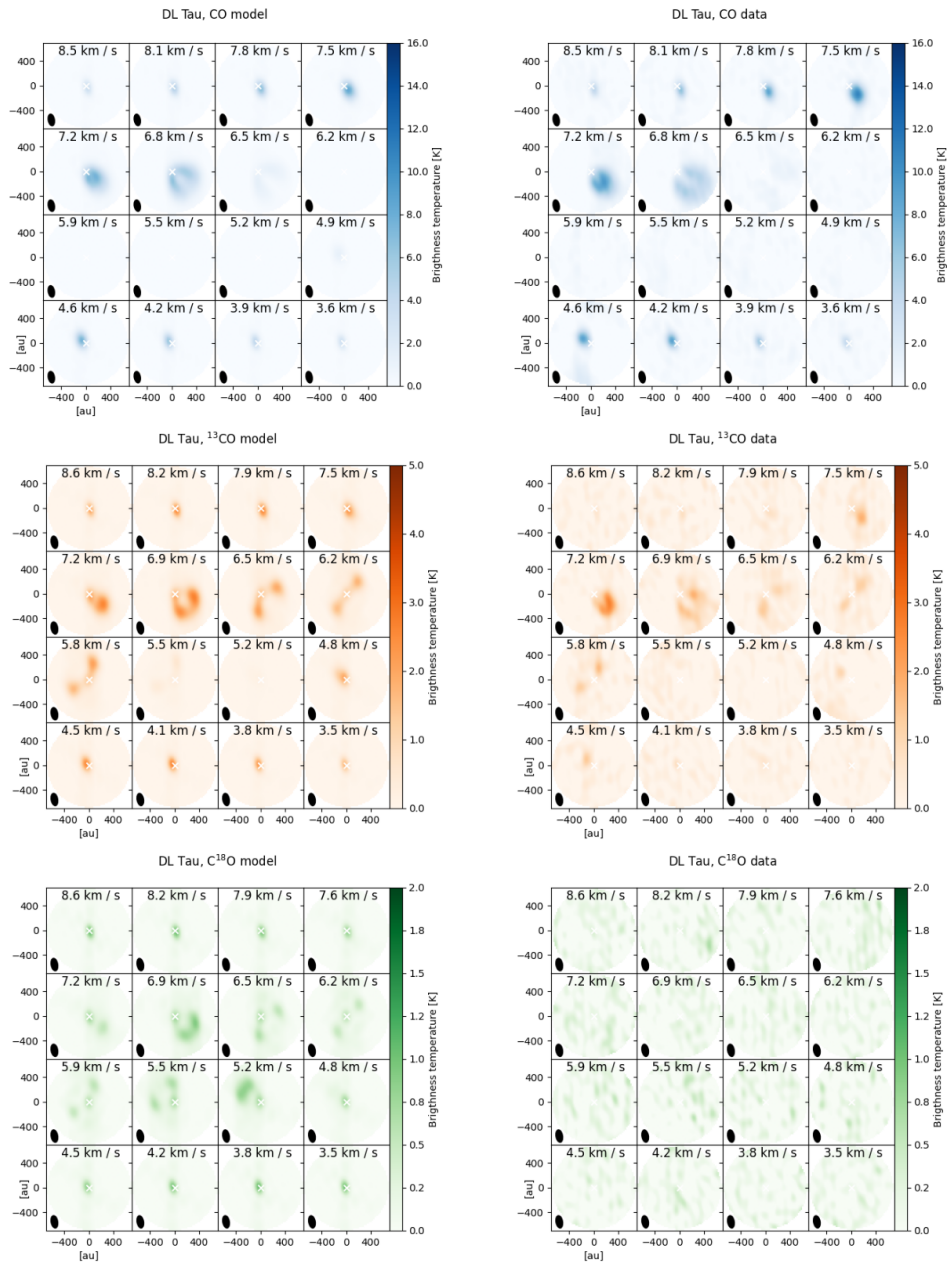


Figure A.5: Comparison between the best-fit model and the observation of DL Tau for the CO, ^{13}CO and C^{18}O isotopologue emission.

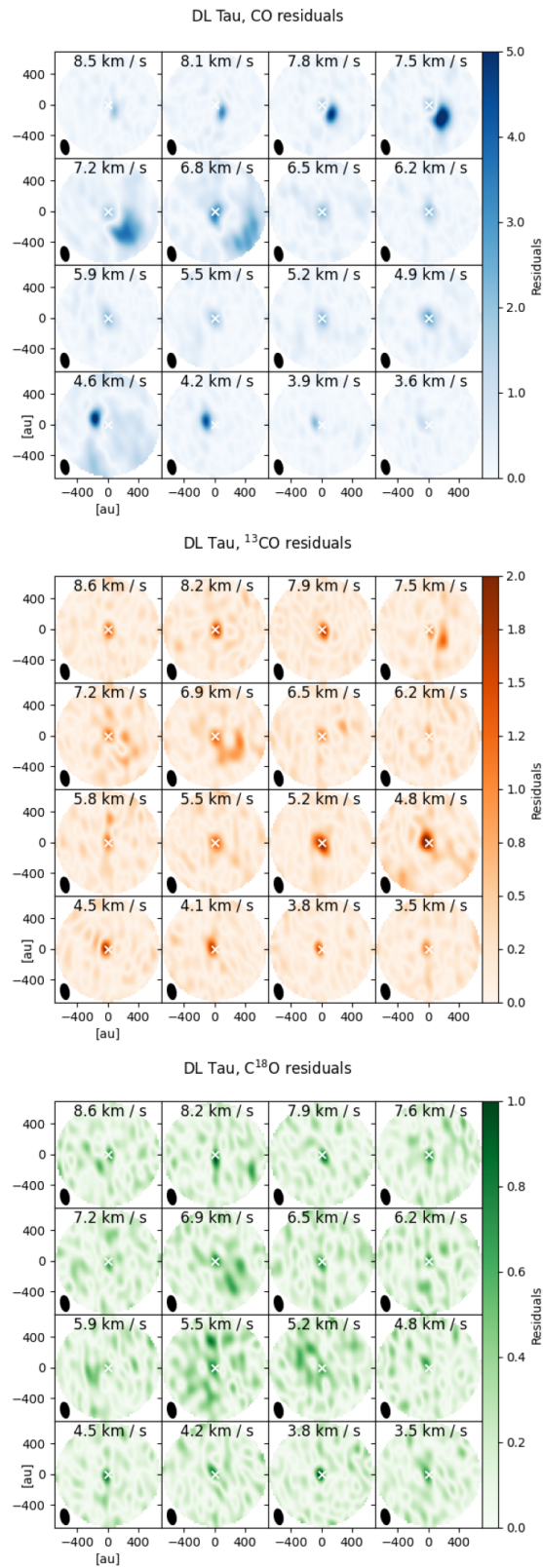


Figure A.6: Residuals of DL Tau best-fit model for the CO, ^{13}CO and C^{18}O isotopologue emission.

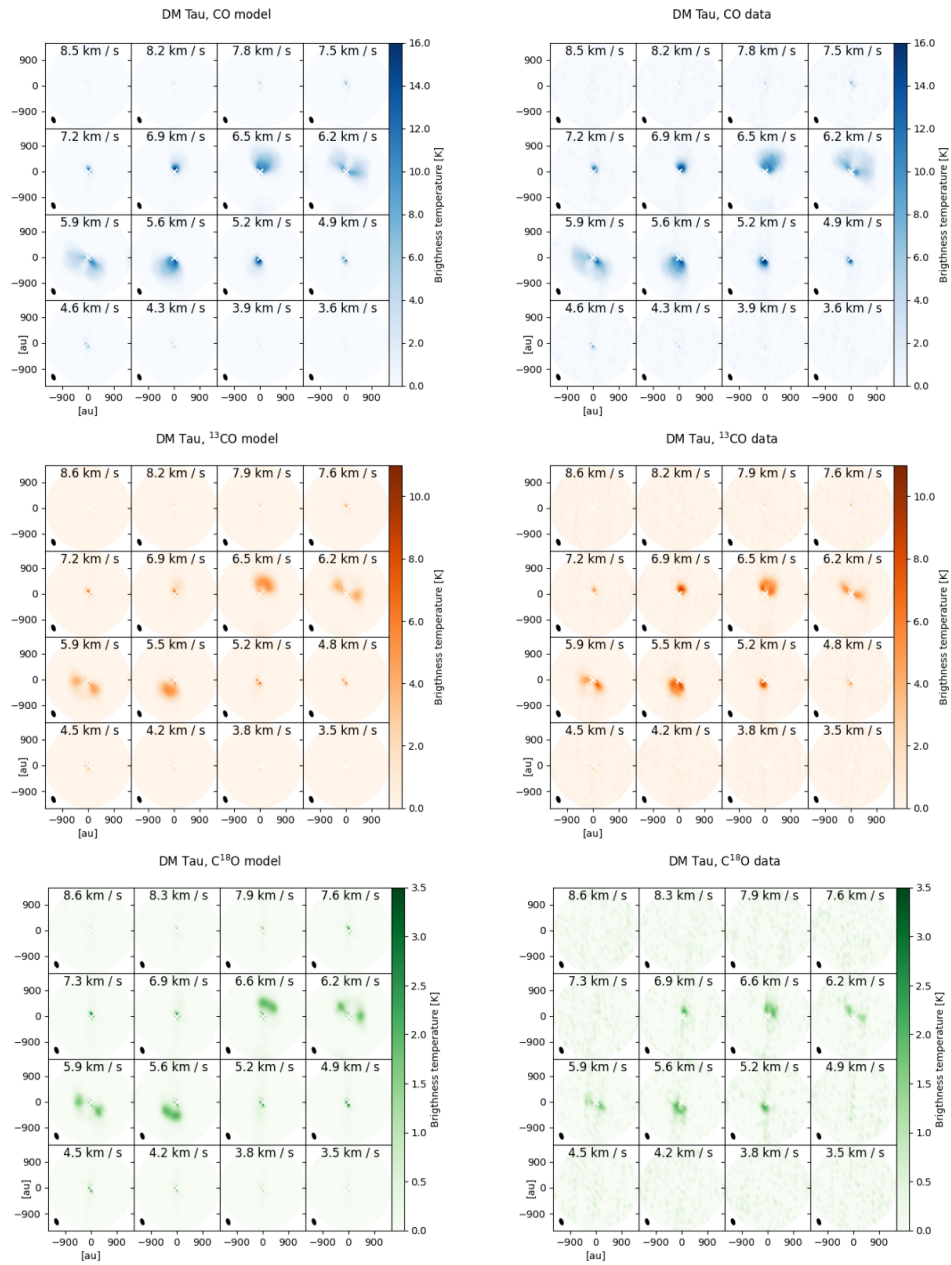


Figure A.7: Comparison between the best-fit model and the observation of DM Tau for the CO, ^{13}CO and C^{18}O isotopologue emission.

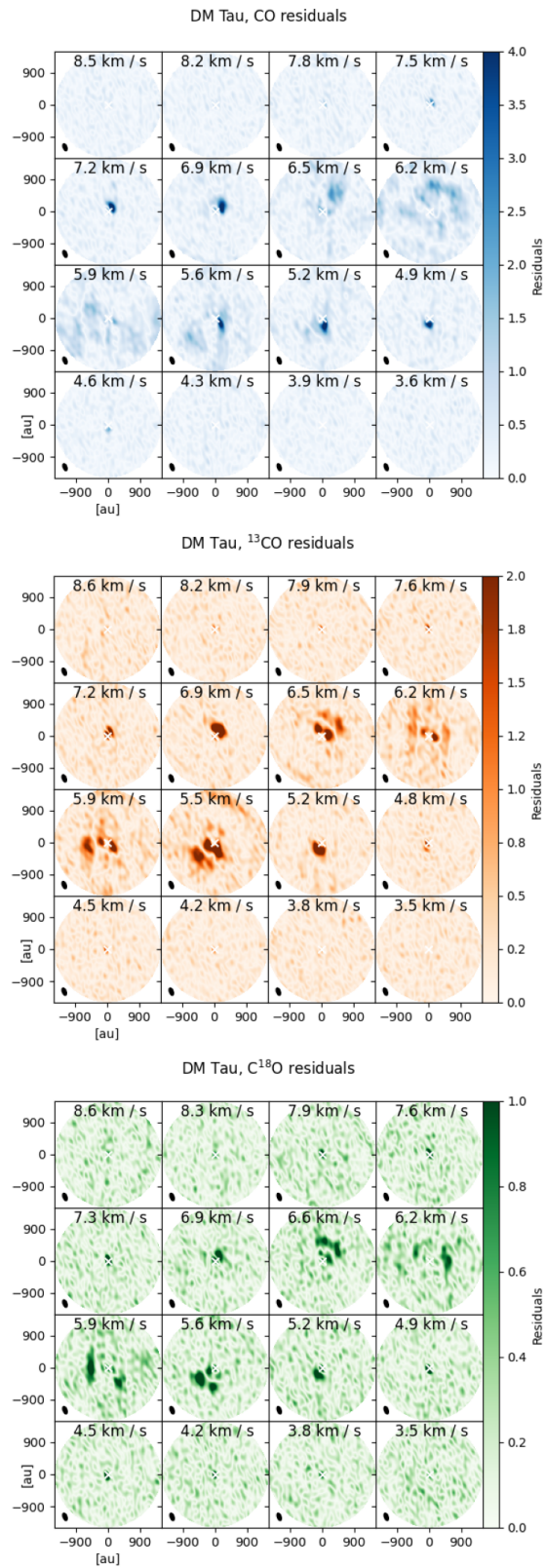


Figure A.8: Residuals of DM Tau best-fit model for the CO, ^{13}CO and C^{18}O isotopologue emission.

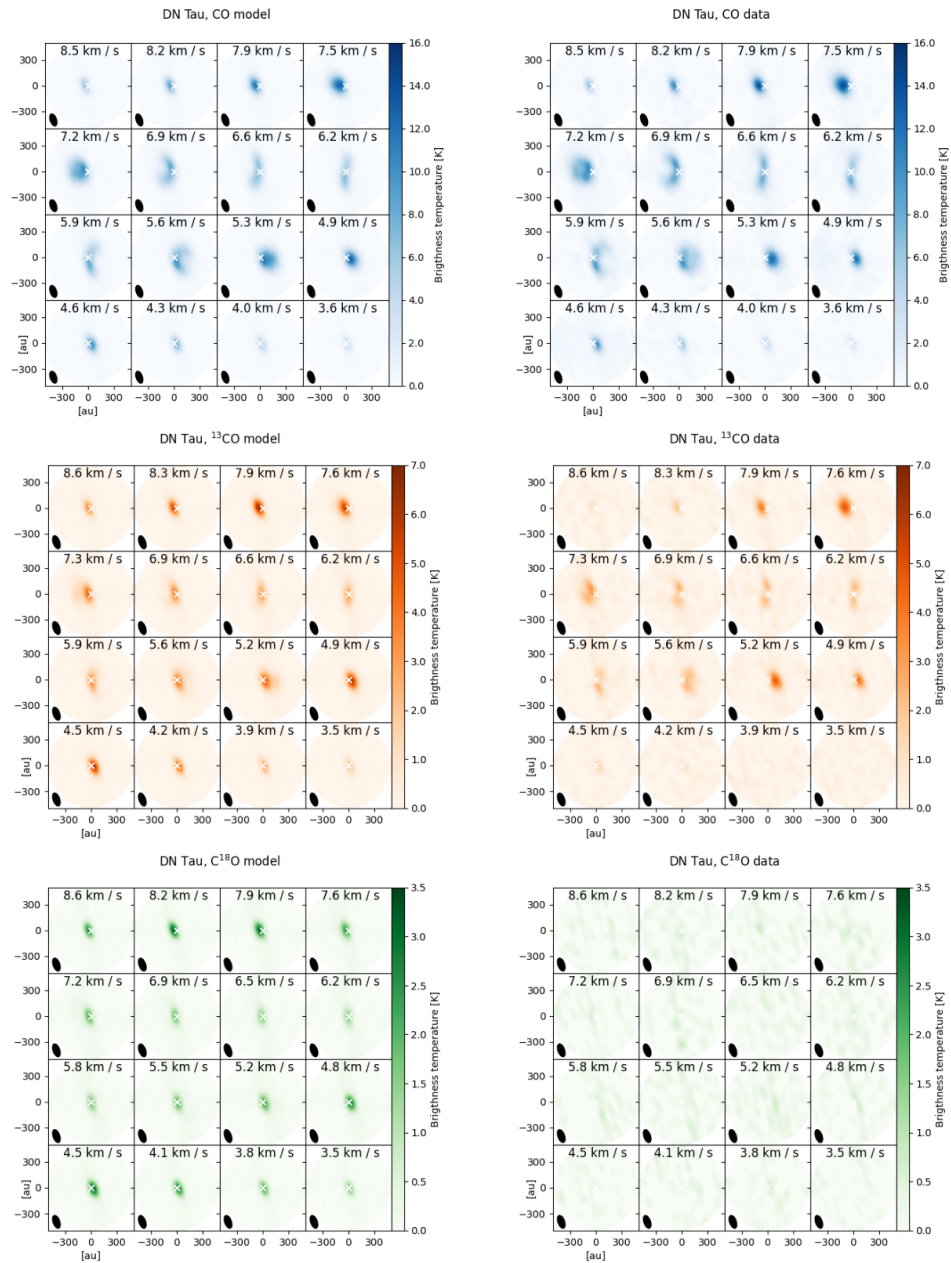


Figure A.9: Comparison between the best-fit model and the observation of DN Tau for the CO, ^{13}CO and C^{18}O isotopologue emission.

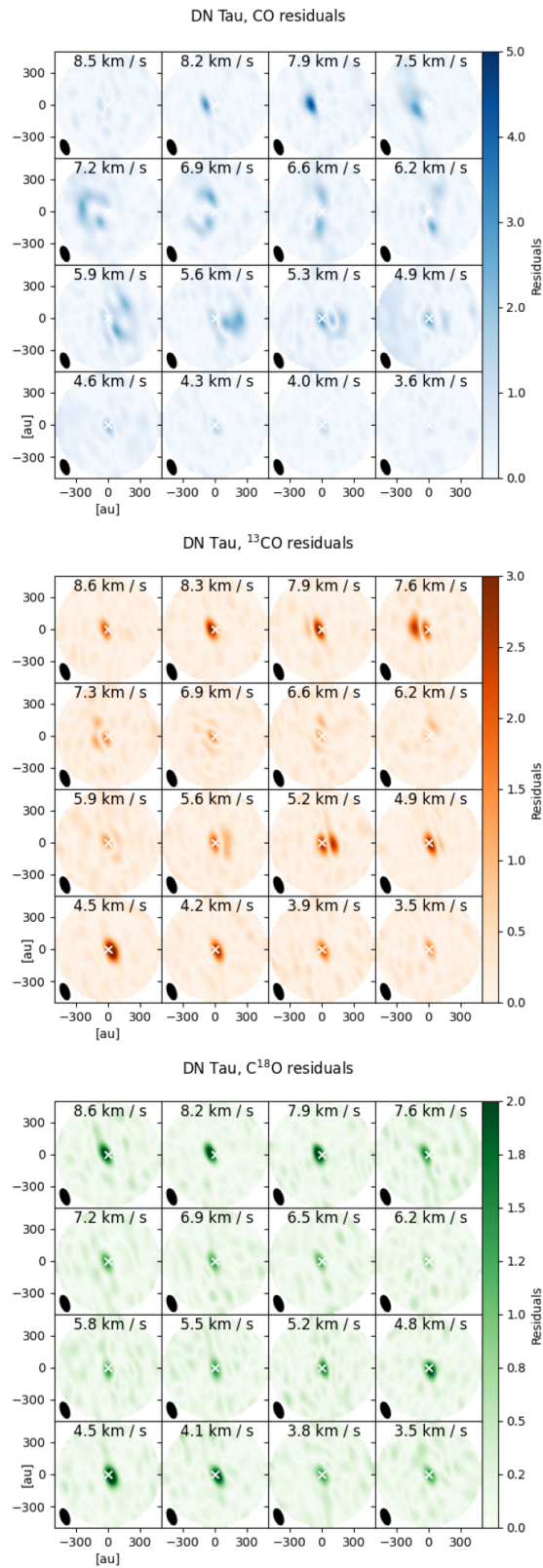


Figure A.10: Residuals of DN Tau best-fit model for the CO, ^{13}CO and C^{18}O isotopologue emission.

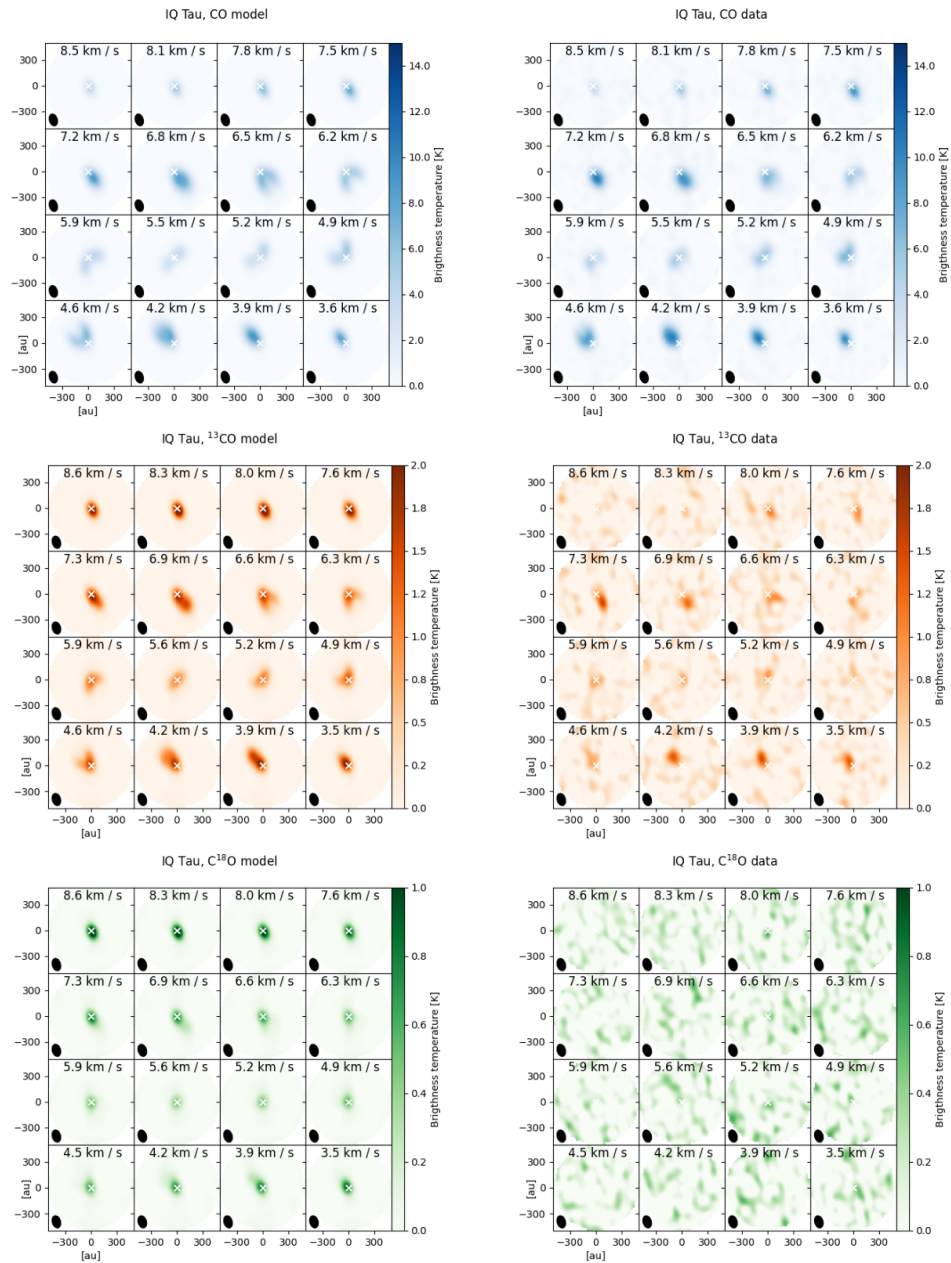


Figure A.11: Comparison between the best-fit model and the observation of IQ Tau for the CO, ^{13}CO and C^{18}O isotopologue emission.

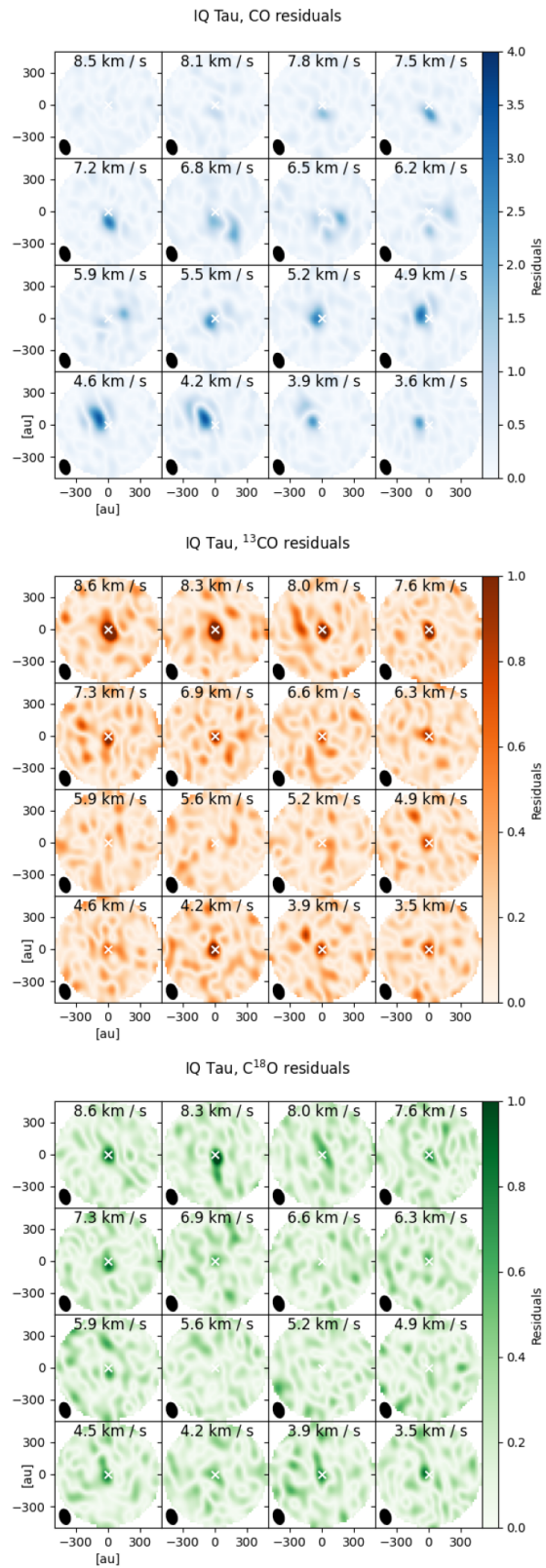


Figure A.12: Residuals of IQ Tau best-fit model for the CO, ^{13}CO and C^{18}O isotopologue emission.

List of Figures

1.1	YSO evolutionary phases.	3
1.2	Dust and gas emission in HD 163296.	6
1.3	Protoplanetary disk structure.	7
1.4	IM Lup continuum and scattered light images.	11
1.5	DSHARP gallery.	12
2.1	Vertical disk structure.	22
3.1	Dust opacity.	37
3.2	Reference model for the dust line parameter study.	39
3.3	Dependence on the disk mass.	40
3.4	Dependence on the stellar mass.	41
3.5	Dependence on the age of the system.	42
3.6	Dependence on the dust to gas ratio.	43
3.7	Dust-to-gas ratio evolution.	44
3.8	Fitting function profile.	45
3.9	Dust line mass estimate.	46
3.10	Posterior probability distribution.	47
3.11	Dust line location with a weak inner bump.	50
3.12	Dust line location with a strong inner bump.	51
3.13	Dust line location with a weak outer bump.	52
3.14	Dust line location with a strong outer bump.	53
3.15	Dust line location with weak bumps.	54
3.16	Dust line in TW Hya.	55
3.17	Brightness and bumpy density profile at 0.87 mm	58
3.18	Brightness and bumpy density profile at 1.3 mm	58
4.1	DSHARP dust opacity.	69
4.2	IM Lup scattered light image.	73
4.3	IM Lup best fit profiles.	77
4.4	Best-fit images.	77

4.5	Best fit posterior distribution.	78
4.6	Model vertical properties.	81
4.7	Micron-size grains vertical distribution.	82
4.8	Submillimeter grains vertical distribution.	82
4.9	Millimeter grains vertical distribution.	83
4.10	Mass ratios for different grain sizes.	84
4.11	Best-fit dust surface density distribution.	85
4.12	Dust time scales.	86
4.13	Turbulence effect on the brightness profile.	88
4.14	Best-fit continuum without outer radius.	89
4.15	Best-fit scattered light without truncation.	90
4.16	Best-fit with truncation	91
5.1	JWST MIRI-MRS continuum-subtracted spectrum of J160532.	96
5.2	J1605 molecular hydrogen lines.	97
5.3	Molecular hydrogen rotational diagram.	99
5.4	J1605 atomic hydrogen recombination lines.	101
5.5	Excitation diagram of atomic hydrogen lines.	102
5.6	Emission lines tracing the accretion rate.	103
5.7	HI (9-7) and HI (7-6) line ratio - Case B model.	105
5.8	Atomic hydrogen line ratios.	107
5.9	HI (9-7) and HI (7-6) line ratio - KF model.	108
5.10	$\dot{M}_{acc} - M_{\star}^2$ diagram.	110
6.1	Outline of the <code>DiskCheF</code> fitting algorithm.	116
6.2	Moment zero map.	119
6.3	Best-fit DM Tau model.	123
6.4	DM Tau model-data comparison.	125
6.5	DM Tau best-fit residuals.	126
A.1	CI Tau model-data comparison.	138
A.2	CI Tau best-fit residuals.	139
A.3	CY Tau model-data comparison.	140
A.4	CY Tau best-fit residuals.	141
A.5	DL Tau model-data comparison.	142
A.6	DL Tau best-fit residuals.	143
A.7	DM Tau model-data comparison.	144
A.8	DM Tau best-fit residuals.	145
A.9	DN Tau model-data comparison.	146
A.10	DN Tau best-fit residuals.	147

A.11 IQ Tau model-data comparison.	148
A.12 IQ Tau best-fit residuals.	149



List of Tables

1.1	Molecular tracers of disk properties.	8
1.2	Key chemical processes in protoplanetary disks.	15
3.1	Physical parameters for the dust line reference model.	39
3.2	Dust line location parameter dependence.	42
3.3	Input parameters of the synthetic disk population.	45
3.4	TW Hya fit parameters	49
3.5	TW Hya mass estimates	53
3.6	Parameter values assumed for TW Hya.	55
3.7	Parameter values assumed for AS 209.	57
4.1	DSHARP dust composition.	69
4.2	IM Lup properties.	71
4.3	IM Lup rings.	72
4.4	IM Lup best fit parameters.	76
5.1	Molecular hydrogen rotational lines parameters.	98
5.2	Atomic hydrogen recombination lines parameters.	102
6.1	Stellar and disk properties.	116
6.2	Best fit of the disk physical parameters.	124

Publications

This thesis is based on these first-authored papers:

- **Franceschi**, Birnstiel, Henning, Pinilla, Semenov, & Zormpas 2022, *Mass determination of protoplanetary disks from dust evolution*, A&A, 657, A74
- **Franceschi**, Birnstiel, Henning, & Sharma 2023, *Constraining the turbulence and the dust disk in IM Lup: Onset of planetesimal formation*, A&A, 671, A125

It also includes the submitted paper:

- **Franceschi**, Henning, Tabone, Perotti, Caratti o Garatti, Bettoni, van Dishoeck, Kamp, Absil, Olofsson, Waters, Arabhavi, Christiaens, Gasman, L. Grant, Jang, Rodgers-Lee, Samland, Schwarz, Temmink, & Güdel, *submitted*, *MINDS: Mid-infrared atomic and molecular hydrogen lines in the inner disk around a low-mass star*, A&A

and one in preparation work:

- **Franceschi**, Henning, Semenov, Dutrey, Chapillon, Guilloteau, van Terwisga, Bouscasse, Caselli, Ceccarelli, Cunningham, Fuente, Hsieh, Lopez-Sepulcre, Segura-Cox, Pineda, Maureira, Möller, Tafalla, & Valdivia-Mena, *in prep.*, *PRODIGE II: modeling the CO isotopologs emission of the T Tauri stars in the Taurus region*

During my doctoral studies, I first-authored the following paper, which is not included in this thesis:

- **Franceschi** & Shore 2022, *A semiempirical approach to low-energy cosmic ray propagation in the diffuse interstellar medium*, A&A, 667, A73

and co-authored the following papers:

- Smirnov-Pinchukov, Molyarova, Semenov, Akimkin, van Terwisga, **Franceschi**, & Henning 2022, *Machine learning-accelerated chemistry modeling of protoplanetary disks*, A&A, 666, L8

- Dietrich, Apai, Schlecker, Hardegree-Ullman, Rackham, Kurtovic, Molaverdikhani, Gabor, Henning, Chen, Mancini, Bixel, Gibbs, Boyle, Brown-Sevilla, Burn, Delage, Flores-Rivera, **Franceschi**, Pichierri, Savvidou, Syed, Bruni, Ip, Ngeow, Tsai, Lin, Hou, Hsiao, Lin, Lin, Basant, & EDEN Project 2023, *EDEN Survey: Small Transiting Planet Detection Limits and Constraints on the Occurrence Rates of Planets around Late-M Dwarfs within 15 pc*, AJ, 165, 149
- Perotti, Christiaens, Henning, Tabone, Waters, Kamp, Olofsson, Grant, Gasman, Bouwman, Samland, **Franceschi**, van Dishoeck, Schwarz, Güdel, Lagage, Ray, Vandenbussche, Abergel, Absil, Arabhavi, Argyriou, Barrado, Boccaletti, Caratti o Garatti, Geers, Glauser, Justannont, Lahuis, Mueller, Nehmé, Pantin, Scheithauer, Waelkens, Guadarrama, Jang, Kanwar, Morales-Calderón, Pawellek, Rodgers-Lee, Schreiber, Colina, Greve, Östlin, & Wright 2023, *Water in the terrestrial planet-forming zone of the PDS 70 disk*, Nature, 620, 516

Bibliography

- Aikawa, Y., Cataldi, G., Yamato, Y., et al. 2021, *ApJS*, 257, 13
- Aikawa, Y., Umebayashi, T., Nakano, T., & Miyama, S. M. 1997, *ApJ*, 486, L51
- Aikawa, Y., van Zadelhoff, G. J., van Dishoeck, E. F., & Herbst, E. 2002, *A&A*, 386, 622
- Alcalá, J. M., Manara, C. F., France, K., et al. 2019, *A&A*, 629, A108
- Alcalá, J. M., Manara, C. F., Natta, A., et al. 2017, *A&A*, 600, A20
- Alcalá, J. M., Natta, A., Manara, C. F., et al. 2014, *A&A*, 561, A2
- An, D., Ramírez, S. V., Sellgren, K., et al. 2011, *ApJ*, 736, 133
- Anderson, D. E., Blake, G. A., Cleeves, L. I., et al. 2021, *ApJ*, 909, 55
- Andrews, S. M. 2015, *PASP*, 127, 961
- Andrews, S. M. 2020, *ARA&A*, 58, 483
- Andrews, S. M., Huang, J., Pérez, L. M., et al. 2018, *ApJ*, 869, L41
- Andrews, S. M., Rosenfeld, K. A., Kraus, A. L., & Wilner, D. J. 2013, *The Astrophysical Journal*, 771, 129
- Andrews, S. M. & Williams, J. P. 2005, *ApJ*, 631, 1134
- Andrews, S. M. & Williams, J. P. 2007, *ApJ*, 671, 1800
- Andrews, S. M., Wilner, D. J., Hughes, A. M., Qi, C., & Dullemond, C. P. 2010, *ApJ*, 723, 1241
- Andrews, S. M., Wilner, D. J., Hughes, A. M., et al. 2012, *ApJ*, 744, 162
- Andrews, S. M., Wilner, D. J., Zhu, Z., et al. 2016, *ApJ*, 820, L40
- Ansdell, M., Williams, J. P., van der Marel, N., et al. 2016, *ApJ*, 828, 46

- Antoniucci, S., García López, R., Nisini, B., et al. 2014, *A&A*, 572, A62
- Antoniucci, S., García López, R., Nisini, B., et al. 2011, *A&A*, 534, A32
- Antoniucci, S., Podio, L., Nisini, B., et al. 2016, *A&A*, 593, L13
- Argyriou, I., Glasse, A., Law, D. R., et al. 2023, *A&A*, 675, A111
- Avenhaus, H., Quanz, S. P., Garufi, A., et al. 2018, *ApJ*, 863, 44
- Bai, X.-N. & Stone, J. M. 2010, *ApJ*, 722, 1437
- Baker, J. G. & Menzel, D. H. 1938, *ApJ*, 88, 52
- Baldovin-Saavedra, C., Audard, M., Carmona, A., et al. 2012, *A&A*, 543, A30
- Baldovin-Saavedra, C., Audard, M., Güdel, M., et al. 2011, *A&A*, 528, A22
- Bally, J. 2016, *ARA&A*, 54, 491
- Barenfeld, S. A., Carpenter, J. M., Ricci, L., & Isella, A. 2016, *ApJ*, 827, 142
- Beck, T. L., Bary, J. S., & McGregor, P. J. 2010, *ApJ*, 722, 1360
- Beck, T. L., McGregor, P. J., Takami, M., & Pyo, T.-S. 2008, *ApJ*, 676, 472
- Beckwith, S. V. W., Sargent, A. I., Chini, R. S., & Guesten, R. 1990, *AJ*, 99, 924
- Bell, K. R., Cassen, P. M., Klahr, H. H., & Henning, T. 1997, *ApJ*, 486, 372
- Bergin, E. A., Cleeves, L. I., Gorti, U., et al. 2013, *Nature*, 493, 644
- Bergin, E. A. & Williams, J. P. 2018, arXiv e-prints, arXiv:1807.09631
- Beuther, H., van Dishoeck, E. F., Tychoniec, L., et al. 2023, *A&A*, 673, A121
- Biazzo, K., Alcalá, J. M., Covino, E., et al. 2012, *A&A*, 547, A104
- Birnstiel, T. & Andrews, S. M. 2014, *ApJ*, 780, 153
- Birnstiel, T., Dullemond, C. P., & Brauer, F. 2010, *A&A*, 513, A79
- Birnstiel, T., Dullemond, C. P., Zhu, Z., et al. 2018, *ApJ*, 869, L45
- Birnstiel, T., Fang, M., & Johansen, A. 2016, *Space Sci. Rev.*, 205, 41
- Birnstiel, T., Klahr, H., & Ercolano, B. 2012, *A&A*, 539, A148
- Birnstiel, T., Ormel, C. W., & Dullemond, C. P. 2011, *A&A*, 525, A11

- Bohren, C. F. & Huffman, D. R. 1998, *Absorption and Scattering of Light by Small Particles*
- Booth, A. S., Walsh, C., Ilee, J. D., et al. 2019, *ApJ*, 882, L31
- Brauer, F., Dullemond, C. P., & Henning, T. 2008, *A&A*, 480, 859
- Bruderer, S. 2013, *A&A*, 559, A46
- Bruderer, S., Doty, S. D., & Benz, A. O. 2009, *ApJS*, 183, 179
- Bruderer, S., van Dishoeck, E. F., Doty, S. D., & Herczeg, G. J. 2012, *A&A*, 541, A91
- Buchner, J. 2016, *Statistics and Computing*, 26, 383
- Buchner, J. 2019, *PASP*, 131, 108005
- Buchner, J. 2021, *The Journal of Open Source Software*, 6, 3001
- Calahan, J. K., Bergin, E. A., Zhang, K., et al. 2021, *ApJS*, 257, 17
- Calvet, N., Muzerolle, J., Briceño, C., et al. 2004, *AJ*, 128, 1294
- Carmona, A., van der Plas, G., van den Ancker, M. E., et al. 2011, *A&A*, 533, A39
- Carpenter, J. M., Ricci, L., & Isella, A. 2014, *ApJ*, 787, 42
- Chiang, E. & Youdin, A. N. 2010, *Annual Review of Earth and Planetary Sciences*, 38, 493
- Chiang, E. I. & Goldreich, P. 1997, *ApJ*, 490, 368
- Cleeves, L. I., Bergin, E. A., & Adams, F. C. 2014, *ApJ*, 794, 123
- Cleeves, L. I., Bergin, E. A., Qi, C., Adams, F. C., & Öberg, K. I. 2015, *ApJ*, 799, 204
- Cleeves, L. I., Öberg, K. I., Wilner, D. J., et al. 2016, *ApJ*, 832, 110
- Cuzzi, J. N., Hogan, R. C., Paque, J. M., & Dobrovolskis, A. R. 2001, *ApJ*, 546, 496
- Dartois, E., Dutrey, A., & Guilloteau, S. 2003, *A&A*, 399, 773
- de Gregorio-Monsalvo, I., Ménard, F., Dent, W., et al. 2013, *A&A*, 557, A133
- Dietrich, J., Apai, D., Schlecker, M., et al. 2023, *AJ*, 165, 149

- Dong, R. & Fung, J. 2017, *ApJ*, 835, 146
- Draine, B. T. 2003, in *Astrophysics of Dust*, 172
- Dressing, C. D. & Charbonneau, D. 2015, *ApJ*, 807, 45
- Dubrulle, B., Morfill, G., & Sterzik, M. 1995, *Icarus*, 114, 237
- Dullemond, C. P., Birnstiel, T., Huang, J., et al. 2018, *ApJ*, 869, L46
- Dullemond, C. P. & Dominik, C. 2004, *A&A*, 421, 1075
- Dullemond, C. P. & Dominik, C. 2005, *A&A*, 434, 971
- Dullemond, C. P., Dominik, C., & Natta, A. 2001, *ApJ*, 560, 957
- Dullemond, C. P., Isella, A., Andrews, S. M., Skobleva, I., & Dzyurkevich, N. 2020, *A&A*, 633, A137
- Dullemond, C. P., Juhasz, A., Pohl, A., et al. 2012a, *RADMC-3D: A multi-purpose radiative transfer tool*
- Dullemond, C. P., Juhasz, A., Pohl, A., et al. 2012b, *RADMC-3D: A multi-purpose radiative transfer tool*, *Astrophysics Source Code Library*, record ascl:1202.015
- Dullemond, C. P., van Zadelhoff, G. J., & Natta, A. 2002, *A&A*, 389, 464
- Dutrey, A., Lecavelier Des Etangs, A., & Augereau, J. C. 2004, in *Comets II*, ed. M. C. Festou, H. U. Keller, & H. A. Weaver, 81
- Dzyurkevich, N., Turner, N. J., Henning, T., & Kley, W. 2013, *ApJ*, 765, 114
- Edwards, S., Kwan, J., Fischer, W., et al. 2013, *ApJ*, 778, 148
- Eistrup, C., Walsh, C., & van Dishoeck, E. F. 2016, *A&A*, 595, A83
- Ercolano, B. & Pascucci, I. 2017, *Royal Society Open Science*, 4, 170114
- Fang, M., Kim, J. S., Pascucci, I., et al. 2017, *AJ*, 153, 188
- Fang, M., Pascucci, I., Edwards, S., et al. 2023, *ApJ*, 945, 112
- Fang, M., van Boekel, R., Wang, W., et al. 2009, *A&A*, 504, 461
- Fedele, D., Tazzari, M., Booth, R., et al. 2018, *A&A*, 610, A24
- Field, G. B., Somerville, W. B., & Dressler, K. 1966, *ARA&A*, 4, 207
- Finkenzeller, U. & Mundt, R. 1984, *A&AS*, 55, 109

- Flaherty, K. M., Hughes, A. M., Rose, S. C., et al. 2017, *ApJ*, 843, 150
- Franceschi**, R., Birnstiel, T., Henning, T., et al. 2022, *A&A*, 657, A74
- Franceschi**, R., Birnstiel, T., Henning, T., & Sharma, A. 2023, *A&A*, 671, A125
- Franceschi**, R. & Shore, S. N. 2022, *A&A*, 667, A73
- Fromang, S. & Nelson, R. P. 2009, *A&A*, 496, 597
- Gaia Collaboration, Prusti, T., de Bruijne, J. H. J., et al. 2016, *A&A*, 595, A1
- Gaia Collaboration, Vallenari, A., Brown, A. G. A., et al. 2022, arXiv e-prints, arXiv:2208.00211
- Gangi, M., Nisini, B., Manara, C. F., et al. 2023, *A&A*, 675, A153
- Gibb, E. L., Whittet, D. C. B., Schutte, W. A., et al. 2000, *ApJ*, 536, 347
- Goldsmith, P. F. & Langer, W. D. 1999, *ApJ*, 517, 209
- Gorti, U., Hollenbach, D., Najita, J., & Pascucci, I. 2011, *ApJ*, 735, 90
- Gorti, U., Liseau, R., Sándor, Z., & Clarke, C. 2016, *Space Sci. Rev.*, 205, 125
- Grady, C. A., Devine, D., Woodgate, B., et al. 2000, *ApJ*, 544, 895
- Grady, C. A., Schneider, G., Sitko, M. L., et al. 2009, *ApJ*, 699, 1822
- Gravity Collaboration, Wojtczak, J. A., Labadie, L., et al. 2023, *A&A*, 669, A59
- Güdel, M., Lahuis, F., Briggs, K. R., et al. 2010, *A&A*, 519, A113
- Gullbring, E., Hartmann, L., Briceño, C., & Calvet, N. 1998a, *ApJ*, 492, 323
- Gullbring, E., Hartmann, L., Briceño, C., & Calvet, N. 1998b, *ApJ*, 492, 323
- Gundlach, B., Kiliyas, S., Beitz, E., & Blum, J. 2011, *Icarus*, 214, 717
- Güttler, C., Blum, J., Zsom, A., Ormel, C. W., & Dullemond, C. P. 2010, *A&A*, 513, A56
- Harsono, D., Bruderer, S., & van Dishoeck, E. F. 2015, *A&A*, 582, A41
- Hartmann, L., Herczeg, G., & Calvet, N. 2016, *ARA&A*, 54, 135
- Hashimoto, J., Tamura, M., Muto, T., et al. 2011, *ApJ*, 729, L17
- Henning, T. & Semenov, D. 2013, *Chemical Reviews*, 113, 9016

- Henning, T. & Stognienko, R. 1996, *A&A*, 311, 291
- Herbig, G. H. 1960, *ApJS*, 4, 337
- Herczeg, G. J. & Hillenbrand, L. A. 2008, *ApJ*, 681, 594
- Hsieh, T. H., Segura-Cox, D. M., Pineda, J. E., et al. 2022, arXiv e-prints, arXiv:2211.05022
- Huang, J., Andrews, S. M., Dullemond, C. P., et al. 2018a, *ApJ*, 869, L42
- Huang, J., Andrews, S. M., Pérez, L. M., et al. 2018b, *ApJ*, 869, L43
- Huang, J., Öberg, K. I., & Andrews, S. M. 2016, *ApJ*, 823, L18
- Huang, J., Öberg, K. I., Qi, C., et al. 2017, *ApJ*, 835, 231
- Hughes, A. M., Wilner, D. J., Andrews, S. M., Qi, C., & Hogerheijde, M. R. 2011, *ApJ*, 727, 85
- Johansen, A. & Klahr, H. 2005, *ApJ*, 634, 1353
- Johansen, A., Klahr, H., & Mee, A. J. 2006, *MNRAS*, 370, L71
- Johansen, A., Youdin, A., & Mac Low, M.-M. 2009, *ApJ*, 704, L75
- Jönsson, H., Holtzman, J. A., Allende Prieto, C., et al. 2020, *AJ*, 160, 120
- Joy, A. H. 1942, *ApJ*, 96, 344
- Joy, A. H. 1945, *ApJ*, 102, 168
- Joy, A. H. 1949, *ApJ*, 110, 424
- Kama, M., Bruderer, S., van Dishoeck, E. F., et al. 2016, *A&A*, 592, A83
- Kama, M., Trapman, L., Fedele, D., et al. 2020, *A&A*, 634, A88
- Kanagawa, K. D., Tanaka, H., Muto, T., Tanigawa, T., & Takeuchi, T. 2015, *MNRAS*, 448, 994
- Kenyon, S. J. & Hartmann, L. 1987, *ApJ*, 323, 714
- Krijt, S., Bosman, A. D., Zhang, K., et al. 2020, *ApJ*, 899, 134
- Krijt, S., Ormel, C. W., Dominik, C., & Tielens, A. G. G. M. 2015, *A&A*, 574, A83
- Kwan, J. & Fischer, W. 2011, *MNRAS*, 411, 2383

- Labiano, A., Argyriou, I., Álvarez-Márquez, J., et al. 2021, *A&A*, 656, A57
- Lahuis, F., van Dishoeck, E. F., Blake, G. A., et al. 2007, *ApJ*, 665, 492
- Lambrechts, M. & Johansen, A. 2014, *A&A*, 572, A107
- Law, C. J., Crystian, S., Teague, R., et al. 2022, *ApJ*, 932, 114
- Law, C. J., Teague, R., Loomis, R. A., et al. 2021, *ApJS*, 257, 4
- Li, H., Finn, J. M., Lovelace, R. V. E., & Colgate, S. A. 2000, *ApJ*, 533, 1023
- Liu, H. B. 2019, *ApJ*, 877, L22
- Lodato, G., Rampinelli, L., Viscardi, E., et al. 2023, *MNRAS*, 518, 4481
- Long, F., Herczeg, G. J., Harsono, D., et al. 2019, *ApJ*, 882, 49
- Long, F., Herczeg, G. J., Pascucci, I., et al. 2017, *ApJ*, 844, 99
- Long, F., Pinilla, P., Herczeg, G. J., et al. 2020, *ApJ*, 898, 36
- Long, F., Pinilla, P., Herczeg, G. J., et al. 2018, *ApJ*, 869, 17
- Lovelace, R. V. E., Li, H., Colgate, S. A., & Nelson, A. F. 1999, *ApJ*, 513, 805
- Luhman, K. L., Herrmann, K. A., Mamajek, E. E., Esplin, T. L., & Pecaut, M. J. 2018, *AJ*, 156, 76
- Lynden-Bell, D. & Pringle, J. E. 1974, *MNRAS*, 168, 603
- Manara, C. F., Ansdell, M., Rosotti, G. P., et al. 2023, in *Astronomical Society of the Pacific Conference Series*, Vol. 534, *Astronomical Society of the Pacific Conference Series*, ed. S. Inutsuka, Y. Aikawa, T. Muto, K. Tomida, & M. Tamura, 539
- Manara, C. F., Frasca, A., Venuti, L., et al. 2021, *A&A*, 650, A196
- Manara, C. F., Rosotti, G., Testi, L., et al. 2016, *A&A*, 591, L3
- Manara, C. F., Testi, L., Herczeg, G. J., et al. 2017, *A&A*, 604, A127
- Mathis, J. S., Rumpl, W., & Nordsieck, K. H. 1977, *ApJ*, 217, 425
- McClure, M. K., Bergin, E. A., Cleeves, L. I., et al. 2016, *ApJ*, 831, 167
- Menu, J., van Boekel, R., Henning, T., et al. 2014, *A&A*, 564, A93
- Miguel, Y., Guilera, O. M., & Brunini, A. 2011, *MNRAS*, 417, 314

- Millar, T. J., Walsh, C., Cordiner, M. A., Ní Chuimín, R., & Herbst, E. 2007, *ApJ*, 662, L87
- Miotello, A., Bruderer, S., & van Dishoeck, E. F. 2014, *A&A*, 572, A96
- Miotello, A., Facchini, S., van Dishoeck, E. F., & Bruderer, S. 2018, *A&A*, 619, A113
- Miotello, A., Kamp, I., Birnstiel, T., Cleeves, L. I., & Kataoka, A. 2022, arXiv e-prints, arXiv:2203.09818
- Miotello, A., van Dishoeck, E. F., Kama, M., & Bruderer, S. 2016, *A&A*, 594, A85
- Miotello, A., van Dishoeck, E. F., Williams, J. P., et al. 2017, *A&A*, 599, A113
- Miret-Roig, N., Galli, P. A. B., Olivares, J., et al. 2022, *A&A*, 667, A163
- Molinari, S., Faustini, F., Testi, L., et al. 2008, *A&A*, 487, 1119
- Molyarova, T., Akimkin, V., Semenov, D., et al. 2017, *ApJ*, 849, 130
- Monnier, J. D., Harries, T. J., Aarnio, A., et al. 2017, *ApJ*, 838, 20
- Morbidelli, A. & Raymond, S. N. 2016, *Journal of Geophysical Research (Planets)*, 121, 1962
- Mordasini, C., Alibert, Y., Klahr, H., & Henning, T. 2012, *A&A*, 547, A111
- Mulders, G. D., Min, M., Dominik, C., Debes, J. H., & Schneider, G. 2013, *A&A*, 549, A112
- Musiolik, G. & Wurm, G. 2019, *ApJ*, 873, 58
- Muzerolle, J., Hartmann, L., & Calvet, N. 1998, *AJ*, 116, 2965
- Nakagawa, Y., Sekiya, M., & Hayashi, C. 1986, *Icarus*, 67, 375
- Natta, A., Testi, L., & Randich, S. 2006, *A&A*, 452, 245
- Öberg, K. I. & Bergin, E. A. 2021, *Phys. Rep.*, 893, 1
- Öberg, K. I., Guzmán, V. V., Walsh, C., et al. 2021, *ApJS*, 257, 1
- Öberg, K. I., Murray-Clay, R., & Bergin, E. A. 2011, *ApJ*, 743, L16
- Ormel, C. W. & Cuzzi, J. N. 2007, *A&A*, 466, 413
- Padovani, M., Ivlev, A. V., Galli, D., & Caselli, P. 2018, *A&A*, 614, A111

-
- Paneque-Carreño, T., Miotello, A., van Dishoeck, E. F., et al. 2023, *A&A*, 669, A126
- Panić, O., Hogerheijde, M. R., Wilner, D., & Qi, C. 2009, *A&A*, 501, 269
- Pascucci, I., Gorti, U., Hollenbach, D., et al. 2006, *ApJ*, 651, 1177
- Pascucci, I., Herczeg, G., Carr, J. S., & Bruderer, S. 2013, *ApJ*, 779, 178
- Pascucci, I., Hollenbach, D., Najita, J., et al. 2007, *ApJ*, 663, 383
- Pascucci, I., Skinner, B. N., Deng, D., et al. 2023, arXiv e-prints, arXiv:2307.02704
- Pedregosa, F., Varoquaux, G., Gramfort, A., et al. 2011, *Journal of Machine Learning Research*, 12, 2825
- Pérez, L. M., Chandler, C. J., Isella, A., et al. 2015, *ApJ*, 813, 41
- Perotti, G., Christiaens, V., Henning, T., et al. 2023, *Nature*, 620, 516
- Pinilla, P., Benisty, M., & Birnstiel, T. 2012, *A&A*, 545, A81
- Pinilla, P., Lenz, C. T., & Stammler, S. M. 2021, *A&A*, 645, A70
- Pinilla, P., Pascucci, I., & Marino, S. 2020, *A&A*, 635, A105
- Pinilla, P., van der Marel, N., Pérez, L. M., et al. 2015, *A&A*, 584, A16
- Pinte, C., Dent, W. R. F., Ménard, F., et al. 2016, *ApJ*, 816, 25
- Pinte, C., Ménard, F., Duchêne, G., et al. 2018, *A&A*, 609, A47
- Pinte, C., Padgett, D. L., Ménard, F., et al. 2008, *A&A*, 489, 633
- Pohl, A. 2018, PhD thesis, Heidelberg University, Germany
- Powell, D., Gao, P., Murray-Clay, R., & Zhang, X. 2022, *Nature Astronomy*, 6, 1147
- Powell, D., Murray-Clay, R., Pérez, L. M., Schlichting, H. E., & Rosenthal, M. 2019, *ApJ*, 878, 116
- Powell, D., Murray-Clay, R., & Schlichting, H. E. 2017, *ApJ*, 840, 93
- Pringle, J. E. 1981, *ARA&A*, 19, 137
- Ricci, L., Maddison, S. T., Wilner, D., et al. 2015, *ApJ*, 813, 138
- Rich, E. A., Teague, R., Monnier, J. D., et al. 2021, *ApJ*, 913, 138

- Rieke, G. H., Wright, G. S., Böker, T., et al. 2015, *PASP*, 127, 584
- Rigliaco, E., Natta, A., Testi, L., et al. 2012, *A&A*, 548, A56
- Rigliaco, E., Pascucci, I., Duchene, G., et al. 2015, *ApJ*, 801, 31
- Rosenfeld, K. A., Qi, C., Andrews, S. M., et al. 2012, *ApJ*, 757, 129
- Rosotti, G. P., Booth, R. A., Tazzari, M., et al. 2019, *MNRAS*, 486, L63
- Rosotti, G. P., Teague, R., Dullemond, C., Booth, R. A., & Clarke, C. J. 2020, *MNRAS*, 495, 173
- Ruud, M., Gorti, U., & Hollenbach, D. J. 2022, *ApJ*, 925, 49
- Sabotta, S., Schlecker, M., Chaturvedi, P., et al. 2021, *A&A*, 653, A114
- Salyk, C., Herczeg, G. J., Brown, J. M., et al. 2013, *ApJ*, 769, 21
- Schräpler, R. & Henning, T. 2004, *ApJ*, 614, 960
- Schwarz, K. R., Bergin, E. A., Cleeves, L. I., et al. 2016, *ApJ*, 823, 91
- Schwarz, K. R., Bergin, E. A., Cleeves, L. I., et al. 2018, *ApJ*, 856, 85
- Schwarz, K. R., Calahan, J. K., Zhang, K., et al. 2021, *ApJS*, 257, 20
- Semenov, D., Hersant, F., Wakelam, V., et al. 2010, *A&A*, 522, A42
- Semenov, D. & Wiebe, D. 2011, *ApJS*, 196, 25
- Shakura, N. I. & Sunyaev, R. A. 1973, *A&A*, 500, 33
- Shu, F. H., Adams, F. C., & Lizano, S. 1987, *ARA&A*, 25, 23
- Simon, M., Guilloteau, S., Beck, T. L., et al. 2019, *ApJ*, 884, 42
- Smirnov-Pinchukov, G. V., Molyarova, T., Semenov, D. A., et al. 2022, *A&A*, 666, L8
- Smirnov-Pinchukov, G. V., Semenov, D. A., Akimkin, V. V., & Henning, T. 2020, *A&A*, 644, A4
- Stapelfeldt, K. R., Duchêne, G., Perrin, M., et al. 2014, in *Exploring the Formation and Evolution of Planetary Systems*, ed. M. Booth, B. C. Matthews, & J. R. Graham, Vol. 299, 99–103
- Storey, P. J. & Hummer, D. G. 1995, *MNRAS*, 272, 41

- Strom, S. E., Strom, K. M., & Grasdalen, G. L. 1975, *ARA&A*, 13, 187
- Tabone, B., Bettoni, G., van Dishoeck, E. F., et al. 2023, *Nature Astronomy* [[arXiv]2304.05954]
- Tazzari, M., Beaujean, F., & Testi, L. 2018, *Monthly Notices of the Royal Astronomical Society*, 476, 4527
- Tazzari, M., Clarke, C. J., Testi, L., et al. 2021, *MNRAS*, 506, 2804
- Tazzari, M., Testi, L., Ercolano, B., et al. 2016, *A&A*, 588, A53
- Teague, R. 2019, *The Journal of Open Source Software*, 4, 1632
- Teague, R., Semenov, D., Guilloteau, S., et al. 2015, *A&A*, 574, A137
- Terebey, S., Shu, F. H., & Cassen, P. 1984, *ApJ*, 286, 529
- Testi, L., Birnstiel, T., Ricci, L., et al. 2014, in *Protostars and Planets VI*, ed. H. Beuther, R. S. Klessen, C. P. Dullemond, & T. Henning, 339–361
- Thi, W. F., Mathews, G., Ménard, F., et al. 2010, *A&A*, 518, L125
- Thi, W. F., van Dishoeck, E. F., Blake, G. A., et al. 2001, *ApJ*, 561, 1074
- Trapman, L., Miotello, A., Kama, M., van Dishoeck, E. F., & Bruderer, S. 2017, *A&A*, 605, A69
- Trapman, L., Zhang, K., van’t Hoff, M. L. R., Hogerheijde, M. R., & Bergin, E. A. 2022, *ApJ*, 926, L2
- Tripathi, A., Andrews, S. M., Birnstiel, T., & Wilner, D. J. 2017, *The Astrophysical Journal*, 845, 44
- Valdivia-Mena, M. T., Pineda, J. E., Segura-Cox, D. M., et al. 2022, *A&A*, 667, A12
- van Boekel, R., Güdel, M., Henning, T., Lahuis, F., & Pantin, E. 2009, *A&A*, 497, 137
- van den Ancker, M. E., Wesseliuss, P. R., & Tielens, A. G. G. M. 2000, *A&A*, 355, 194
- van Dishoeck, E. F., Wright, C. M., Cernicharo, J., et al. 1998, *ApJ*, 502, L173
- van Zadelhoff, G. J., van Dishoeck, E. F., Thi, W. F., & Blake, G. A. 2001, *A&A*, 377, 566

- Venuti, L., Bouvier, J., Flaccomio, E., et al. 2014, *A&A*, 570, A82
- Venuti, L., Stelzer, B., Alcalá, J. M., et al. 2019, *A&A*, 632, A46
- Villenave, M., Ménard, F., Dent, W. R. F., et al. 2020, *A&A*, 642, A164
- Visser, R., van Dishoeck, E. F., & Black, J. H. 2009, *A&A*, 503, 323
- Wada, K., Tanaka, H., Suyama, T., Kimura, H., & Yamamoto, T. 2009, *ApJ*, 702, 1490
- Walsh, C., Millar, T. J., Nomura, H., et al. 2014, *A&A*, 563, A33
- Warren, S. G. & Brandt, R. E. 2008, *Journal of Geophysical Research (Atmospheres)*, 113, D14220
- Weidenschilling, S. J. 1977, *MNRAS*, 180, 57
- Wells, M., Pel, J. W., Glasse, A., et al. 2015, *PASP*, 127, 646
- Whipple, F. L. 1972, in *From Plasma to Planet*, ed. A. Elvius, 211
- Wichmann, R., Bastian, U., Krautter, J., Jankovics, I., & Rucinski, S. M. 1998, *MNRAS*, 301, L39
- Williams, J. P. & Best, W. M. J. 2014, *ApJ*, 788, 59
- Williams, J. P. & Cieza, L. A. 2011, *ARA&A*, 49, 67
- Woitke, P., Min, M., Pinte, C., et al. 2016, *A&A*, 586, A103
- Wright, G. S., Rieke, G. H., Glasse, A., et al. 2023, *PASP*, 135, 048003
- Wright, G. S., Wright, D., Goodson, G. B., et al. 2015, *PASP*, 127, 595
- Yorke, H. W. & Bodenheimer, P. 2008, in *Astronomical Society of the Pacific Conference Series*, Vol. 387, *Massive Star Formation: Observations Confront Theory*, ed. H. Beuther, H. Linz, & T. Henning, 189
- Yoshida, T. C., Nomura, H., Tsukagoshi, T., Furuya, K., & Ueda, T. 2022, *ApJ*, 937, L14
- Youdin, A. N. & Lithwick, Y. 2007, *Icarus*, 192, 588
- Zhang, K., Bergin, E. A., Blake, G. A., Cleaves, L. I., & Schwarz, K. R. 2017, *Nature Astronomy*, 1, 0130
- Zhang, K., Booth, A. S., Law, C. J., et al. 2021, *ApJS*, 257, 5

Zhang, K., Schwarz, K. R., & Bergin, E. A. 2020, *ApJ*, 891, L17

Zhang, S., Zhu, Z., Huang, J., et al. 2018, *ApJ*, 869, L47

Zhu, Z., Zhang, S., Jiang, Y.-F., et al. 2019, *ApJ*, 877, L18

Zsom, A., Ormel, C. W., Dullemond, C. P., & Henning, T. 2011, *A&A*, 534, A73

Zsom, A., Ormel, C. W., Güttler, C., Blum, J., & Dullemond, C. P. 2010, *A&A*, 513, A57

Acknowledgements

Looking back at these past four years, I realize this has been the most significant and shaping time of my life, both scientifically and personally. I am most grateful I have been given this opportunity, and to all the people who made this possible.

I want to express my profound gratitude, starting with my supervisor, Thomas for giving me this opportunity, I am grateful for his unwavering support and guidance, and I will forever appreciate his role in my journey. A heartfelt thank you goes to Dima, whose invaluable assistance, kindness, and guidance supported me during the most challenging phases of my scientific development. I extend my deep appreciation to Greg, his friendship and mentorship made it possible for me to accomplish everything I have.

To all the friends at MPIA. They not only created an incredibly enjoyable and welcoming environment but also offered invaluable support by engaging in discussions, facing challenges together, and most of all for all the coffee breaks. I wish you all good luck for all that has to come after this time we shared together.

To the Italiani ad HD, you've been a constant reminder of our home during these years far away. And, of course, a profound thank you to Giulia for everything we've shared together.

Finally, my deepest thanks to my family. You have been my anchor even from afar. Without your unconditional support, this would not have been possible. I know I can always count on you, and I will always be grateful.